

FIRST DETECTION OF COHERENT ELASTIC
NEUTRINO-NUCLEUS SCATTERING ON AN ARGON TARGET

Jacob C. Zetlemoyer

Submitted to the faculty of the University Graduate School

in partial fulfillment of the requirements

for the degree

Doctor of Philosophy

in the Department of Physics,

Indiana University

May 2020

Accepted by the Graduate Faculty, Indiana University, in partial fulfillment of the requirements
for the degree of Doctor of Philosophy.

Doctoral Committee

Rex Tayloe, Ph.D.

Mark Messier, Ph.D.

Emilie Passemar, Ph.D.

W. Michael Snow, Ph.D.

April 24, 2020

Copyright © 2020

Jacob C. Zettlemoyer

ACKNOWLEDGMENTS

First I want to thank my parents, who have wholeheartedly supported me throughout my graduate school career. They were always there whenever I needed support to get me through to the end of this work.

To my thesis advisor, Prof. Rex Tayloe, I thank you for everything you have done for me during my time at IU. You gave me an opportunity to achieve my goals when I joined your group after my second year at IU. I always appreciate your willingness to spend the time necessary explaining a concept until I understand it and have a path forward. Thank you for your support and help over the years.

I would also like to thank Lisa Kaufman and Josh Albert for allowing me to get started with research work and their patience with a young graduate student learning the ropes of simulation and analysis during my first two years at IU.

I want to thank Ivan Tolstukhin for his help teaching me how to operate the CENNS-10 detector and working with me in detector operations and the analysis of the data. His contributions to the project made this work possible.

Next I need to thank Mike Febraro for all of his help and support. It's safe to say without his knowledge and patience at the beginning of my time at Oak Ridge that the CENNS-10 detector upgrade would not have been successful. I always enjoy our conversations about the next new idea that comes to his mind. I look forward to working together in the future.

I also want to thank Jason Newby, whose help is always greatly appreciated in shepherding the necessary technical and support work through to the end. He is always ready to lend a hand and his mentorship during my time at Oak Ridge in the detector operation and analysis was invaluable.

I had the support of many people within the COHERENT collaboration while I was stationed at Oak Ridge National Laboratory for the CENNS-10 detector work and performing the data analysis. Also, I need to mention the generous support of the staff at the Spallation Neutron

Source at Oak Ridge National Laboratory for allowing us to install the CENNS-10 detector in the basement and for all the technical support we received over the duration of the experiment.

I would also like to thank Fermilab for the continued loan of the CENNS-10 detector to IU for use in COHERENT and to Jonghee Yoo for his vision to design and build the CENNS-10 detector. Without their generosity none of this work is possible.

I would like to thank the friends I have made over my time at IU, especially among my classmates as we navigated the rigors of graduate school. I appreciate your friendship and all the memories we have made.

I would like to thank the United States Department of Energy Office of Science for awarding me their Graduate Student Research Fellowship. The award covered part of my time at Oak Ridge working on the CENNS-10 detector upgrades and preliminary analysis studies. The award gave me valuable experience working at a national laboratory and in close proximity to the detector that is the focus of this work.

Finally, my research committee: Mark Messier, Emilie Passemar, and Michael Snow, for their time in evaluating my work.

Jacob C. Zettlemoyer

FIRST DETECTION OF COHERENT ELASTIC NEUTRINO-NUCLEUS SCATTERING ON
AN ARGON TARGET

Coherent elastic neutrino-nucleus scattering (CEvNS) was first proposed in 1974 but eluded detection for 40 years. The COHERENT collaboration made the first observation of CEvNS at the Oak Ridge National Laboratory Spallation Neutron Source (SNS) with a 14.6 kg CsI[Na] detector. One of the physics goals of the COHERENT experiment is to test the square of the neutron number dependence of the CEvNS cross section predicted in the Standard Model by observing CEvNS in multiple nuclei. To that end, the ~ 24 kg CENNS-10 liquid argon detector was deployed at the low-background Neutrino Alley at the SNS in early 2017. The detector was upgraded to allow for sensitivity to CEvNS in mid-2017. We analyzed 1.5 years of data taken after this upgrade to provide the first detection of CEvNS on an argon nucleus at $> 3\sigma$ significance. The measured CEvNS cross section of $(2.3 \pm 0.7) \times 10^{-39}$ cm², averaged over the incident neutrino flux, is consistent with the Standard Model prediction. This result represents a detection of CEvNS on the lightest nuclei so far and improves bounds on beyond-the-standard-model physics in the form of non-standard neutrino interactions.

Rex Tayloe, Ph.D.

Mark Messier, Ph.D.

Emilie Passemar, Ph.D.

W. Michael Snow, Ph.D.

CONTENTS

1	Coherent Elastic Neutrino Nucleus Scattering (CEvNS)	1
1.1	The CEvNS Process	1
1.2	Beyond-the-Standard-Model Interactions	5
1.3	Dark Matter Searches and the "Neutrino Floor"	8
1.3.1	WIMP Direct Detection	8
1.3.2	sub-GeV Dark Matter	9
1.4	Nuclear Structure	10
1.5	Supernova Neutrino Detection	12
1.6	Summary	13
2	The COHERENT Experiment at the Spallation Neutron Source	14
2.1	The Spallation Neutron Source	14
2.1.1	The SNS as a Neutrino Source	15
2.2	The COHERENT Experiment at the SNS	17
2.2.1	Neutrino Alley and the COHERENT Program	17
2.2.2	First observation of CEvNS with CsI[Na]	18
2.3	Background Measurements at the SNS	20
2.3.1	Beam-unrelated backgrounds	20
2.3.2	Beam-related backgrounds	22
2.4	Other CEvNS Searches Around the World	26
3	The CENNS-10 Liquid Argon Detector	28
3.1	Liquid Argon as a CEvNS Target Nucleus	28
3.1.1	LAr Quenching Factor Analysis	32
3.2	The CENNS-10 Detector	32

3.2.1	Inner Detector Cryostat	34
3.2.2	Cryogenic and Gas Handling Systems	35
3.2.3	Data Acquisition System	36
3.2.4	Detector Shielding	39
3.3	CENNS-10 Photon Collection System Upgrade	41
3.4	CENNS-10 SNS Production Run Operation	44
3.4.1	CENNS-10 Triggering Scheme	47
3.4.2	CENNS-10 Run Selection	49
4	Calibration of the CENNS-10 Detector	52
4.1	The daqman Framework	52
4.1.1	Event Integration Algorithm	55
4.2	Single Photoelectron Calibration	58
4.3	Detector Response Calibration	61
4.4	The $^{83\text{m}}\text{Kr}$ Calibration Source	64
4.4.1	$^{83\text{m}}\text{Kr}$ Injection System Design	66
4.4.2	$^{83\text{m}}\text{Kr}$ Source Deposition	71
4.4.3	Calibration of CENNS-10 using $^{83\text{m}}\text{Kr}$	72
4.5	CENNS-10 Neutron Calibrations	77
5	Simulation of the CENNS-10 Detector	80
5.1	Overview	80
5.2	Detector Geometry	80
5.3	The Optical Model and Tuning to Data	82
5.3.1	Liquid Argon Scintillation and Wavelength Shifting	82
5.3.2	Comparison with Calibration Data	83
5.4	Event Simulations	87

5.4.1	Beam-Unrelated Background Simulations	88
5.4.2	CEvNS Simulation	89
5.4.3	NINs Simulation	90
5.4.4	Beam-related Neutron Simulation	91
5.5	Simulated Efficiencies	92
5.5.1	Waveform Cuts	93
5.5.2	Event Cuts	94
5.5.3	Summary of Efficiencies	96
6	Beam-Related Neutron Studies with the CENNS-10 Detector	98
6.1	Run Summary and Analysis Regions	98
6.2	F_{90} Cut Formation	99
6.2.1	Figure of Merit	100
6.2.2	Cut Formation	101
6.3	Event Selection	104
6.4	Signal Predictions	104
6.5	Pre-Beam Region Analysis	105
6.6	Beam-Related Neutron Analysis	106
6.6.1	Systematic Effects	108
6.6.2	χ^2 Analysis in Prompt Region	111
6.6.3	Beam-Related Neutron Arrival Time	112
6.6.4	Delayed Region Investigations	114
6.7	Summary	115
7	First Detection of CEvNS with the CENNS-10 Detector	117
7.1	Run Summary and Analysis Regions	117
7.2	Event Selection	118

7.3	Single-Bin Counting Experiment	118
7.3.1	Signal/Background Predictions	118
7.3.2	Rate Systematic Effects	120
7.3.3	Pre-Unblinding Checks	122
7.3.4	Prompt Region	126
7.3.5	Delayed Region	128
7.4	3D Binned Likelihood Analysis	130
7.4.1	PDF Generation	130
7.4.2	Pseudo-data Studies	136
7.4.3	Likelihood Fit Systematic Errors	139
7.4.4	Fit to Data	142
7.4.5	Measurement of CEvNS Cross Section	144
7.4.6	Constraints on Non-Standard Neutrino Interactions	147
8	Conclusions	150
	Bibliography	153
A	Tuned Simulation Parameters	167
	Curriculum Vitae	

LIST OF FIGURES

1.1	CEvNS cross section	2
1.2	Standard Model CEvNS recoil spectra	4
1.3	Weak mixing angle with CsI[Na]	5
1.4	COHERENT NSI limits	6
1.5	Dark Matter Limits and the “neutrino floor”	9
1.6	sub-GeV dark matter exclusion limits with tonne-scale LAr detector in COHERENT	11
2.1	SNS neutrino energy and timing spectra	16
2.2	Current COHERENT detectors	18
2.3	Future COHERENT detectors	19
2.4	First observation of CEvNS on a CsI[Na] target	20
2.5	SNS beam-related neutron measurements	24
2.6	Beam-related neutron flux measurement with SciBath detector	25
3.1	Liquid argon scintillation diagram	29
3.2	LAr SM predicted CEvNS recoil spectrum	31
3.3	World LAr quenching factor data	31
3.4	World LAr quenching factor data fit	33
3.5	The CENNS-10 detector	34
3.6	The CENNS-10 plumbing diagram	37
3.7	CENNS-10 Slow Monitoring System	39
3.8	CENNS-10 Installation in Neutrino Alley	40
3.9	Test operation of bell jar evaporator	42
3.10	Spectrometer measurement of TPB-coated parts	43
3.11	Rotating system for TPB coating of Teflon cylinder pieces	44

3.12	Teflon cylinder section after TPB coating in ORNL evaporator	45
3.13	CENNS-10 inner detector volume after photon collection upgrade	46
3.14	Temperatures and level reading during CENNS-10 detector fill	47
3.15	CENNS-10 Production Run SNS Trigger Diagram	49
3.16	Prompt and delayed windows	50
3.17	SNS integrated beam power over time for CENNS-10 Production Run	51
4.1	Illustration of pulse finding algorithm	55
4.2	CENNS-10 raw waveform example before deconvolution method applied	56
4.3	CENNS-10 data waveform example after deconvolution algorithm applied	58
4.4	Example LED fit to extract single photoelectron response	60
4.5	Single photoelectron calibration over time	61
4.6	Example calibration data fit	63
4.7	Stability of detector response over run period	64
4.8	Linear fit to calibrated detector response using three gamma sources	65
4.9	^{83}Rb decay scheme	66
4.10	Diagram of $^{83\text{m}}\text{Kr}$ source design	68
4.11	Position of ^{83}Rb charcoal inside source vessel	69
4.12	Detector parameters during $^{83\text{m}}\text{Kr}$ source vessel tests	70
4.13	Piece of activated carbon inside $^{83\text{m}}\text{Kr}$ source vessel before deposition	72
4.14	$^{83\text{m}}\text{Kr}$ source attached to the CENNS-10 gas handling system	73
4.15	Full CENNS-10 gas handling system with $^{83\text{m}}\text{Kr}$ source attached	74
4.16	$^{83\text{m}}\text{Kr}$ event waveform in CENNS-10	75
4.17	DAQ Trigger rate over time in $^{83\text{m}}\text{Kr}$ calibration data	76
4.18	$^{83\text{m}}\text{Kr}$ event waveform in CENNS-10	77
4.19	Distribution of f_{top} over time for $^{83\text{m}}\text{Kr}$ calibration data	78
4.20	Results of AmBe calibration of the CENNS-10 detector	79

5.1	Rendering of simulated CENNS-10 inner detector geometry	81
5.2	Data and tuned MC comparison for ^{57}Co data	85
5.3	MC comparison to data of z-dependence	86
5.4	Example beta spectrum fit to AmBe data slice	87
5.5	Spline fits used to adjust simulated F_{90} values	88
5.6	Fit of MC background model to measured off-beam data	89
5.7	CEvNS SM predicted recoil spectrum for each neutrino flavor	90
5.8	Linear fit to SciBath flux result	92
5.9	Efficiency curve including analysis-independent data quality cuts	97
6.1	Off-beam trigger event distribution in t_{trig} in DAQ window	102
6.2	Figure-of-merit-optimized PSD cut for counting experiment analyses	103
6.3	Full efficiency curve for no-water and full-shielded data single-bin counting experiment	103
6.4	No-water shielding beam-related neutron initial predictions	105
6.5	No-water shielding pre-beam window results	106
6.6	No-water shielding prompt window results compared to initial MC predictions . . .	107
6.7	Scaled MC prediction compared to no-water beam-related excess	107
6.8	Covariance matrix for no-water analysis	113
6.9	Results of χ^2 analysis on no-water prompt excess	113
6.10	No-water residual time distribution	114
6.11	BRN Arrival Time vs energy	115
6.12	No-water shielding prompt window results compared to initial MC predictions . . .	116
7.1	Prompt window full-shielded data predictions	120
7.2	Delayed window full shielded data predictions	121
7.3	Off-beam trigger time and energy distributions for six equivalent sections of the CENNS-10 dataset	123

7.4	Off-beam subtracted data in a t_{trig} window away from the beam spill	124
7.5	Prompt neutron excess time dependence check	125
7.6	High energy sideband prompt window energy and F_{90} excess comparison with beam-related neutron MC	126
7.7	High energy sideband prompt window timing excess	127
7.8	Counting experiment results in prompt window	128
7.9	Counting experiment results	129
7.10	Efficiency curve for likelihood analysis	132
7.11	CEvNS pdf for likelihood analysis	133
7.12	Prompt BRN pdf for likelihood analysis	133
7.13	Steady-state, beam-unrelated background pdf for likelihood analysis	134
7.14	Delayed BRN pdf for likelihood analysis	135
7.15	Projection of likelihood fit pdfs	136
7.16	Projection of CEvNS and BRN pdfs	137
7.17	Distributions of best-fit results from pseudo-data study	138
7.18	Central-value predicted significance of CEvNS result from pseudo-data studies	139
7.19	Profile-likelihood curve of CEvNS result	143
7.20	1D projections of 3D binned likelihood fit best-fit result	144
7.21	1D projections of null hypothesis likelihood fit	145
7.22	N^2 dependence of CEvNS cross section with CENNS-10 measurement	146
7.23	Comparison of CEvNS cross section measurement of parallel analyses	147
7.24	Constraining non-standard neutrino interaction parameters	148
7.25	Non-standard neutrino interaction exclusion limits	149
8.1	Non-standard neutrino interactions constraints from CENNS-10 measurement and CsI[Na]	151

LIST OF TABLES

2.1	Beam-unrelated background flux measurement summary	22
4.1	Results of CENNS-10 detector calibration	64
5.1	Summary of sources of efficiency loss in CEvNS region of interest	96
6.1	Time,energy, and PSD windows for regions considered in the no-water shielding data analysis	99
6.2	No-water shielding data predictions	105
6.3	Beam-related neutron systematic errors	111
6.4	Table of rates seen in prompt/delayed windows for the no-water shielding data. . .	116
7.1	Time,energy, and F_{90} windows for the two analyses of full-shielded data	118
7.2	Predicted rates for the full shielded single-bin counting experiment	120
7.3	Rate systematics for full-shielded data analysis	122
7.4	Results of high-energy sideband MC prediction check	125
7.5	Measured neutron timing distribution	127
7.6	Prompt counting experiment results	128
7.7	Results of the single-bin counting experiment in the delayed region	129
7.8	Likelihood fit predicted rates and normalization constraints	136
7.9	Results of pseudo-data studies to test likelihood code	137
7.10	Likelihood fit systematic errors	141
7.11	On-beam data likelihood fit results	143
A.1	Tuned parameter inputs to MC which match the measured calibration data	167

CHAPTER 1

COHERENT ELASTIC NEUTRINO NUCLEUS SCATTERING (CEvNS)

1.1 THE CEvNS PROCESS

Coherent elastic neutrino-nucleus scattering (CEvNS) was first theorized in 1974 [1,2] by Freedman and soon after by Kopeliovich and Frankfurt, not long after the discovery of the weak neutral current process in neutrino-nucleus interactions [3]. Generally the interaction between a neutrino and the nucleus is complex as the neutrino interacts with the individual nucleons within the nucleus. However, if the momentum transfer between the neutrino and the nucleus is small, then the neutrino can interact with the nucleus as a whole. The purely quantum mechanical process leads to a “coherent” enhancement of the cross section proportional to the number of neutrons in the target nucleus squared (N^2). The quantum mechanical enhancement leads to a cross section that is much larger for an $\mathcal{O}(10 \text{ MeV})$ neutrino than other neutrino interactions such as inverse beta decay (IBD), electron scattering, and other charged/neutral current interactions and is shown in Fig. 1.1.

The form of the CEvNS differential cross section [5] is:

$$\frac{d\sigma}{dT} = \frac{G_F^2 M}{2\pi} \left\{ (G_V + G_A)^2 + (G_V - G_A)^2 \left(1 - \frac{T}{E_\nu}\right)^2 - (G_V^2 + G_A^2) \frac{MT}{E_\nu^2} \right\} \quad (1.1)$$

where $G_F = 1.1663787(6) \times 10^{-5} \text{ GeV}^2$ is the Fermi coupling constant, M is the mass of the target nucleus, T is the energy of the recoiling nucleus, and E_ν is the neutrino energy. G_V and G_A are

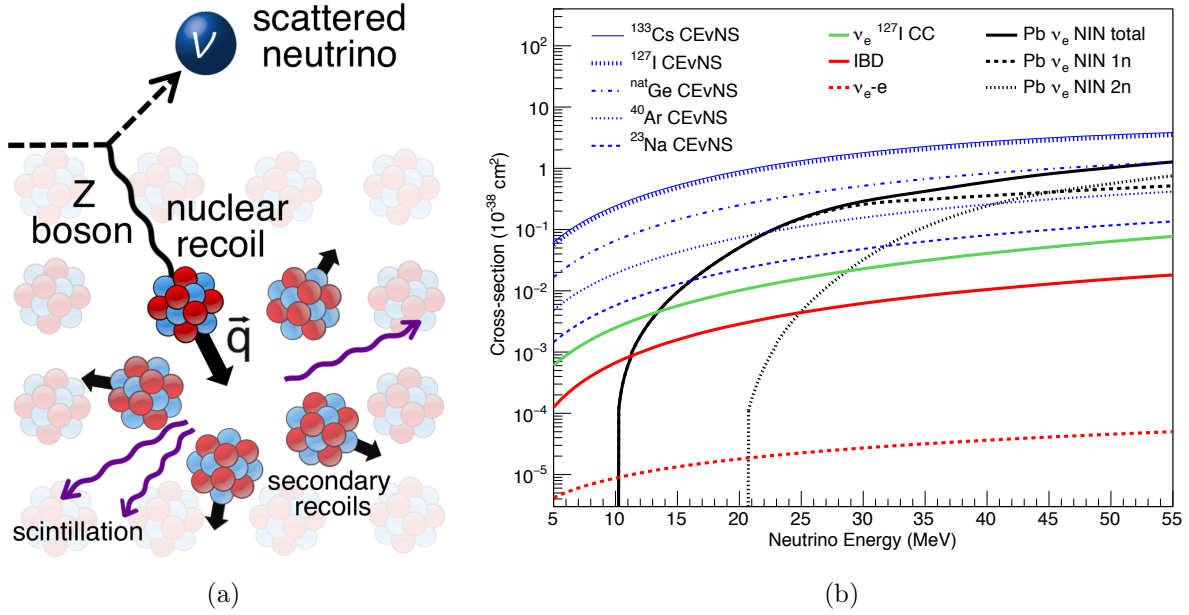


Figure 1.1: (a) Cartoon schematic of the CEvNS interaction. (b) Comparison of $\mathcal{O}(10 \text{ MeV})$ neutrino interaction cross sections. CEvNS has an enhanced cross section in this energy regime for a given target nucleus when compared to other interaction channels such as charged/neutral current scattering and IBD. Figure taken from [4].

coupling constants for quark level interactions with nucleons and are given by:

$$\begin{aligned}
 G_V &= (g_V^p Z + g_V^n N) F_{nuc}^V(Q^2) \\
 G_A &= (g_A^p (Z_+ - Z_-) + g_A^n (N_+ - N_-)) F_{nuc}^A(Q^2)
 \end{aligned}
 \tag{1.2}$$

where $Z(N)_{+(-)}$ are the number of spin up(down) protons(neutrons) in the target nucleus, $F_{nuc}^{V(A)}(Q^2)$ is the vector(axial vector) nuclear form factors which are a function of the square of the momentum transfer $Q^2 = 2MT$. Different parametrizations of the form factor in [6, 7] give small differences in the recoil spectrum for CEvNS on light nuclei. The nuclear form factor decreases for higher recoil energies, therefore requiring a lower neutrino energy. For spin-0 nuclei such as ^{40}Ar , $Z(N)_+ = Z(N)_-$, $G_A = 0$ and there is no axial vector contribution to the cross section. The vector coupling

constants for neutral current interactions of neutrinos with protons and neutrons within G_V is

$$\begin{aligned} g_V^p &= \rho_{\nu N}^{NC} \left(\frac{1}{2} - 2\hat{\kappa}_{\nu N} \hat{s}_Z^2 \right) + 2\lambda^{uL} + 2\lambda^{uR} + \lambda^{dL} + \lambda^{dR} \\ g_V^n &= -\frac{1}{2} \rho_{\nu N}^{NC} + \lambda^{uL} + \lambda^{uR} + 2\lambda^{dL} + 2\lambda^{dR} \end{aligned} \quad (1.3)$$

with $\hat{s}_Z^2 = 0.23122(3) = \sin^2 \theta_W$, the weak mixing angle, defined in the modified minimal subtraction (\overline{MS}) renormalization scheme [8] and $\rho_{\nu N}^{NC}$, $\hat{\kappa}_{\nu N}$, and the various λ parameters being radiative corrections with values also given in [8].

In the case of spin-0 nuclei, another form of the CEvNS cross section from [9] can be written when neglecting radiative corrections from Eqn. 1.1:

$$\frac{d\sigma}{dT} = \frac{G_F^2 M}{2\pi} \left\{ 2 - \frac{2T}{E_\nu} + \left(\frac{T}{E_\nu} \right)^2 - \frac{MT}{E_\nu^2} \right\} \frac{Q_W^2}{4} F^2(Q^2) \quad (1.4)$$

where $Q_W = N - (1 - 4\sin^2 \theta_W)Z$. As $4\sin^2 \theta_W \simeq 1$, $Q_W \simeq N$ and the CEvNS cross section takes on a distinct N^2 dependence as shown in Fig. 1.2.

Although the first theories of the CEvNS process appeared over 40 years ago, it was not discovered until recently by the COHERENT collaboration using a CsI[Na] target [4]. The time between the first prediction and detection was due to the innate challenges in the detection of CEvNS. Freedman himself noted that his suggestion might be “an act of hubris” [1]. The main challenge in a CEvNS measurement is that the only detectable signal is a very low energy nuclear recoil from the target nucleus. The energy of the recoiling nucleus ranges from $0 \leq T \leq T_{max} = \frac{2E_\nu^2}{M+2E_\nu}$. An example of the detector threshold requirement is for a ~ 30 MeV neutrino scattering off a heavy nucleus such as argon, $T_{max} \simeq 50$ keV. Compounding the challenge is the fact that detector signals from nuclear recoils are also quenched in comparison to electron recoils. The main effect of the quenching is that less light is produced from a nuclear recoil than an electron recoil of the same energy. The “quenching factor”, described further for argon nuclei in Sec. 3.1, provides a conversion from energy units of keVnr (nr = nuclear recoil) to keVee (ee = electron equivalent). For

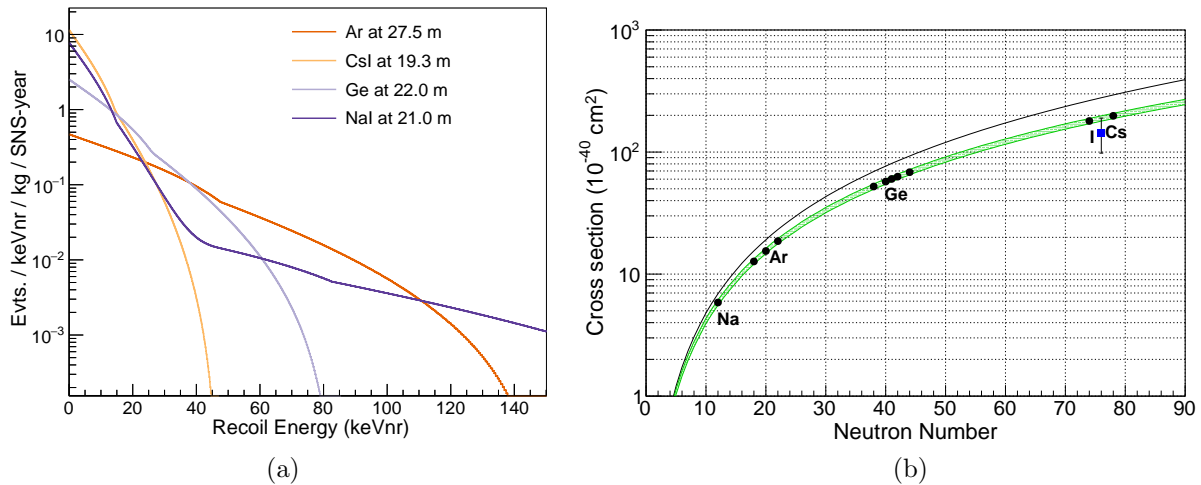


Figure 1.2: (a) The Standard Model (SM) predicted CEvNS recoil spectra as a function of nuclear recoil energy for several target nuclei of interest within the COHERENT experiment. (b) CEvNS SM predicted cross section as a function of the number of neutrons in the target nucleus averaged over the neutrino flux from the SNS (Fig. 2.1). The black line indicates the N^2 dependence for $F(Q^2) = 1$. The green band indicates the N^2 dependence of the cross section using the parameterization of $F(Q^2)$ from [7]. The points indicate nuclei of interest for the COHERENT experiment (Chapter 2). The width of the band is from a 3% uncertainty on the value of R_n . The blue point and associated error bars are associated with [4].

neutrino energies relevant for CEvNS, $M \gg E_\nu$, so $T_{max} \simeq \frac{2E_\nu^2}{M}$. The maximum recoil energy of the target nucleus is $\mathcal{O}(10 \text{ keV})$ for a $\mathcal{O}(10 \text{ MeV})$ neutrino. Detector technologies have only advanced enough recently to detect the low-energy nuclear recoil signals relevant for CEvNS, mainly for use in direct dark matter detection experiments. CEvNS allows access to a variety of physics due to its relatively large cross section and simple nature as a coherent elastic neutrino-nucleus interaction whose structure is relatively insensitive to unknown aspects of nuclear structure.

As the CEvNS cross section includes the weak mixing angle, CEvNS provides a complementary measurement at low Q from the low energy nuclear recoil signal [10]. The neutron rms radius computed using the 2017 CsI[Na] result in [4] has been combined with atomic parity violation (APV) experiments [11] to reinterpret the constraints from the APV result on $\sin^2 \theta_W$ at low Q as seen in Fig. 1.3.

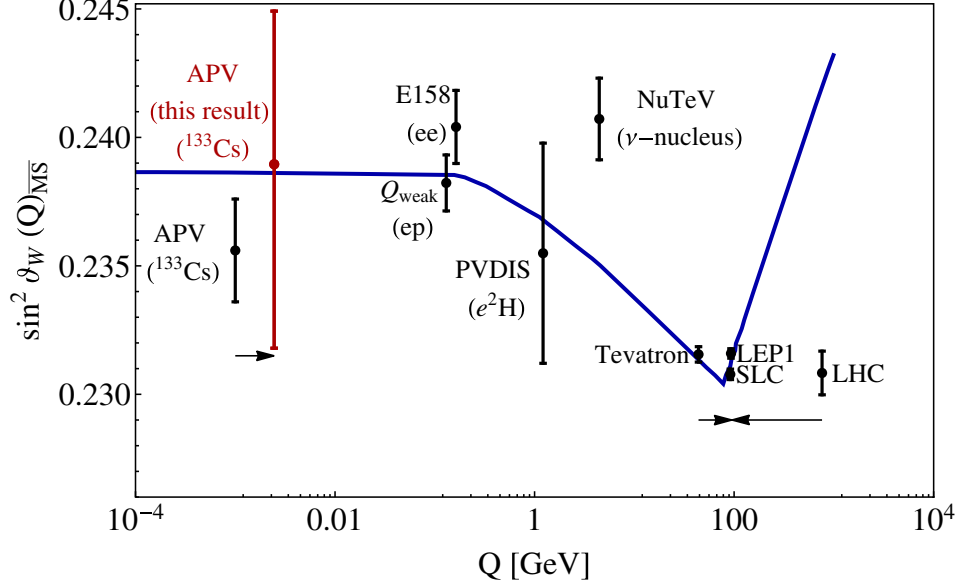


Figure 1.3: Weak mixing angle measurements as a function of momentum transfer Q . CEvNS provides another low Q regime along with atomic parity violation experiments. The red point is a reinterpretation of the APV result using a value for the neutron skin derived from the COHERENT CsI[Na] data. Using the calculated neutron skin, the APV result is in better agreement with the SM predicted value for $\sin^2 \theta_W$. Figure from [11].

1.2 BEYOND-THE-STANDARD-MODEL INTERACTIONS

As the CEvNS cross-section is cleanly predicted in the Standard Model (SM), any deviation can be evidence of beyond-the-Standard-Model (BSM) physics. One example of this is non-standard neutrino interactions (NSI), which can be written by extending the SM Lagrangian in the following way [5, 12]:

$$\mathcal{L}_{\nu A}^{NSI} = -\frac{G_F}{\sqrt{2}} \sum_{\substack{q=u,d \\ \alpha,\beta=e,\mu,\tau}} [\bar{\nu}_\alpha \gamma^\mu (1 - \gamma^5) \nu_\beta] (\epsilon_{\alpha\beta}^{qL} [\bar{q} \gamma^\mu (1 - \gamma^5) q] + \epsilon_{\alpha\beta}^{qR} [\bar{q} \gamma^\mu (1 + \gamma^5) q]) \quad (1.5)$$

which when added to the SM Lagrangian modifies the expressions in Eqn. 1.1 and Eqn. 1.2 as:

$$\begin{aligned} G_V &= [(g_V^p + 2\epsilon_{ee}^{uV} + \epsilon_{ee}^{dV})Z + (g_V^n + \epsilon_{ee}^{uV} + 2\epsilon_{ee}^{dV})N] F_{nuc}^V(Q^2) \\ G_A &= [(g_A^p + 2\epsilon_{ee}^{uA} + \epsilon_{ee}^{dA})(Z_+ - Z_-) + (g_A^n + \epsilon_{ee}^{uA} + 2\epsilon_{ee}^{dA})(N_+ - N_-)] F_{nuc}^A(Q^2) \end{aligned} \quad (1.6)$$

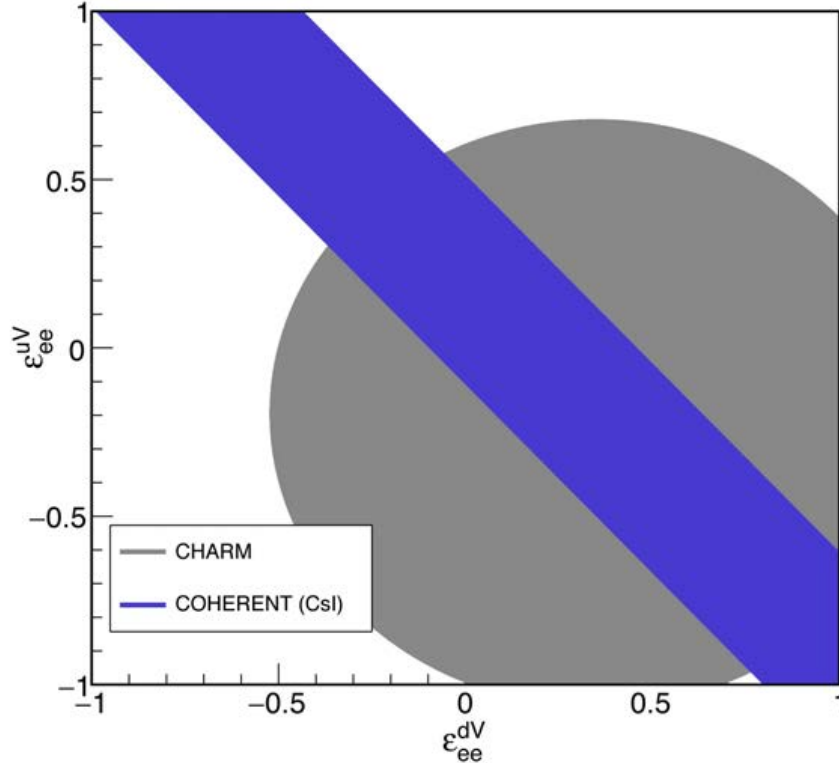


Figure 1.4: Limits on a non-universal quark-vector NSI including the constraints from the measurement of CEvNS with a CsI[Na] crystal in [4] assuming all other $\epsilon = 0$. Previous limits on this parameter space are from the CHARM experiment [13].

where $\epsilon_{\alpha\beta}^{qV}$ are the NSI coupling constants with $\alpha, \beta = e, \mu, \tau$ the three neutrino flavors associated with the SM, $q = u, d$ being the quark involved in the interaction, and V being a vector-mediated interaction. Within the ϵ coupling constants, $\alpha = \beta$ represent non-universal and $\alpha \neq \beta$ flavor-changing possibilities for NSI. There are similar terms in Eqn. 1.6 The presence of NSI results in an enhancement or deficit in the CEvNS cross section. A CEvNS cross section measurement can place limits on the allowed NSI parameter space. Limits were placed on a subset of the NSI coupling constants using the COHERENT CsI[Na] result in [4] and are shown in Fig. 1.4.

The existence of NSI can confuse a measurement of the neutrino mass hierarchy in long-baseline neutrino oscillation experiments such as the Deep Underground Neutrino Experiment (DUNE). Allowing for NSI, a fit to the normal mass hierarchy (NH) looks like a fit to the inverted mass

hierarchy (IH) when NSI are applied as [14]:

$$\begin{aligned}
(\epsilon_{ee} - \epsilon_{\mu\mu}) &\rightarrow -(\epsilon_{ee} - \epsilon_{\mu\mu}) - 2 \\
(\epsilon_{\tau\tau} - \epsilon_{\mu\mu}) &\rightarrow -(\epsilon_{\tau\tau} - \epsilon_{\mu\mu}) \\
\epsilon_{\alpha\beta} &\rightarrow -\epsilon_{\alpha\beta}^* \quad (\alpha \neq \beta)
\end{aligned}
\tag{1.7}$$

in addition to NH→IH which allows for $H \rightarrow -H^*$ to be invariant [14]. The existence of NSI could also confuse a measurement by DUNE of the CP violating phase introduced in the neutrino mass mixing matrix [15], so constraining the NSI coupling constants is of paramount importance for the success of the DUNE physics program. The NSI degeneracy in the neutrino mass hierarchy is disfavored at a 3σ [16] level when the constraints placed by the CsI[Na] CEvNS measurement are combined with the global data on neutrino oscillations.

Other physics models that can be tested using a CEvNS measurement may include "dark photons" or an anomalously large neutrino magnetic moment. The muon g-2 discrepancy between theory and experiment can be explained by the existence of a light vector boson within a dark sector that couples to the SM through kinetic mixing with the photon [17, 18]. At low Q , measurements of the weak mixing angle are sensitive to this additional dark boson. A precision measurement of the weak mixing angle at low Q , where CEvNS is sensitive, would constrain the dark boson theories. The resulting CEvNS recoil spectrum is also sensitive to a measurement of the neutrino magnetic moment [19] resulting in a deviation from the predictions from the SM. Detectors with a lower threshold are more sensitive to the changes in the CEvNS recoil spectrum from an anomalous neutrino magnetic moment. The deviation in the recoil spectrum appears at low recoil energies, generally $\mathcal{O}(1 \text{ keVnr})$. Near future CEvNS experiments at both stopped-pion neutrino sources such as the SNS (Sec. 2.2) and reactors (Sec. 2.4) are expected to have sensitivities to a neutrino magnetic moment of $\sim 6 \times 10^{-10} \mu_B$ [20, 21]. While not currently competitive with the astrophysical limits from solar neutrinos of $< 2.8 \times 10^{-11} \mu_B$ (Borexino [22]), a competitive measurement from

CEvNS would provide an important cross-check.

1.3 DARK MATTER SEARCHES AND THE "NEUTRINO FLOOR"

The presence of a source of “dark matter” was first used to describe differences in the predictions from measurements of rotation curves of galaxies through observations of the Coma Cluster [23]. The predictions are derived from the known amount of gravitational material within the galaxy. Observations of further galaxies and nebulae [24] confirmed this measurement and made a strong case for the existence of additional matter that is not detected gravitationally. There are considerable ongoing efforts to determine the identity of dark matter. In certain dark matter search experiments, CEvNS becomes an important background.

1.3.1 WIMP DIRECT DETECTION

Weakly Interacting Massive Particles (WIMPs) are a leading candidate for the identity of the dark matter particle. Many experiments have been designed in order to push lower into the dark matter parameter space. In particular, noble liquid detectors [25–29] are a popular detector target due to their scalability and ability to measure low nuclear recoil energies. The dark matter signal of interest from ~ 1 GeV mass WIMPs is also a low energy nuclear recoil, a signature identical to a CEvNS interaction. CEvNS is an irreducible background to a direct detection dark matter search due to the relative lack of separable information of dark matter interactions (directionality, pulse shape, etc.) from CEvNS interactions.

A “neutrino floor”, where WIMP dark matter cannot be resolved from CEvNS, can be formed from the SM prediction of the CEvNS cross section. The relevant limits in the dark matter mass parameter space are derived from the ${}^7\text{Be}$ and ${}^8\text{B}$ solar neutrino flux at $\mathcal{O}(1 \text{ GeV})$ dark matter masses and the atmospheric neutrino and diffuse supernova neutrino backgrounds (DSNB) at $> 10 \text{ GeV}$ dark matter masses. The current generation of liquid noble gas direct detection WIMP detectors [26, 28, 29], shown in Fig. 1.5, are beginning to probe far enough into the dark matter

produced dark matter particle can travel to a detector and interact in a CEvNS-like fashion with the nucleus. Limits have recently been set on the sub-GeV dark matter models using accelerated protons into a fixed target [37–39]. The parameters in the sub-GeV dark matter models include two coupling constants, ϵ and α' , the vector mediator mass m_V , and the dark matter mass m_χ .

As with direct detection of WIMPs, sub-GeV dark matter-nucleus interactions in these models are also low-energy nuclear recoils and are indistinguishable from CEvNS. A recent study by the COHERENT collaboration, seen in Fig. 1.6, shows that a tonne-scale liquid argon detector at the SNS can place world-leading limits on vector-portal sub-GeV dark matter models [40]. The SNS takes advantage of the well known neutrino timing signature from a stopped-pion source to separate the dark matter signal from the CEvNS background. This study applies systematic errors and background predictions from the results presented in this work to a tonne-scale exposure. Optimization of the detector location relative to the beam could improve sensitivity to dark matter as the resulting angular distribution of the dark matter is forward-peaked [40].

1.4 NUCLEAR STRUCTURE

A CEvNS measurement can also make important contributions to nuclear physics. CEvNS provides access to nuclear structure effects through the nuclear form factor $F(Q^2)$, including the neutron radius and neutron skin. The radius difference between the neutron and proton distributions in the nucleus defines the neutron skin. The neutron radius is poorly known as the lack of charge of the neutron makes for a much more difficult measurement than for the proton, which has been well constrained using electron-proton scattering [41] and atomic hydrogen measurements [42]. A precise measurement of the neutron skin can have important astrophysical considerations for neutron stars. The radius of a neutron star is poorly constrained due to the dependence of the neutron skin on the equation of state of a neutron star. An estimate of the neutron radius for ^{133}Cs of $5.5_{-1.1}^{+0.9}$ and the neutron skin was made with the COHERENT CsI[Na] result in [43, 44] using the well-measured proton radius for ^{133}Cs [45]. The neutron radius estimate was made purely

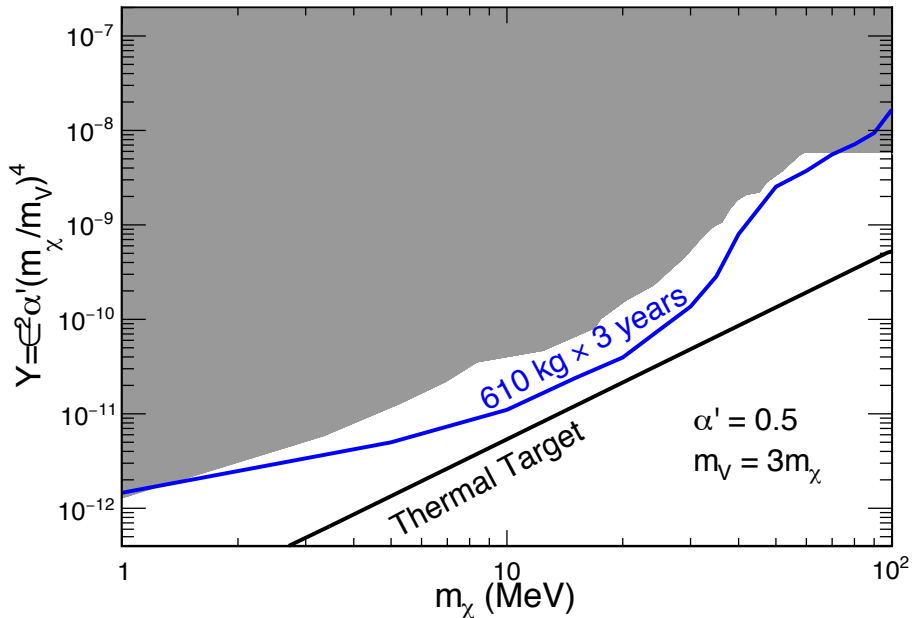


Figure 1.6: Exclusion limits on the sub-GeV dark matter model presented in [32] with a tonne-scale liquid argon detector proposed as part of the COHERENT experiment. The parameter Y on the vertical axis is a dimensionless quantity which allows comparison of the vector-portal model parameters to the cosmological dark matter density. The relic density is shown as the black line on the curve. This study, presented in detail in [40], shows that world-leading limits can be placed with this detector assuming similar CEvNS and background levels to those presented in this work.

with CEvNS event rate considerations and a larger event rate and more precise measurements can extract a more precise estimate of the nuclear structure effects. Measurements of the neutron radius with CEvNS experiments are currently not as powerful as parity violating measurements such as PREX [46,47] and CREX [48] which expect to measure the neutron radius to 3% or better. However, CEvNS measurements provide a complementary measurement of the neutron radius and neutron skin with a different set of systematic considerations.

A precise measurement of the CEvNS recoil spectrum shape can also be used to measure the neutron radius [49]. The neutron radius is encoded in the moments of the neutron density distribution by expanding the nuclear form factor using a Fourier transform. Using the form factor model described in [49], there is a difference of 780 events/(tonne year) with a 10% change in the RMS neutron radius, representing 1.2% of the total event rate. The difference in events is

concentrated at a recoil energy of 30 keV (Fig. 2 of [49]). This model extracts the neutron radius using the information provided in the nuclear form factor through the measured CEvNS recoil spectrum.

1.5 SUPERNOVA NEUTRINO DETECTION

When a massive star reaches the end of its life, it collapses into a neutron star. The gravitational binding energy of the star is released in the form of an explosion called a supernova. The release of $> 10^{53}$ erg of energy is almost all in the form of neutrinos with energy $\mathcal{O}(10 \text{ MeV})$, making a supernova the most powerful source of neutrinos at those energies in the universe. A total of 25 neutrino events were detected by the Kamiokande II [50], Irvine-Michigan-Brookhaven (IMB) [51], and Baksan [52] experiments from a supernova, SN1987A, that occurred in 1987 in the Large Magellanic Cloud. The detection of the neutrinos from SN1987A confirmed the baseline model of gravitational collapse but was too sparse of a signal to greatly distinguish between theoretical models of core collapse and supernova explosions. As neutrinos produced in a supernova can escape the core of the collapsing star faster than the light produced, neutrinos are the first detectable signal from a supernova explosion. Neutrinos of all flavors are produced in a supernova for a length of several seconds, starting with a prompt burst of ν_e within the first milliseconds after the core bounce [53].

A measurement of the energy spectrum of supernova neutrinos from the resulting nuclear recoils via CEvNS can provide insight on different core collapse models [54], as CEvNS is predicted to be a main energy transport mechanism in Type II supernovae [55, 56]. The CEvNS interaction has the largest cross section at supernova neutrino energy scales and as a neutral current interaction is also flavor-blind. A CEvNS detector would be sensitive to the full flavor range of neutrinos produced by a supernova. Specifically, a CEvNS detector is sensitive to a few events per tonne of ν_x , collectively ν_μ , $\bar{\nu}_\mu$, ν_τ , and $\bar{\nu}_\tau$ at a distance of 10 kpc. The expected rate is ~ 20 times larger than the expected hundreds of $\bar{\nu}_e$ and tens of ν_x per kilotonne in light-water detectors [57]. As

CEvNS is cleanly predicted by the SM, the well-predicted cross section provides a useful tool to understand the mechanics of a supernova explosion with a detection of a supernova.

1.6 SUMMARY

As presented in this chapter, measurements of CEvNS provide an exciting scientific opportunity with access to a wide variety of interesting physics channels. A powerful tool for CEvNS measurements, the Spallation Neutron Source (SNS) at Oak Ridge National Laboratory is presented in Chapter 2 along with the ongoing measurements at the SNS by the COHERENT experiment in Neutrino Alley and important background measurements. The CENNS-10 detector deployment at the SNS, focusing on a detector upgrade to lower the energy threshold and allow sensitivity to CEvNS and subsequent data taking after the upgrade is presented in Chapter 3. The energy calibration of the upgraded CENNS-10 detector, showing an eight-fold increase in the detector light collection efficiency from a prior run before the upgrade along with the design, construction, and deployment of a low-energy *in-situ* $^{83\text{m}}\text{Kr}$ calibration source is presented in Chapter 4. The detector simulation used to generate signal and background predictions is presented in Chapter 5. Characterization of an important background related to the SNS operation is presented in Chapter 6 using a run of CENNS-10 with minimal detector shielding. In Chapter 7, the analysis of the first 1.5 years of physics data using both a single-bin counting experiment and full 3D binned likelihood analysis is presented. The results of the analysis provide the first detection of CEvNS on argon nuclei, the first measurement of the CEvNS cross section, and new neutrino NSI constraints. Finally, the main conclusions from this work are presented in Chapter 8.

CHAPTER 2

THE COHERENT EXPERIMENT AT THE SPALLATION NEUTRON SOURCE

This chapter describes the Spallation Neutron Source (SNS), which generates a flux of neutrinos through proton collisions with mercury. The COHERENT experiment located at the SNS uses those neutrinos for CEvNS detection with multiple detectors. Initial background measurements determined a suitable location for CEvNS detectors at the SNS in a basement hallway of the target building.

2.1 THE SPALLATION NEUTRON SOURCE

The SNS at Oak Ridge National Laboratory (ORNL) is a DOE Office of Science user facility and currently the most powerful pulsed-beam neutron source in the world [58]. Spallation neutrons are created from a ~ 1 GeV, 1.4 MW proton beam impinging on a liquid mercury target, producing 20-30 neutrons per proton-Hg collision. The SNS produces $\sim 1 \times 10^{16}$ protons-on-target (POT)/second at its designed operating power of 1.4 MW. The spallation neutrons from the SNS are sent through moderators to beamlines used to study a wide variety of physics, chemistry, and materials science topics. The proton beam is pulsed at 60 Hz with a full width at half maximum (FWHM) of ~ 350 ns. Knowledge of when the beam pulse occurs allows for the rejection of the steady-state backgrounds in a CEvNS experiment.

2.1.1 THE SNS AS A NEUTRINO SOURCE

The SNS is also the best stopped-pion neutrino source in the world with its combination of beam power and background rejection via the pulsed beam structure. Charged and neutral pions are created along with the spallation neutrons when the proton beam hits the mercury target. Of the π^- produced, $\sim 99\%$ are captured within the mercury target. Neutrinos are produced from the decay of charged pions produced in the proton collisions with the mercury target. First, the π^+ decays into a μ^+ and a ν_μ . Then the μ^+ decays into a e^+ , ν_e , and $\bar{\nu}_\mu$, producing three distinct neutrino flavors for each π^+ decay. The energy spectrum of neutrinos produced by the SNS represents a pion-decay-at-rest (π -DAR) neutrino spectrum. The resulting neutrino energy for the ν_μ is mono-energetic from the resulting 2-body decay of the π^+ and is given by

$$\begin{aligned} f(E_{\nu_\mu}) &= \delta(E_{\nu_\mu} - E_\pi) \\ E_\pi &= \frac{m_\pi^2 - m_\mu^2}{2m_\pi} = 29.8 \text{ MeV} \end{aligned} \tag{2.1}$$

The energy spectra for the ν_e and $\bar{\nu}_\mu$ are produced from the decay of the μ^+ and are described by the Michel spectrum [9, 59]:

$$\begin{aligned} f(E_{\nu_e}) &= \frac{96}{m_\mu^4} E_{\nu_e}^2 (m_\mu - 2E_{\nu_e}) dE_{\nu_e} \\ f(E_{\bar{\nu}_\mu}) &= \frac{16}{m_\mu^4} E_{\bar{\nu}_\mu}^2 (3m_\mu - 4E_{\bar{\nu}_\mu}) dE_{\bar{\nu}_\mu} \end{aligned} \tag{2.2}$$

with a possible range of resulting neutrino energies of $0 \leq E_\nu \leq \frac{m_\mu}{2} = 52.8 \text{ MeV}$.

A GEANT4 [60, 61] simulation shows the SNS produces (0.09 ± 0.009) π^+ for each proton on target [62] at a proton energy of $\sim 1 \text{ GeV}$. The 10% error on the neutrino flux comes from applying different pre-compiled physics lists within GEANT4. The simulation is used to predict the neutrino flux and also validate the predicted neutrino energy spectrum. The design parameters of the SNS target and facility details are included within the simulation. These simulations also show a

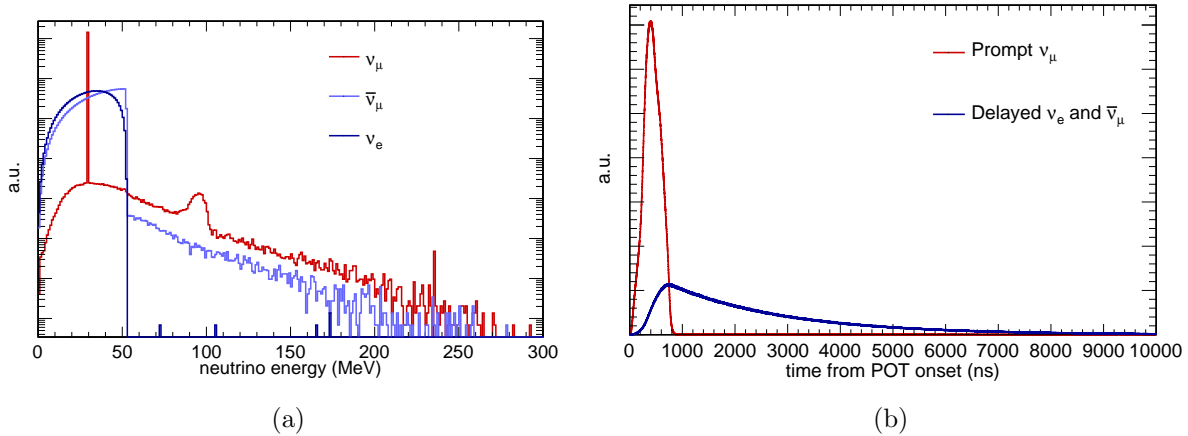


Figure 2.1: (a) Energy spectra for the different neutrino flavors produced by the SNS. The idealized energy spectra given in Equations 2.1 and 2.2 at $E_\nu \leq 52.8$ MeV from π -DAR dominate over the small ($\sim 1\%$) DIF component. (b) Predicted neutrino timing spectra from the SNS.

$\sim 1\%$ decay-in-flight component, which is small compared to other facilities such as the MLF at J-PARC [63]. The SNS is predicted to produce a very clean spectrum of neutrinos as $> 99\%$ of the π^+ produced decay at rest. The idealized energy description given in Eqn. 2.1 and Eqn. 2.2 represent a very good approximation of the resulting neutrino energy spectra from the SNS. The decay-in-flight (DIF) component is at a level of $\sim 1\%$ from the decay-at-rest components for the different neutrino flavors as seen in Figure 2.1 from the SNS target simulations.

The SNS also produces a very clean neutrino signal in time. The π^+ decay occurs with a lifetime of 26 ns and the μ^+ decay with a lifetime of 2.2 μ s. An exponential representing the lifetime for each neutrino flavor is convolved with the SNS beam width described previously to produce the predicted CEvNS timing spectra shown in Fig. 2.1. The ν_μ are referred to as the “prompt” neutrinos as they occur in time with the SNS beam pulse. The ν_e and $\bar{\nu}_\mu$ are referred to as the “delayed” neutrinos as they are delayed by the muon decay lifetime from the SNS beam pulse. Generally, any event that occurs within $\sim 1 \mu$ s of the beam spill is considered prompt and events seen later in the beam spill are considered delayed. The exact definitions of these windows vary between analyses.

2.2 THE COHERENT EXPERIMENT AT THE SNS

The COHERENT collaboration was formed in 2013 in order to make the first detection of CEvNS, which was done using a CsI[Na] detector [4] in 2017 and further described in Sec. 2.2.2. Another goal of the COHERENT experiment is to test the predicted N^2 dependence of the CEvNS cross section through detection on multiple nuclear targets to make an unambiguous discovery. Currently, the collaboration consists of ~ 80 members from ~ 20 institutions.

2.2.1 NEUTRINO ALLEY AND THE COHERENT PROGRAM

The COHERENT suite of detectors is located in a basement hallway of the SNS known as “Neutrino Alley” (Fig. 2.2) that has been turned into a dedicated neutrino laboratory [64]. Neutrino Alley is located at a distance ranging from 19-28 m from the SNS target. Neutrino Alley was determined to be a suitable low-background location for the placement of CEvNS-sensitive detectors during a campaign of background measurements at the SNS target building, described further in Sec. 2.3. The high flux of neutrons produced by the SNS target precludes the use of the target floor level as a suitable site for low-threshold CEvNS detectors. In addition, Neutrino Alley is located at a depth of 8 m.w.e. which reduces the cosmic muon flux.

COHERENT plans to deploy several detectors to measure CEvNS on multiple nuclei. Currently operational is a $\mathcal{O}(20 \text{ kg})$ active mass liquid argon detector CENNS-10, which is described in detail in Chapter 3 for a CEvNS measurement and is the focus of this work. A 185 kg NaI[Tl] crystal array not sensitive to a CEvNS measurement is deployed to measure the neutrino charged current interaction on ^{127}I [65, 66]. The suite of detectors and siting for COHERENT which are currently taking data within Neutrino Alley is shown in Fig. 2.2. Deployments of a 16 kg p-type point contact HPGe crystal array and a tonne-scale NaI[Tl] crystal array are planned to map out the N^2 dependence of the CEvNS cross section. The tonne-scale NaI[Tl] array will be both sensitive to CEvNS and the ^{127}I charged current interaction. A tonne-scale liquid argon detector and a tonne-scale heavy water detector [62] are planned further in the future to begin precision measurements

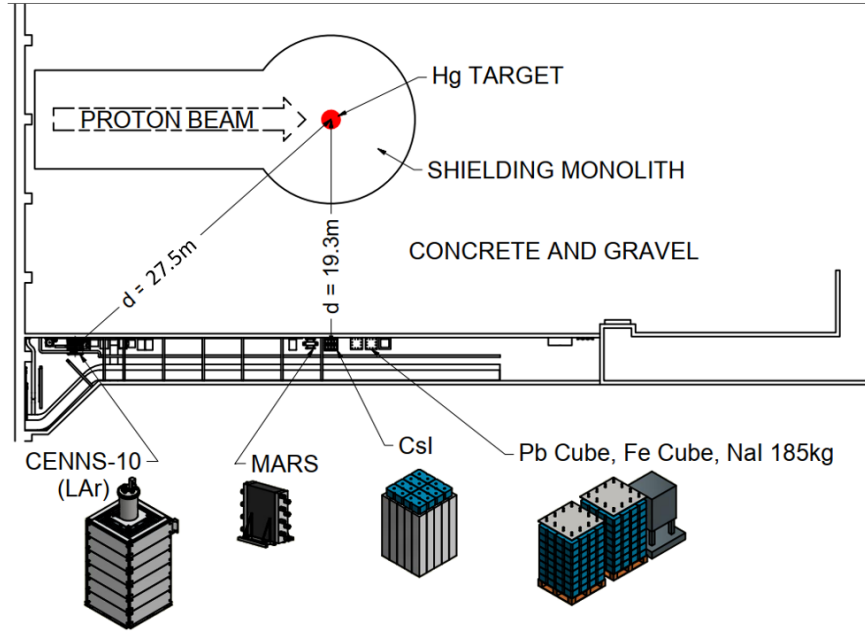


Figure 2.2: Current detector suite and siting in Neutrino Alley for the COHERENT experiment. The CsI[Na] detector was decommissioned in June 2019. CENNS-10 is sensitive to a CEvNS measurement. The 185 kg NaI[Tl] is not sensitive to CEvNS but to the charged current interaction on ^{127}I . MARS is a Gd-loaded plastic scintillator detector to measure beam-related neutron backgrounds. The Pb and Fe cubes are designed to measure neutrino-induced neutrons, another beam-related background described in Sec. 2.3.

using CEvNS. The well known neutrino-deuterium charged current interaction cross section allows the heavy water detector to better constrain the SNS neutrino flux. The ν_e -d charged current interaction has been theoretically measured to 2-3% [67]. The planned COHERENT detectors and possible siting in Neutrino Alley is shown in Fig. 2.3.

2.2.2 FIRST OBSERVATION OF CEvNS WITH CSI[NA]

A 14.6 kg CsI[Na] crystal detector was the first COHERENT detector installed in Neutrino Alley in June 2015 and was responsible for the first detection of CEvNS in 2017 [4]. The neutron numbers for cesium(78) and iodine(74) provide a large enhancement to the CEvNS cross section. The similarity of the neutron numbers also ensures a comparable energy nuclear recoil if a neutrino scatters off either cesium or iodine. This allows for a simpler understanding of the expected recoil spectrum from the crystal. CsI crystals can be commercially produced and are relatively

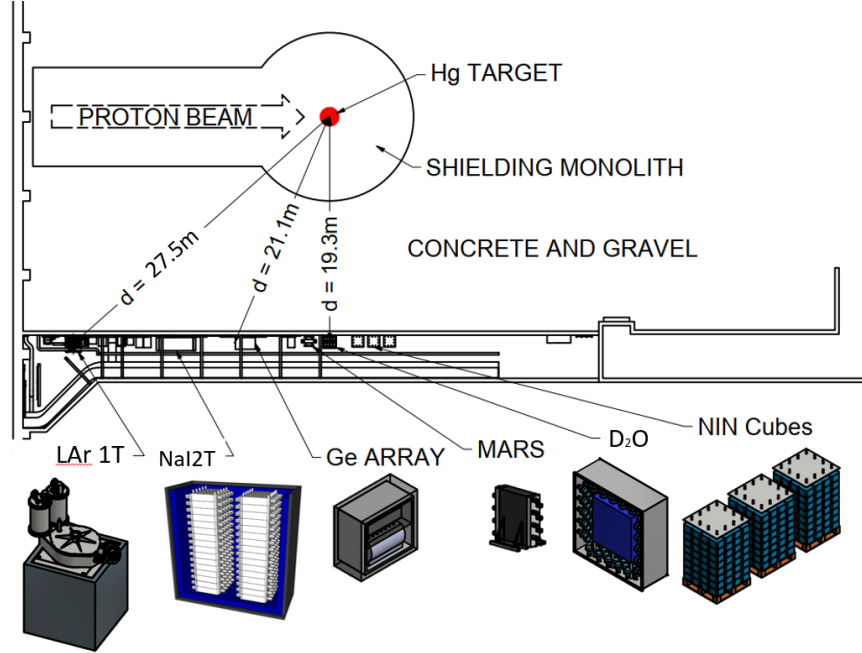


Figure 2.3: Planned future COHERENT deployments for precision measurements include a tonne-scale liquid argon detector, CENNS-750, a tonne-scale NaI[Tl] array and a 16 kg p-type point contact HPGe detector array for CEvNS detection.

inexpensive (~ 1 \$/g). Na doping was chosen due to the lower afterglow than that of a Tl doped crystal [68]. The large light yield from these crystals of ~ 45 photons/keVee [69] allows for sufficiently low thresholds for CEvNS sensitivity.

To measure beam-related backgrounds before the installation of the CsI[Na] crystal, a liquid scintillator cell was installed inside the CsI[Na] detector shielding container in Neutrino Alley. The measured fluxes of these backgrounds, namely fast neutrons produced by the beam and neutrino induced neutrons (NINs) (Sec. 2.3.2) are sufficiently low for a CEvNS measurement.

Two years of data from June 2015-May 2017 were included in the analysis showing the first observation of CEvNS in [4]. There is a clear excess between beam-on and beam-off data, shown in Fig. 2.4, that is consistent with the SM predicted CEvNS rate. Using a 2D maximum-likelihood fit, the null CEvNS hypothesis is rejected at 6.7σ and the measured event rate is within 1σ of the SM prediction.

The CsI[Na] detector was decommissioned and removed from Neutrino Alley in June 2019. The

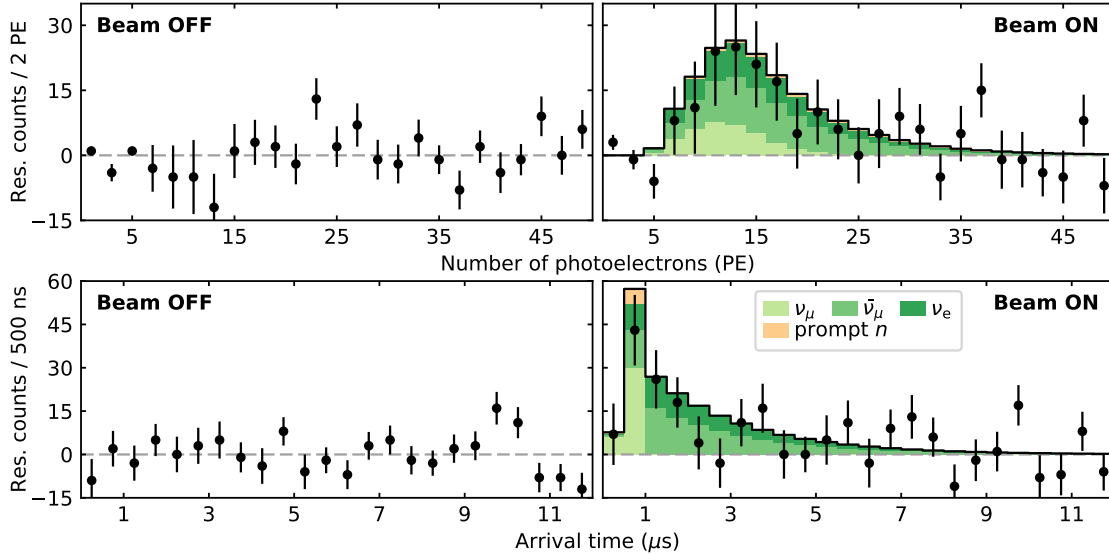


Figure 2.4: Results after background subtraction of \sim two years of data from the CsI[Na] detector shown in [4]. There is a clear excess in both reconstructed event energy (top) and time relative to the beam pulse (bottom) between beam-on and beam-off data consistent with the CEvNS prediction. The null hypothesis is rejected at 6.7σ using a 2D maximum-likelihood analysis

detector has approximately doubled the exposure used in [4] at the time of its decommissioning. A further analysis of the entire dataset collected with the detector is expected to provide a more precise measurement of the CEvNS cross section on CsI[Na].

2.3 BACKGROUND MEASUREMENTS AT THE SNS

The COHERENT collaboration began a series of background measurements in 2013 in order to find a suitable location to deploy a CEvNS-sensitive detector. The backgrounds to a CEvNS search at the SNS are generally grouped into categories of beam-unrelated, described in Sec. 2.3.1 and beam-related backgrounds, described in Sec. 2.3.2.

2.3.1 BEAM-UNRELATED BACKGROUNDS

The beam-unrelated backgrounds are those classified as unassociated directly with the SNS beam pulse. These fall into two categories for all COHERENT detectors. The first is background from 511 keV gamma rays emanating from a pipe known as the “Hot-Off Gas (HOG) pipe”

running through Neutrino Alley. The HOG pipe carries away radioactive material from the SNS target related to the SNS Mercury Off-Gas Treatment System (MOTS) [70]. The second source of background are naturally occurring environmental gamma rays from the ^{238}U , ^{232}Th , and ^{40}K decay chains in the concrete walls within Neutrino Alley. Another background in this category specific to CENNS-10 is ^{39}Ar in the atmospheric argon that is used during detector operations.

^{39}Ar IN CENNS-10

^{39}Ar is present in atmospheric argon through neutron induced reactions from cosmic rays at a level of ~ 1 Bq/kg [71, 72]. It is often the largest beam-unrelated background in a low-threshold, low-background liquid argon detector. ^{39}Ar is the largest beam-unrelated background component in the current CENNS-10 deployment from simulations described in Sec. 5.4.1 which agree well with the measured beam-unrelated backgrounds. A method to reduce this background is the use of argon extracted from underground wells (underground argon or UAr) instead of the atmosphere [73, 74]. The DarkSide-50 WIMP direct detection dark matter detector was filled with underground argon extracted from a source in Colorado [75] and purified [76]. The use of underground argon reduced the ^{39}Ar background by a factor of (1400 ± 200) as compared to atmospheric argon in the same detector [77]. Underground argon is being considered for use in the COHERENT tonne-scale liquid argon deployment to greatly reduce the ^{39}Ar background.

ENVIRONMENTAL BACKGROUNDS

A measurement of the flux of the environmental gamma rays in Neutrino Alley was performed at ORNL in 2014. The measurement was carried out using an ORTEC Detective-100T HPGe detector. A flux value was extracted from the agreement between the measured energy spectrum from the data and an MCNP6 [78] simulation. The measured fluxes were ~ 1 $\gamma/(\text{cm}^2 \text{ s})$ coming from the concrete walls and floor as a flux was computed separately for each case.

Background Source	Measured Flux
^{39}Ar	1 Bq/kg
Concrete Wall	1 $\gamma/(\text{cm}^2 \text{ s})$
Concrete Floor	1 $\gamma/(\text{cm}^2 \text{ s})$
Hot-Off Gas Pipe	25 $\gamma/(\text{cm}^2 \text{ s})$

Table 2.1: Summary of the flux calculations from Sec. 2.3.1

HOT OFF GAS PIPE

Radioactive gases are carried away from the target through the HOG pipe that runs directly through Neutrino Alley as the SNS beam is operating. A large flux of 511 keV gamma rays emanates from the pipe when the SNS is operational. The gases include large quantities of ^{11}C , which is a positron emitter. There is some fluctuation in the flux of these gamma rays over a matter of hours, measured using a commercial radiation monitor attached to the pipe. However, the HOG flux is steady-state on the timescale of an individual beam pulse. There is no noticeable change in the measured rates from the fluctuation of the HOG flux with the addition of the lead shielding to CENNS-10 described in Chapter 3. The flux of gamma rays was measured from this pipe using the same Ortec Detective-100T used for the environmental gamma measurements. An analysis of this data measures a flux of 25 $\gamma/(\text{cm}^2 \text{ s})$ at the time of the measurement. A summary of all the beam-unrelated flux measurements, extracted from the various measurements and simulations, is shown in Tab. 2.1.

2.3.2 BEAM-RELATED BACKGROUNDS

The beam-related backgrounds are those directly associated with the SNS beam pulse and the proton-Hg collisions. These are important backgrounds to understand for a CEvNS search as they can generate low-energy nuclear recoils that mimic the CEvNS signal. These backgrounds cannot be measured and subtracted in the same fashion as the beam-unrelated backgrounds with SNS timing as they are generated by the SNS beam pulse itself. Also, as these backgrounds produce

low-energy nuclear recoils, pulse-shape analysis also does not reject these backgrounds.

BEAM-RELATED NEUTRON BACKGROUNDS

Fast neutrons produced by the SNS beam represent the most important background for a CEvNS search at the SNS. To measure the flux of beam-related neutrons (BRN) in different locations on the SNS target floor and in Neutrino Alley, ~ 5 liter liquid scintillator detectors were deployed at the SNS. This work led to the identification of Neutrino Alley as a possibly suitable location for a CEvNS detector. Later, the Sandia Neutron Scatter Camera [79] was brought to locations on the target floor and Neutrino Alley to better measure the energy and time spectra of the BRN produced by the SNS. As seen in Fig. 2.5, Neutrino Alley was found to have a BRN flux that is approximately eight orders of magnitude lower than locations on the target floor. This is mainly due to the ~ 20 m of engineered backfill (concrete+steel) between the SNS target and a detector in Neutrino Alley, which drastically lowers the neutron flux in Neutrino Alley. Further measurements have shown that Neutrino Alley has a neutron flux which is low enough for CEvNS measurements in CsI[Na] (Sec. 2.2.2) and liquid argon (this work). The measured BRN in Neutrino Alley were also confined to a $1 \mu\text{s}$ window in time around the beam pulse so there was no large delayed neutron component. The measured BRN timing spectrum allows for a clean measurement of the delayed neutrinos from the muon decay without the presence of the BRN backgrounds.

A separate measurement of the beam-related neutron flux at the CENNS-10 detector location in advance of the installation of the CENNS-10 detector was made using the SciBath detector [80,81]. SciBath is an 82-liter liquid scintillator detector with 3D event reconstruction capabilities and is read out with a cubical 3D grid of wavelength shifting fibers connected to multi-channel PMTs. The SciBath detector ran for two months from September-November 2015 at this location and demonstrated that the measured BRN flux of ~ 10 neutrons/day is low enough for a CEvNS measurement, although the BRN flux at the CENNS-10 location is larger than that in the CsI[Na] detector location. After background subtraction, an unfolding method extracts the true neutron

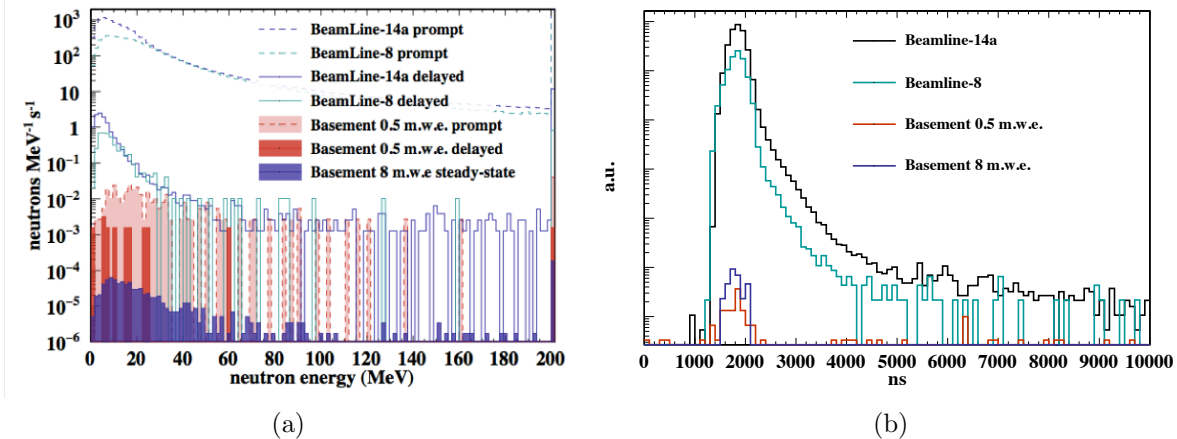


Figure 2.5: (a) Measured beam-related neutron energy spectrum from the Sandia Neutron Scatter Camera in locations on the SNS target floor (labeled BeamLine 14a and 8a) and Neutrino Alley (labeled 8 m.w.e. steady-state). (b) Measured beam-related neutron timing spectrum from the Scatter Camera measurements.

spectrum in the prompt beam window ($\sim 1 \mu\text{s}$ after beam spill) from the SciBath run [82, 83]. The extracted flux as a function of true neutron energy in the prompt window is shown in Fig. 2.6. Further, a background subtraction in the delayed region ($> 1 \mu\text{s}$ after beam spill) shows no measurable excess and is consistent with zero.

NEUTRINO-INDUCED NEUTRON (NIN) BACKGROUNDS

Another possibility for a beam-related background for a CEvNS search at the SNS are neutrino-induced neutrons (NINs) generated from (ν, yn) reactions where y is the neutron multiplicity. NINs are produced by the neutrinos from the SNS interacting in shielding components such as lead [84–86]. NINs are also used as a detection channel for the Helium and Lead Observatory (HALO) supernova neutrino detector [87]. The NIN interactions produce neutrons through the

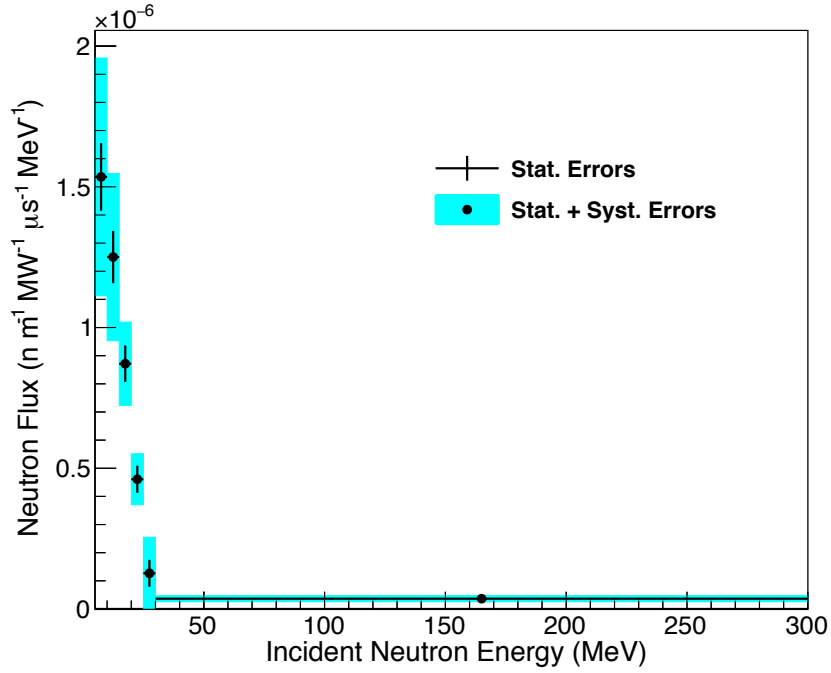
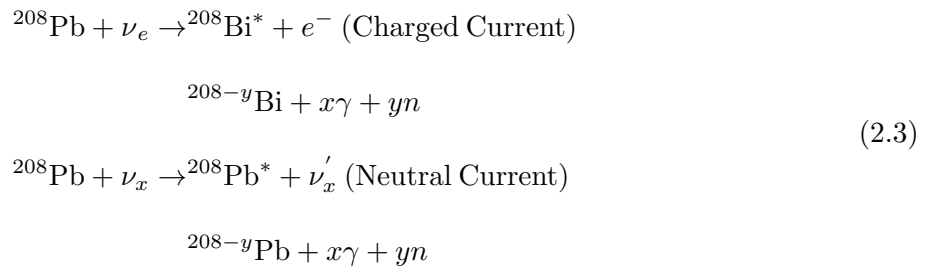


Figure 2.6: Unfolded prompt beam-related neutron (BRN) spectrum from the measurement at the CENNS-10 location with the SciBath detector. The measured rate of BRN in the SciBath detector [82], $\mathcal{O}(10)$ /day, shows that BRN are not a prohibitive background for a CEvNS detection with CENNS-10. From this measurement, there is no evidence of a delayed beam-related neutron component at the CENNS-10 location. This spectrum is used as the input for the beam-related neutron simulations described in Chapter 5.

reactions [88]:



where x represents the γ multiplicity of the reaction. As this is an interesting measurement in its own right due to the similarity to supernova neutrino detection [87], COHERENT has developed dedicated NIN detectors known as the “neutrino cubes”. The neutrino cubes instrument several hundred kg of lead and iron with ~ 1 liter liquid scintillator cells in Neutrino Alley to measure this

cross section. A non-zero NIN measurement was made in [4] with a liquid scintillator cell in the shielding structure used for the CsI[Na] detector and was larger than the theoretical prediction. A simulation of the process with the shielding structure described in Chapter 3 predicts that NINs are a negligible background to a CEvNS search in CENNS-10.

2.4 OTHER CEvNS SEARCHES AROUND THE WORLD

Now that detector technologies have advanced to the point where low-energy nuclear recoils are measurable, many experiments in addition to COHERENT are attempting to harness the vast physics potential of CEvNS. Stopped-pion sources such as the SNS (Sec. 2.1.1) and nuclear reactors are the most common sources of neutrinos for a CEvNS measurement. Detector advancements allow the community to harness the power of these intense, low-energy neutrino sources. A selection of other experiments searching for CEvNS are covered in this section, although none have successfully detected it.

One other experiment currently operating at a stopped-pion source is the Coherent Captain-Mills experiment [89] which operates a tonne-scale scintillation-only liquid argon detector at the Lujan Center at Los Alamos National Laboratory. Lujan is an 80 kW accelerator with similar background rejection capabilities to the SNS. This results in a factor of 20 reduction in neutrino flux compared to the SNS operation at 1.4 MW at the same distance from the target.

The neutrino flux at a reactor is approximately six orders of magnitude higher than that of a stopped-pion source. However, there is no natural background rejection from timing as the reactor is a continuous source of neutrinos. Also, the mean neutrino energy for a reactor is $\langle E_\nu \rangle \sim 3$ MeV, so the resulting nuclear recoil energies from CEvNS interactions are ~ 100 times lower than the recoils from a stopped-pion source. Sub-keV detector thresholds are required to detect reactor neutrino CEvNS.

There are several experiments that are attempting to use the low-threshold and excellent energy resolution of cryogenic HPGe detectors for CEvNS measurements. HPGe detectors are popular

as the necessary thresholds are demonstrated to measure the very low-energy nuclear recoils from reactor neutrinos. These experiments are located at different reactor sources around the world and include the CONUS experiment [90], the ν GeN experiment [91], the TEXONO experiment [92], and the MINER experiment [93].

A sample of other detector technologies are also proposed to measure the sub-keV recoils from reactor neutrino CEvNS interactions include gram-scale calorimeters with a $\mathcal{O}(\lesssim 10 \text{ eV})$ threshold [94], composite Ge and Zn bolometers with $\sim 10 \text{ kg}$ masses [95], liquid noble gas time projection chambers, and charge-coupled device arrays [96]. The CEvNS community is a burgeoning one and this list is just a small sample of the ideas designed to take full advantage of the exciting physics capabilities of CEvNS. A more full scope of plans within this community can be found within [97, 98].

CHAPTER 3

THE CENNS-10 LIQUID ARGON DETECTOR

Liquid argon is a good candidate target nucleus for a CEvNS measurement due to the possibility of a low-threshold detector and the relative scalability of liquid noble gas detectors. The CENNS-10 liquid argon detector was installed in Neutrino Alley as part of the COHERENT experiment for a CEvNS detection on argon and is outlined in this chapter. It concludes with a CENNS-10 detector upgrade to allow for sensitivity to CEvNS after an engineering run at the SNS and the subsequent data collection period used in this work.

3.1 LIQUID ARGON AS A CEVNS TARGET NUCLEUS

Liquid argon (LAr) provides a low- N nucleus ($N = 22$) for CEvNS detection, between sodium and germanium in the COHERENT suite of target nuclei. Liquid argon is a scintillator with a scintillation yield of 40 photons/keVee [99]. The large scintillation yield enables a low-threshold detector, a key requirement for CEvNS detection. Therefore it is a sensible choice of low N nucleus to map out the N^2 dependence of the CEvNS cross section, a goal of the COHERENT program.

Liquid argon scintillation occurs via two pathways when energy is deposited in the argon. The first is atomic excitation of argon atoms forming excited Ar_2 dimers. A VUV scintillation photon is emitted when the dimer subsequently de-excites. The other method is via recombination, where an argon atom is ionized and ionization electrons are emitted. An Ar_2^+ ionized dimer is formed and the same excited dimer state is ultimately formed when an emitted electron recombines with the

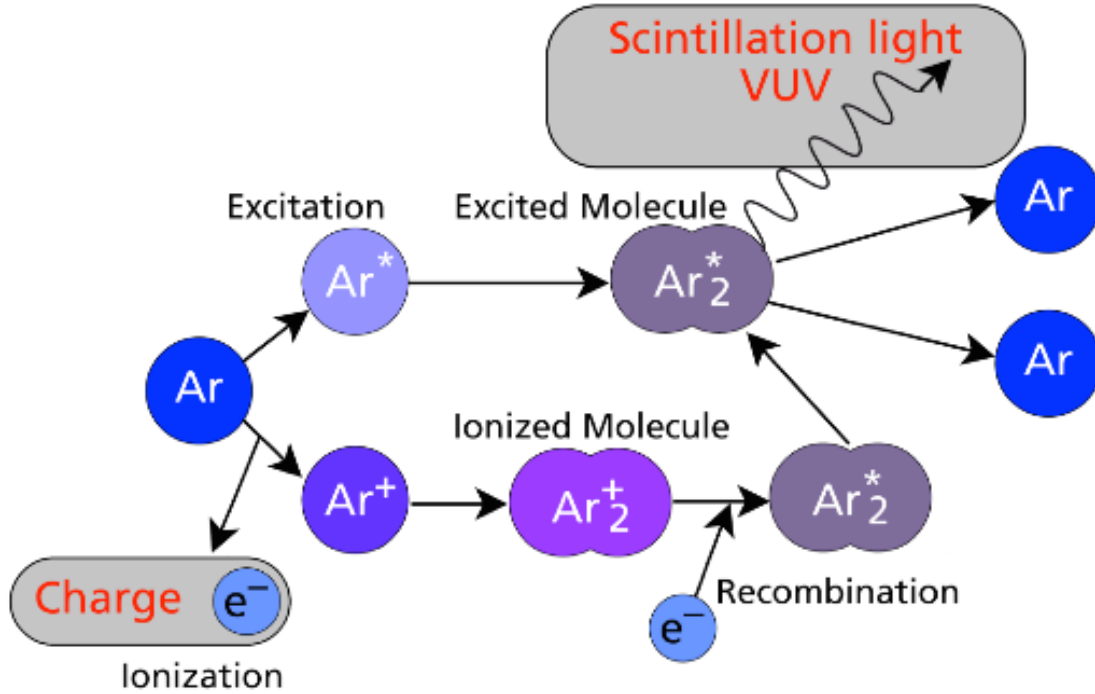


Figure 3.1: Scintillation mechanisms of liquid argon. Both the atomic excitation and ionization/recombination pathways allow for the emission of a VUV scintillation photon from the excited Ar₂ dimer. Figure from [100].

ionized dimer. The dimer then de-excites in the same manner and a VUV scintillation photon is emitted. These two scintillation emission methods are described pictorially in Fig. 3.1. For liquid argon, the ratio of ionized to excited argon atoms is 0.21 [99].

The argon atoms can be excited into two states, a singlet state and a triplet state. The two states have characteristic decay times of $\tau_s \sim 6$ ns for the singlet state and $\tau_t \sim 1600$ ns for the triplet state. The singlet to triplet state ratio depends on the localized energy loss and therefore on particle type and the amount of energy deposited [101]. The difference in the singlet/triplet ratio for nuclear/electron recoils (NR/ER) and the decay times of the states allows for powerful pulse shape discrimination (PSD) capabilities in liquid argon to suppress ER backgrounds. The purity of the argon in the detector is important as the triplet light can be quenched from impurities such as nitrogen [102] and methane. A measurement of the triplet state lifetime can provide insight on the impurity level in the detector. For a scintillation-only detector such as CENNS-10, impurity

levels of ~ 1 ppm are acceptable.

Liquid argon scintillates with a emission spectrum which is narrowly peaked at 128 nm, a wavelength in the vacuum ultraviolet (VUV) region [103,104]. Due to the strong absorption of VUV in most materials, the liquid argon scintillation light is outside the detectable range of standard photomultiplier tubes. A wavelength shifter such as 1,1,4,4-tetraphenyl-1,3-butadiene (TPB) shifts the wavelength of the emitted scintillation photons to a range where the photomultiplier can readily detect the scintillation photon in liquid argon applications. TPB shifts the wavelength of the argon scintillation light by absorbing the 128 nm scintillation light and re-emitting photons at a range around 400 nm with efficiencies approaching 100% [105,106]. The emission spectrum of TPB matches up well with the peak quantum efficiency of standard bialkali photomultiplier tubes and provides a mechanism to detect the re-emitted light.

Liquid argon also has a well-measured quenching factor (QF or L_{eff}) [107–110] at energies relevant to CEvNS. A measurement of the quenching factor allows for knowledge of the response of liquid argon detectors to nuclear recoils in the CEvNS region of interest, which for the SNS neutrino spectrum is $0 < E_{nr} < 125$ keVnr as seen in Fig. 3.2. An analysis was performed within the COHERENT collaboration [111] of the world liquid argon quenching factor data in order to determine the optimal quenching factor for use in the CENNS-10 data analysis. The world quenching factor data for liquid argon is seen in Fig. 3.3. The quenching factor in CsI[Na] is the largest source of uncertainty on the CsI[Na] measurement made by the COHERENT collaboration. As a reminder, the quenching factor is roughly defined as the relative quenching of light produced by a nuclear recoil in keVnr, again where nr is nuclear recoil, compared to an electron recoil at the same energy in keVee, again where ee is electron equivalent. Generally, the measurements in [107–110] defined the quenching factor by comparing a known nuclear recoil energy to a reference electron recoil energy from a detector calibration source, which differs between experiments. The detector response to electron recoils is then assumed linear down to 0 keVee.

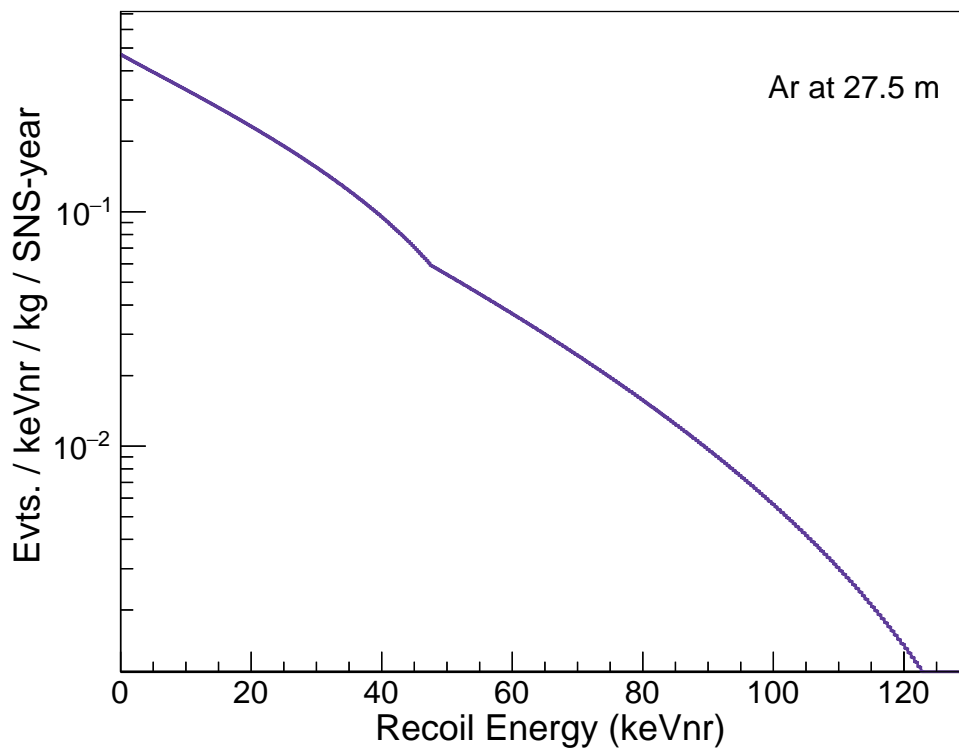


Figure 3.2: SM predicted CEvNS recoil spectrum for the SNS neutrino spectrum for a liquid argon target at 27.5 m from the SNS Hg target where the CENNS-10 detector is located.

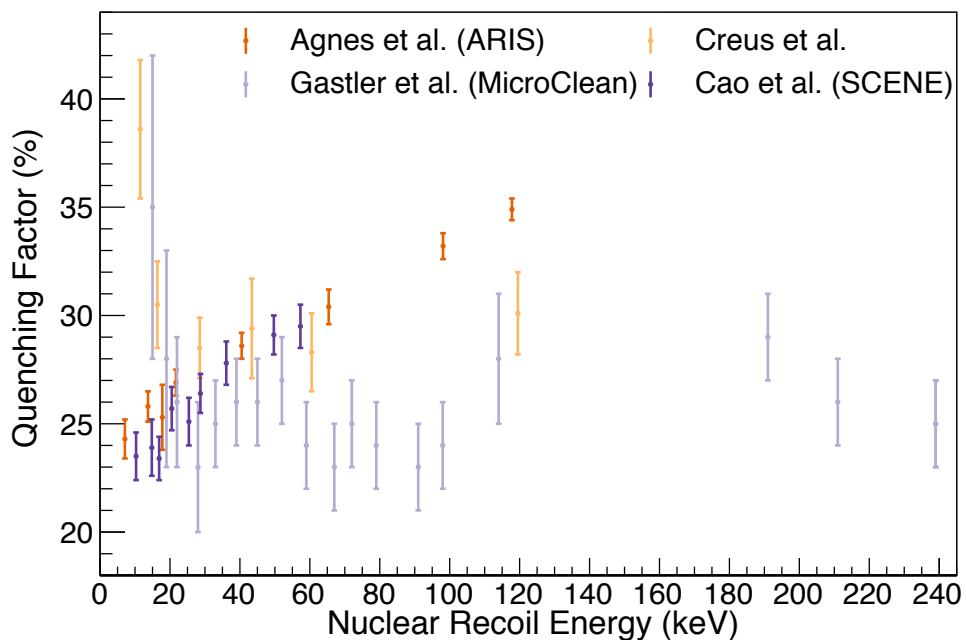


Figure 3.3: The world liquid argon quenching factor data. The data are not in obvious agreement so an analysis was performed considering all data points within the range 0-125 keVnr.

3.1.1 LAR QUENCHING FACTOR ANALYSIS

Although the data in Fig. 3.3 are not in obvious agreement, there was no valid reason to throw away any data sets or points within a data set so all data was considered following the guidelines of the Particle Data Group (PDG) [8] for a combined data set. All data provided within the range of 0-125 keVnr was fit with a linear model to determine the best fit quenching factor for use in the analysis of the CENNS-10 data. With the CENNS-10 detector not expected to have high efficiency for recoils < 20 keVnr, the need for a more complex energy dependence is not clear for the analysis presented in this work. Correlated systematic errors that are directly reported in [107] were taken into account during the fit to the data. The linear fit to the data produced a χ^2/dof value of 138.1/36. Again following the PDG, the resulting errors on the data points were scaled by $\sqrt{\chi^2/\text{dof}} \sim 2$ so that $\chi^2/\text{dof} = 1$ for the linear fit and the full fit result is

$$\begin{aligned} \text{QF} &= p_0 + p_1 T(\text{keVnr}) \\ p_0 &= 0.246 \pm 0.006 \\ p_1 &= (7.84 \pm 0.95) \times 10^{-4} \\ \rho &= -0.79 \end{aligned} \tag{3.1}$$

where ρ is the correlation coefficient between p_0 and p_1 . The resulting fit and error band is seen in Fig. 3.4. The results of this analysis are applied to the quenching factor used in the CENNS-10 simulation (Chapter 5). The resulting error from the fit given by the error band only produces a small change of $\mathcal{O}(\pm 1\%)$ in the predicted CEvNS rate.

3.2 THE CENNS-10 DETECTOR

CENNS-10 is a single-phase, scintillation-only liquid argon detector that was designed and built at Fermilab for a CEvNS effort at the Booster Neutrino Beam [112]. The detector was initially moved to IU in 2014 for commissioning and testing. It was brought to the SNS in late 2016 and installed

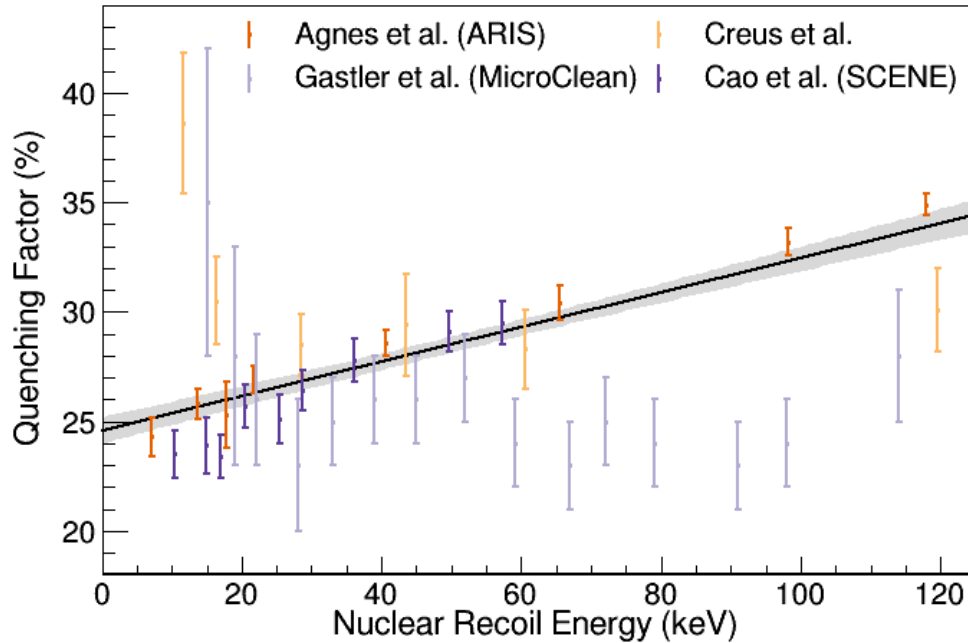


Figure 3.4: Results of a fit to the world liquid argon quenching factor data. The error bands come from the fit and the scaling procedure described in the text.

in Neutrino Alley for an “Engineering Run” from January 2017-May 2017 with reduced shielding and a high energy threshold. Details of the Engineering Run are not mentioned in detail in this work except in the context of subsequent detector upgrades. The setup of the photon detection system for the Engineering Run did not allow for a low enough energy threshold for a sensitive CEvNS search but it provides an opportunity to understand the operation of the detector and study backgrounds. A CEvNS analysis on the Engineering Run ultimately placed a limit on the CEvNS cross section [82, 83].

The period after the detector was then upgraded for better light collection (Sec. 3.3) and improved background shielding (Sec. 3.2.4) in June 2017 during a planned SNS shutdown is the focus of this work. CENNS-10 was re-installed in Neutrino Alley after the upgrade for SNS operation beginning in July 2017. CENNS-10 continues to operate in this configuration as of August 2017 to the present taking production data with an improved threshold (“Production Run”). The full CENNS-10 detector is shown in Fig. 3.5 and the important components are subsequently described in the following sections.

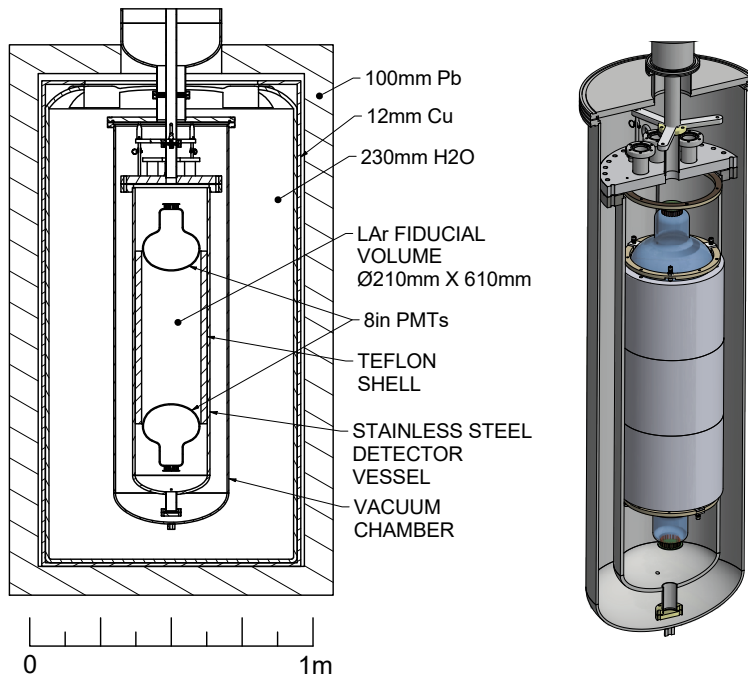


Figure 3.5: (Left) Layout of the CENNS-10 detector with the important components labeled. The shielding structure is described further in Sec. 3.2.4. (Right) Engineering drawing of the CENNS-10 inner detector volume showing the definition of the active volume between the two PMTs and the Teflon reflector.

3.2.1 INNER DETECTOR CRYOSTAT

The full CENNS-10 detector volume is defined by a stainless steel vessel with a diameter of 10.5” and height of 40”. The vessel can hold up to 56.8 L of pure liquid argon, or 79.5 kg with the density of liquid argon of 1.4 kg/L at 87 K, without the photon detection system installed. The active detector volume is roughly defined by the cylindrical volume between two 8” Hamamatsu R5912-02 MOD photomultiplier tubes (PMTs) on the top and bottom of the detector and a TPB-coated Teflon cylindrical shell reflector as seen in Fig. 3.5. For the Engineering Run, this reflector was a TPB-coated acrylic shell backed by a thin Teflon sheet and a total active detector mass of 29 kg. For the Production Run, the acrylic shell was replaced with the TPB-coated Teflon cylindrical shell which reduced the active detector mass to 24.4 kg.

3.2.2 CRYOGENIC AND GAS HANDLING SYSTEMS

The CENNS-10 detector is initially filled using the cold boil-off gas from a 180 L liquid argon dewar provided by AirGas. Consultations with AirGas provided expectations that the boil-off gas from the dewar is as pure as the high purity (99.999% pure Ar) gas bottles, although the purity of the boil-off gas is not directly tested. Before filling CENNS-10 for the first time at IU in 2016, it was verified using a Stanford Research Systems Universal Gas Analyzer [113] that the boil-off gas from the dewar was sufficient for our initial purity requirements to fill CENNS-10.

For cooling and liquefying argon, CENNS-10 relies on the operation of a Cryomech PT-90 pulse-tube cryocooler which maintains a cooling capacity of 90 W at 80 K [114]. The cryocooler operates continuously during filling and normal operation of CENNS-10 and eliminates the need for liquid nitrogen or any other cryogenics to maintain liquid argon temperature within the detector vessel.

The argon level in CENNS-10 is kept constant by a system of circulating and re-liquifying the boil-off gas argon from the detector through the cryogenic and gas handling system as seen in Fig. 3.6. To liquefy the argon, the outgoing cold boil-off gas from the vessel runs through a heat exchanger along with incoming gas circulated through the gas handling system. The cooled argon then enters a condenser which is held at liquid argon temperatures by the cryocooler and a heater mounted on the cold head. The heater power is monitored remotely as part of the CENNS-10 slow control system described in Sec. 3.2.3. The heater prevents the freezing of the argon in the condenser as the power output of the cryocompressor itself is constant. Here the gas argon condenses on a set of copper fins and drips down into a small pipe at the end of the condenser which then fills the CENNS-10 detector volume. The detector is filled from the bottom to avoid cooling detector components too quickly.

The re-circulation is accomplished using a Metal Bellows MB-111 circulation pump [115] controlled by a Sierra flow meter which restricts the flow rate to 5 slpm. The recirculating gas is also continuously purified using a SAES MonoTorr PS4-MT3-R-1 Zr getter [116,117] which can remove

impurities such as nitrogen, oxygen, and methane to a level of < 1 ppb. The flow rate is chosen to match the optimal flow rate for argon gas through the getter.

To prevent rapid boiling of the liquid argon, the insulating vacuum jacket is evacuated to a level of $\leq 1 \times 10^{-6}$ torr using a Pfeiffer-Balzers TPU-510 Turbo Molecular High Vacuum Pump before filling CENNS-10. This vacuum level has been consistently achieved both during the Engineering Run and throughout the now > 2 year period after the light collection upgrade. A high insulating vacuum level aids in the stability of the CENNS-10 detector over its operation period. In the case of a power failure of the pumping station and subsequent vacuum increase, an electrical latch system requires a manual reset of the turbo pump. The latch system prevents the turbo pump from operating in a low-vacuum environment to avoid damage to the pump.

3.2.3 DATA ACQUISITION SYSTEM

The CENNS-10 data acquisition (DAQ) system consists of two parts: a fast DAQ for PMT signal extraction and a slow DAQ for remote detector health monitoring.

FAST DAQ

The fast DAQ system consists of the readout for the two 8" Hamamatsu PMTs that make up the CENNS-10 photon detection system. All of the readout electronics for CENNS-10 are warm electronics and not located within the liquid argon volume. A base for the PMTs was designed following the recommended voltage drop specifications from Hamamatsu across the various dynodes. Both PMTs are powered to +1650 V and draw a current of $\sim 65 \mu\text{A}$ using a Wiener iSeg positive high voltage power supply and a Wiener MPOD mini-crate. The PMT signals are AC-coupled with the digitizer through signal splitters. The signal from the PMT is read out through a CAEN V1720, a 12-bit, 8-channel, 250-MHz digitizer with an onboard FPGA. Each PMT signal is passed through a Mini-Circuits BBLP-39+ 23-MHz Low Pass, Flat Time Delay Filter before being digitized. Signals from the SNS are digitized and used to trigger the DAQ during SNS operations.

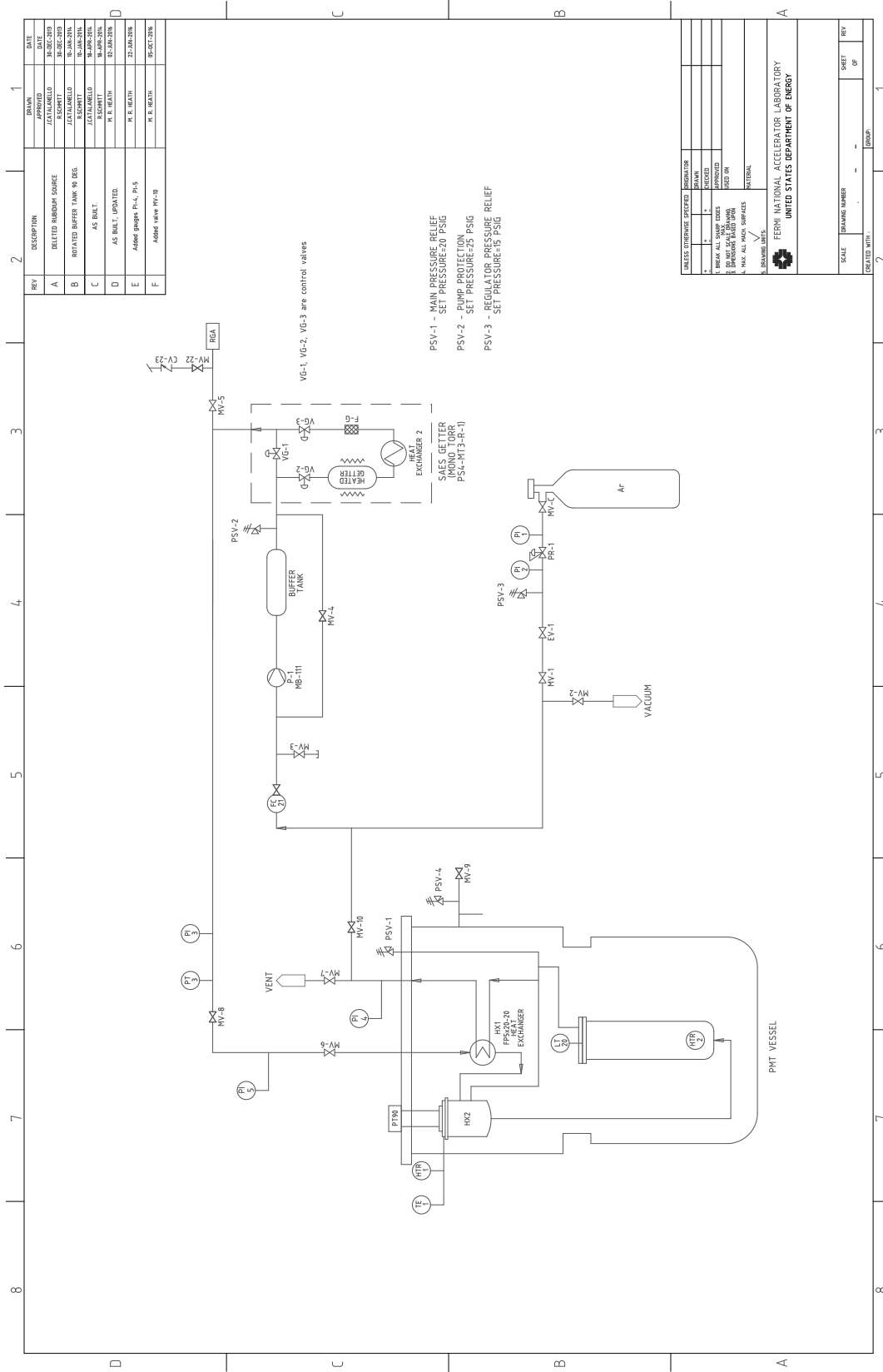


Figure 3.6: The CENNS-10 plumbing diagram. This system transports and circulates the boil-off gas from the liquid argon dewar and liquefies the gas argon in order to fill the detector. Boil-off argon gas from the detector is also circulated and constantly purified using the Zr getter system detailed on the right hand side of the diagram.

REMOTE SLOW MONITORING SYSTEM

The CENNS-10 slow DAQ system is designed to allow for 24/7 monitoring of important detector operation parameters. The liquid argon level is roughly monitored with five PT-100 resistive temperature detectors (RTDs) at approximately equal spacing from the bottom of the CENNS-10 inner detector structure to the top of the detector flange. An American Magnetics Inc. capacitive level sensor that extends from the top of the detector flange to the top PMT and finely measures the liquid argon level near the top PMT. The cryostat is further monitored through the detector vessel pressure, argon gas flow rate, the insulating vacuum vessel pressure, and the resistive heater power. The fast DAQ is monitored to ensure it is operational at any given time when the SNS is operational. Simple processing of the fast DAQ runs occurs in order to check for changes in the baseline and anomalous trigger rates. The SNS beam information is also monitored as part of this system.

For the CENNS-10 Production Run, data from the slow monitoring system is collected using the Experimental Physics and Industrial Control System (EPICS) [118] archiving system that is widely used by the SNS for accelerator monitoring. The data are then fed into a CENNS-10 GUI using Control System Studio (CSS or CS-Studio) [119] that operates on a Ubuntu Linux PC in Neutrino Alley. The GUI allows for remote monitoring of the CENNS-10 system. The CENNS-10 detector is monitored 24/7 in three 8 hour shift periods per day. Alarms are set using CSS and are present to alert shift takers of any anomalous readings or changes to the CENNS-10 operating parameters. The current alarms range from a high temperature measurement to an increase in insulating vacuum pressure or a DAQ system crash. The data are saved and can be accessed later to look at parameter trends over time for any period during detector operation. A picture of the monitoring GUI is shown in Fig. 3.7.

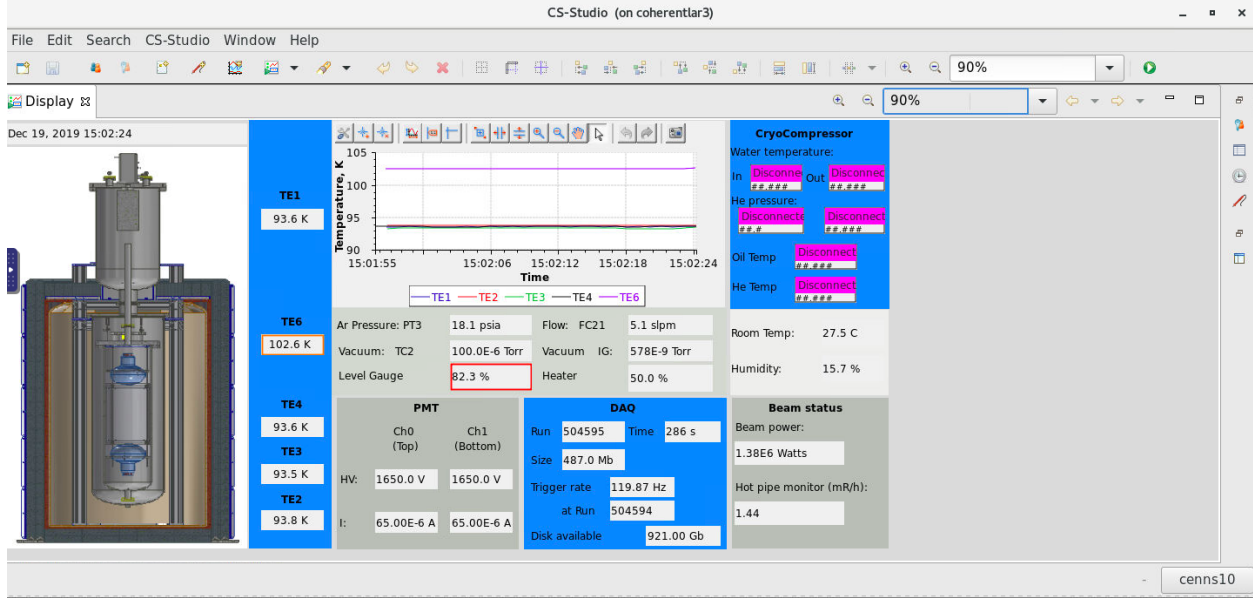


Figure 3.7: The CENNS-10 slow monitoring system. Detector information is read out for 24/7 shift taking. Major (red box) and minor (orange box) alarms are set to alert shift takers of any problematic readings in the detector. Note at this time, the capacitive level gauge reading was acceptable but the GUI had not been adjusted for a lower nominal liquid argon level.

3.2.4 DETECTOR SHIELDING

The flux calculations and energy spectra from the measurements described in Sec. 2.3.1 were used as inputs to simple MCNP6 and FLUKA [120,121] simulations of the CENNS-10 detector with varying shielding configurations. These simulations were used to inform the shielding design in CENNS-10 to reduce the detected rate of these backgrounds. The successful reduction of the beam-unrelated steady-state backgrounds is confirmed with a complete GEANT4 simulation described in Chapter 5 and measurements of the steady-state background rates.

The CENNS-10 detector shielding consists of 20 cm of water shielding to help reject the beam-related neutron backgrounds that mimic the CEvNS signal. The detector cryostat and vacuum vessel are placed inside of an Assmann model ICT250 [122] 250 gallon polyethylene tank filled with deionized water from the SNS. The water shielding can be removed by emptying the tank for dedicated data runs without the water shielding installed, described further in Sec. 3.4. Running without the water shield allows for further understanding of the neutron backgrounds present in



Figure 3.8: The CENNS-10 detector and all components installed in Neutrino Alley. The shielding structure can be seen around the detector along with the associated systems for the vacuum pumps, gas handling rack, fast and slow DAQ, and the cryocompressor.

the CENNS-10 detector. To shield gamma ray and electron backgrounds, there is a 1.25 cm layer of Cu shielding and 10 cm of Pb shielding that fully enclose the detector. The environmental gamma ray backgrounds and the large flux of 511 keV gamma rays coming from the hot off gas pipe are reduced to negligible levels with the installation of the Cu and Pb shielding. The dominant electron recoil background in this configuration is ^{39}Ar , which cannot be shielded in this way as it is naturally present in the atmospheric argon used in CENNS-10. The complete CENNS-10 shielding structure is shown in Fig. 3.5 and the complete CENNS-10 as installed in Neutrino Alley is shown in Fig. 3.8.

3.3 CENNS-10 PHOTON COLLECTION SYSTEM UPGRADE

An upgrade to the CENNS-10 photon collection was made after determining that the detector threshold of ~ 80 keVnr seen in the Engineering Run configuration was not sufficient for a sensitive CEvNS search. The upgrade consisted of replacing the TPB-coated acrylic parts used in the Engineering Run with a TPB-coated Teflon side reflector and direct TPB coating on the PMTs. Separate 8" PMTs were acquired from those used in the Engineering Run. Both of the TPB coating methods are shown to be successful in previous experiments [77,123] and could provide the improved threshold necessary for a sensitive CEvNS search. From previous studies in [124,125], a TPB thickness of 0.1-0.2 mg/cm² obtained the highest fluorescence efficiency with a sufficiently thick coating to absorb the 128 nm photon and re-emit in the visible spectrum but not overly thick so that the re-emitted photon is then re-absorbed by the TPB layer. The new PMTs had a frosted glass window and were directly coated with TPB commercially by Intlvac [126] to a thickness of 0.2 mg/cm² on each PMT.

The Teflon cylinder coating was performed at ORNL using a vacuum bell jar evaporator. The TPB coating thickness depends on the initial mass of TPB in the crucible and the distance of the sample from the crucible. Nominally as in Fig. 3.9, the operation of the evaporator is such that a sample to be coated is set above the evaporating TPB which sits inside the ceramic crucible. The evaporator operates in a high vacuum to prevent splattering of the evaporating TPB. The vacuum is created inside the evaporator volume with a turbomolecular pump backed with a diffusion pump and reaches vacuum levels < 1 mTorr. The TPB evaporates outward from the crucible within the field of view by applying a current which heats the crucible.

Initially with the setup shown in Fig. 3.9, test runs were performed with the evaporator using 1" diameter Teflon disks. The successful evaporation on these disks ensured that it was feasible to both coat Teflon with TPB and coat an 8" long cylinder. A UV light in combination with a UV-VIS spectrometer and a equivalent length TPB-coated acrylic plate tests the thickness uniformity across the length of the cylinder. The results of that test, seen in Fig. 3.10 show that an even coating



Figure 3.9: Operation of the bell jar evaporator at ORNL with test Teflon pieces to ensure that the TPB adhered to the Teflon surface before use on the Teflon cylinders in CENNS-10. The TPB is in the crucible (the ceramic bowl in the center) which is wrapped with tungsten wire and heated to a point where the TPB evaporates from the crucible.

was achieved on a length equivalent to the Teflon cylinder that were planned for the CENNS-10 upgrade. Further tests were run showing the reproducibility of the desired coating thickness to $\sim 10\%$ by using the same initial mass of TPB at the same crucible distance.

The Teflon cylinder was split into three 8" long, 0.75" thick sections as the maximum < 12 " height cylinder that could fit inside the evaporator and be coated at one time was smaller than the 24" total height needed for the CENNS-10 fiducial volume. Each section was coated individually using the same procedure. Evaporating in the same manner as the test runs for the Teflon cylinders installed in CENNS-10 would necessitate cutting the cylinder into yet more sections to expose the inner radius of the cylinder to the crucible field of view. Needing to further section the cylinders has the added detriment of increasing the area where scintillation light can escape the active volume

TPB Spectrometer Intensity Measurement

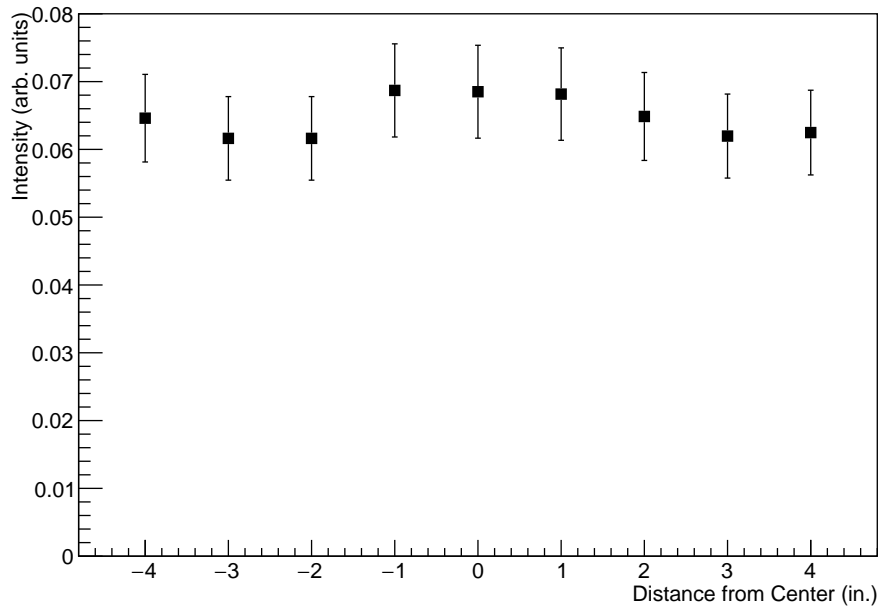


Figure 3.10: Results of a spectrometer measurement showing the peak light intensity seen vs the distance from the center of the acrylic plate. The intensity across an 8” section about the center of the plate was seen to be constant within error, so it was seen an even coating could be achieved using the Teflon cylinders of the same length.

of CENNS-10. To avoid sectioning and coat each 8” cylinder as one piece in the evaporator, a system was designed to allow the cylinder to slowly rotate within the evaporator. The crucible is placed inside the cylinder at the same distance from the edge of the cylinder as in the test runs. This system consisted of a roller platform powered by a small motor and is seen in Fig. 3.11.

Each cylinder was pumped out in the evaporator for ~ 5 hours before any current was applied to the evaporator to ensure a high vacuum level within the evaporator chamber. Then the current was applied as the cylinder rotated within the evacuated evaporator using the same operating parameters as those used in the test runs. The coating on each cylinder was checked before being taken out of the evaporator by shining a UV light across the surface of the cylinder to check for any obvious deficiencies. The three cylinders were coated to a thickness of $(0.19(0.19)[0.22] \pm 0.02)$ mg/cm^2 for the 1st(2nd)[3rd] cylinder section run of the evaporator. Fig. 3.12 shows one of the cylinder sections immediately after coating and before removing it from the evaporator.



Figure 3.11: The platform designed for the TPB coating of the Teflon cylinders shown inside the evaporator. The Teflon cylinder rotates on the rollers which are powered by a small motor. The crucible, not seen here but in Fig. 3.12, is placed inside the cylinder such that the crucible is located the same distance away from the cylinder coating surface as in the previous test runs.

The coated cylinders were then installed in the CENNS-10 inner detector. The cylinder with the thicker coating was placed in the center of the detector. As shown in Fig. 3.13, the coating method used for the cylinders allowed for an enclosed active volume. The longevity of the TPB coatings is demonstrated from the stability of the CENNS-10 light collection efficiency as shown in Fig. 4.7 over the 1.5 year continuous operation period of CENNS-10 considered here.

3.4 CENNS-10 SNS PRODUCTION RUN OPERATION

After the completion of the Engineering Run in May 2017, the detector was disassembled and the upgrade described in Sec. 3.3 took place. The timing of the upgrade coincided with a planned SNS

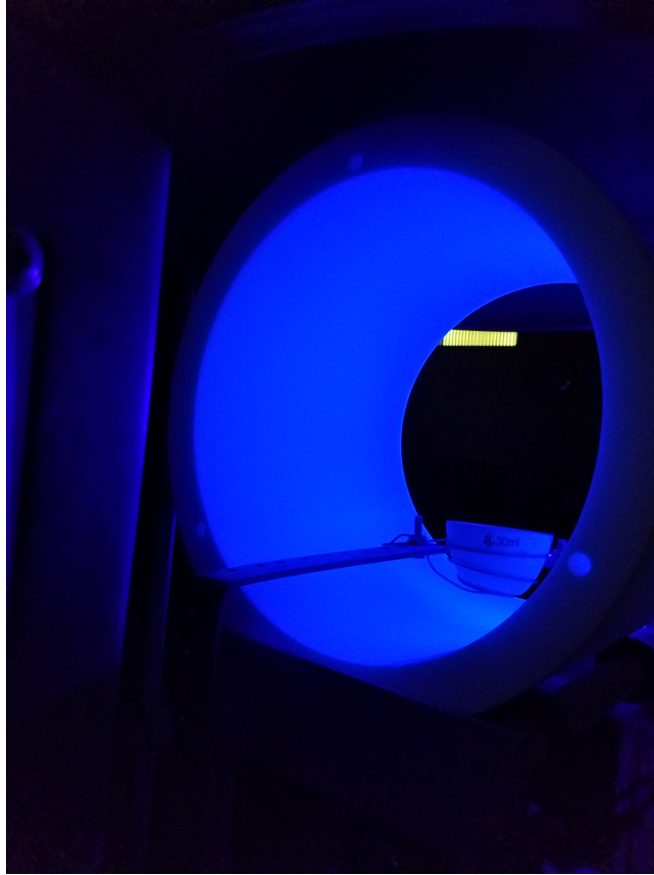


Figure 3.12: One of the TPB-coated cylinder sections immediately after coating in the evaporator. A UV light checks for obvious deficiencies in the coating and none were seen in any of the cylinders. Here the position of the crucible inside the cylinder can be clearly seen.

shutdown that ended in July 2017 so that the upgraded detector was full with liquid argon upon return of the beam on July 13, 2017.

The filling procedure began on July 3, 2017 after the installation of the detector in Neutrino Alley. The detector was full of liquid argon on July 10, 2017. The liquid argon level is tracked during filling using the temperature readings from the five RTDs placed inside the detector. The first, TE1, monitors the temperature of the cold head and this reading controls the heater operation as well to prevent the freezing of the argon. Three of them, labeled TE2-TE4, are placed near the bottom PMT, near the center of the detector, and near the top PMT respectively and are the best monitor of the increasing liquid argon level during filling. The final RTD is placed slightly up the neck of the detector vessel and is not submerged in liquid argon during normal operation and reads



Figure 3.13: The CENNS-10 inner detector volume as constructed in Neutrino Alley after the upgrades described in this section. The three TPB-coated Teflon cylinder sections and the two PMTs make up the total active volume of the detector.

slightly above liquid argon temperature. The level gauge is 9" long and extends down from the top flange of the detector vessel below the top PMT. The levels closely monitors the level around the top PMT so that if the liquid level goes below the base on the top PMT, it can be shut off to prevent sparking in gaseous argon. The trends of the RTDs and level gauge during the CENNS-10 filling can be seen in Fig. 3.14.

The complete shielding package was installed on July 28, 2017 with the completion of the lead shielding. Tracking the steady-state detector trigger rate as the shielding components were installed shows that the rate drops by a factor of 40 with the addition of the full shielding structure as compared to only the copper shielding installed.

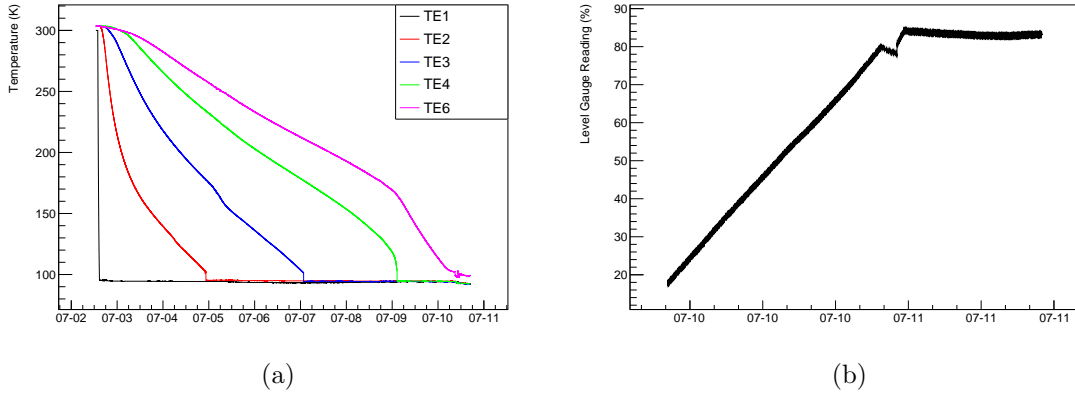


Figure 3.14: Data from the remote slow monitoring system during CENNS-10 liquid argon filling. (a) System temperature readings along the detector. The different TE labels represent RTDs placed at different depths in the CENNS-10 detector. The sensor TE1 is located near the bottom of CENNS-10 and they increase until TE6, which is located at the top of the detector inside the neck. TE6 is not covered with liquid argon when the detector volume is full. (b) the capacitive level gauge. The level gauge will read a non-zero as the liquid argon level is $\sim 9''$ from the top of the detector volume. The approximate level of the liquid argon can be seen by studying the temperature values. When a sensor stabilizes at ~ 92 K, the liquid argon is covering that sensor.

3.4.1 CENNS-10 TRIGGERING SCHEME

This section describes the digitizer triggering scheme for both CENNS-10 detector calibrations and constant operation during SNS beam-on periods.

CENNS-10 CALIBRATION

Calibration runs are taken approximately weekly during regularly scheduled SNS accelerator maintenance periods in order to monitor the CENNS-10 detector performance over time. For single photoelectron calibration (Sec. 4.2), a low-light LED pulser driven by a Rigol DG4162 [127] waveform generator which can be tuned to provide a range of light levels based on the driving voltage supplied to the LED. In this configuration, the digitizer is externally triggered with no set hardware threshold.

The second type of calibration runs are radioactive sources of known energies (Sec. 4.3) to measure the light collection efficiency of the detector. The digitizer is internally triggered with signals from the top (Ch.1) and bottom (Ch.3) PMTs are read into the digitizer. The waveform

window extends from $-1.5 < t_{\text{trig}} < 6 \mu\text{s}$ where $t_{\text{trig}} = 0$ is set by a hardware threshold crossing of 25 ADC units. The $6 \mu\text{s}$ window after the trigger occurs is chosen to allow the collection of a large fraction of the triplet scintillation light to be included. The individual signal from both PMTs must cross the hardware threshold within 24 ns in order to trigger the digitizer.

SNS OPERATIONS

Two accelerator signals for the timing of the 60 Hz pulsed beam (“Event 39”, Ch. 4) and determining whether a pulse contains protons-on-target (POT) (“Event 61”, Ch. 6) are also digitized as TTL signals during data taking at the SNS. These signals are nominally 2.5 V and are passed through an 20 dB attenuator to avoid saturation of the digitizer. The Event 61 is digitized as one in every 600 beam spills ($\sim 0.2\%$) are empty so they contain an Event 39 signal but no Event 61 signal is recorded. The digitizer is externally triggered with no set hardware threshold by a SRS DG535 gate/delay generator to produce an identical waveform with a $33 \mu\text{s}$ window on-beam (or “beam trigger”) and off-beam (or “strobe trigger”). The digitizer is triggered by the logic OR of the Event 39 signal and a NIM signal produced by the gate/delay generator for the off-beam trigger. This scheme produces a nominal 120 Hz trigger rate (60 Hz each for on-beam and off-beam triggers) for CENNS-10 during beam operations. Both windows contain data recorded with a time range of $-18 < t_{\text{trig}} < 15 \mu\text{s}$ with $t_{\text{trig}} = 0$ from the Event 39 signal (T_0) in the on-beam trigger. For the off-beam trigger, $t_{\text{trig}} = 0$ is set as $T_0 + 14 \text{ ms}$ to capture a equivalent window before the next beam spill. The off-beam trigger measures the steady-state, beam-unrelated backgrounds *in situ*. The SNS trigger scheme for the CENNS-10 Production Run is seen in Fig. 3.15.

The on-beam and off-beam windows are further broken down into prompt and delayed windows during the analysis of the SNS data in Chapter 6 and Chapter 7. The exact definition of these windows varies during the data analysis and are defined for each analysis separately. The beam-related neutron background is expected to only be non-zero in the prompt window. The CEvNS recoils from the neutrino produced by pion decays are exclusively expected in this window. In the

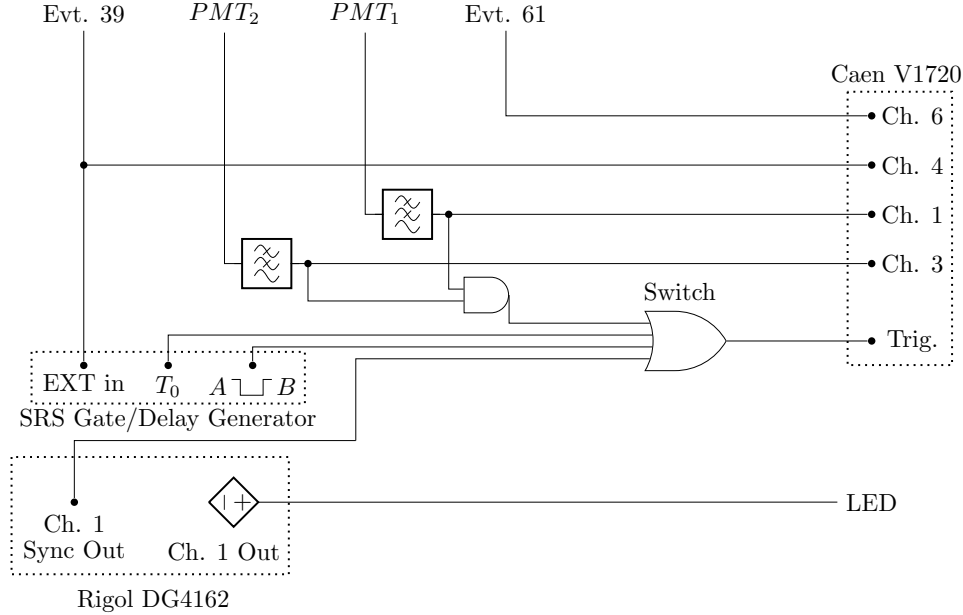


Figure 3.15: Diagram showing the trigger setup for the CENNS-10 Production Run. The SNS accelerator signals and the two PMTs are digitized signals while the on-beam and off-beam triggers are set by the SRS gate/delay generator.

delayed window, there is no beam-related neutron component expected with the CEvNS signal coming from the neutrinos produced by muon decays being the only predicted beam-related signal. A representation of the prompt and delayed windows along with the SNS neutrino spectrum is shown in Fig. 3.16.

3.4.2 CENNS-10 RUN SELECTION

A total of 7.37 GWhr ($\sim 16 \times 10^{22}$ POT) of integrated beam power spanning July 2017-December 2018 is the dataset considered for the first measurement of CEvNS with the CENNS-10 detector. The average beam power during this period is ~ 1.2 MW. The data are split up into 15 minute runs throughout this period with approximately constant SNS operations outside of planned maintenance and shutdown periods. The dataset is further reduced with a series of run quality cuts to produce a list of “golden runs” where the accelerator performance was stable and the full detector shielding was installed. The cuts placed to form the golden run selection for the CEvNS analysis (Chapter 7) are as follows:

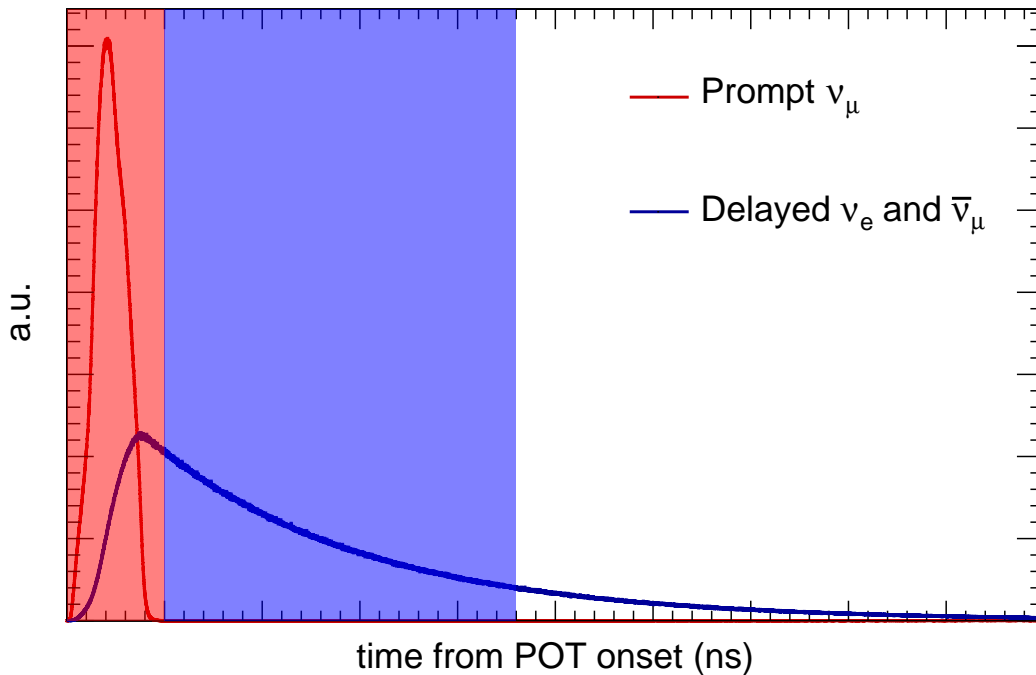


Figure 3.16: Representation of defined prompt (red box) and delayed (blue box) windows with the SNS neutrino spectrum overlaid. The neutrino spectrum gives an idea of the sections of the spectrum are included in the two windows. In the ultimate CEvNS analysis, the prompt window is $1.5 \mu\text{s}$ long and the delayed window is $3.5 \mu\text{s}$ long with the exact definitions with respect to t_{trig} given in Chapter 7.

- Full detector shielding installed and trigger rate of 120 Hz
- Hot-Off Gas pipe radiation monitor level
- $> 90\%$ nominal average beam power during run
- $> 90\%$ nominal integrated beam power during run
- $> 90\%$ beam power at start of run

The golden run cuts produce a final data set consisting of 6.12 GWhr (13.8×10^{22} POT) of integrated beam power for the CEvNS analysis with the full detector shielding installed (“full-shielded” dataset). A run list is also produced that identifies the golden runs during data processing. Fig. 3.17 shows the effect of the golden run cuts on the full dataset.

Further, a three-week, 0.54 GWhr (1.2×10^{22} POT) run was taken without the water shielding installed (“no-water dataset”, Chapter 6) to characterize beam-related neutrons *in situ*. The same

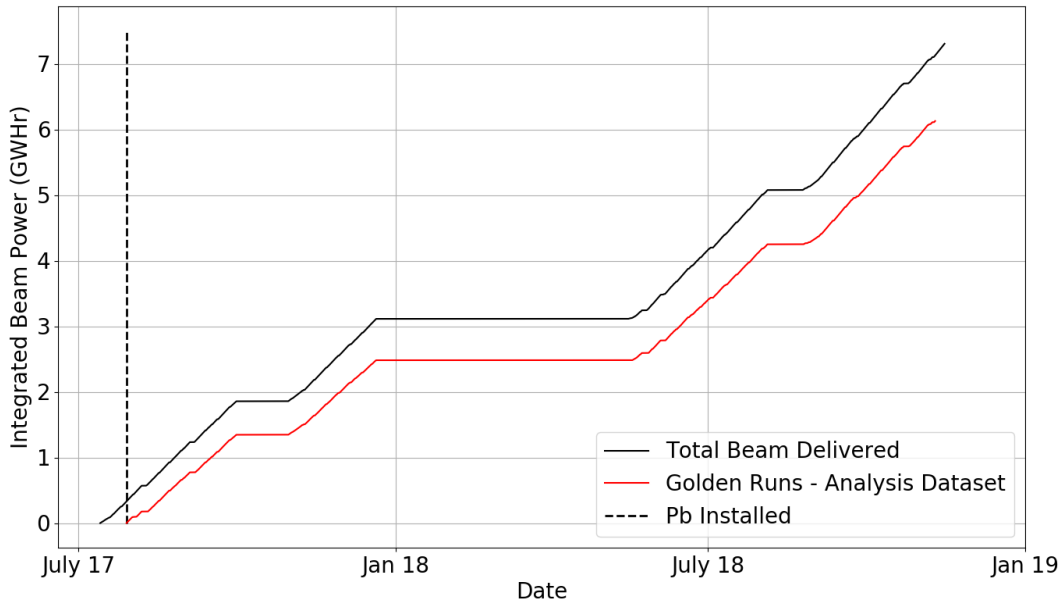


Figure 3.17: Integrated beam power over the run period considered for this work. About 10% of the total beam power is lost applying the golden run cuts after the installation of the full detector shielding. A total 6.12 GWhr dataset is produced. The accumulated beam power after the end of the golden runs is data without the water shielding for BRN characterization.

cuts are used on the no-water dataset in order to create a golden run list for the no-water analysis. The information from the no-water dataset constrains the BRN rate in the full-shielded dataset along with the previous measurements with SciBath and the CENNS-10 Engineering Run [82,83]. The BRN simulation predictions are tested using the no-water dataset.

CHAPTER 4

CALIBRATION OF THE CENNS-10 DETECTOR

In this chapter, the waveform analysis and calibration of the CENNS-10 detector after the upgrade is detailed. It begins with a description of the analysis framework used for the analysis of all data used in this work. Then the methods to determine the light collection efficiency through calibration with gamma ray sources is described. Included in the calibration set is the low-energy $^{83\text{m}}\text{Kr}$ source, which provides an *in situ* calibration near the CEvNS region of interest. Finally, the results of an AmBe source calibration show the PSD response of CENNS-10.

4.1 THE DAQMAN FRAMEWORK

The `daqman` framework [128] was originally written as data acquisition and analysis framework for the DarkSide-10 experiment [129]. A modified version of `daqman` is the data acquisition and main analysis framework for the CENNS-10 detector. The software is capable of both acquiring and processing data taken with the CAEN V1720 digitizer with each PMT using a separate digitizer channel as shown in Fig. 3.15. The analysis framework is designed as modular with existing modules for digitized waveform baseline finding, integration, and pulse finding being the most relevant in the context of this analysis. There are also various executables built in such as a waveform viewer and a digitizer output file converter from binary to a ROOT tree format. Certain parameters are passed into the modules by way of a configuration file. Some definitions used throughout this work to refer to different portions of the digitized triggers and are defined below:

- Waveform or DAQ window: ADC values over time, a vector spanning the entire length of the triggered data window. With the 250 MHz digitizer used in CENNS-10, each waveform sample is 4 ns long.
- Baseline: Representative of the digitizer offset value. The value of the baseline is determined from the pre-pulse samples in the first μs of the waveform. The baseline is subtracted from the individual waveform samples when evaluating the argon interactions.
- Pulse: Particle interactions are made up of groups of pulses seen in each PMT. A pulse is defined when a defined threshold over baseline is crossed in either PMT.
- Event (or Scintillation Event): An event is formed when a pulse is seen in both tubes within a 20 ns window from the earliest pulse seen in either PMT.

A 6 μs window is defined from the time the coincident pulse is seen in the PMTs to collect both the singlet and triplet scintillation light seen from an event. A description of the `daqman` modules used that are used to process and convert the data are defined below:

- ConvertData: Convert the data from a binary format output from the digitizer and convert to vectors which contain the waveform sample values vs time. The total length of the DAQ window is defined by the the given amount of pre-trigger and post-trigger time. For the SNS triggers, this is a total of 33 μs as described in Section 3.4. The total window length is 7.5 μs for calibration data as described in Section 4.3.
- BaselineFinder: Calculates the waveform baseline
 - FixedBaseline: Calculates the average values of samples in the first μs of the waveform. This calculation takes 15 sample segments and computes the mean and variance of the segments. It then compares to a threshold for the mean and variance passed to the `daqman` configuration file. If the mean and variance of the 15 sample segment are below the threshold, then the segment gets added to the good baseline and a new 15 sample segment is obtained. If there are a number of good segments where the samples cross a threshold, a good baseline is found and the procedure ends. This value is then used as

the baseline for the entire waveform. It requires a number of samples of a given length with a variance less than a given threshold for a valid baseline to be determined. These sample and variance thresholds are passed via a configuration file and are set to 50 and 1.2 respectively.

- **BallisticCorrection:** Further described in Section 4.1.1 and added to the `daqman` framework for this analysis. This algorithm provides a simple deconvolution for RC-time effects of the signal pickoff electronics chain which after the detector upgrade are on timescales similar to the triplet scintillation light.
- **Integrator:** Integrates the waveform by summing up the values of the waveform samples in the event window.
- **PulseFinder:** Find pulses in the PMTs within the waveforms. The two PMTs are considered separately with the pulse finding algorithm.
 - **DiscriminatorSearch:** Below is a description of the method used in this analysis to identify pulses in a waveform from one of the PMTs
 - * Move through waveform sample by sample
 - * When a 20 ADC threshold is crossed, the start of the pulse is defined as (WF_{n-i}) , with $i = 3$ and WF_n being the waveform value at sample n .
 - * Skip the next $6 \mu s$ in the waveform.
- **ScinEvtFinder:** Groups pulses found in the digitizer channels into events (or scintillation events).
 - Takes into account the start times of pulses in each PMT and collects them from earliest to latest in time within the waveform
 - If there is a pulse in both channels within in a 20 ns window, then an scintillation event (event) is formed.
 - Advance $6 \mu s$ from the start of the event. This mirrors the pulse finding condition. This ensures enough of the triplet light is included within the integration window of the event.

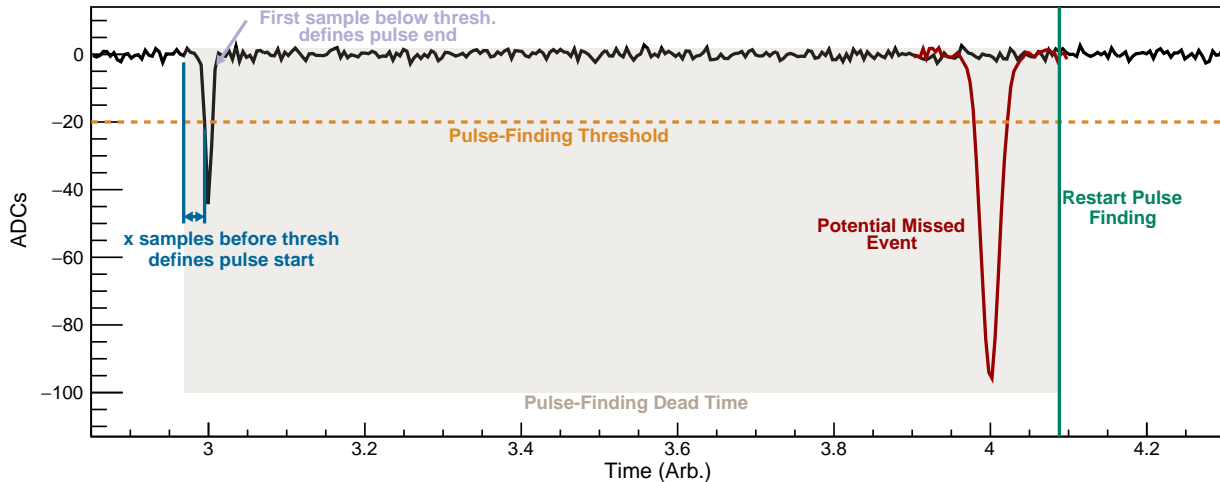


Figure 4.1: Illustration of the pulse finding algorithm. The waveform is stepped through sample-by-sample until a sample is found above the set threshold of 20 ADC units below baseline. trigger a dead time in the window before searching for another pulse. In this analysis, the dead time is $6 \mu\text{s}$. With the dead time is possible to miss events, shown as the red pulse, that occur during the dead time window. After the dead time window, shown as the green line, the pulse finding search continues until another pulse is identified. This search is performed in both PMTs independent of the other. Figure from [82].

- Compute parameters of the event such as the event integral, etc.

A cartoon example of the pulse finding/event forming method is shown in Figure 4.1.

4.1.1 EVENT INTEGRATION ALGORITHM

An RC-time decay effect is seen in the PMT signals due to the high voltage and PMT signals are carried on a single cable from the detector and then capacitively picked-off before the digitizer. The RC-time effect causes the value of the waveform to return below baseline after charge is distributed in the PMT. If not corrected, then this effect causes an underestimation of the total charge collected by the PMT as the RC time constant \simeq the triplet lifetime and the fixed baseline value is taken from pre-pulse samples. Fig. 4.2 shows an example of a waveform and demonstrates the RC-time effect.

An algorithm to deconvolve the RC effect seen in the waveform is contained in the module `BallisticCorrection` and included within the `daqman` framework. The effective RC-time constant is computed using single-photoelectron-level data taken from an LED pulser at and looking at the

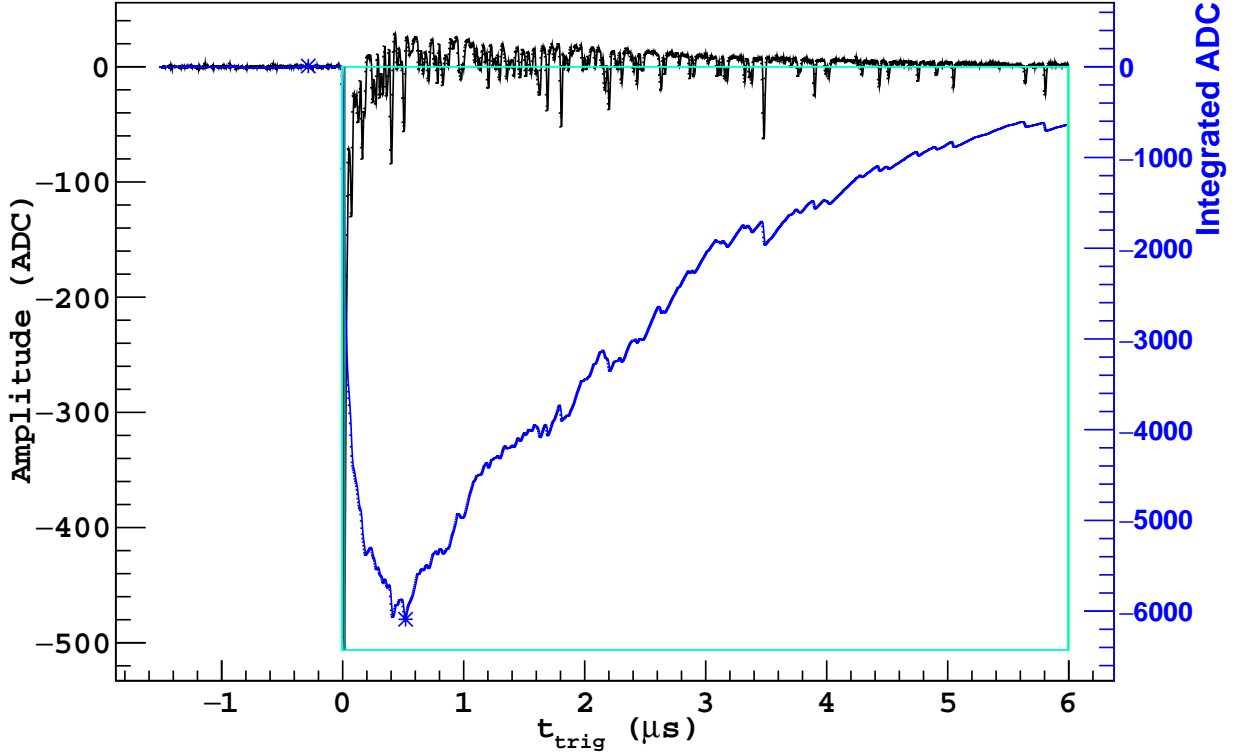


Figure 4.2: Example of raw baseline-subtracted waveform taken from the CENNS-10 detector calibration data. Note the integral, which is the dark blue line, reaching a maximum and then decaying while integrating through the waveform. This is the effect of the AC coupling in the PMT electronics. A simple integration, as is performed here, would not give a good representation of the true energy of this event as the integral of the waveform decays with the RC-time response.

decay of the average of the event integral in a small window after the known location of the LED pulse.

$$O_i = (M_i - A_i) = O_{i-1}e^{(-t/\tau)} + \kappa A_i \quad (4.1)$$

where:

- A_i : Real amplitude of the signal at the sample number (time) i
- M_i : Measured amplitude of the signal at the time i after baseline subtraction
- $O_i = (M_i - A_i)$: Effect of the charge build-up at the time i .
- τ : Decay time of the charge ($\sim \mu\text{s}$). This value is the effective RC time constant seen with the electronics. This is computed by looking at single photoelectron level signals.

- κ : A coefficient of proportionality (negative, less than 1%)

Inserting the expression for A_i gives:

$$O_i = (M_i - A_i) = O_{i-1}e^{(-t/\tau)} + \kappa(M_i - O_i) \quad (4.2)$$

Solving for O_i and introducing a threshold for the charge to accumulate, which is designed to only include the scintillation pulses in the charge accumulation and not the digitizer noise. If the sample is below this given threshold, the accumulated charge decays using the computed RC time constant. The integral at time i is given by:

$$O(i) = \begin{cases} \frac{O_{i-1}e^{(-t/\tau)} + \kappa M_i}{1 + \kappa}, & (M_i - O_i) \geq A_{ac} \\ O_{i-1} \cdot e^{(-t/\tau)}, & (M_i - O_i) < A_{ac} \end{cases} \quad (4.3)$$

the measured parameters for τ and κ for the two PMTs are:

$$\begin{aligned} \tau_1 = \tau_3 &= 840 \text{ ns} \\ \kappa_1 = \kappa_3 &= 0.00472 \end{aligned} \quad (4.4)$$

Then, a conditional moving average (CMA) filter is applied to the event to smooth out any variations in the baseline after applying the RC-time deconvolution procedure to the waveform. After the correction procedure is applied, the integral of an event is computed by simply summing the waveform samples contained within the event. Fig. 4.3 shows an example of the waveform after this RC-time deconvolution algorithm is applied. After the application of the algorithm, the waveform does not rise above the baseline measured from the pre-pulse samples.

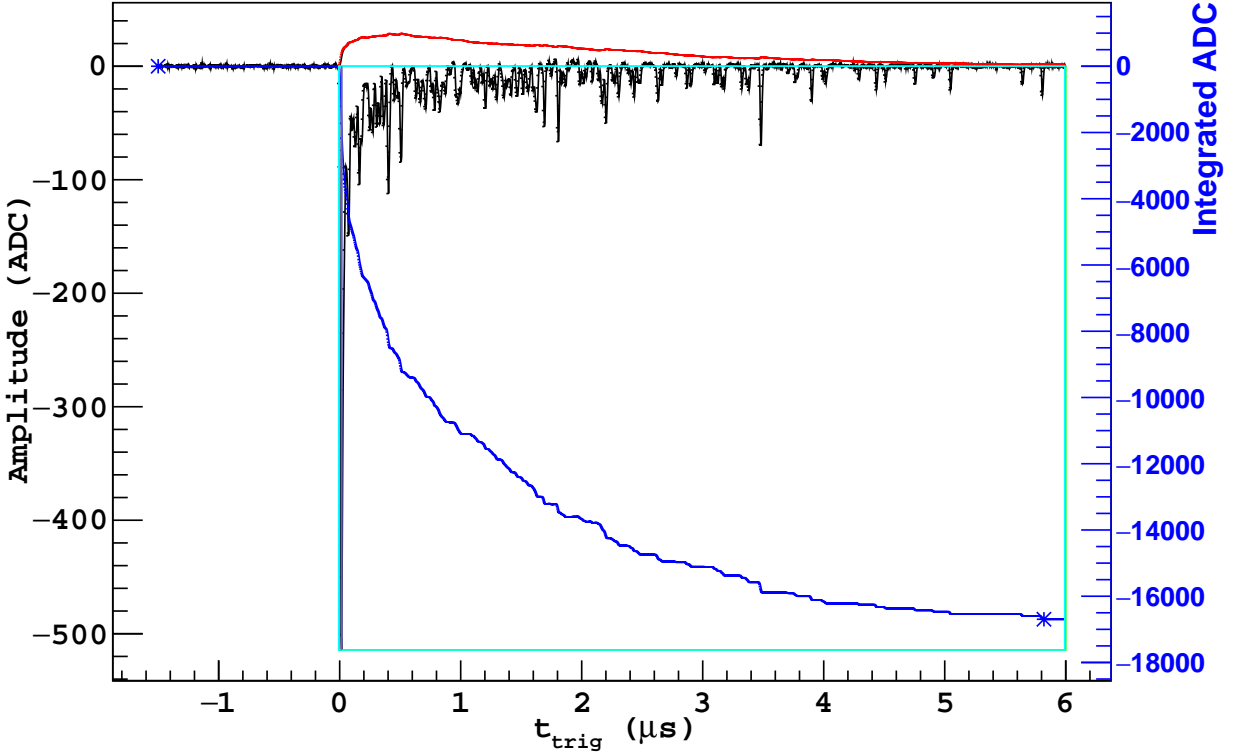


Figure 4.3: Example of raw baseline-subtracted waveform taken from CENNS-10 calibration data after deconvolution method applied. Note the dark blue line again representing the integral but now it follows a more physical increase over time. Again the fixed baseline is calculated from pre-pulse samples and noted by the dark blue line before the cyan box representing the event and the cyan line afterwards. The red curve is the calculated RC-time response of the algorithm, which is subtracted from the original waveform to get the waveform shown in this picture.

4.2 SINGLE PHOTOELECTRON CALIBRATION

Two calibrations are performed to measure the energy response of the CENNS-10 detector. The first of these represents a single photoelectron (SPE) calibration which provides a conversion from integrated ADC (charge) units used by the digitizer to a measured number of photoelectrons. SPE signals are generated using an LED pulser attached to the top of the CENNS-10 liquefier vessel and routed into the active volume using a fiber-optic cable. The driving voltage of the LED pulser is set such that a signal correlated with the LED pulser is seen in $\sim 10\%$ of the waveforms. Due to the position of the LED pulser in CENNS-10, which is above the top PMT, the voltage to achieve

the desired SPE signal rate is different between the two PMTs. A small window of 100 ns in the waveforms around the location of the LED signal in time is integrated after the application of the deconvolution procedure described in Sec. 4.1.1. The resulting spectrum of integrated charge values is then fit with a function described in Eqn. 4.5 which is also used for a similar SPE calibration in [130].

$$SPE(q) = \eta_1 \text{Gamma}(q; \mu, b) + \eta_2 \text{Gamma}(q; \mu f_\mu, b f_\mu) + \begin{cases} \eta_3 l e^{-qt} & q < \mu \\ 0 & q > \mu \end{cases} \quad (4.5)$$

$$\text{Gamma}(q; \mu, b) = \frac{1}{b\mu\Gamma(\frac{1}{b})} \left(\frac{q}{b\mu}\right)^{\frac{1}{b}-1} e^{-\frac{q}{b\mu}}$$

where μ is the mean of the distribution, b is an arbitrary shape parameter, and the various η parameters and f_μ are normalizations. Fig. 4.4 shows an example of the full SPE fit on one of the LED data sets for one of the PMTs.

The different components in the fit corresponding to the colors of the curves seen in Fig. 4.4 are as follows

- Red curve: Pedestal showing events where no pulses are seen in the LED search window.
- Green curve: Scattering of the photoelectron on the dynode structure, as an exponentially falling term that cuts off at the mean of the primary Gamma distribution.
- Blue curve: Incomplete electron distribution, when the primary photoelectron impacts the second dynode instead of the first dynode. Modeled as a Gamma as it is the same multiplication process, it just begins at the second dynode instead of the first.
- Magenta curve: Fully amplified single photoelectron component.
- Gray curve: Fully amplified double photoelectron (DPE) contribution.

The approximately weekly available LED calibration data was fit with Eqn. 4.5 and the mean of the fully amplified component of the SPE is taken as the calibrated LED value. The two

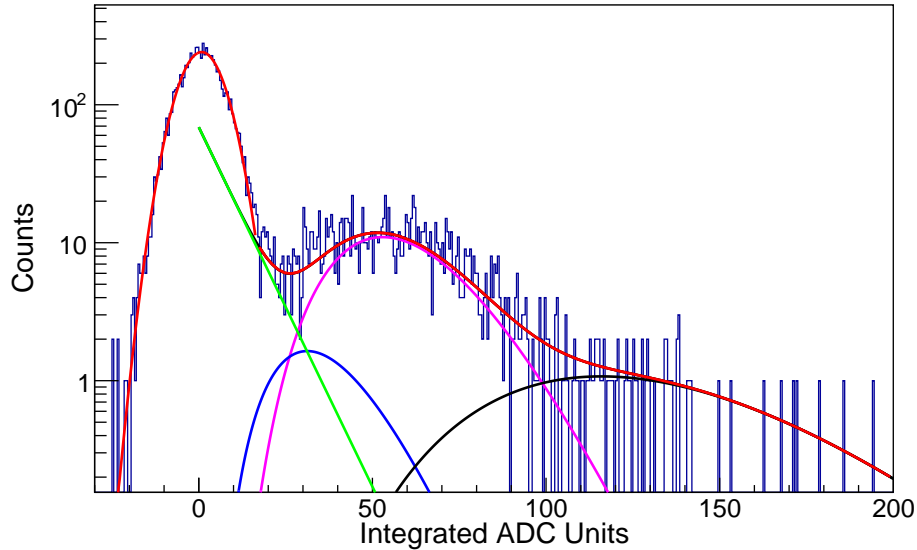


Figure 4.4: Example of full fit the single photoelectron spectrum to extract the measured SPE charge which is extracted from the mean of the full SPE component shown in the magenta curve. Shown here is the SPE calibration from a selected run for the top PMT. The two PMTs are handled separately in this procedure.

photomultiplier tubes are considered and calibrated separately with this procedure. Fig. 4.5 shows the evolution of the measured SPE values for the two PMTs over the course of the run. The value of the SPE calibration increases over time in the first months of operation and the stabilizes after a long SNS shutdown in early 2018. The increase in the SPE value before stabilizing is likely attributed to improvement in the vacuum of the PMT over time as the coated PMTs installed during the upgrade had not been used previous to their installation in CENNS-10.

The data are fit with the function described in Eqn. 4.6. This function describes the data well over the period of time considered for the first physics result. The subscripts used in Eqn. 4.6 represent the digitizer channel for the top(1) and bottom(3) PMTs. For each PMT, the error on the fit represented in Fig. 4.5 is $\sim 1\%$ from the standard deviation of the data and the fit. The pulse rate of the LED is increased after a long SNS shutdown which lowers the errors on the

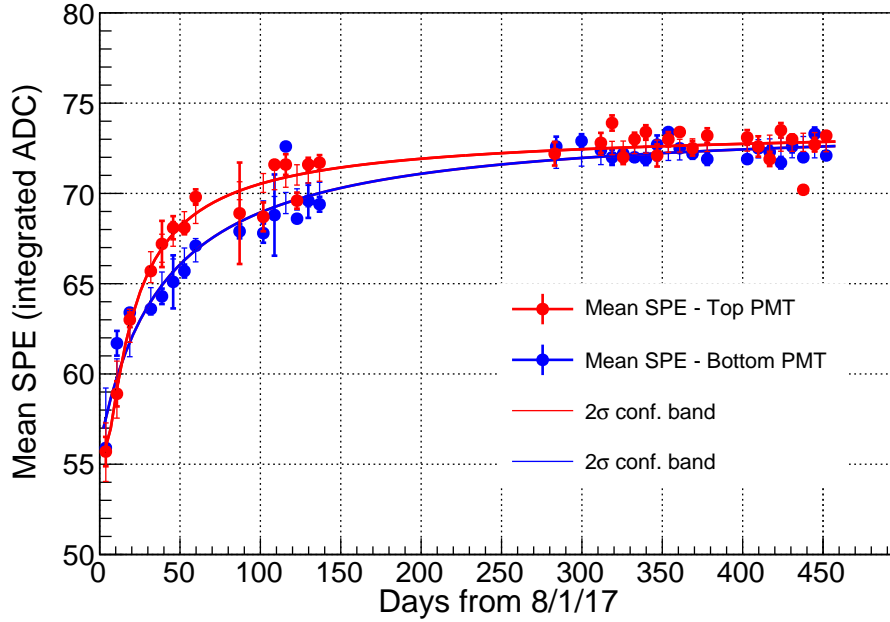


Figure 4.5: Results of weekly LED calibration to determine the SPE calibration for the two PMTs. The two PMTs were calibrated separately. This data was then fit with a function described in Eqn. 4.6 which provides an SPE calibration value over time for the data considered in this work.

individual points from the improved statistics.

$$f(x) = a + bx + ce^{-\frac{d}{x+e}}$$

$$a_1 = 55.44 \pm 1.70, a_3 = 29.21 \pm 2.14$$

$$b_1 = 5.765 \times 10^{-4} \pm 2.886 \times 10^{-3}, b_3 = -8.978 \times 10^{-5} \pm 3.206 \times 10^{-3} \quad (4.6)$$

$$c_1 = 17.81 \pm 2.67, c_3 = 44.74 \pm 2.27$$

$$d_1 = 16.98 \pm 4.55, d_3 = 16.01 \pm 5.02$$

$$e_1 = 0.03096 \pm 5.27, e_3 = 30.87 \pm 8.90$$

4.3 DETECTOR RESPONSE CALIBRATION

The second part of the CENNS-10 detector calibration uses gamma ray sources at known energies to study the linearity of the detector response as a function of energy. The measured detector

response in photoelectrons is compared to the known energy of the gamma ray source to compute a conversion factor between the measured photoelectron value and the reconstructed energy E_{reco} [keVee]. Three sources, ^{83m}Kr (41.5 keVee), ^{241}Am (59.5 keVee), and ^{57}Co (122 keVee), are used to measure the light response of the detector and test the linearity of the detector response. Taken in combination with the SPE calibration, the calibration procedure provides a full conversion from integrated ADC units to the reconstructed energy of an event in the CENNS-10 detector.

The ^{57}Co calibrations are performed approximately weekly along with the SPE calibration. The calibration method consists of a 1 μCi ^{57}Co button source attached to a rod which is lowered into the detector water shielding tank through an opening in the lead shielding. The goal is to get the source as close to the detector volume as possible. The ^{57}Co calibration is performed in three locations: the center of the detector and near both PMTs to check the detector response in multiple positions. A finer scan along the length of the detector was performed with the ^{57}Co source to compare the response to the simulation described in Chapter 5. The ^{241}Am calibration was performed sparingly using a 60 μCi button source deployed in the same way as the ^{57}Co source. The ^{83m}Kr source represents a low-energy, *in-situ* calibration. The design and implementation of that source is further detailed in Sec. 4.4. A further calibration using the endpoint of ^{39}Ar at 565 keVee is not possible as the detector response is seen to be non-linear, verified by simulations, at the relevant energy due to the PMT electronics chain.

To extract the measured number of photoelectrons in a calibration dataset, the deconvolution, pulse finding, and integration algorithms described in Sec. 4.1 are applied to the data. Simple event selection cuts requiring a valid baseline, > 2 photoelectron signal in the first 90 ns of each PMTs, that the event begin in a 100 ns window around $t_{\text{trig}} = 0$, and that the maximum ADC value seen in the event occur in the first 90 ns (mainly the singlet light) are also applied to the calibration data. A value for the SPE calibration to convert to measured photoelectrons is extracted event-by-event for the signals in each PMT using the event timestamp and Eqn. 4.6. The resulting number of photoelectrons seen in each PMT is then summed event-by-event. The photopeak of

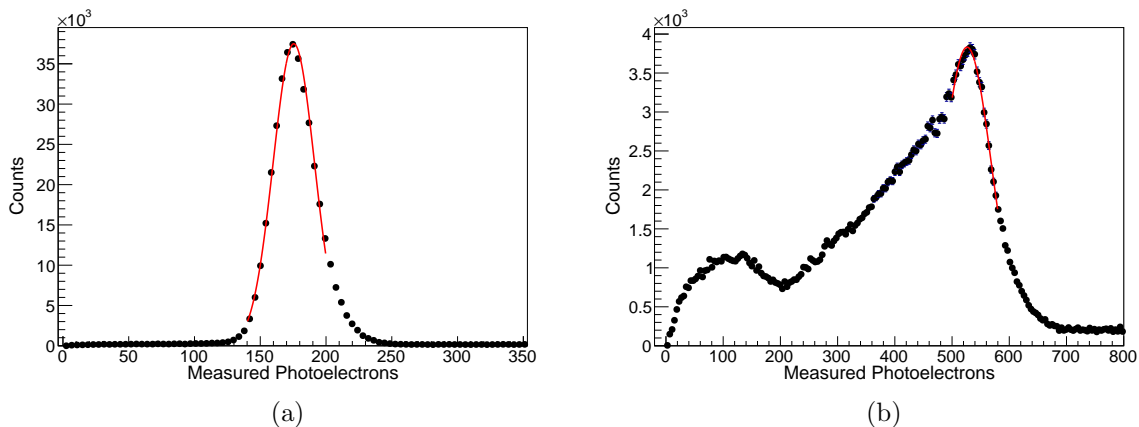


Figure 4.6: Example fit from one calibration data set using for (a) Internal $^{83\text{m}}\text{Kr}$ source and (b) ^{57}Co source run with the source positioned in the center of the detector. These sources, along with ^{241}Am , are used to calibrate the CENNS-10 detector response.

the resulting spectrum is fit with a single-Gaussian model (Fig. 4.6) to compute the mean number of photoelectrons for the calibration dataset.

The datasets used for all three sources can be plotted over the time considered (Fig. 4.7) for the first physics result for CENNS-10. The detector response is stable over the data taking period for all three sources. Sources of error on the measured number of photoelectrons in each individual dataset include a total of 2.1% from the SPE calibration and knowledge of the deconvolution parameters. A constant fit over the entire available data provides the calibrated number of photoelectrons for a given source energy. Additional errors corresponding to the fit model used and spread of the results over time give a total 3.3(3.3)[2.2]% error on the ^{57}Co (^{241}Am)[$^{83\text{m}}\text{Kr}$] measurements.

A linear model is fit to the measured photoelectrons from the three sources as given in Tab. 4.1. The result of the linear fit shows a measured light yield, or measured number of photoelectrons per keVee of energy deposited, of 4.3 ± 0.1 photoelectrons/keVee for CENNS-10 in the upgraded configuration. The linear fit and the calibration results are seen in Fig. 4.8. The model is extrapolated down to zero photoelectrons at a reconstructed energy of zero keVee. The extrapolation is also used in the analyses of the liquid argon quenching factor with various sources in [107–110] to compute the electron recoil response. The measured energy resolution of the CENNS-10 detector

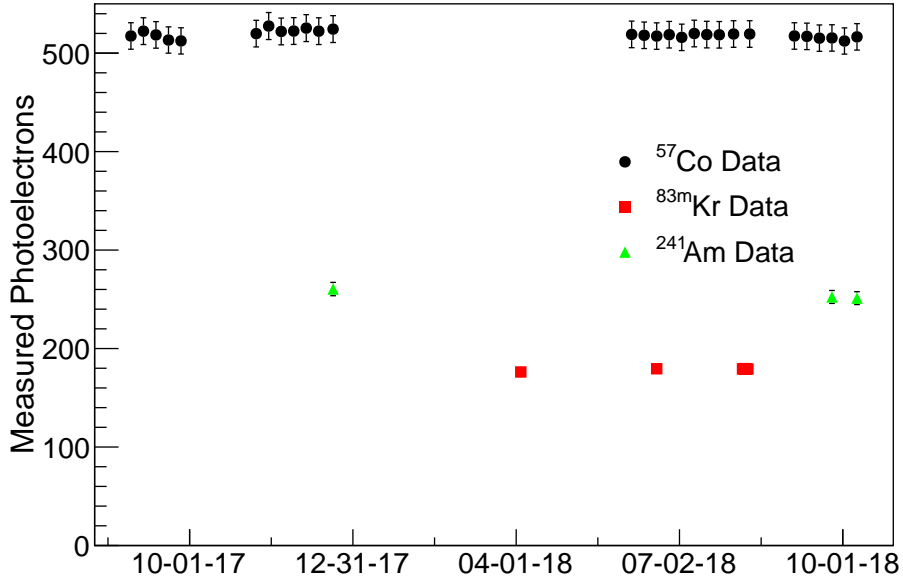


Figure 4.7: Measured photoelectrons from CENNS-10 source calibrations vs time period covered by this dataset. For each source, the detector response is stable over the length of the run. The ^{57}Co calibration is performed most often as it was easier to deploy. The $^{83\text{m}}\text{Kr}$ source (Sec. 4.4) was included when the source was built during the run. ^{241}Am calibration source runs were performed sparingly. From the ^{57}Co source data at early times during the run, there is no drift in the measured detector response from the changing SPE value seen in Fig 4.5 and the SPE drift gets calibrated out in the source calibrations.

	Measured Photoelectrons	Source Energy (keVee)
$^{83\text{m}}\text{Kr}$	178.8 ± 4.0	41.5
^{241}Am	254.5 ± 8.4	59.5
^{57}Co	518.7 ± 17.7	122

Table 4.1: Results of CENNS-10 detector calibrations for the three gamma sources used during this run period. The resulting measured photoelectron value for each source represents the mean value over the entire run period.

is 9.5% at 41.5 keVee using the $^{83\text{m}}\text{Kr}$ source.

4.4 THE $^{83\text{m}}\text{Kr}$ CALIBRATION SOURCE

At low energies, the gamma rays from a button calibration source deployed in the same way as the ^{57}Co and ^{241}Am calibrations will not penetrate into the CENNS-10 active volume and allow for a

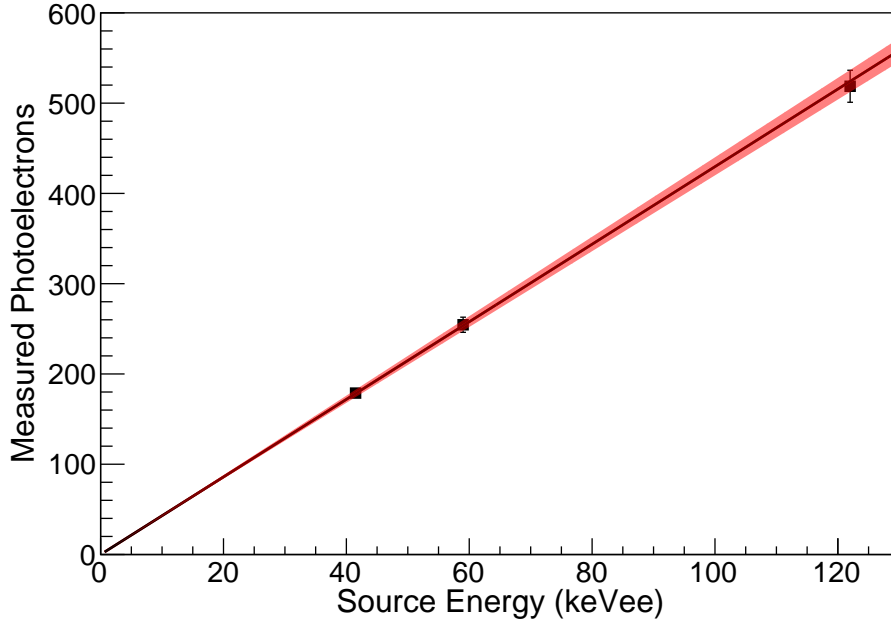


Figure 4.8: Fit to CENNS-10 calibration points using the three gamma sources. The black line represents the central value fit to the CENNS-10 light yield. The red band represents the region covered by the error on the slope of the calibration line.

measurable calibration. To provide a calibration of the CENNS-10 detector close to the CEvNS region of interest, an internal calibration source which can be inserted directly into the detector volume was developed. The expected CEvNS signal deposits energy with $E_{reco} \lesssim 40$ keVee with the definition of the quenching factor in Sec. 3.1.1.

The radioactive isotope ^{83m}Kr , with an excitation energy of 41.5 keVee [131] as shown in Fig. 4.9, is a suitable source for the necessary calibration. ^{83m}Kr is generated through the decay of ^{83}Rb via electron capture ($t_{1/2} = 86.2$ days). The decay of ^{83}Rb produces a range of gamma rays, with the most abundant being ~ 500 keVee. Approximately 75% of ^{83}Rb decays produce a metastable state of ^{83}Kr , ^{83m}Kr which decays into the ground state of ^{83}Kr via internal transition. The resulting decay of ^{83m}Kr emits two gamma rays, the first with an energy of 32.1 keVee and the second with an energy of 9.4 keVee with a half-life $t_{1/2} = 154$ ns after the 32.1 keVee gamma. The scintillation light from the two gamma rays occurs in the same event window and it is difficult to completely separate them due to the 1.6 μs triplet state lifetime. Also, with the 1.8 hour half-life

cylinder of high purity argon gas and the CENNS-10 gas handling system (“injection method”) to admix the $^{83\text{m}}\text{Kr}$ gas with the argon from the cylinder. The gas injection method allows for controlled amounts of $^{83\text{m}}\text{Kr}$ to be introduced into the system. There is concern that introducing fresh argon gas from a commercial cylinder, albeit a high purity argon gas cylinder (99.999% pure argon gas), would degrade the light collection efficiency of the detector. The injection of argon gas from the bottle through the $^{83\text{m}}\text{Kr}$ source before ^{83}Rb deposition shows no change in the measured light yield of the detector. The other operation mode is that the $^{83\text{m}}\text{Kr}$ source can be introduced into the CENNS-10 gas argon recirculation loop (“circulation method”). The circulation method allows for an eventual steady-state $^{83\text{m}}\text{Kr}$ decay rate in CENNS-10.

The $^{83\text{m}}\text{Kr}$ source is designed to operate in either injection or circulation mode but not both simultaneously. The introduction methods are controlled by a series of valves while also containing a bypass from the argon gas cylinder to the CENNS-10 gas handling system. The system is connected to a turbomolecular pumping station used for the CENNS-10 gas handling system to evacuate the $^{83\text{m}}\text{Kr}$ source. The diagram in Fig. 4.10 shows the design of the system where the ^{83}Rb infused charcoal is located in the center.

A holder for the charcoal piece was designed using steel mesh and fine quartz wool to create a container which also allowed for the flow of argon through the source and into CENNS-10. A cartoon of the charcoal inside the source vessel and the actual mesh holder used in the $^{83\text{m}}\text{Kr}$ source is seen in Figure 4.11. To ensure that no ^{83}Rb is introduced into the detector volume, $2\ \mu\text{m}$ sintered metal filters are also used to prevent charcoal particulates possibly containing ^{83}Rb from entering the gas handling system. As the ^{83}Rb has a fairly long half-life of 86.2 days and the decay to $^{83\text{m}}\text{Kr}$ also produces ~ 500 keV gamma rays, an additional source of background on a long timescale would be added if ^{83}Rb decays occurred inside the detector.

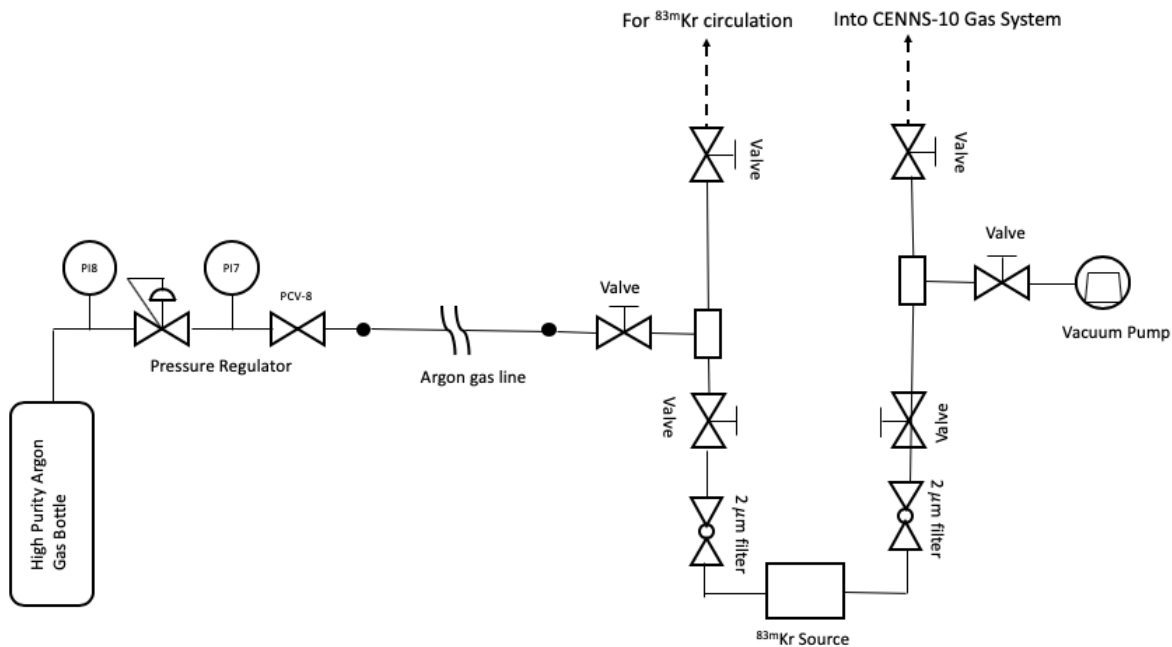


Figure 4.10: Diagram of $^{83\text{m}}\text{Kr}$ source. This system is attached directly to the CENNS-10 gas handling system. The gas can either be injected into the detector or be added to the existing gas argon circulation loop.

SOURCE TESTS

Tests of the introduction of the high purity argon gas from the cylinder were done at various stages of the design process to ensure the $^{83\text{m}}\text{Kr}$ injection did not effect the light collection efficiency or the steady-state operation of the detector. During these tests, only a small amount of argon is introduced into CENNS-10. After the source vessel was built, it was attached to the CENNS-10 gas handling system and tests of the gas flow and circulation methods were performed. This served as a check for any adverse effects on CENNS-10 operation before the deposition of the ^{83}Rb solution. Specifically, the detector temperatures/ambient pressure and the detector light collection were checked.

The light collection was tested by deploying the ^{57}Co source as a check in three configurations. These ^{57}Co source deployments were performed after tests of the $^{83\text{m}}\text{Kr}$ injection method. The first run was before the empty $^{83\text{m}}\text{Kr}$ source vessel was attached to the CENNS-10 gas handling system with the measurement of the number of photoelectrons serving as a control. Two further ^{57}Co

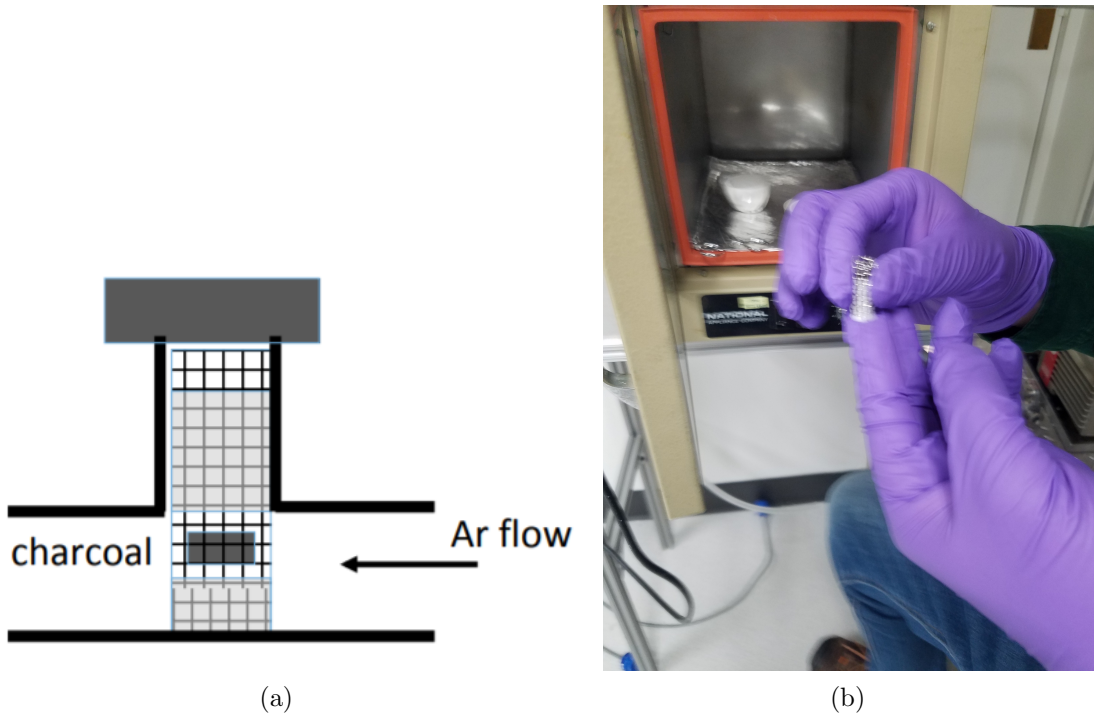


Figure 4.11: (a) Cartoon showing the position of the activated carbon inside the source vessel. This keeps the carbon in place while allowing argon flow through the source vessel. (b) Steel mesh holding the piece of activated carbon. The carbon is not visible as it is between the two pieces of quartz wool.

source measurements were performed, The first measurement with an empty source vessel and the second with the steel mesh container shown in Figure 4.11 including a piece of charcoal without ^{83}Rb deposited onto it. The ^{57}Co source deployments to test for any changes to the light output were done after the $^{83\text{m}}\text{Kr}$ source was attached and after gas argon was injected into CENNS-10 through the source vessel. Results show that the operation of the $^{83\text{m}}\text{Kr}$ source does not adversely affect the light collection efficiency of the detector.

The other concern in the introduction of this source is the effect on the steady-state operation of CENNS-10. Normal operations show < 1 K fluctuations in the temperature of the liquid argon throughout the detector, which is kept stable by the cryocompressor and the resistive heater. During the $^{83\text{m}}\text{Kr}$ source tests, the detector parameters were monitored for any adverse effects on the temperature and pressure values for both the injection and circulation methods. With the injection method, no change was seen in these parameters from normal detector operations. A

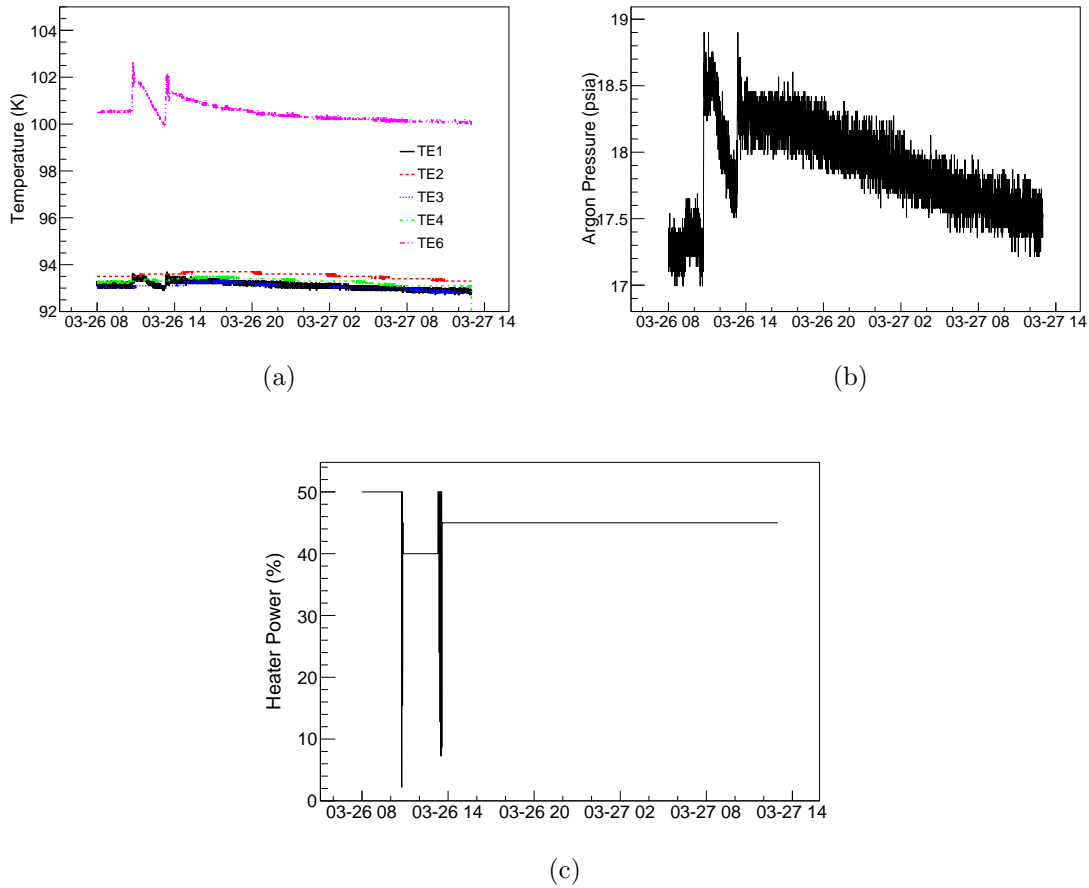


Figure 4.12: The trends of the (a) detector temperatures, (b) detector pressures, and (c) heater power value during the circulation method test before the ^{83}Rb deposition. With the change in the re-circulation rate from the standard detector operation, the parameters become less stable and the heater power needs to be adjusted. The variations seen show the time where the $^{83\text{m}}\text{Kr}$ source vessel was part of the re-circulation loop.

test of the circulation method was performed during the test where the full charcoal was installed. With operation of the $^{83\text{m}}\text{Kr}$ source in the circulation mode, the flow meter which controls the recirculation rate is bypassed by the source vessel. The argon recirculates at a higher rate (~ 20 slpm) in the circulation method than during normal detector operations. The heater power settings, which stay constant during normal operations, needed to be adjusted. The injection method is the standard method for the introduction of the $^{83\text{m}}\text{Kr}$ due to the changes seen in the steady-state detector operation with the circulation method. Fig. 4.12 shows the variation of the detector parameters during the circulation method test.

4.4.2 $^{83\text{m}}\text{Kr}$ SOURCE DEPOSITION

The activated carbon used in the source deposition had a mass of ~ 35 mg and was prepared by heating it at $\mathcal{O}(100^\circ\text{C})$ for a total of 16 hours in a vacuum oven to remove impurities in the carbon. The mass of the carbon was measured before and after the bake-out and no change was observed. After the bake-out, the carbon was placed inside of the stainless steel mesh cylinder shown in Fig. 4.11. The carbon was then placed inside the source vessel in preparation for deposition (Fig. 4.13). The vial of ^{83}Rb solution used for the deposition was ordered with an activity of 1 mCi on February 6, 2018. The ^{83}Rb is aqueous in a 0.1 M HCl solution with a total volume of 1.65 mL. The remaining ^{83}Rb activity was 0.64 mCi when the ^{83}Rb was deposited onto the activated carbon on April 2, 2018. As the efficiency of the $^{83\text{m}}\text{Kr}$ gas to escape the activated carbon and enter the detector volume was largely unknown, the plan was to deposit 10 μL of the solution onto the activated carbon. A 10 μL deposition volume would produce a $^{83\text{m}}\text{Kr}$ source with an activity of 3.8 μCi and ensure a reasonable rate of $^{83\text{m}}\text{Kr}$ inside the detector.

The $^{83\text{m}}\text{Kr}$ source was generated by extracting ~ 10 μL of the ^{83}Rb solution using a micro-syringe and depositing it onto the activated carbon. Due to radiation safety concerns, the deposition had to be performed in a fume hood with the activated carbon inside the source vessel at all times. Placing the activated carbon inside the source vessel minimized the possibility of ^{83}Rb contamination on any surface other than the carbon or inside the source vessel. Unfortunately, this procedure did not allow for the exact measurement of the volume of ^{83}Rb deposited onto the activated carbon via a change in its mass. A conservative uncertainty of 50% is assigned to the deposition volume from studies done from extracting water using the same syringe.

After ^{83}Rb deposition, a second piece of fine quartz wool was placed above the carbon as in Fig. 4.11. The cap was placed onto the vessel to seal the carbon in place. The source vessel was then continuously purged with 3 psig high purity argon while being heated in this way to again remove any possible impurities after deposition:

1. 60°C for ~ 2 hours



Figure 4.13: Activated carbon inside the source vessel after bake-out in a vacuum oven and before the ^{83}Rb deposition.

2. 80°C for ~ 1 hour
3. 100°C for ~ 1 hour

The source was then attached to the CENNS-10 gas handling system and was ready to use for the $^{83\text{m}}\text{Kr}$ calibration runs (Fig. 4.14 and Fig. 4.15).

4.4.3 CALIBRATION OF CENNS-10 USING $^{83\text{m}}\text{Kr}$

Before operation of the $^{83\text{m}}\text{Kr}$ source, the source vessel was checked for vacuum leaks using a helium leak checker and there were no leaks found. The source was then evacuated using the HiCube pumping station located on the CENNS-10 gas handling rack overnight with the vacuum level inside the source vessel adequate to remove any possible impurities before the calibration runs were performed. The line to the argon gas cylinder was purged with 3 psig high purity gas argon

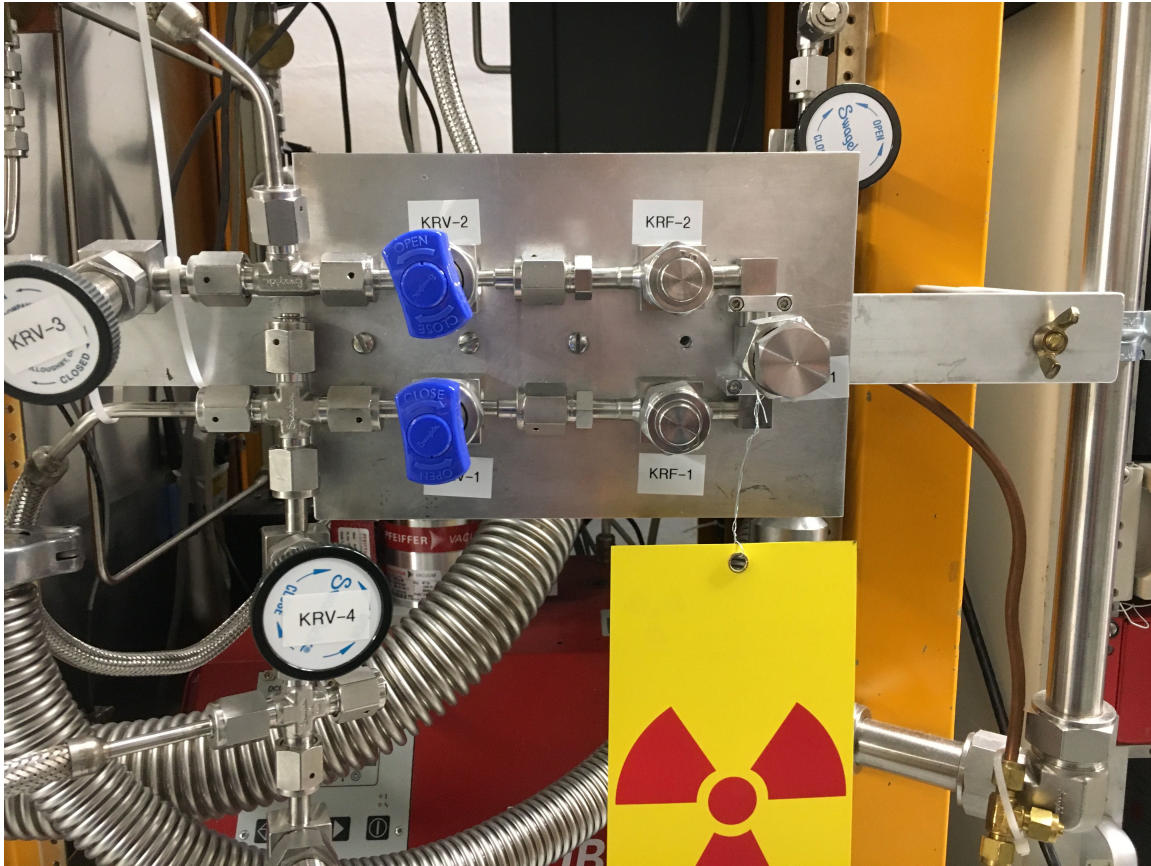


Figure 4.14: Finished $^{83\text{m}}\text{Kr}$ source attached to the CENNS-10 gas handling system showing the source vessel. The valve labeled “KRV-4” leads to the high purity argon gas cylinder for the injection method. The valve labeled “KRV-3” leads to the CENNS-10 gas handling system. The activated carbon is located in the large central piece on the right side of the figure.

from the cylinder for ~ 10 minutes to clean the line to the argon gas cylinder as much as possible before injection of the $^{83\text{m}}\text{Kr}$ gas. The source vessel was backfilled with the high purity argon for 1 minute to allow the $^{83\text{m}}\text{Kr}$ to admix with the argon gas before the $^{83\text{m}}\text{Kr}$ is injected into the detector. The valve between the source vessel and the CENNS-10 gas handling re-circulation system was opened for 30 seconds while the gas argon from the cylinder is flowing through the source vessel to inject the $^{83\text{m}}\text{Kr}$ into the detector. After 30 seconds, the valve was closed and the DAQ trigger rates were monitored to measure the introduced $^{83\text{m}}\text{Kr}$ rate in the detector.

The DAQ was setup in the same manner as for other gamma source calibration runs, with a 25 ADC hardware threshold and a required 24 ns coincidence between the two PMTs to trigger the digitizer. It was setup to begin a new run every 30 seconds, with ~ 5 seconds of dead time

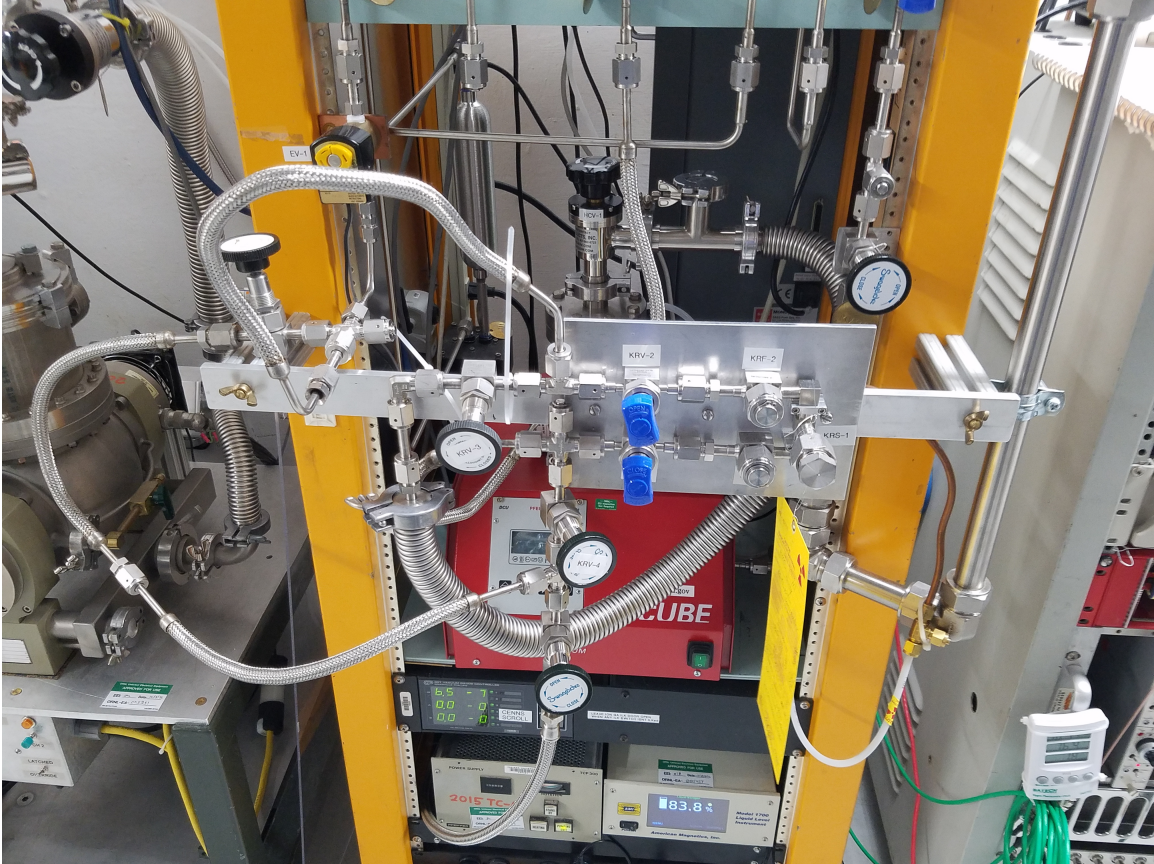


Figure 4.15: Finished $^{83\text{m}}\text{Kr}$ source attached to the CENNS-10 gas handling system showing the full system.

between each run. In this configuration the average DAQ trigger rate can be tracked over several hours as the $^{83\text{m}}\text{Kr}$ begins to decay after the injection. The post-trigger window recorded is $6 \mu\text{s}$, so the two gammas from the $^{83\text{m}}\text{Kr}$ decay are seen in the same window. The singlet light from the two gammas are distinguishable in the event waveform by the presence of a second pulse larger than the SPE-level triplet light that occurs after a liquid argon scintillation event. Fig. 4.16 shows an example of an event from a $^{83\text{m}}\text{Kr}$ decay where the singlet light from the two gamma rays are distinguishable. It is difficult to extract an exact value to use to calibrate at the separate gamma ray energies as the triplet light from the two gamma rays is contained in the same event window. Instead, the total energy deposited by both gamma rays of 41.5 keV provides the calibration (Fig. 4.8) by integrating all the light seen in the event window after the trigger.

Another confirmation that the calibration was successful and the $^{83\text{m}}\text{Kr}$ does enter the CENNS-

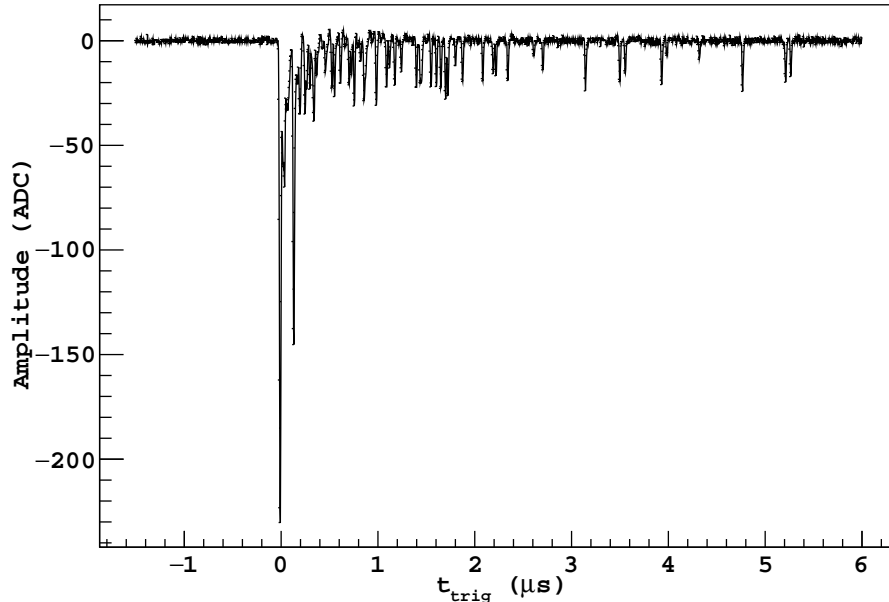


Figure 4.16: Waveform in one PMT showing an event from $^{83\text{m}}\text{Kr}$ decay. The two gamma ray events are distinguishable by the initial prompt pulse at $t_{\text{trig}} = 0$ representing the singlet light from the 32.1 keVee gamma ray. The second larger pulse with an amplitude of ~ 100 ADC at $t_{\text{trig}} \sim 0.2 \mu\text{s}$ is from the singlet light from the 9.4 keVee gamma ray.

10 active volume is given by the DAQ trigger rates as a function of time after the injection is performed. The peak trigger rate above background during the initial $^{83\text{m}}\text{Kr}$ calibrations was ~ 2 kHz, so the event rate is dominated by $^{83\text{m}}\text{Kr}$ decays for several hours. At the high trigger rates, the $^{83\text{m}}\text{Kr}$ source provides a clear concentration of events for calibration at 41.5 keVee above the steady-state background, mainly ^{39}Ar . Even at this high trigger rate, there is minimal concern with dead time occurring within a run and no evidence of adverse effects on the measured PMT current which could affect the measured light level from the calibration. As seen in Fig. 4.17, there is a rise to a maximum soon after the injection and then an exponential decay after reaching the maximal rate. The decay constant of the exponential can be measured and compared to the $^{83\text{m}}\text{Kr}$ decay half-life from nuclear data tables [131]. The extracted rate of 112 ± 2 min is in agreement with the literature value of 110 min.

Combining the three data sets taken with this source during the run measures an energy

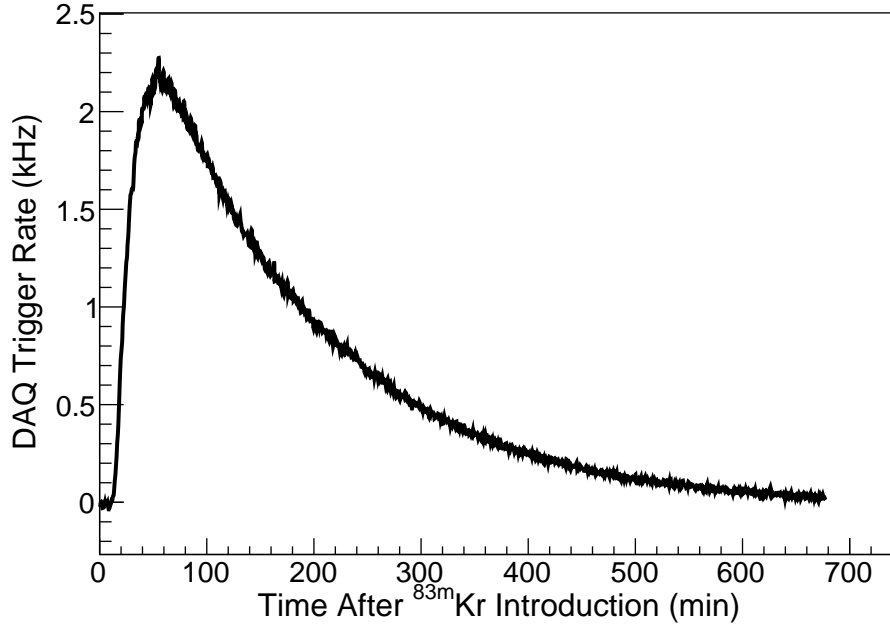


Figure 4.17: DAQ trigger rate vs time after $^{83\text{m}}\text{Kr}$ was injected into CENNS-10. A period of rate increase can be seen in the first ~ 30 min of the run, then a steady decay as no new $^{83\text{m}}\text{Kr}$ enters the detector.

response of 178.8 ± 4.0 photoelectrons at 41.5 keVee for a light yield of 4.31 ± 0.10 , in excellent agreement with the calibration combining all three sources shown in Fig. 4.8. A single calibration data set is provided in Fig. 4.18 to show the reconstructed energy spectrum from the $^{83\text{m}}\text{Kr}$ source along with the width of the $^{83\text{m}}\text{Kr}$ peak, which is measured at 9.5% at 41.5 keVee.

Another interesting aspect of this calibration is to look at how the $^{83\text{m}}\text{Kr}$ distributes itself in the CENNS-10 active volume. If the events are evenly distributed throughout the detector, then the $^{83\text{m}}\text{Kr}$ source can be used to check how the light level differs in different sections of the detector. One method of looking into where an event occurs within the detector is to compute the fraction of the light seen in an event in one PMT as:

$$f_{\text{top}} = \frac{I_{\text{top}}}{I_{\text{total}}} \quad (4.7)$$

where I_{top} is the number of photoelectrons measured in the top PMT and I_{total} is the total number

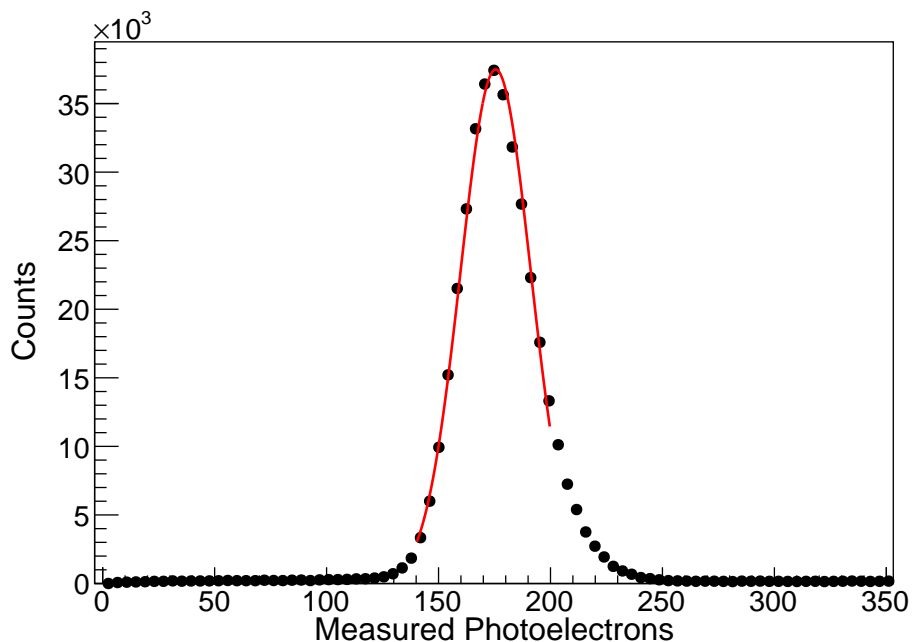


Figure 4.18: Results of $^{83\text{m}}\text{Kr}$ calibration run in CENNS-10. There is a clear peak from $^{83\text{m}}\text{Kr}$ decays seen in the data above the steady-state background. This is a single run over a \sim day timescale after the $^{83\text{m}}\text{Kr}$ injection.

of photoelectrons in both PMTs. Only the relative height, or “z-position”, of an event can be computed as CENNS-10 only has a single PMT on each end. The distribution seen in the $^{83\text{m}}\text{Kr}$ data (Fig. 4.19) shows that the decays are roughly evenly distributed in the detector volume after a time which corresponds to the maximum in Fig. 4.17. The distribution of f_{top} shows the event position is largely uniform as the $^{83\text{m}}\text{Kr}$ decays away.

4.5 CENNS-10 NEUTRON CALIBRATIONS

An americium-beryllium (AmBe) source is used to calibrate the CENNS-10 nuclear recoil response. The AmBe source generates a spectrum of neutrons with an endpoint ~ 10 MeV [139] and an average neutron energy of ~ 5 MeV. The main use of the AmBe source is to demonstrate the pulse shape discrimination (PSD) capabilities of CENNS-10, especially at low energies relevant to CEvNS. PSD is important in CENNS-10 as the CEvNS signal is a nuclear recoil (NR) and the beam-unrelated backgrounds are electron recoils (ER). In order to minimize the gamma ray

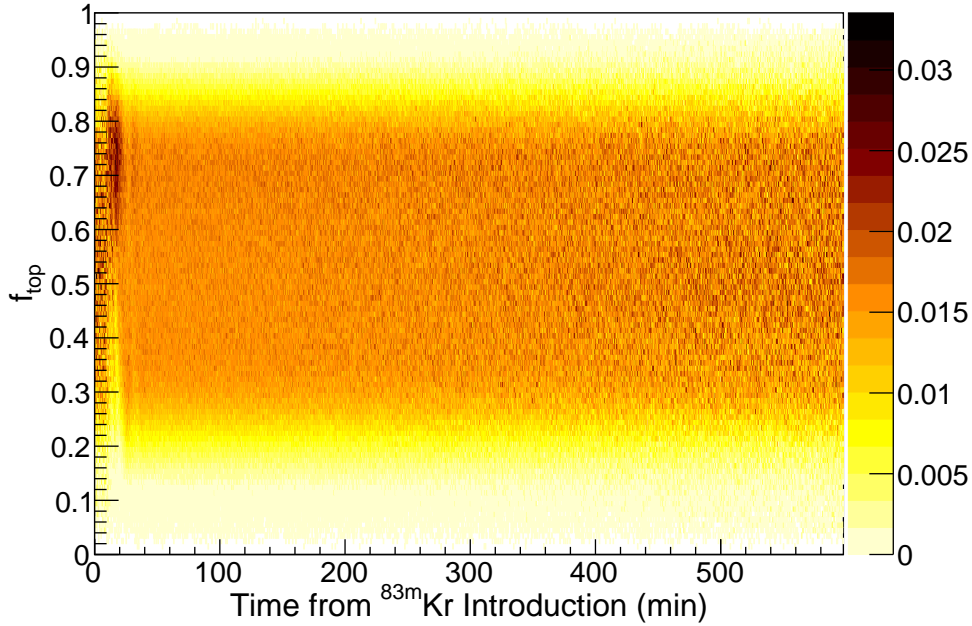


Figure 4.19: f_{top} over time for $^{83\text{m}}\text{Kr}$ calibration data. The $^{83\text{m}}\text{Kr}$ events are more concentrated closer to the top of the detector at the beginning of the run. After this period, there is an even distribution of events in the detector seen in the value of f_{top} .

contribution to this measurement, the source is positioned outside of the full CENNS-10 shielding apparatus. Further, the water shielding is removed by draining the water tank and a lead brick structure is created around the source.

In liquid argon, NR and ER events contain differing fractions of the singlet light and triplet light. The different fractions give rise to the PSD capabilities of liquid argon detectors. A standard used in liquid argon detectors for PSD measurements is the F_{90} parameter, defined as:

$$F_{90} = \frac{I_{90}}{I_{\text{total}}} \quad (4.8)$$

where I_{90} represents the integral of the first 90 ns of the event. F_{90} is approximately a ratio of the measured singlet light in an event to the total light seen in the event. F_{90} then can be used to separate nuclear recoils from electron recoils. This calibration (Fig. 4.20) shows that CENNS-10 has good PSD capabilities at low energy. At the lowest energies, the NR and ER bands begin to come together and are more difficult to distinguish. The results of this calibration are used to

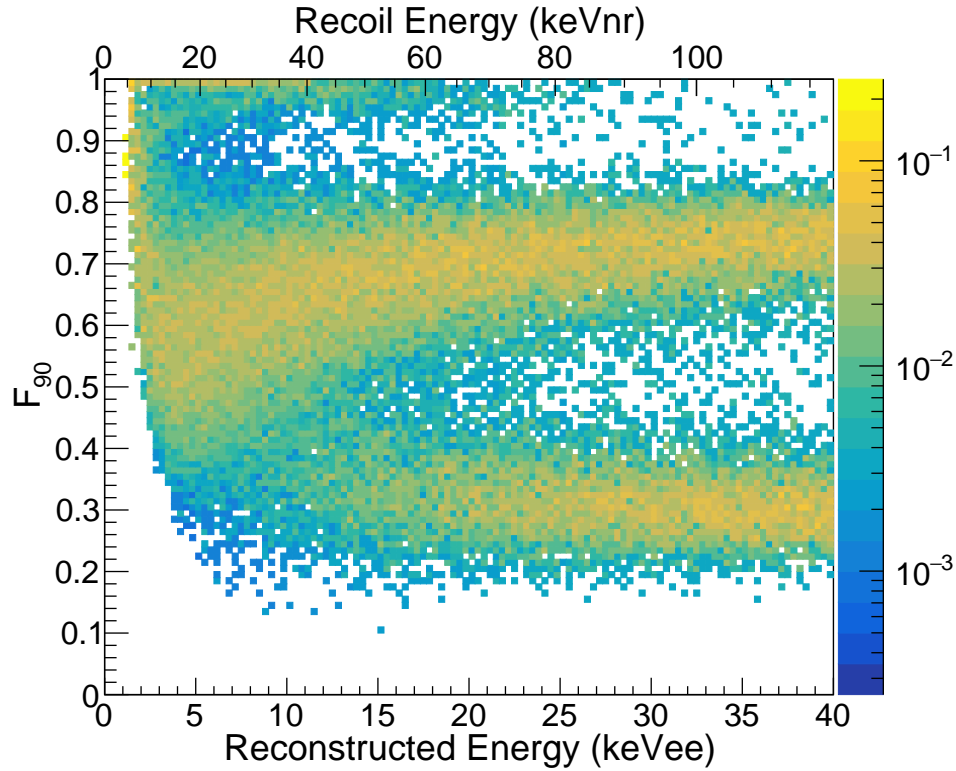


Figure 4.20: Results of the AmBe calibration of the CENNS-10 detector in the region of interest for CEvNS events. The band at $F_{90} \sim 0.7(0.3)$ corresponds to NR (ER) events. The results of this calibration are consistent with previous liquid argon measurements such as that in [101] and show good separation between ER and NR events at low energies. Note the NR and ER bands begin to merge together at the lowest energies. The band around $F_{90} \sim 1$ at low energies is theorized to be from Cherenkov light events and is removed by a hard F_{90} cut when looking at SNS data. The data has been normalized to represent an arbitrary value on the z -axis.

inform the CENNS-10 simulations described in Chap. 5.

CHAPTER 5

SIMULATION OF THE CENNS-10 DETECTOR

This chapter describes the CENNS-10 detector simulation, subdivided into an overview of the simulation and the physics processes involved. It concludes with the method of generating signal and background predictions for the CENNS-10 analyses of the no-water shielding data in Chapter 6 and the full shielded data in Chapter 7. See Sec. 2.3 for an overview of the backgrounds.

5.1 OVERVIEW

The CENNS-10 detector Monte Carlo (MC) simulation employed for this work uses the GEANT4 package [60, 61], version 10.2. The physics included within the simulation is a custom list including electromagnetic, low energy neutron, radioactive decay, and optical processes and is further described in [140]. The optical processes are applied to the simulation to replicate the liquid argon scintillation mechanisms and wavelength shifting in the detector response.

5.2 DETECTOR GEOMETRY

The entire CENNS-10 detector including the shielding package is modeled as installed in Neutrino Alley. The liquid argon volume fills the inner detector and is represented approximately as a cylinder with a radius of 26.7 cm and a height of 101.6 cm. There is a hemispherical bottom as part of the liquid argon volume to represent the designed detector vessel. The active liquid argon volume is that within the Teflon cylinder walls and 8" PMTs on the ends. The active liquid argon is

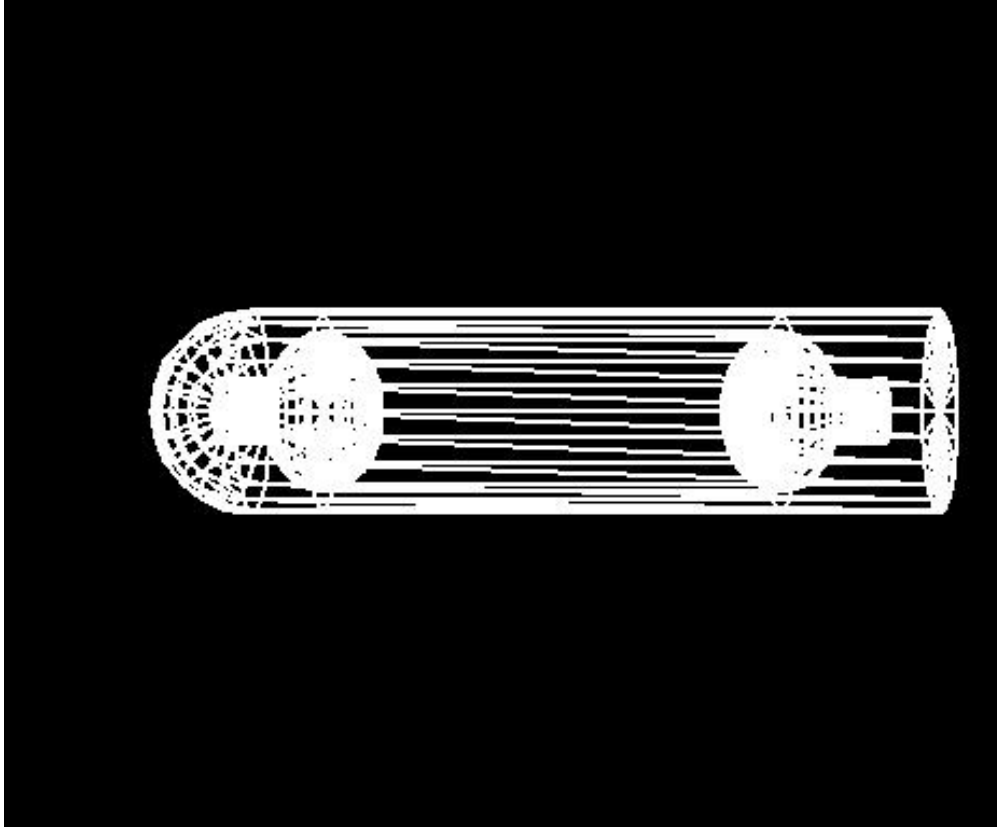


Figure 5.1: Wireframe rendering of the simulated CENNS-10 inner detector geometry. This rendering shows the liquid argon volume and the active volume between the PMTs and the Teflon cylinder. The top of the detector volume is the right side of the rendering.

not a separate volume definition, but no events generated outside the active volume pass selection cuts and are reconstructed. As the GEANT4 optical physics package requires that wavelength shifting occurs in a bulk material and not on a surface, the TPB is modeled as $2 \mu\text{m}$ thick coatings on the Teflon and PMTs. The $2 \mu\text{m}$ TPB thickness results from the product of the 0.2 mg/cm^2 TPB coating and a density of 1 g/cm^3 for the TPB hydrocarbon. A rendering of the simulated inner detector is shown in Fig.5.1.

The simulated detector shielding consists of a cylindrical water tank surrounding the CENNS-10 vacuum jacket with a thickness of 20.3 cm, a copper box outside of the water tank with a thickness of 1.3 cm, and a lead box outside the copper box with a thickness of 10.2 cm. The shielding container volumes can be easily removed or replaced based on the simulation, such as simulations where the water tank is removed for the BRN studies in Chapter 6.

5.3 THE OPTICAL MODEL AND TUNING TO DATA

The optical simulation includes all processes from liquid argon scintillation to the detection of wavelength-shifted light by the two PMTs. When a photon hits either PMT, it is counted as a photoelectron. Smearing of the single photoelectron response is also included and occurs in post-processing after the simulation is run. The CENNS-10 GEANT4 simulation contains optical physics for transmission, reflection, scattering, wavelength shifting, and scintillation for a separate particle definition known as an “optical photon”. The optical model used in the CENNS-10 simulation is tuned to replicate the light yield, position, and PSD response of the detector seen in the data.

5.3.1 LIQUID ARGON SCINTILLATION AND WAVELENGTH SHIFTING

The scintillation process in the CENNS-10 simulation can be broken down into three processes:

1. Generation of liquid argon scintillation photons
2. Propagation through liquid argon
3. Wavelength shifting on the TPB surface
4. Propagation of the shifted photons through liquid argon to the PMTs

When energy is deposited in the liquid argon volume, the scintillation process generates a number of 128 nm wavelength optical photons Poisson distributed around a mean value of $Y_\gamma = 4.3$ photons/keVee that is tuned to match calibration data. The process of tuning the simulation parameters to obtain Y_γ is further described in Sec. 5.3.2. Birks’ law [141, 142] provides the electron recoil quenching. The value of Birks’ constant provided in the CENNS-10 simulations is 0.068 cm/MeV [143]. Energy-dependent quenching of the produced number of scintillation photons is included within the simulation for nuclear recoils. The liquid argon quenching factor in Eqn. 3.1 multiplies the value of Y_γ when a nuclear recoil occurs with a known energy deposition. An energy independent quenching factor value is applied for any NR energy deposition with $E_{dep} > 125$ keVnr.

The time distribution of the scintillation light in the simulation applies the approximate lifetimes of the singlet and triplet states measured in the data. GEANT4 allows the use of two scintilla-

tion constants `FASTTIMECONSTANT` and `SLOWTIMECONSTANT` to represent the two states. For the CENNS-10 simulation, these values are set to 6 and 1300 ns respectively to represent the approximate lifetimes measured in the CENNS-10 detector.

A 128 nm optical photon can undergo wavelength shifting when it interacts with a TPB surface, either the Teflon cylinder or the PMTs. The simulation transmits the 128 nm photons into the TPB layer 100% of the time. The wavelength shifting process will also occur 100% of the time due to the very small “wavelength shifting absorption length”, which GEANT4 uses to absorb the 128 nm photon and produce a separate optical photon at the shifted wavelength. The wavelength-shifted spectrum in TPB is well measured and the resulting photon wavelength distribution in the simulation is pulled from these measurements [105, 106]. The resulting optical photons after wavelength shifting are mainly in the visible range of the spectrum.

The resulting optical photons from the TPB emit isotropically and can reflect from the Teflon surface back into the liquid argon volume and detected by one of the two PMTs. To reflect from the Teflon surface, the wavelength-shifted optical photon must travel through the bulk TPB layer twice to re-enter the liquid argon volume. The efficiency for collecting the wavelength-shifted photons with the PMTs is determined by tuning the transmission, reflectivity, and absorption parameters for visible light on the TPB, Teflon, and liquid argon volumes to match the measured calibration data.

5.3.2 COMPARISON WITH CALIBRATION DATA

Tuning of the CENNS-10 simulation parameters is performed with the goal to match the calibration data in three areas: the measured light yield, f_{top} distribution, and F_{90} distribution.

LIGHT YIELD

The effective scintillation yield Y_γ is computed by combining the initial scintillation yield in argon of 40 γ/keV [99], Y_{abs} , with two efficiency corrections. The first is a flat 18% for all wavelengths

representing the quantum efficiency (ε_{QE}). The PMT quantum efficiency is applied to the number of generated photons when energy is deposited to reduce the computation time of the simulation. The second is an efficiency correction to the flat quantum efficiency accounting for the detection of the wavelength-shifted photons by the PMTs and is driven by the results of the CENNS-10 gamma calibrations. Using these corrections, Y_γ can be further broken down into:

$$Y_\gamma = Y_{\text{abs}}\varepsilon_{\text{QE}}\varepsilon_{\text{WLS}} \quad (5.1)$$

The main parameters that go into the determination of ε_{WLS} include the absorption length of the visible photons through the TPB layer, the reflectivity of visible photons incident on the Teflon layer, the reflectivity of visible photons incident on the PMTs, and the number of wavelength-shifted photons produced per VUV photon. In this case, the parameters are highly degenerate in producing an absolute light yield value. These parameters can be energy and material dependent and apply to either the bulk material or the surface of a volume. The properties used in the simulation are described in Tab. A.1. A value of $\varepsilon_{\text{WLS}} = 0.6$ is applied via the tuned MC parameters to match the measured detector light yield. A comparison of the tuned MC to the measured ^{57}Co source data is seen in Fig. 5.2, showing good agreement of the MC to an individual ^{57}Co run taken during this period.

Z-DEPENDENCE OF SIMULATED EVENTS

Another important check on the simulation is the ability to replicate the z-position dependence of events seen in the calibration data. The z-position referenced in this section refers to the axis along the length of the Teflon cylinder and quantifies the energy deposition to PMT distance. With only one PMT on each end of the detector, CENNS-10 is not sensitive to x-y reconstruction. The choice of parameters in Tab. A.1 is largely coupled to this comparison as well as the measured light yield. Again, the z-dependence manifests as the fraction of light seen by the top PMT (f_{top}). The f_{top} parameter can be reconstructed with the CENNS-10 simulation using the optical photon

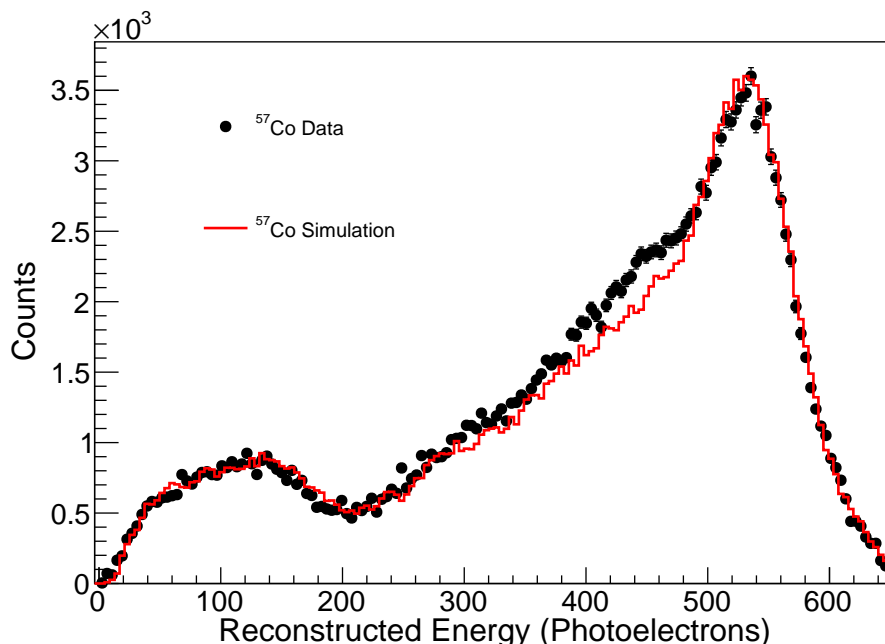


Figure 5.2: Comparison of the energy shape of the fully tuned simulation and the measured ^{57}Co data. For the simulated source, the ^{57}Co is generated as a isotropic point source located against the walls of the CENNS-10 vacuum vessel.

tracking. Agreement between the MC and data represents an important check on the ability of the simulation to accurately reconstruct signal events that occur in all parts of the detector. No cut is explicitly made on this value for the data analysis presented in Chapter 7.

Two separate datasets are used to compare the tuned MC response to the calibration data. The first is a “z-scan” using the ^{57}Co source where the source is moved along the length of the detector between the two PMTs at a fixed step length. An equivalent-length run is taken for each point. The mean value of f_{top} is extracted for each position and compared to the mean value extracted from a simulation run placing the ^{57}Co source at the same location as in the data. The second dataset is formed from off-beam, beam-unrelated, steady-state (SS) electron recoil backgrounds to compare with a simulation of the $^{83\text{m}}\text{Kr}$ source. Both of these distributions are expected to consist largely of events evenly distributed throughout the detector. Seen in Fig. 5.3, the simulation is able to reproduce the f_{top} distributions seen in the two datasets. The residual differences between the data and MC are minimized and are considered to set systematic errors for the MC parameters

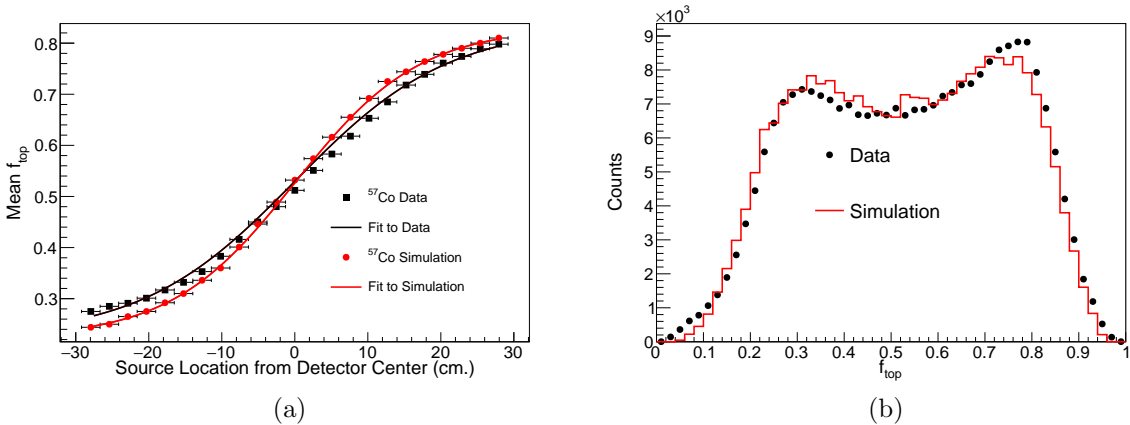


Figure 5.3: Comparison of the z -dependence of the simulated sources and the corresponding data. (a) ^{57}Co simulation compared with the data taken during the ^{57}Co z -scan. Each point represents the mean top fraction value from a separate data set taken with the source at a different location. (b) $^{83\text{m}}\text{Kr}$ simulation compared with the off-beam data distribution.

in the data analysis in Chapter 7.

PULSE SHAPE DISCRIMINATION

The final tuning of the simulation is performed by examining the reconstructed F_{90} distribution for the AmBe calibration data. Initially, the simulated events are generated using an energy-independent fraction of singlet/triplet photons with different values for ER and NR events set with the mean F_{90} determined at $E_{\text{reco}} > 100$ keVee. An energy independent ratio between the two states is the default in the GEANT4 scintillation framework. However, this energy independent value does not represent what is seen in the data (Fig. 4.20) as the ER and NR bands begin to come together at low energies. To better match the data, energy-dependent slices in the calibration data create a data-driven correction to the ER/NR F_{90} value in the simulation. A beta spectrum is fit to the NR region of the distribution of F_{90} values for each slice. An example of a fit to one of the slices in the AmBe data is shown in Fig. 5.4. For the ER adjustment, a beta spectrum is fit to slices of data from the ^{57}Co calibration. A cubic spline interpolates between the mean F_{90} values of the slices and produces an energy-dependent function (Fig. 5.5) that adjusts the simulated F_{90} for both ER and NR events.

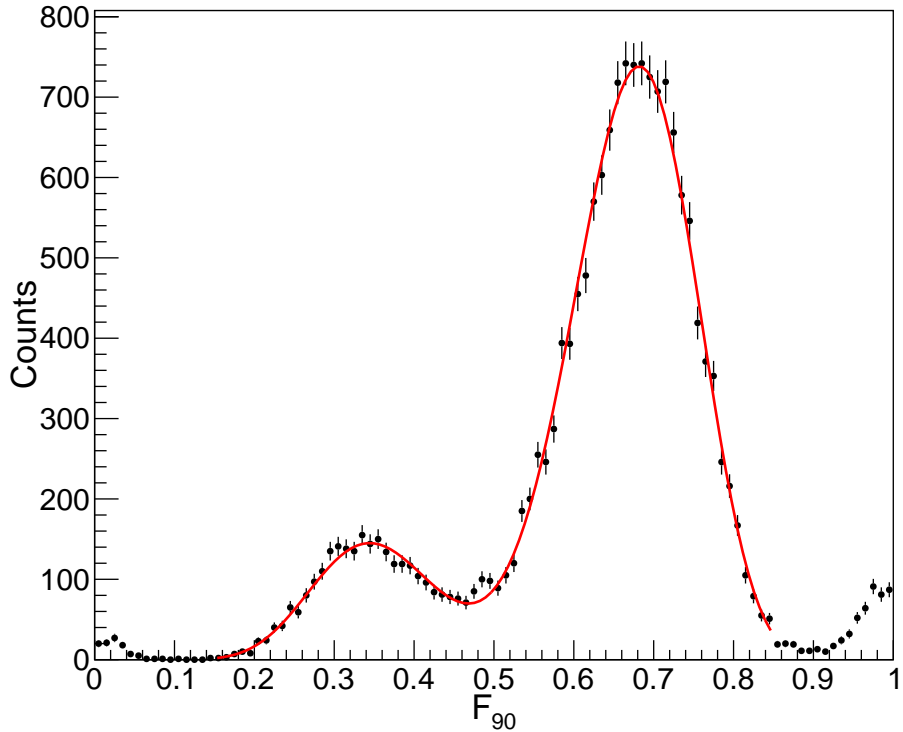


Figure 5.4: Double beta spectrum fit to NR/ER regions in a slice of the AmBe calibration data. The mean of the NR beta spectrum fit at $F_{90} \sim 0.68$ provides a point for the NR post-processing F_{90} adjustment in the simulation. A double beta spectrum fit to the AmBe data is shown here, but a beta spectrum fit to the ^{57}Co calibration data provides the ER values in Fig. 5.5.

The distributions in Fig. 5.5 are applied in post-processing to adjust the mean F_{90} values extracted from the simulation. The F_{90} adjustment is done by taking the difference of the mean value from the initial energy-independent input to the simulation and the spline value at that same energy for both NR and ER events. The post-processing adjustment allows for a better simulation of the F_{90} as extracted from the AmBe calibration data.

5.4 EVENT SIMULATIONS

This section describes the method of simulating the various signal/background components needed for the data analyses presented in Chapter 6 and Chapter 7.

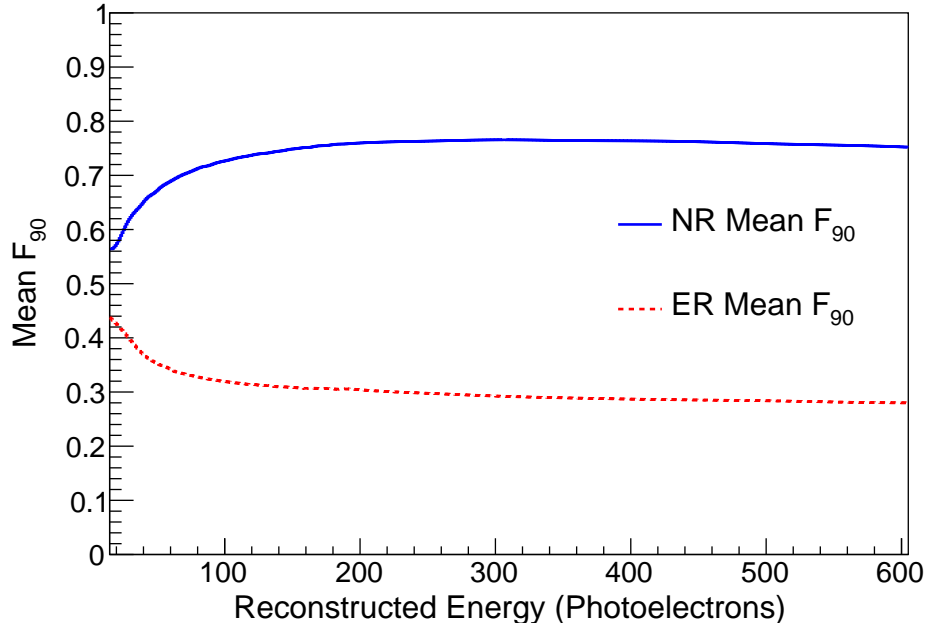


Figure 5.5: Spline functions used to adjust the NR and ER F_{90} values within the simulations from a flat value to better match the data distributions seen in Fig. 4.20.

5.4.1 BEAM-UNRELATED BACKGROUND SIMULATIONS

The SS backgrounds are measured *in situ* using the off-beam data and then subtracted when analyzing the on-beam data, so a detailed simulation of these backgrounds is not required to perform this analysis. With the addition of the lead shielding, the SS backgrounds external to the detector are expected to be greatly reduced. The largest source of background is predicted to be from ^{39}Ar . Simulations of the SS backgrounds are used to determine that the sources of SS background are reasonably consistent with the expectations.

Decays from ^{39}Ar were simulated, along with natural radioactivity from concrete and 511 keV gamma rays from the Hot-Off Gas pipe and compared to the measured off-beam triggered data. It was seen in early simulations that CENNS-10 does not appear to be sensitive to the flux of 511 keV gamma rays from the Hot-Off Gas pipe. A simulation of 1×10^9 events showed zero events that produce an interaction within the liquid argon volume in the CEvNS region of interest. As seen in Fig. 5.6, these simulations show that a large fraction of the SS background can be attributed to

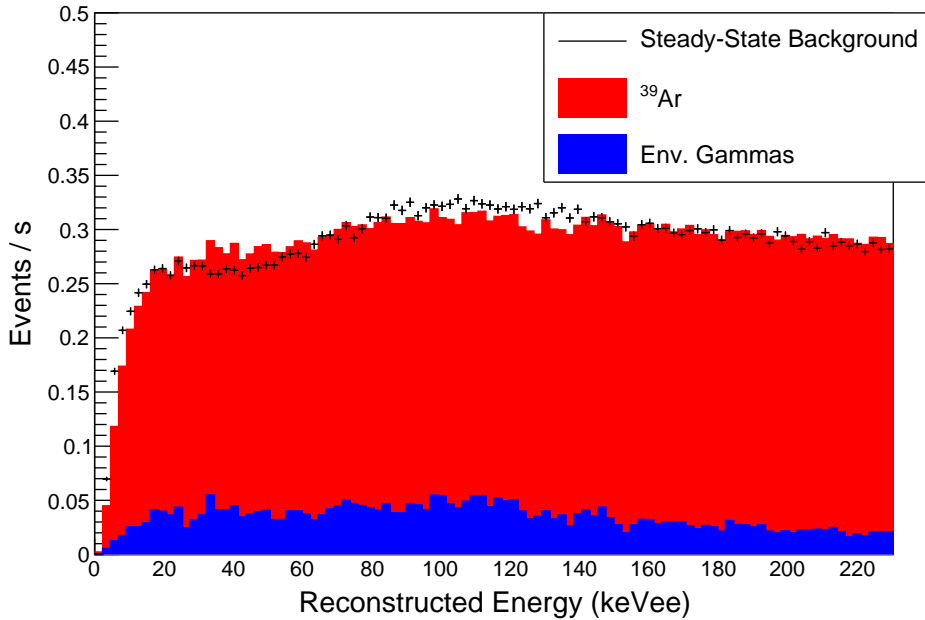


Figure 5.6: Fit of off-beam data to the various simulated beam-unrelated MC components. The results show that ^{39}Ar decays are a large fraction of the steady state backgrounds. The black points represent the data and the stacked red/blue histograms represent the simulated beam-unrelated backgrounds.

^{39}Ar decays. There is good agreement between the SS background data and the MC with the SS background model in the simulation.

5.4.2 CEvNS SIMULATION

To predict the CEvNS signal, a simulation is run with 2.5×10^7 ^{40}Ar recoil events generated with a constant energy distribution from $0 < E_{nr} < 100$ keVnr uniformly throughout the full CENNS-10 detector volume. The energy-dependent quenching factor was applied along with the post-processing F_{90} adjustment from the AmBe data to form the CEvNS prediction in energy and F_{90} space.

The time distribution of the predicted CEvNS signal is derived from a convolution of the SNS POT trace with the appropriate exponential decay for the prompt ν_μ and delayed $\bar{\nu}_\mu$ and ν_e and is shown in Fig. 2.1. The leading-edge time of the SNS neutrino pulse at the CENNS-10 detector is determined from the CsI measurement [4] of CEvNS events in time with corrections for neutrino

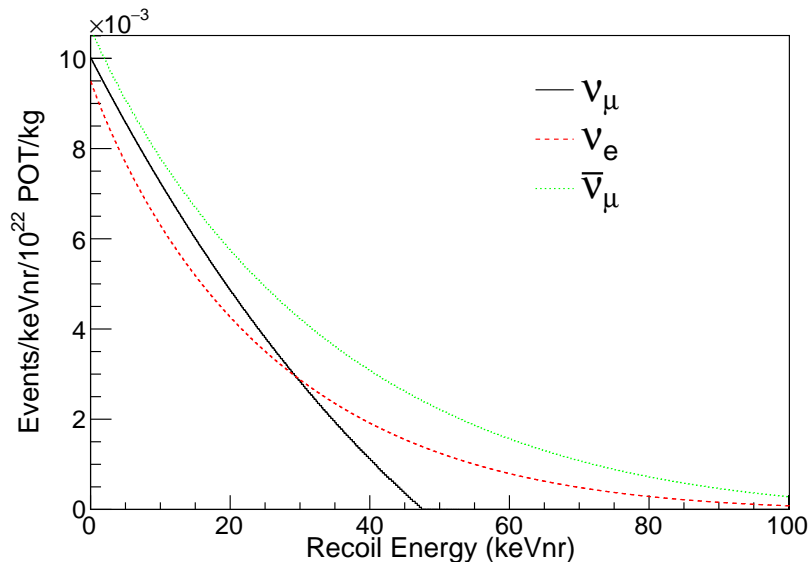


Figure 5.7: CEvNS SM predicted recoil spectrum broken down into each neutrino flavor (ν_μ , $\bar{\nu}_\mu$, ν_e). These spectra are used in combination with the detector active mass and the beam exposure to re-weight the CEvNS simulation to form the SM predicted rates.

time of flight and cable delays. This is necessary because the absolute time of the accelerator signal was not precisely known for this analysis. Work is ongoing to better measure the absolute time of the acceleration signal for future data analyses. A large uncertainty is placed on the leading-edge time of the neutrino pulse from this determination of the leading-edge and is described in Sec. 7.4.3.

The resulting energy distribution is reweighted by the SM CEvNS recoil spectrum (Fig. 5.7) separated into each different neutrino flavor. To form the CEvNS prediction for a given data set, the resulting spectrum is scaled by the detector mass and exposure. As these events are internal to the detector volume, there is no need to repeat these simulations for different shielding configurations.

5.4.3 NINS SIMULATION

To estimate the event rate due to neutrino-induced neutrons (NINs, see Sec. 5.4.3) produced in the CENNS-10 lead shielding, simulations are run with and without the water shielding in place. An identical neutron spectrum is generated as for the CsI[Na] analysis in [4] with neutrons generated

< 5 MeV. A total sample of 1.5×10^8 neutrons are generated isotropically in the CENNS-10 lead shielding. The same time distribution is used as for the CEvNS simulation as these events are also produced by SNS neutrino interactions. The resulting spectrum is then reweighted to the measured NIN rate in [4] for the mass of lead in the CENNS-10 shielding and appropriate beam exposure. These simulations show NINs are a negligible background to the CEvNS analysis presented in Chapter 7 as the low energy neutrons do not penetrate the 20 cm water shielding.

5.4.4 BEAM-RELATED NEUTRON SIMULATION

Beam-related neutrons (BRN, see Sec. 2.3.2) are simulated both with and without the water shielding. The neutron distribution has a constant rate in energy from $0 < E_n < 300$ MeV in a 2x2 m planar geometry at a distance of 0.7 m from the detector center with a cosine angular distribution. The BRN source is located just outside the CENNS-10 lead shielding. The resulting energy spectrum is reweighted to the results of the SciBath measurement (Fig. 2.6) to produce the initial neutron flux results.

The energy-dependent quenching factor derived from Eqn. 3.1 is applied to the BRN simulations. The BRN simulations are the main driver for including the energy-dependent quenching factor directly into the simulation at the energy deposition level. It is difficult to extract individual energy deposition information from the BRN simulations in post-processing to apply an energy-dependent quenching factor there. The post-processing F_{90} correction is applied to these simulations.

As SciBath had sensitivity to neutrons > 5 MeV, an extrapolation was done to $0 < E_n < 5$ MeV using a linear fit to the measured SciBath flux from $5 < E_n < 30$ MeV. The flux extrapolation and linear fit, shown in Fig. 5.8, allows for a low-energy neutron flux to be estimated.

The BRN timing spectrum used in the CEvNS analysis presented in Chapter 7 is derived from measurements from the no-water-shield dataset in Chapter 6.

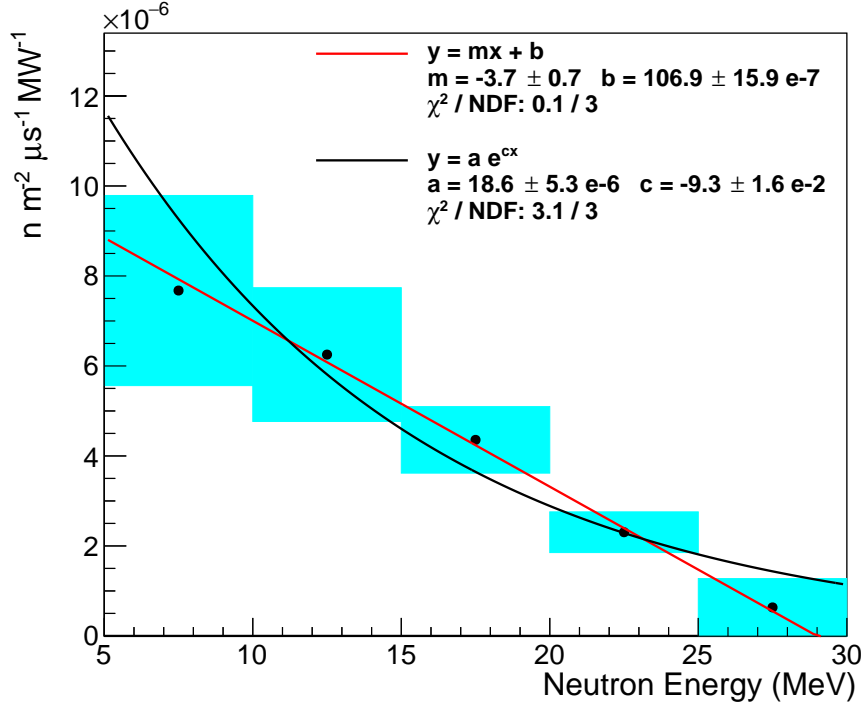


Figure 5.8: Linear fit to SciBath flux from $5 < E_n < 30$ MeV. This model is extrapolated to 0 MeV to provide an estimated flux used to reweight the BRN simulations for neutrons with energies < 5 MeV.

5.5 SIMULATED EFFICIENCIES

Quality cuts are placed on the SNS data when it is processed using the definitions for waveforms and events in Sec. 4.1. The MC does not generate waveforms so some of the quality cuts that are applied to the beam triggered data cannot be directly applied to the simulation output. The data quality cuts and their effect on the data are described within this section and are used to determine efficiencies for the analyses in Chapter 6 and Chapter 7.

As photons are generated and propagated to the PMTs, the coincidence (or threshold) cut can be directly applied to the simulated data. The rest of the efficiencies are computed from other sources of data, mainly the off-beam triggered data, and applied together with the MC efficiency. Note there are also higher-level selection cuts in F_{90} , energy, and time, but those vary with the data being analyzed and are described further in Chapter 6 and Chapter 7. The efficiencies from selection cuts that stay constant between datasets are described in the following sections.

5.5.1 WAVEFORM CUTS

Inefficiencies from cuts applied directly to waveforms cannot be directly computed in the MC. The inefficiencies attributed to waveforms are from PMT dark noise and overall waveform quality cuts. The possibility of events being missed due to PMT dark noise is measured. The waveform quality cuts represent a check on the quality of the baseline and whether an event saturated the digitizer.

EVENTS MISSED FROM PMT DARK NOISE

If dark noise in the PMT crosses the pulse finding threshold in either PMT, it can cause a missed scintillation event from the $6 \mu\text{s}$ dead time introduced in the DAQ window. If this were to happen around the SNS beam spill, a CEvNS event can be missed. An example of a missed pulse during the dead time window is shown in Fig. 4.1. It is unlikely that dark noise would be correlated between the two PMTs and pass the event building cuts, so dark noise would rarely be considered an event.

The singles rate from each PMT that crosses the pulse finding threshold is computed using the off-beam data from selected runs over time to compute the inefficiency due to PMT dark noise. A dark rate is computed for each PMT independent of the other PMT as these dark pulses rarely occur in coincidence between the two PMTs. The average value between the minimum and maximum rate seen in each PMT was adopted as an overall rate as the dark rate increases in each PMT over time in the same manner as the value of the SPE. This increase is attributed to more dark noise pulses passing the pulse finding cut as the mean SPE amplitude increases. As the PMTs installed during the upgrade had not been used before installation in CENNS-10, the PMT gain and therefore the SPE amplitude increases as the PMT vacuum improves. This increase is attributed to more dark noise pulses passing the pulse finding cut as the mean SPE value increases. The average pulse rate measured is 0.59 kHz(0.53 kHz) in the top(bottom) PMT for a combined rate of 1.12 kHz in the two PMTs. The inefficiency is computed by finding the Poisson probability of one of these pulses occurring in a $6 \mu\text{s}$ window. The overall inefficiency from dark noise is an

energy-independent value of 0.66% and is applied to the MC predictions.

WAVEFORM QUALITY

Waveforms are removed when the `daqman` analysis framework cannot compute a good baseline. This can happen, for example, if a pulse occurs at the beginning of the waveform. As a fixed baseline value is applied for the entire waveform, it is important to compute a good baseline value for a waveform. If a good baseline value is not found, the waveform is cut.

The DAQ for the CENNS-10 detector is a CAEN V1720, which is a 12 bit digitizer and has a 2 V range. Another cut applied to a waveform is if the digitizer saturates at any point in the waveform. The signals in the CENNS-10 PMTs are negative polarity so saturation occurs when the sample value hits 0 within a recorded waveform. If saturation is recorded by the digitizer, the waveform is cut.

A “pre-trace” cut is applied by looking at the measured integral in the first μs of the waveform and cutting the waveform if that value is > 1 SPE. There is little concern of cutting a large majority of events due to digitizer noise as only samples above this range are counted within the integral of the waveform.

Overall, these three cuts contribute a total inefficiency of 0.02% from examination of the steady-state background data. As with the PMT dark noise, this is applied as an energy-independent inefficiency in addition to the MC predictions.

5.5.2 EVENT CUTS

There are also cuts placed on events within the waveform. Of these, the threshold cut can be replicated by the simulated events. The rest are computed from either calibration data or the off-beam triggered data.

THRESHOLD (COINCIDENCE)

The threshold cut of > 2 photoelectrons measured in both PMTs in the first 90 ns of the event is directly applied to the simulation. As the simulation reconstructs the scintillation photon timing and propagates the photons to the PMTs, the information is available to include this cut directly on simulated events. The coincidence cut replicates the event-building requirement, which uses an ADC level threshold set to the level of ~ 2 photoelectrons at the beginning of CENNS-10 operation. Due to the changing SPE calibration over time, the application of the threshold cut ensures the same condition is applied to all data in the run. It represents a cut on the amount of singlet light in the event. The inefficiency is computed by directly applying the threshold cut to simulated CEvNS events. The threshold cut contributes an inefficiency of 14.9% in the CEvNS region of interest ($0 < E_{reco} < 40$ keVee) using the energy-dependent quenching factor along with the detector calibration. Events lost with this cut are either too low in energy to be reconstructed or the scintillation light is seen in only one PMT.

EVENT PILE-UP

Another cut placed on the individual events removes event pile-up. An event fails the pile-up cut if the maximum ADC value of the event is not found in the first 90 ns in either PMT. In this analysis, the inefficiency from this cut is computed from the AmBe data in the CEvNS region of interest as it contains samples of NR data. As the concentration of singlet/triplet states varies between NR and ER events, the AmBe data should give a better representation of the CEvNS data at these energies. An energy-dependent inefficiency of 3.6% is computed for this cut from the AmBe data in the CEvNS region of interest.

EVENT SPACING

A further cut requires an event to begin $> 7 \mu\text{s}$ after the preceding event begins. The event spacing cut prevents the possibility of triggering on the triplet light from a preceding event if there is a

Source of CEvNS Inefficiency	Inefficiency in ROI
Random Rate	0.66%
Waveform Quality	0.02%
Threshold	14.9%
Pile-up	3.6%
Event Spacing	0.13%

Table 5.1: Summary of efficiencies presented in this section. For the threshold and pile-up cuts, an energy-dependent efficiency loss in the CEvNS ROI is computed and applied to the MC predictions. The rest are energy-independent and manifest as a scaling on the overall efficiency when applied to the MC predictions.

coincidence in both tubes. The inefficiency is measured using the SNS off-beam data as multiple events can be seen within the $33 \mu\text{s}$ waveform. The energy-independent inefficiency due to this cut is 0.13% from examination of the steady-state background data.

5.5.3 SUMMARY OF EFFICIENCIES

A summary of the efficiencies described in this section is given in Tab. 5.1. There are additional inefficiencies due to energy, F_{90} , and time cuts that are further described in Chapter 6 and Chapter 7. The energy, F_{90} , and time cuts applied differ in the no-water data and full-shielded data single-bin counting experiment from those in the full-shielded data likelihood analysis.

The efficiency curve in the CEvNS region of interest including the cuts described in this section is shown in Fig. 5.9. The analysis specific energy, F_{90} and time cuts are included in Fig. 6.3 for the no-water data and full-shielded data counting experiment and Fig. 7.10 for the 3D binned likelihood analysis.

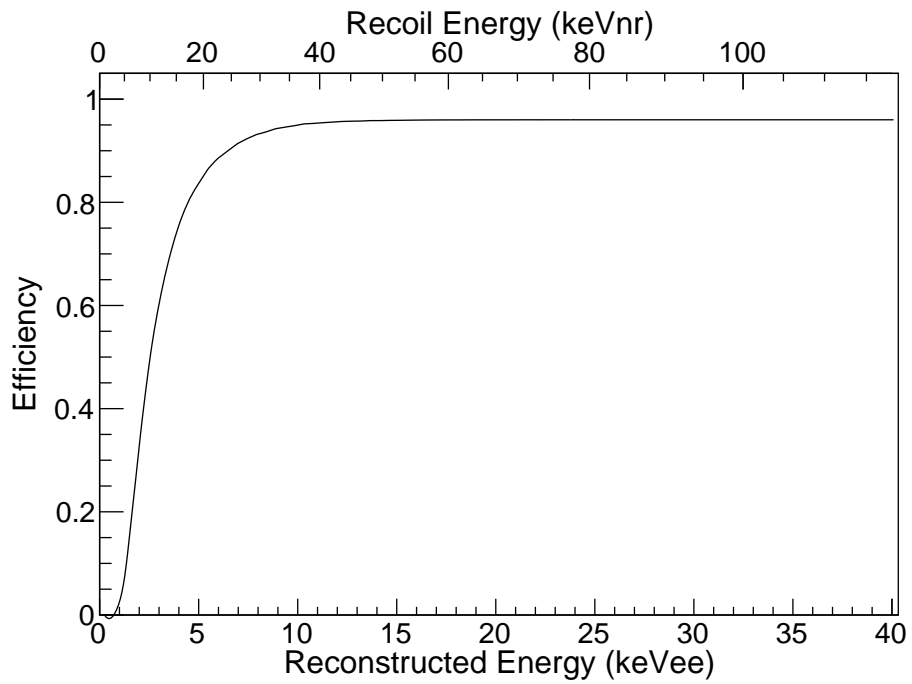


Figure 5.9: Predicted efficiency curve for all cuts described in this section including the energy-independent contributions. The CEvNS region of interest is shown to look closer at the near-threshold behavior where the signal is expected. The detector efficiency is constant for energy values greater than those shown in the figure.

CHAPTER 6

BEAM-RELATED NEUTRON STUDIES WITH THE CENNS-10 DETECTOR

Understanding of the beam-related neutron (BRN) background rate is vital for the analysis of the full-shielded data. To that end, this chapter characterizes this rate using a data collection period where the water shielding is removed in order to minimize sensitivity to the CEvNS signal. The measured BRN rates in the no-water dataset are compared to the MC predictions computed with the measured BRN flux from the SciBath measurement. These results are propagated into the full-shielding analysis BRN predictions.

6.1 RUN SUMMARY AND ANALYSIS REGIONS

The BRN rate is measured during a three-week long run (0.54 GWhr of integrated beam power) of CENNS-10 with the water shielding removed. The no-water run also tests the MC prediction (Sec. 5.4.4) based on the SciBath measurement at the CENNS-10 location (Sec. 2.3.2). This chapter describes the results of the no-water shielding run and how the results are carried over into the full shielded data analysis presented in Chapter 7. The main result of the no-water shielding run is the validation of the energy shape of the BRN from the MC and a flux normalization scaling factor that is later applied to the full-shielded BRN prediction. This factor accounts for differences between the SciBath and CENNS-10 runs such as detector location and beam power among others.

To create the run list for the no-water analysis, the golden run cuts described in Sec. 3.4 are

	Pre-beam	Prompt	Delayed
Time Range (μs)	(-4.1–(-0.6))	(0.4–1.4)	1.4–4.9
Energy Range (keVee)	0–200		
PSD Range	Optimized Energy Dependent		

Table 6.1: Time windows for the different regions considered in the no-water shielding analysis with respect to t_{trig} . The energy window used is constant throughout the different time regions and is selected to provide a higher range than a CEvNS search to better study the BRN. The PSD cut is an energy-dependent function optimized for signal/background and is described in Sec. 6.2.

applied to this dataset. The optimized F_{90} cut used for the no-water analysis is also used for the single-bin counting experiment analysis for the full shielded dataset (Sec. 7.3).

A blinding scheme ensures there was no bias in the cut selection for the no-water analysis and that of Chapter 7. All cuts and predictions are finalized before the examination of the SNS on-beam triggers. The off-beam triggers are not blinded and are used for the beam-unrelated background predictions.

Three time regions are considered for this analysis of the no-water shielding data. The pre-beam window checks the validity of the steady-state background subtraction. If the subtraction procedure is valid, then the pre-beam window should only contain steady-state background and the measured beam-related excess should agree with zero. The prompt window provides the main result and the measured beam-related excess that is compared to the MC predictions. An analysis of the delayed window searches for a possible beam-related excess from neutrons.

6.2 F_{90} CUT FORMATION

The F_{90} cut for the beam-related neutron studies and the full-shielded data single-bin counting experiment analysis (Sec. 7.3) is derived using a figure of merit optimization for the expected CEvNS signal and backgrounds with the full shielding installed.

6.2.1 FIGURE OF MERIT

The figure of merit, \mathcal{F} , for this dataset takes into account the off-beam (or steady-state, SS) data subtraction and creates the F_{90} cut used in the analysis of the no-water data. The optimized figure of merit is defined as $\mathcal{F} = N_{\text{sig}}/\sigma_{\text{sig}}$ given an expected CEvNS signal rate N_{sig} and the error on that signal rate after the steady-state subtraction. The formalism in this section is derived from [144] and finds a convenient form for \mathcal{F} in terms of signal and background events by minimizing the relative error on N_{sig} . The selection of \mathcal{F} is meant to maximize the sensitivity to the CEvNS signal. The on-beam data sample, N_{beam} , contains both the signal and the steady-state beam-unrelated background sample. N_{ss} is the measured steady-state beam-unrelated background sample and is derived from the off-beam triggered data with a sample size N_{off} . With the subtraction of the off-beam component, N_{sig} is represented as

$$N_{\text{sig}} = N_{\text{beam}} - N_{\text{ss}} \quad (6.1)$$

The off-beam data trigger is identical in length and frequency to the on-beam trigger, such that

$$N_{\text{ss}} = f N_{\text{off}} \quad (6.2)$$

where f is a scaling factor between the time window considered for the on-beam and off-beam triggered data. If the time window considered in the on-beam and off-beam samples are equal, then $f = 1$. If a larger window is used to estimate N_{ss} , then the use of a larger window decreases the value of f and reduces the statistical error on N_{off} . The lower statistical error on N_{off} has the

added effect of reducing the value of σ_{sig} , which is computed using Eqn. 6.1 and Eqn 6.2 as:

$$\begin{aligned}
\sigma_{\text{sig}}^2 &= \sigma_{\text{beam}}^2 + \sigma_{\text{bub}}^2 \\
&= N_{\text{beam}} + f^2 N_{\text{off}} \\
&= (N_{\text{sig}} + N_{\text{ss}}) + f^2 N_{\text{off}}
\end{aligned} \tag{6.3}$$

Applying Eqn. 6.2, Eqn. 6.3 further reduces to:

$$\begin{aligned}
\sigma_{\text{sig}}^2 &= (N_{\text{sig}} + N_{\text{bub}}) + f N_{\text{ss}} \\
&= N_{\text{sig}} + (1 + f) N_{\text{ss}}
\end{aligned} \tag{6.4}$$

Then \mathcal{F} can be written as:

$$\mathcal{F} = \frac{N_{\text{sig}}}{\sqrt{N_{\text{sig}} + (1 + f) N_{\text{ss}}}} \tag{6.5}$$

and the selection cuts can be chosen to maximize this quantity.

6.2.2 CUT FORMATION

The CEvNS analysis presented in Sec. 7.3 drives the formation of the optimized F_{90} cut. Therefore, the full shielded CEvNS prediction in the delayed window computes the value of N_{sig} and the measured full-shielded SS-background data computes N_{ss} in Eqn. 6.5.

The value of N_{ss} is estimated from a larger, 25 μs time window of $-16 < t_{\text{trig}} < 9 \mu\text{s}$, as compared to a 3.5 μs window for the signal region to determine N_{sig} . The window definition for N_{ss} yields $f = 7/50$ for the formation of the F_{90} cut. From an investigation of the full-shielded off-beam triggered data, the distribution of SS-background events is flat with respect to t_{trig} (Fig. 6.1). As a result, there is no concern about simply scaling the number of off-beam events to match the length of the window considered for the analysis. During the event selection, events that begin in the first two μs and last six μs of the waveform are cut. The first two μs are not considered to avoid events from interactions that occur immediately prior to that trigger window. The last

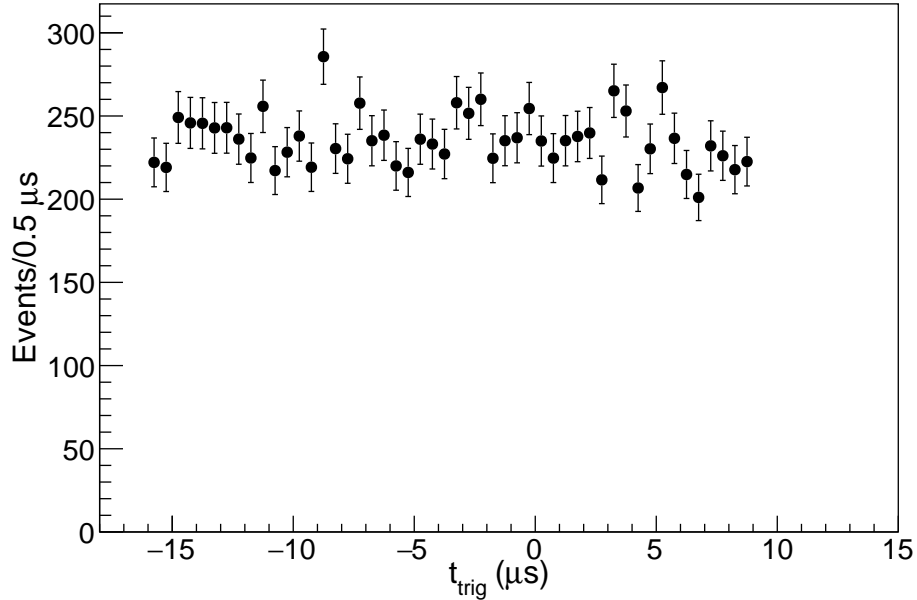


Figure 6.1: Distribution of events with respect to t_{trig} in full-shielded off-beam trigger data. The distribution of events is relatively flat throughout the window and a larger window can be used to reduce the statistical error on the off-beam sample.

six μs are not considered to allow for a full six μs event length to occur within the waveform.

The energy-dependent optimized F_{90} cut is computed from the predicted CEvNS signal following Eqn. 6.5. A flat PSD value is applied for reconstructed events with an energy above the CEvNS signal range. A cut of events with $F_{90} > 0.9$ is also applied to remove the events at high F_{90} values seen in Fig. 4.20, theorized to be Cherenkov in origin. The optimized F_{90} cut used for the counting analyses is shown in Fig. 6.2 overlaid over the BRN MC prediction from the no-water run.

The efficiency curve including the PSD cut found here is shown in Fig. 6.3. The same efficiency curve is applied in this analysis and in the full-shielded data single-bin counting experiment described in Sec. 7.3.

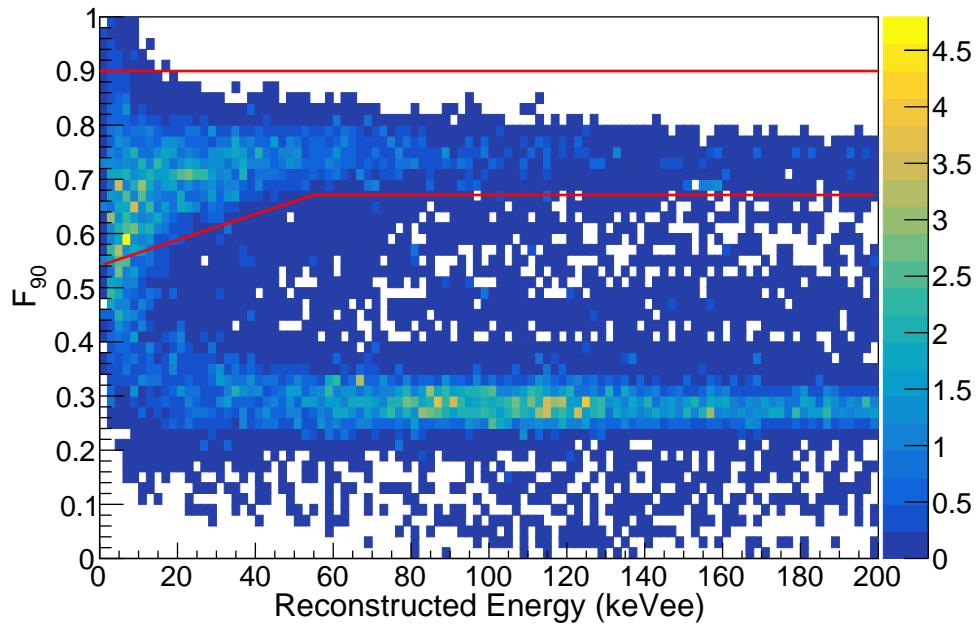


Figure 6.2: Predicted BRN spectrum with optimized energy-dependent F_{90} cut overlaid.

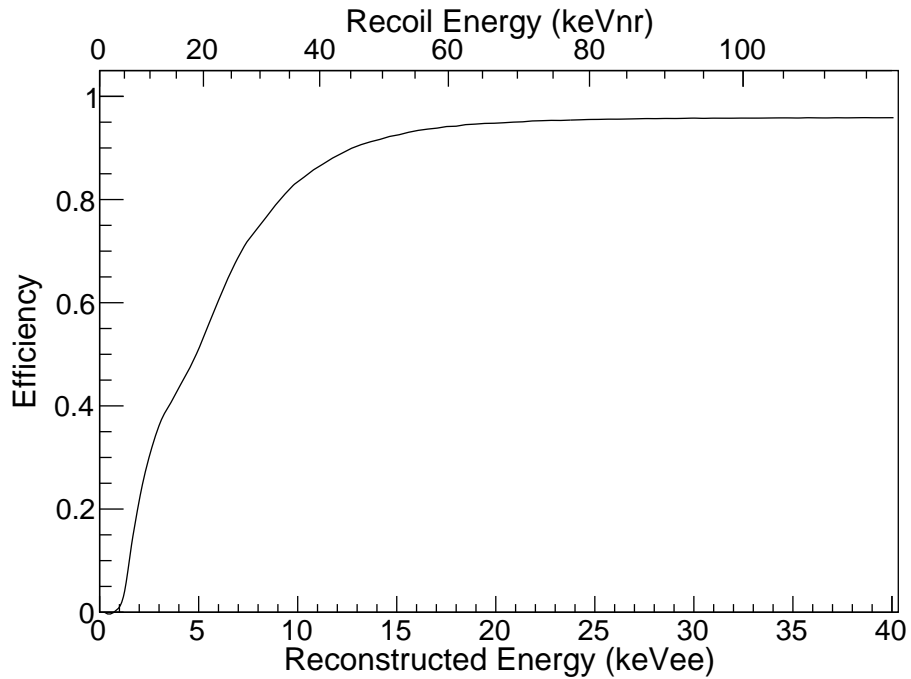


Figure 6.3: Predicted efficiency for CEvNS events using the cut for the no-water analysis and the single-bin counting experiment analysis for the full shielded data. The CEvNS energy region of interest is shown and the efficiency curve is flat at energy values greater than those shown in the figure.

6.3 EVENT SELECTION

The waveform and event cuts from Sec. 5.5 are applied to form the event samples in the on-beam and off-beam triggered data. The energy and optimized F_{90} cut are also applied to the data. For the on-beam data, a time cut is made to select events being considered in that t_{trig} window in Tab. 6.1. A 25 μs window is taken between $-16 < t_{\text{trig}} < 9 \mu\text{s}$ in the off-beam data in order to reduce the statistical error on the off-beam sample.

6.4 SIGNAL PREDICTIONS

The predicted rate of BRN in this run are computed from the CENNS-10 simulation described in Sec. 5.4.4. The resulting MC distribution then reweighted by the prompt BRN flux from the SciBath measurement (Fig. 2.6) in units of $\text{n}/(\text{m}^2\mu\text{sMWMeV})$ and is normalized by the number of triggers in units of μs , the average beam power during the run in units of MW, and the area of the neutron generation plane used in the simulation in units of m^2 . The average SNS beam power is included due to the difference in the value between the SciBath measurement ($\sim 1 \text{ MW}$) and operation during the no-water data taking ($\sim 1.3 \text{ MW}$). All of the efficiencies from Sec. 5.5 are applied to these predictions. Additional inefficiencies occur when the F_{90} cut shown in Fig. 6.2 is applied to the simulated data to generate the BRN predictions (Fig. 6.4).

The BRN predictions are ultimately compared to the steady-state-background subtracted on-beam data. For this analysis, predictions are only generated in the prompt window. The delayed time window checks for any excess that could arise from beam-related neutrons. The predicted BRN and beam-unrelated background rates are shown in Tab. 6.2. In all results presented here, the optimized F_{90} cut is applied to the data and the simulation predictions.

Other sources of beam-related events are expected to be small in comparison to the BRN prediction in the no-water dataset. Running a simulation of CEvNS and NINs using the methods in Sec. 5.4.2 and Sec. 5.4.3 for the expected exposure and shielding configuration of the no-water

Time Window	Energy Range (keVee)	N_{BRN}	N_{ss}
Prompt	0-200	387	48

Table 6.2: Initial predicted BRN rates for the no-water shielding analysis of the prompt window. These are derived from the SciBath flux measurement at the CENNS-10 location. This prediction is compared to the BRN seen in the data to determine how well the SciBath predictions apply to the measured data rates.

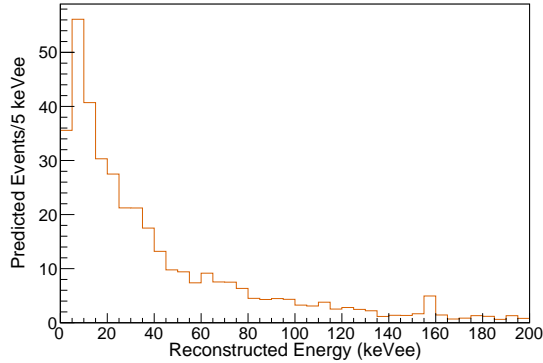


Figure 6.4: Reconstructed energy distribution of the initial BRN prediction for the no-water analysis after applying the optimized F_{90} cut shown in Fig. 6.2 to select NR events.

dataset show an expected ~ 1 event exposure in the prompt and delayed window for both samples. The predicted CEvNS rate in this dataset shows there is no concern to extract a signal using this dataset and it is clear that any excess in the prompt window is caused by beam-related neutrons. The resulting BRN prediction tests the SciBath prediction against the resulting BRN dominated data.

6.5 PRE-BEAM REGION ANALYSIS

A pre-beam region prior to the beam spill checks the validity of the off-beam subtraction before the prompt time window was examined. The use of a larger window of off-beam data reduces statistical fluctuations when performing the off-beam subtraction on the on-beam data. As seen in Fig. 6.5 and Tab. 6.4, the measured excess in the pre-beam window after off-beam subtraction of 7 ± 14 is consistent with zero. The agreement of the excess with zero means the off-beam data is a good representation of the steady-state background measured in the on-beam data and no

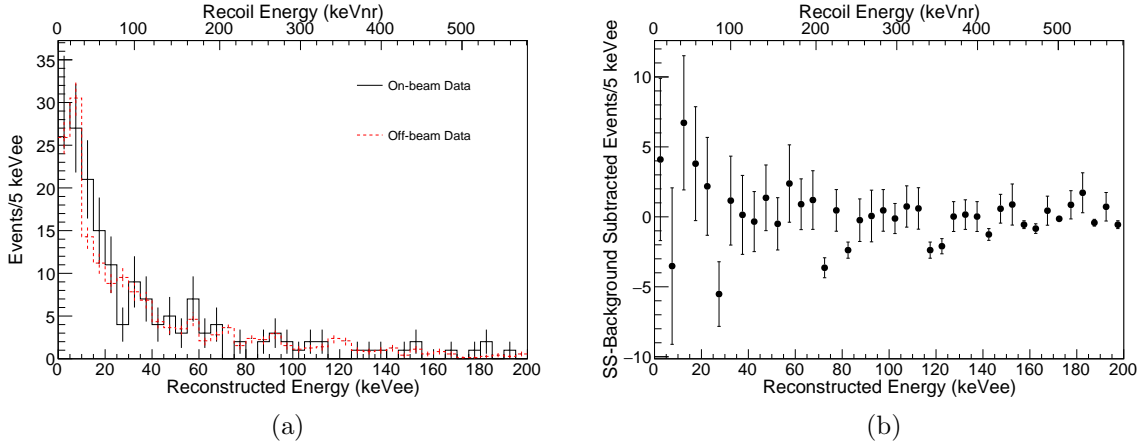


Figure 6.5: Results of an analysis of the no-water shielding data in the pre-beam window. (a) Distribution of on-beam and off-beam triggers. Note the off-beam distribution is generated from a larger window to reduce statistical fluctuations. (b) Distribution of excess events after subtraction of off-beam data which is consistent with zero within 1σ .

unexpected backgrounds are present. A constant fit to zero steady-state subtracted events gives a χ^2/ndf of 118/39. A Kolmogorov-Smirnov test between the pre-beam sample and the off-beam triggered data results in a value of 0.76 and the two samples are compatible.

6.6 BEAM-RELATED NEUTRON ANALYSIS

The on-beam and off-beam data for the prompt region ($0.4 < t_{\text{trig}} < 1.4 \mu\text{s}$) is shown in Fig. 6.6. The subtraction of the SS background yields an excess of 580 ± 25 events. The results overlaid with the initial MC predictions are also shown in Fig. 6.6.

The BRN prediction from Fig. 6.4 is fit to the data to compute a normalization factor to ensure data-MC agreement. As the energy shape of the MC initially agrees very well with the data, only the overall normalization of the BRN was allowed to float during the fit. The best-fit normalization increases the BRN flux by a factor of 1.5 in order to match the data. The results of this scaling, along with the systematic errors described in Sec. 6.6.1 are shown in Fig. 6.7.

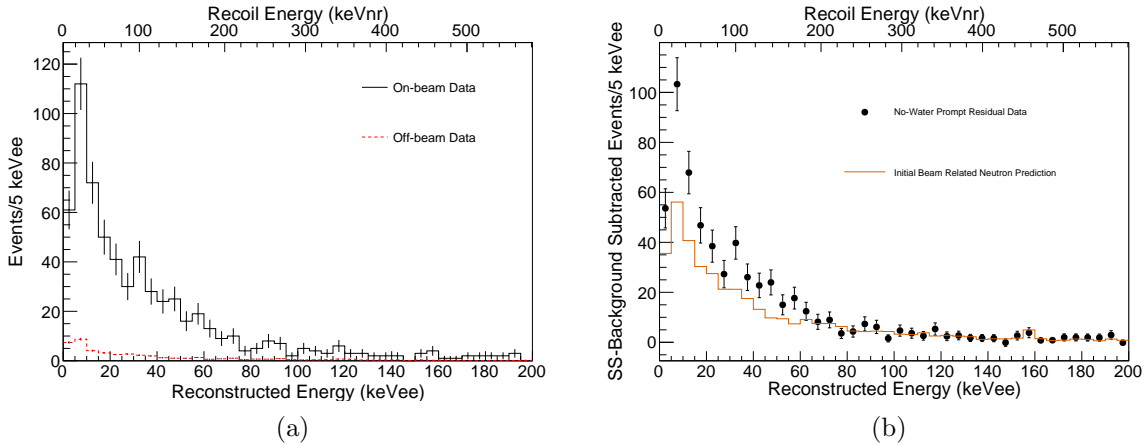


Figure 6.6: Results of an analysis of the no-water shielding data in the prompt on-beam window. (a) Distribution of on-beam and off-beam triggers. Note the off-beam distribution is generated from a larger window to reduce statistical fluctuations. (b) Distribution of events after subtraction of off-beam data. The shape of the excess is consistent with the initial BRN predictions.

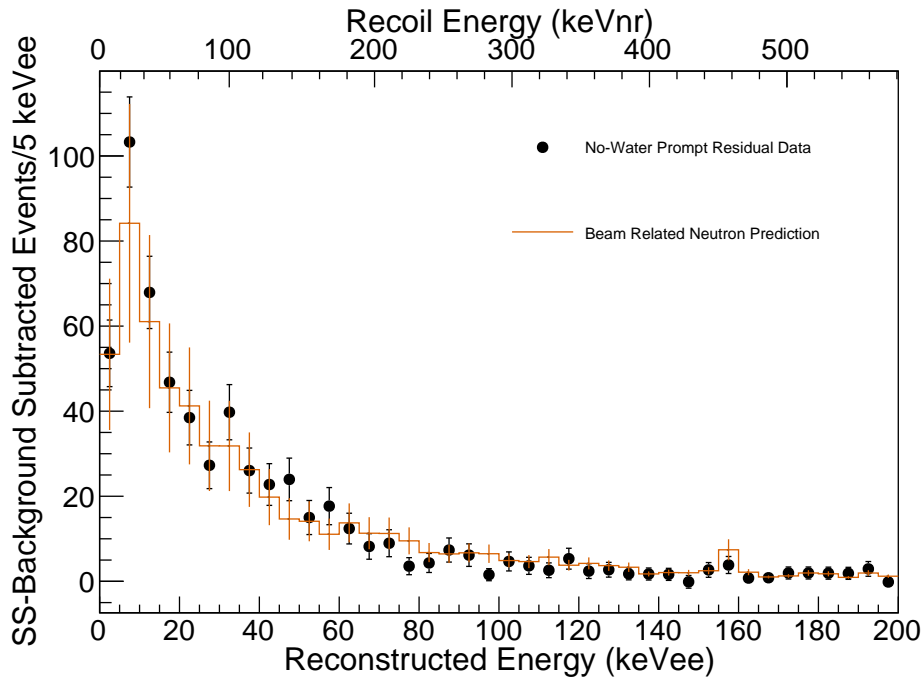


Figure 6.7: Scaled BRN MC compared to the data after applying the best-fit scaling factor of 1.5 to the prediction shown in Fig. 6.6. After scaling the normalization of the BRN prediction by the results of a fit to the data, the data agrees with the MC very well in both shape and rate. Systematic errors are also applied at this stage and further described in Sec. 6.6.1.

6.6.1 SYSTEMATIC EFFECTS

Several systematic errors are applied to the beam-related neutron predictions in the no-water shielding analysis. The systematics are evaluated using excursions on the central-value prediction shown in Fig. 6.4.

QUENCHING FACTOR

The error on the quenching factor is taken from the errors on the parameters on the linear fit model (Eqn. 3.1) presented in Sec. 3.1.1. For a given value of the quenching factor, the error on that value can be computed as:

$$\begin{aligned}\sigma_{QF}^2 &= \left(\frac{d(QF)}{da}\right)^2 \sigma_a^2 + \left(\frac{d(QF)}{db}\right)^2 \sigma_b^2 + 2\rho \left(\frac{d(QF)}{da}\right) \left(\frac{d(QF)}{db}\right) \sigma_a \sigma_b \\ \sigma_{QF}^2 &= \sigma_a^2 + 2E\rho\sigma_a\sigma_b + E^2\sigma_b^2\end{aligned}\tag{6.6}$$

To evaluate the systematic error, simulations are run applying the $\pm 1\sigma$ values of the quenching factor for a given energy deposition.

PULSE SHAPE DISCRIMINATION

To evaluate the systematic error on the F_{90} value generated by the simulation, an energy-dependent error is applied based upon the degree of separation between the NR and ER bands in Fig. 4.20. As the reconstructed energy value increases, the bands are more easily separated and less contamination of ER events in the NR band. Also, with an adjustment to the F_{90} value made in post-processing of the simulation from the AmBe data, the systematic also takes into account an uncertainty on determining that value from the data. The energy-dependent uncertainty that is

applied to the data is:

$$\begin{aligned} 0 - 5 \text{ keVee: } & 10\% \\ 5 - 10 \text{ keVee: } & 5\% \\ 15 - 20 \text{ keVee: } & 1\% \\ 10 - 15 \text{ keVee: } & 2\% \\ > 20 \text{ keVee: } & 0.5\% \end{aligned} \tag{6.7}$$

The systematic is evaluated by generating $\pm 1\sigma$ excursions based on Eqn. 6.7 and comparing to the central-value prediction.

LIGHT YIELD

The systematic on the light yield is evaluated by taking the resulting error on the CENNS-10 detector calibration given by Fig. 4.8. To evaluate this systematic error, simulations are regenerated adjusting the value of Y_γ to the $\pm 1\sigma$ values determined by the resulting fit.

EVENT ACCEPTANCE

The acceptance (or efficiency) error is computed using the errors on the energy independent cuts along with an adjustment to the Gaussian smearing of the single photoelectron in the simulation. Simulations are run adjusting the single photoelectron smearing width by ± 0.1 photoelectrons from the nominal Gaussian width of 0.4 photoelectrons. The threshold cut of > 2 photoelectrons seen by each PMT is then applied to the resulting simulations to generate the systematic error.

SIMULATION OPTICAL MODEL

The CENNS-10 simulation described in Chapter 5 applies a data-driven optical model and contains modeled parameters for the reflection off the PMT layer, the absorption length of the TPB layer,

and reflectivity of the Teflon cylinders. To account for a systematic effect on the optical model used in the CENNS-10 simulations, the reflection off the PMT layer, the absorption length of the TPB layer, and reflectivity of the Teflon cylinders are varied in a reasonable way from the nominal values which lead to the agreement between data and simulation shown in Table A.1. In each adjustment, the value of Y_γ is kept constant to evaluate the effect of changing the optical parameter, not the light yield. The simulations are regenerated with these parameters adjusted and evaluate the total error on the predicted rate.

LOW ENERGY NEUTRON FLUX

A systematic error is applied to the extrapolation of the measured SciBath flux to the lowest energies. A conservative error of 21% is extracted on the value of the low energy neutron flux by taking the difference of the extrapolated flux value with the measured flux value in the (5-10) MeV bin. Predictions are generated by re-weighting the SciBath flux using the $\pm 1\sigma$ flux values in this low energy bin to compute the flux error. As these very low energy neutrons are not expected to penetrate the shielding structure, this error has a very small effect on the BRN rate.

BRN SCALING TO FULL-SHIELDED DATA

The Engineering Run analysis [82,83] applied a similar strategy to the one described in this section. A period of data was taken before the CENNS-10 shielding was installed to characterize the beam-related neutron rates. The results of an analysis of this data show the beam-related neutron rate was $\sim 30\%$ higher than the SciBath predictions. The Engineering Run has a much higher energy threshold of ~ 80 keVnr so the no-water shielding data was acquired here to repeat this analysis with the upgraded CENNS-10 detector. After the no-water shielding data was analyzed in the Engineering Run, a scaling factor of 1.3 was applied to the beam-related neutron rates so the data and MC results agreed. The same scaling factor is applied to the full-shielded data predictions so the MC is only relied upon to transport neutrons through the shielding. The Engineering Run

results in [83] show that this procedure is valid to 30% from the final analysis of the full shielded data, which is uncorrelated with the applied scaling factor. Variations in the neutron rate which cover the results of the Engineering Run is applied to the beam-related neutron predictions during the analysis of the no-water data.

TOTAL SYSTEMATIC CONTRIBUTION

For each systematic, the resulting uncertainty on the predicted BRN rate is extracted and is shown in Tab. 6.3. The total error is dominated by the normalization uncertainty extracted from the Engineering Run results.

BRN Rate Measurement Systematic Errors	
Error Source	Total Event Uncertainty
Quenching Factor	2.0%
Energy Calibration	0.3%
Detector Model	2.3%
F_{90}	1.8%
Event Acceptance	0.7%
Low Energy Neutron Flux	0.1%
BRN Scaling	30%
Total Error	30.2%

Table 6.3: Systematic errors relating to the predicted rate of beam-related neutrons. The error is dominated by the uncertainty on the scaling procedure determined from the Engineering Run results [82, 83].

6.6.2 χ^2 ANALYSIS IN PROMPT REGION

A full 2D χ^2 analysis is performed assuming fully-correlated errors after the computation of the scaled BRN MC and systematic uncertainties. A covariance matrix is formed using the prediction including systematic uncertainties and the data and is used to compute a goodness-of-fit between the scaled BRN MC and the no-water data excess. The χ^2 analysis shows how well the prediction agrees with the data before applying this scaling procedure to the full-shielded data. The χ^2 value

between two distributions including correlated errors is given by:

$$\chi^2 = \sum_{i=1}^N \sum_{j=1}^N (x_i - \bar{x}_i) V_{ij}^{-1} (x_j - \bar{x}_j) \quad (6.8)$$

where the sum over i and j represent the bin numbers in the distribution, x_i represents the measured value in a bin i and \bar{x}_i represents the central-value prediction in a bin i . The covariance matrix V_{ij} is computed from the distributions representing the systematic excursions in Sec. 6.6.1.

COVARIANCE MATRIX FORMATION

The covariance matrix is formed using all systematic excursions and is computed for a given set of k excursions:

$$V_{ij} = \frac{1}{N_{\text{excursion}}} \sum_{\text{excursion}} \sum_{i=1}^N \sum_{j=1}^N (x_i - \bar{x})(x_j - \bar{x}) \quad (6.9)$$

A matrix of this form is computed for each systematic and then summed together to create the final covariance matrix (Fig. 6.8) used in the χ^2 calculation.

χ^2 CALCULATION

One adjustment made during the χ^2 calculation following Eqn. 6.8 correctly accounts for the errors on the data if there are no beam events in a given energy bin. If there are no beam events, then the error on the bin is given as the error on the predicted value in that bin. With the larger off-beam window used to suppress statistical errors on that sample, the error in that bin is small. The result shows a χ^2/ndf of 35.3/39 when comparing the scaled MC to the resulting beam-related neutron excess.

6.6.3 BEAM-RELATED NEUTRON ARRIVAL TIME

The arrival time of the BRN with respect to the trigger time t_{trig} is another distribution in this dataset that will inform the full-shielded data. The off-beam-subtracted timing spectrum is shown

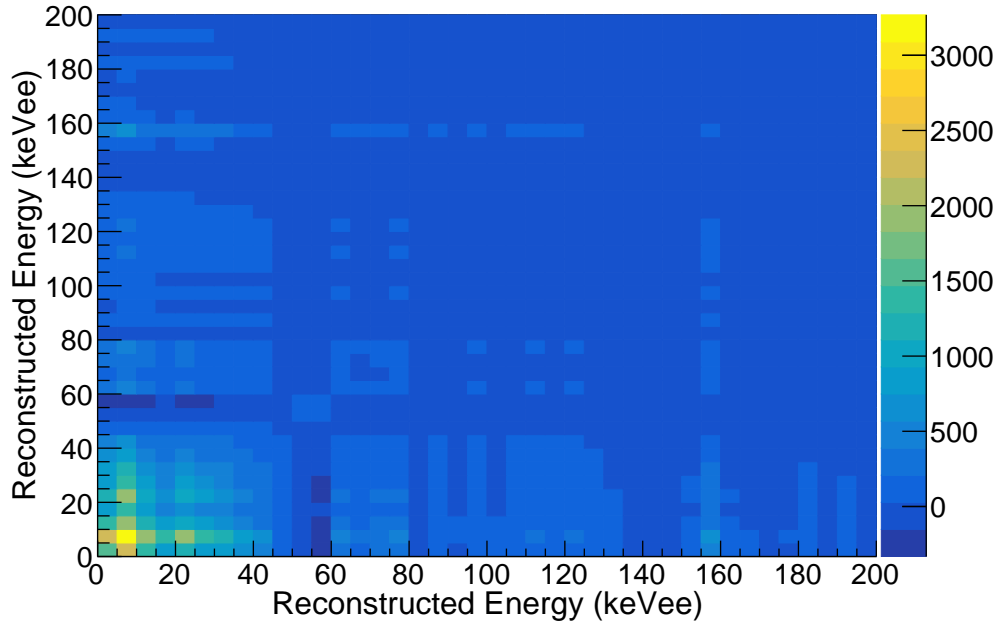


Figure 6.8: Covariance matrix used for the χ^2 analysis with fully correlated errors. All systematic error contributions from Sec. 6.6.1 are included here.

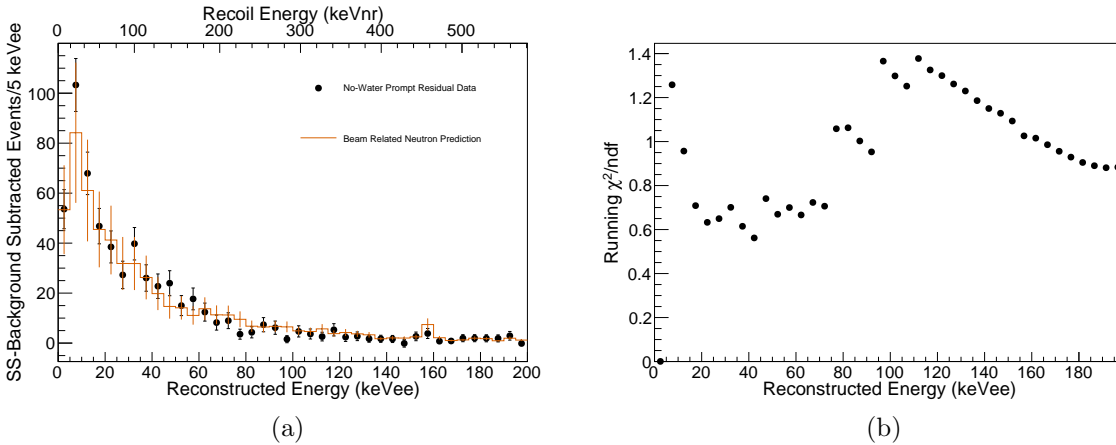


Figure 6.9: (a) Scaled BRN MC compared to the data. (b) Full 2D χ^2 calculation for the no-water data comparing the data to the scaled predicted BRN spectrum. The MC agrees well with the data given by a χ^2/ndf of 35.3/39. Note that the resulting value for each bin is the running total value of χ^2/ndf , not the value solely in that one bin.

in Fig. 6.10 and shows a clear excess in the prompt region. A Gaussian fit to the prompt window informs the initial BRN timing predictions in the full-shielded data analysis presented in Chapter 7. The Gaussian fit to the measured timing excess in the prompt window computes a mean value of 810 ns with a width of 257 ns. The width in particular is larger than the expected SNS beam

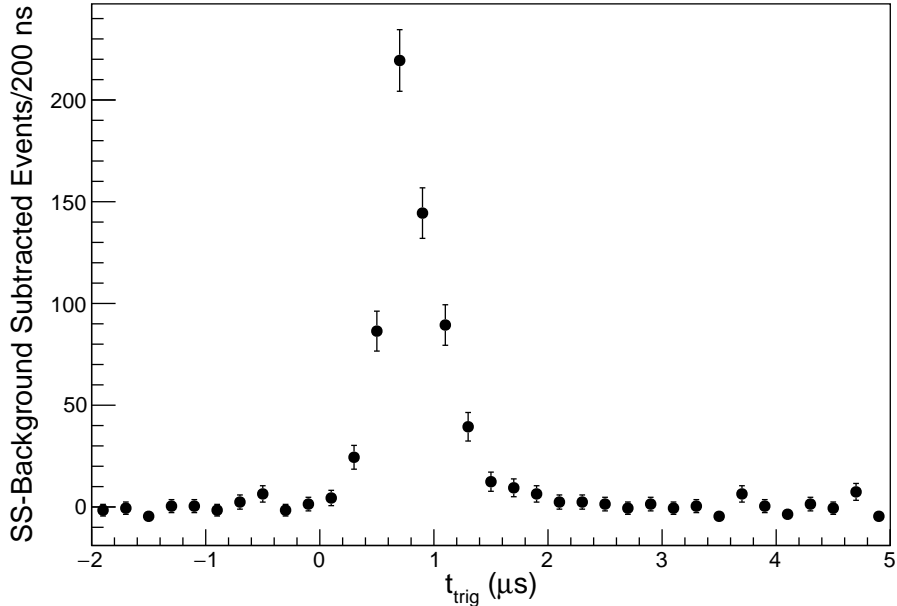


Figure 6.10: Time distribution of residual events in the no-water dataset after the off-beam subtraction is performed. There is a noticeable excess in the prompt region ($0.4 < t_{\text{trig}} < 1.4 \mu\text{s}$). There is also a visible excess at early times in the delayed region, which is studied in Sec. 6.6.4.

pulse width of ~ 150 ns. The SciBath run and the CENNS-10 Engineering Run both show relative agreement with the SNS pulse width of ~ 150 ns, so interactions of low-energy neutrons in the detector is thought as the cause of the larger width measured in the no-water dataset.

Looking closer at the arrival time of events in a 2D space (Fig. 6.11), there is a larger concentration of low energy recoil events which appear to spread out the arrival time distribution and contribute to the larger measured width.

6.6.4 DELAYED REGION INVESTIGATIONS

In previous measurements with SciBath and the CENNS-10 Engineering Run [82, 83], there is no evidence of beam-related neutrons occurring outside of the prompt window. However, the no-water dataset with the upgraded CENNS-10 detector has a much lower energy threshold than any previous BRN measurement. Thus, the delayed time region is examined for a beam-related excess. An excess of 43 ± 15 events is measured in the full delayed window. After investigations arising

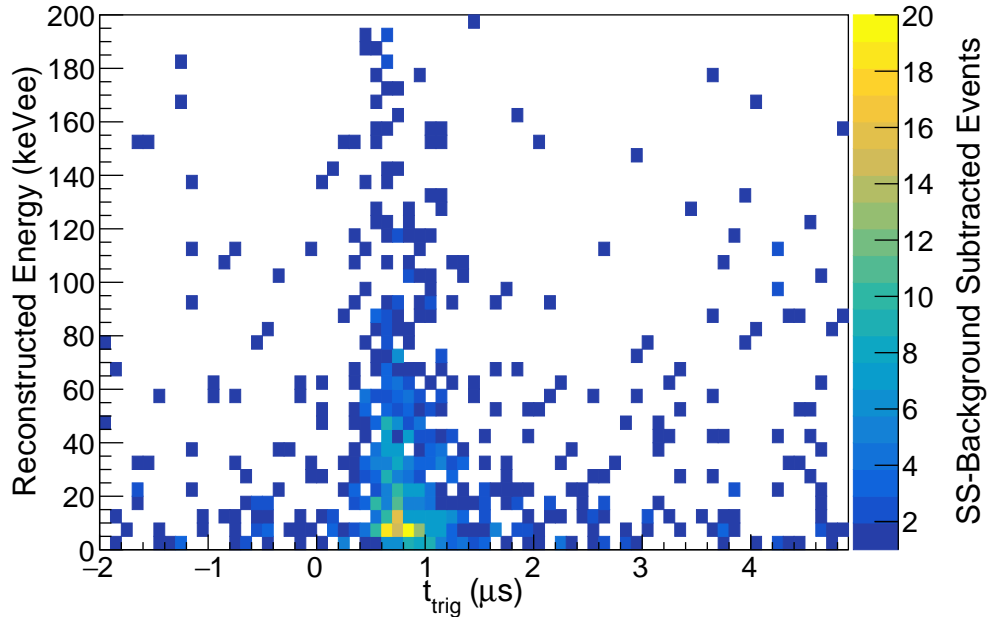


Figure 6.11: Distribution of reconstructed energy of an event vs event arrival time with respect to the beam spill for on-beam trigger events after the subtraction of the steady-state background, which are dominated by beam-related neutrons. There appears to be a correlation between energy and arrival time with lower energy events occurring later and with more of a spread. This is consistent with low-energy neutrons interacting within the detector.

from Fig. 6.10, a region from $1.4 < t_{\text{trig}} < 1.9 \mu\text{s}$, just outside the prompt window is examined separately. If there is a measurable excess in this range, it could represent neutrons bleeding into the delayed region from the prompt region. The theory of neutrons bleeding into the delayed window is supported by the fact that there is less of a visible excess over time in the delayed region. The subsample of the delayed window shows a beam-related excess of 26 ± 7 events after the off-beam subtraction is performed. The excess in the delayed window is not expected to be from NINs generated in the lead shielding given the small NIN prediction in the no-water dataset.

6.7 SUMMARY

The full results of all regions analyzed in this dataset are shown in Tab. 6.4. The results from this analysis, mainly the scaling factor determined from examination of the prompt window, are used to inform predictions for the analysis of the full-shielded data in Chapter 7. A prediction for a

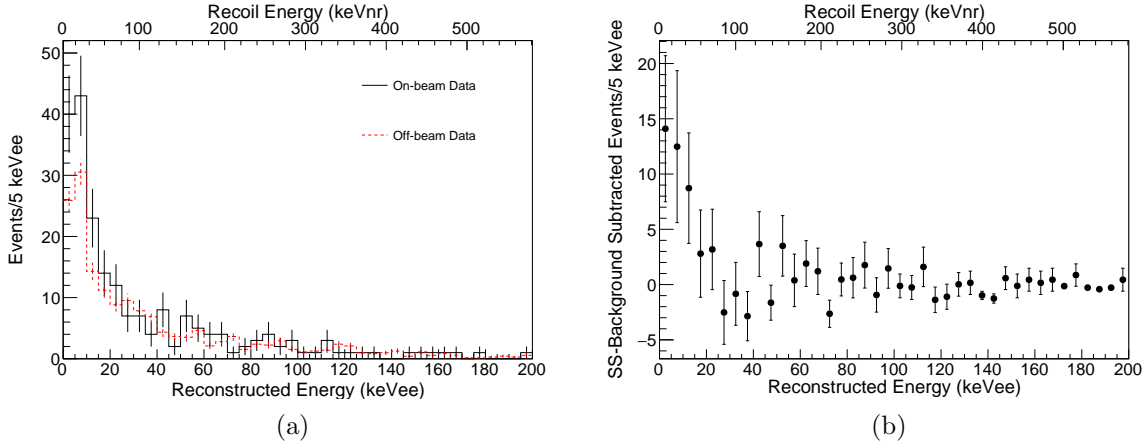


Figure 6.12: Results of an analysis of the no-water shielding data in the prompt on-beam window. (a) Distribution of on-beam and off-beam triggers. Note the off-beam distribution is generated from a larger window to reduce statistical fluctuations. (b) Distribution of events after subtraction of off-beam data. The shape of the excess is consistent with the initial BRN predictions.

Sample	Prompt	Delayed	Pre-beam
On-beam	628 ± 25	211 ± 15	175 ± 13
Steady-state (SS) Background	48 ± 1	168 ± 4	168 ± 4
SS-Background Subtracted Residual	580 ± 25	43 ± 15	7 ± 14
Initial Prompt MC Prediction	387		
BRN Best Fit Data-MC Scaling Factor	1.5		
Scaled Prompt MC Prediction	581		

Table 6.4: Table of rates seen in prompt/delayed windows for the no-water shielding data.

delayed BRN component is included into the likelihood analysis in Sec. 7.4, providing a test for the hypothesis of the presence of BRN-like events bleeding into the delayed window.

CHAPTER 7

FIRST DETECTION OF CE ν NS WITH THE CENNS-10 DETECTOR

In this chapter, two analyses are performed on the full-shielded dataset: a single-bin counting experiment (Sec. 7.3) and a 3D binned maximum likelihood analysis in energy, F_{90} , and time space (Sec. 7.4). The counting experiment has minimal statistical power due to the presence of the BRN background in the prompt window and low statistics in the delayed region. The likelihood analysis can better distinguish the CE ν NS signal from the backgrounds using the difference in shape between the distributions in the full 3D space. The likelihood fit provides the final results of this analysis and ultimately the first detection of CE ν NS on an argon target. The likelihood analysis places new constraints on neutrino NSI parameters.

7.1 RUN SUMMARY AND ANALYSIS REGIONS

The CENNS-10 full-shielded dataset covers a total of 6.12 GWhr (13.8×10^{22} POT) in a period from July 2017-December 2018 after the installation of the full detector shielding. A selection of golden runs is made with the criteria in Sec. 3.4.2 and these runs are processed and analyzed as part of the dataset.

The counting experiment and likelihood analyses of the full-shielded data contain different energy, F_{90} , and time windows. The regions considered for the two analyses are described in Tab. 7.1.

	Single-bin Counting Experiment			Likelihood Analysis
	Pre-beam	Prompt	Delayed	
Time Range (μs)	(-4.1–(-0.6))	(0.4–1.4)	(1.4–4.9)	(-0.1–4.9)
Energy Range (keVee)	(0–200)		(0–40)	(0–120)
F_{90} Range	Optimized Energy Dependent			(0.5–0.9)

Table 7.1: Ranges of energy, F_{90} , and time used in the two analyses of the full-shielded data. The F_{90} cut in the single-bin counting experiment is the same energy-dependent function used in the no-water data and described in Sec. 6.2.

7.2 EVENT SELECTION

The waveform and event cuts from Sec. 5.5 are applied to form the event samples in the on-beam and off-beam triggered data. The energy and F_{90} cuts differ for the counting experiment and the likelihood fit. A time cut is made on the on-beam data to select events in the t_{trig} window in Tab .7.1 for each analysis. A 25 μs long window from $-16 < t_{\text{trig}} < 9 \mu\text{s}$ selects events for the off-beam data and is scaled to the appropriate time window for a given analysis.

7.3 SINGLE-BIN COUNTING EXPERIMENT

7.3.1 SIGNAL/BACKGROUND PREDICTIONS

The GEANT4 simulation was run including the full detector shielding to form the signal predictions for the full-shielded analysis. The efficiencies in Sec. 5.5 are applied to the resulting simulation output. Finally, energy and F_{90} cuts are applied to each prediction. A time cut is placed on the data from the region under consideration (prompt, delayed). The detector efficiency for the single-bin counting experiment is identical to the no-water data shown in Fig. 6.3 as the same F_{90} cut is applied to this dataset.

CEvNS PREDICTION

The CEvNS prediction is formed by running the simulation described in Sec. 5.4.2, normalizing by the detector mass and integrated beam power of the dataset and applying the energy and F_{90}

cuts. The predictions are separated into prompt and delayed by the value of t_{trig} , not the specific neutrino flavor.

BRN PREDICTIONS

The prompt BRN prediction is formed in the exact same manner as in Sec. 6.4, with only differences in the total beam exposure and the addition of the water shielding. The same F_{90} cut in the no-water shielding analysis is applied to the full-shielded BRN prediction. The timing distribution is derived from the Gaussian fit to the no-water shielding data excess. Further described in Sec. 7.3.3, different mean values for the Gaussian timing distribution are used between Sec. 7.3.3 and Sec. 7.3.4.

From the results in Sec. 6.6.4, a delayed BRN prediction is generated in the time window $1.4 < t_{\text{trig}} < 1.9 \mu\text{s}$, the width of one time bin in both the delayed counting experiment and likelihood analysis. The expected rate for this component is derived from the excess seen in the no-water data, the ratio of beam exposure and the ratio of expected BRN rates between the no-water and full-shielded data. The predicted energy and F_{90} distributions are identical to the prompt BRN predictions due to the small statistics of the delayed no-water sample.

BEAM-UNRELATED BACKGROUND PREDICTION

The predicted beam-related background is measured from the off-beam triggered data. The event quality cuts are applied to the sample, as well as the energy and F_{90} cuts. As in the no-water analysis, a larger 25- μs DAQ window allows for increased statistics, again as the beam-unrelated background is measured to be relatively flat with respect to t_{trig} as shown in Fig. 6.1. The rate is then scaled down to the window being considered in the analysis to form the final beam-unrelated background prediction.

Single-bin Counting Experiment Rates		
Sample	Prompt	Delayed
N_{CEvNS}	52	52
N_{BRN}	453	18
N_{ss}	454	1075

Table 7.2: Predicted signal/background rates for the full shielded data single-bin counting experiment.

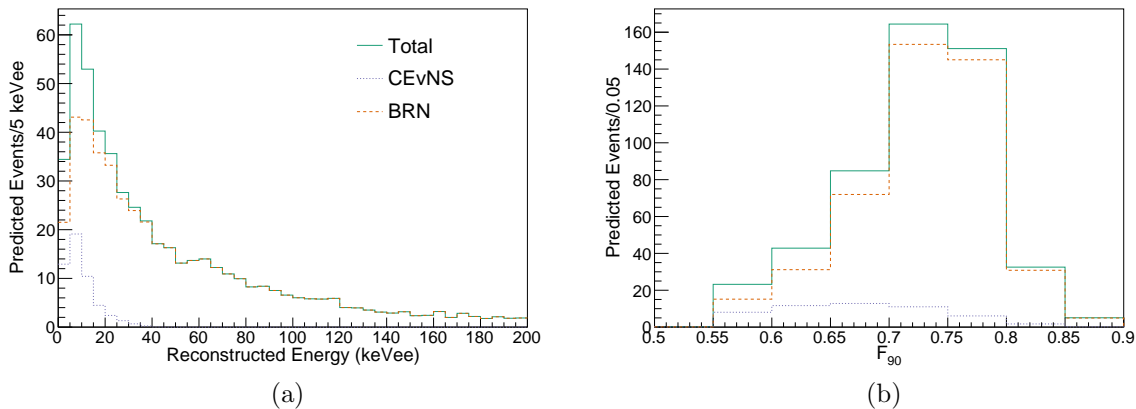


Figure 7.1: MC predictions for the prompt window CEvNS and BRN distribution in (a) energy and (b) F_{90} .

SUMMARY

The predicted rates for the CEvNS and BRN backgrounds in the prompt and delayed window are summarized in Tab. 7.2. The prompt(delayed) energy and F_{90} MC predicted CEvNS and BRN distributions are shown in Fig. 7.1(Fig. 7.2).

7.3.2 RATE SYSTEMATIC EFFECTS

Systematics are considered on the overall CEvNS predicted rate by creating alternative distributions from $\pm 1\sigma$ excursions. The largest change in the accepted number of events from a given excursion is computed as the systematic error on that parameter. The quenching factor, energy calibration, detector model, F_{90} , and event acceptance systematics are computed in the same way as in Sec. 6.6.1 and are not described again here. Further systematics on the fiducial volume,

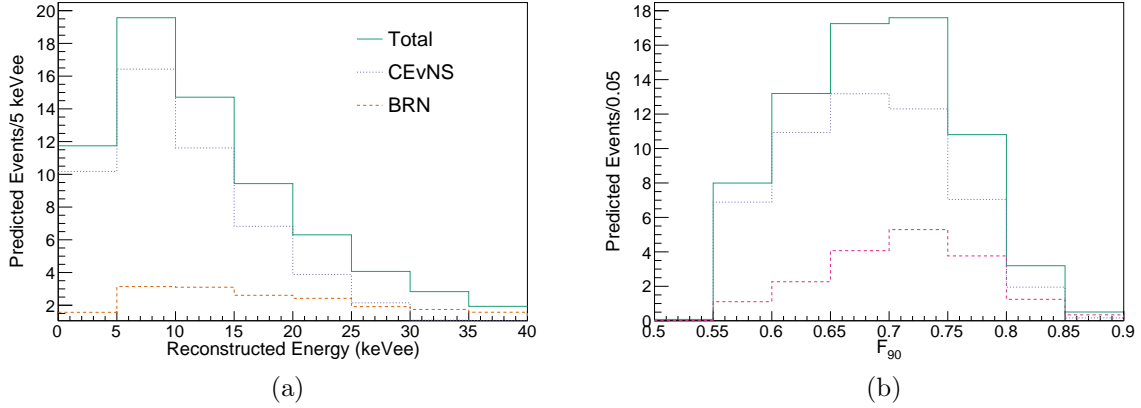


Figure 7.2: MC predictions for the delayed window CEvNS and BRN distribution in (a) energy and (b) F_{90} .

nuclear form factor, and neutrino flux are considered and described within this section.

ACTIVE VOLUME

An active detector volume error is estimated from the geometry of the active volume in the inner detector. The volume enclosed by the PMTs and the Teflon cylinders defines the active volume. Assigning a 1 mm error on the machined Teflon cylinders and applying available errors on the PMT dimensions from Hamamatsu, a 2.5% error is assigned to the active detector volume. The relative change in CEvNS events resulting from this error is equal to the relative error on the active volume.

FORM FACTOR

An uncertainty on the form factor is estimated by creating alternative CEvNS recoil spectra with the neutron radius value adjusted by $\pm 3\%$. This shift is derived from the uncertainties in measurements of the neutron skin such as from PREX.

CEvNS Rate Measurement Systematic Errors	
Error Source	Total Event Uncertainty
Quenching Factor	1.0%
Energy Calibration	0.8%
Detector Model	2.2%
F_{90}	7.8%
Active Volume	2.5%
Event Acceptance	1.0%
Nuclear Form Factor	2.0%
SNS Predicted Neutrino Flux	10%
Total Error	13.4%

Table 7.3: Measured systematics that only affect the overall CEvNS rate. Further systematics that affect the 3D likelihood pdf shape are considered during the likelihood analysis.

NEUTRINO FLUX

The neutrino flux systematic is taken from the uncertainty in the neutrino flux from the SNS simulations with different GEANT4 pre-compiled physics lists. The simulation and the resulting error is described in Sec. 2.1.1. The neutrino flux error is included as a flat 10% error on the CEvNS prediction, as it constitutes a normalization error on the CEvNS recoil spectrum.

TOTAL PREDICTED RATE SYSTEMATIC ERROR

The total contribution after computing the effect on the CEvNS rate predictions for each systematic is given in Table 7.3.

7.3.3 PRE-UNBLINDING CHECKS

Before unblinding the full-shielded on-beam data, checks are made for any unexpected time dependence in either the off-beam data or the prompt neutron rate over the ~ 1.5 year period of the run. Both the off-beam data and the prompt neutron rate are not expected to exhibit any time dependence. The beam-related neutron MC is compared to the data in a high-energy regime where there is no CEvNS signal expected to test the MC prediction. Further, a pre-beam window similar

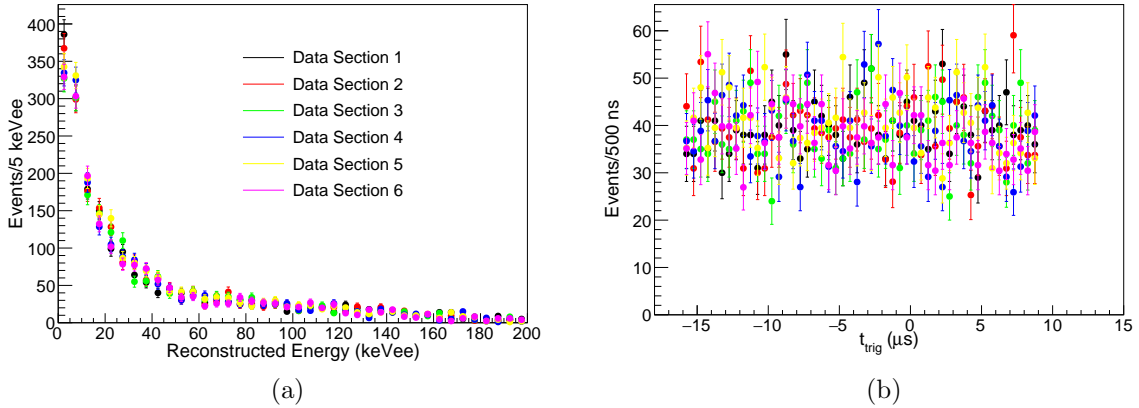


Figure 7.3: For six beam-power equivalent subsets of the CENNS-10 dataset, the (a) energy and (b) time relative to trigger (t_{trig}). In either case, there is no dependence seen in the distribution on the data subset. The t_{trig} distribution also shows no evidence of a dependence on the location of the event in the window for the off-beam triggered data.

to the one in Chapter 6 with respect to t_{trig} is analyzed to confirm the off-beam data subtraction did not show a significant excess in this window.

TIME DEPENDENCE OVER RUN PERIOD

To check for time dependence in the data, the entire dataset is split into six 1.02 GWhr equivalent subsets in both the on-beam and off-beam triggers after applying the event selection cuts described in Sec. 7.2 for the single-bin counting experiment. There is no time dependence in the off-beam data over the run period and the event time relative to the trigger, t_{trig} , is also relatively constant for the off-beam data as seen in Fig. 7.3.

Next, a pre-beam window from $-4.1 < t_{\text{trig}} < -0.6 \mu\text{s}$ checks for any excess away from the beam spill. An equivalent pre-beam window length to the delayed region ($3.5 \mu\text{s}$) provides similar beam data statistics. The off-beam data subtraction is performed in this window to compute the subtracted residual. The results (Fig. 7.4 show no significant excess in any data section and the measured residual in the entire dataset is 5 ± 43 with a fit of a constant value of 0 to Fig. 7.4 yielding a χ^2/dof of 8.3/5.

Lastly, the BRN rate in the prompt window is checked for any time dependence. In order to

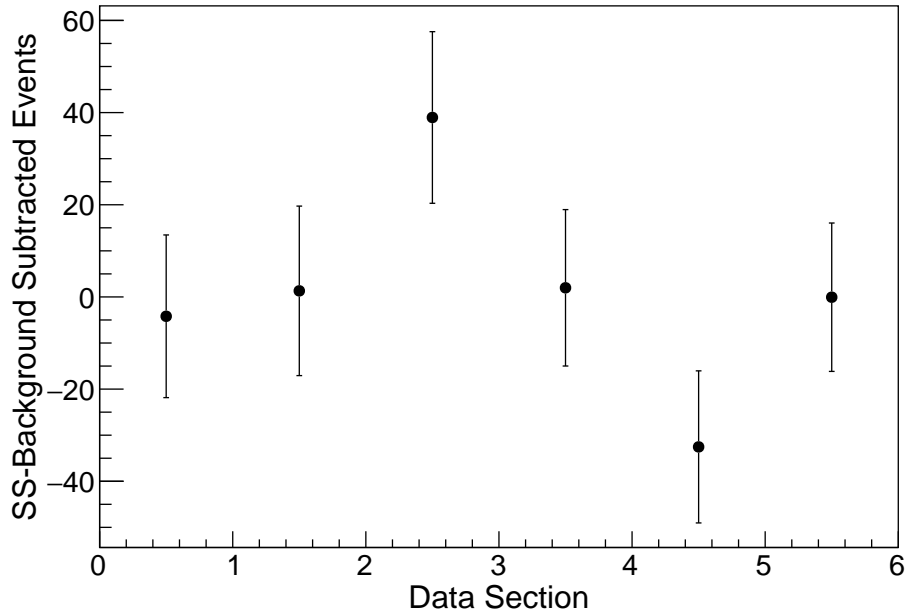


Figure 7.4: Residuals in a pre-beam ($-4.1 < t_{\text{trig}} < -0.6 \mu\text{s}$) window for the six subsets of the CENNS-10 dataset. There is no evidence of an excess in this window. A fit to a constant at 0 yields a χ^2/dof of 8.3/5. The total measured excess over the entire dataset is 5 ± 43 and is within errors of zero.

maintain blindness at this time, the measured excess in each data subset is computed as a fraction of the excess measured in the first data subset, which by this procedure is equal to one. Computing a ratio without knowledge of the absolute rates allows a check for time dependence maintaining blindness. There is no evidence for time dependence of the BRN rate in the data (Fig. 7.5). A constant fit to a ratio of one to the five data subsets that are scaled relative to the first subset yields a χ^2/dof of 4.2/4.

HIGH-ENERGY SIDEBAND

After the time dependence checks, a further check on a high-energy sideband of the full-shielded dataset validates the BRN simulation predictions. The high-energy sideband contains data from $40 < E_{\text{reco}} < 120 \text{ keVee}$ where the detector response is linear (Fig. 4.8) and a negligible CEvNS contribution. The measured excess at high energy is compared to the beam-related neutron predictions after applying the event selection cuts described in Sec. 7.2 to the full dataset and performing

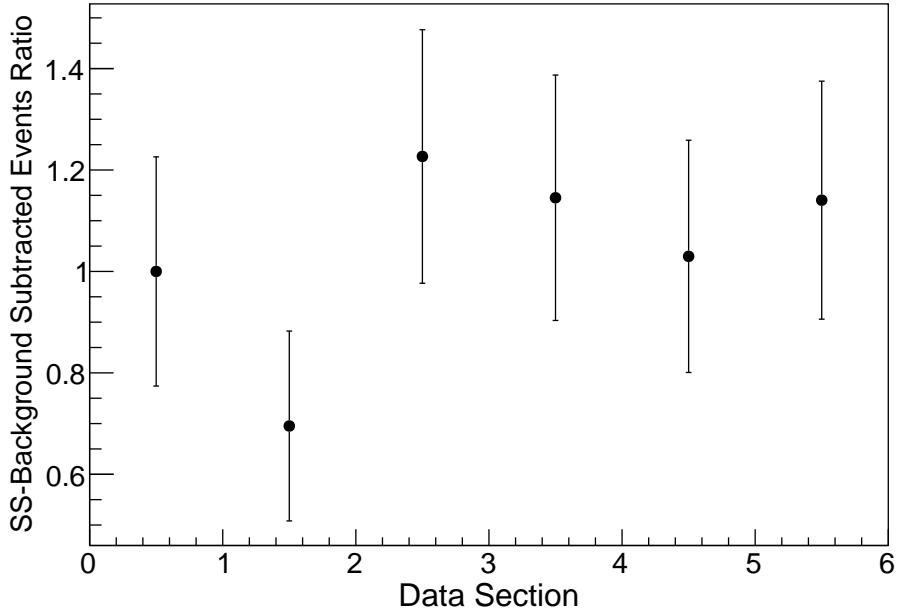


Figure 7.5: Prompt window excess in the six data subsets as a ratio of the computed excess in the first subset in order to maintain data blindness. There is no time dependence seen in the data.

Counting Experiment Results, Prompt Window, $40 < E_{reco} < 120$ keVee	
On-beam Events	269 ± 16
Off-beam Events	111 ± 2
Residual	159 ± 16
Predicted Residual	175 ± 58

Table 7.4: Results of a high-energy sideband meant to test the MC predictions before proceeding to the single-bin counting experiment. The measured excess agrees with the BRN predictions.

the steady-state background subtraction.

As seen in Tab. 7.4, the measured off-beam subtracted excess of 159 ± 17 agrees with the beam-related neutron MC prediction of 176 ± 58 within 1σ . The predicted beam-related neutron MC agrees well with the high-energy data in energy and F_{90} space (Fig. 7.6). The large error ($\sim 30\%$) on the MC prediction is dominated by the measured errors from the Engineering Run results in [82, 83]. The main error on the BRN MC prediction represents the uncertainty in the procedure described in Chapter 6 where the flux normalization for the beam-related neutron MC prediction from the no-water data is propagated to the full-shielded MC.

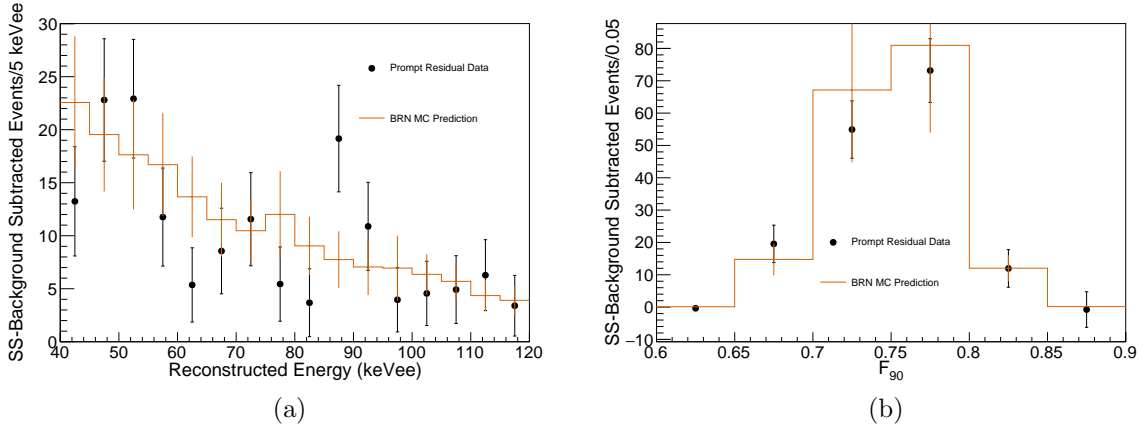


Figure 7.6: Results of the high energy sideband comparison with beam-related neutron MC in (a) energy and (b) F_{90} . The data agrees with the MC well within 1σ in both energy and F_{90} space.

Computing the correlated 2D χ^2 in energy space in the same manner as for the no-water data in Sec. 6.6.2 yields a χ^2/dof of 19.3/15. The measured excess in the high-energy sideband is consistent with the beam-related neutron simulation model.

A comparison of the timing distribution in this high energy sideband (Fig. 7.7) with the no-water data (Fig. 6.10) shows an excess earlier in time and with a smaller Gaussian width. A Gaussian fit in the prompt window of each dataset computes the best-fit mean and width values. After viewing this sideband, a selection of the no-water data is examined applying the same high-energy cut of $40 < E_{reco} < 120$ keVee. The high-energy sideband in the no-water data checks for any difference between the high energy regime and one that includes low-energy neutron interactions. Looking at the beam-related neutron timing information (Tab. 7.5) for all CENNS-10 datasets, the beam-related neutron time distribution mean is shifted earlier in time by 100 ns. A conservative error of ± 100 ns on the resulting BRN time distribution mean in the final analysis of the full dataset covers all measurements described in Tab. 7.5.

7.3.4 PROMPT REGION

In the prompt window ($0.4 < t_{\text{trig}} < 1.4 \mu\text{s}$), an equivalent energy window of $0 < E_{reco} < 200$ keVee as the no-water data is used as the excess is expected to largely consist of beam-related neutrons

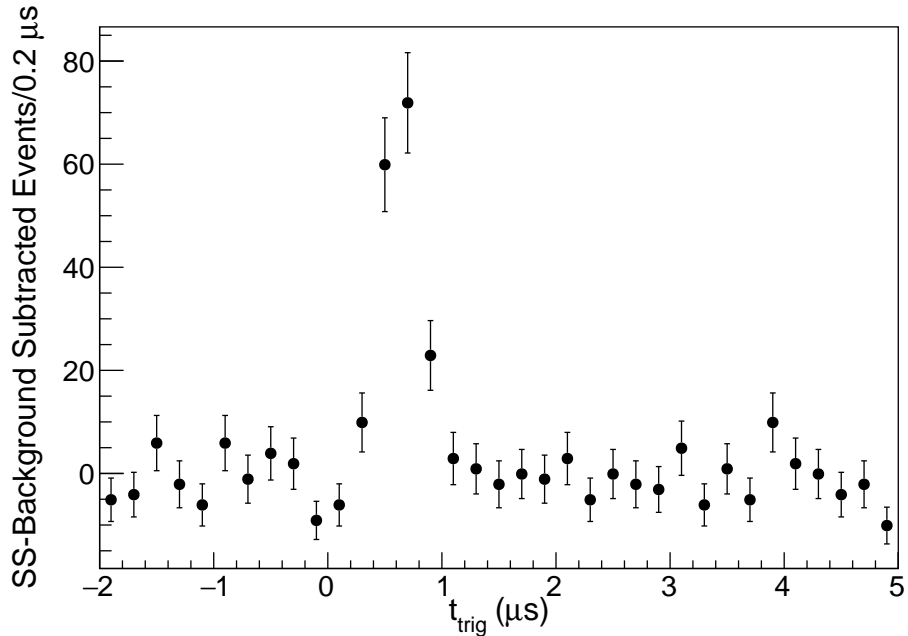


Figure 7.7: Distribution of excess events vs t_{trig} . There is a similar excess attributed to BRN seen in the high energy sideband. Fitting the prompt window with a Gaussian yields an earlier mean value and a smaller width than the no-water data. The measured width agrees with the width of the SNS POT trace.

Configuration	Energy Range	BRN Timing Mean (ns)	BRN Timing Width (ns)
No-water	0-200 keVee	808	257
No-water	40-120 keVee	754	212
Full-shield	40-120 keVee	630	146

Table 7.5: Measured means and widths of Gaussian fits to the no-water data and the high-energy sideband. From these measurements, the BRN MC timing distribution is shifted with a 100 ns conservative error to account for all possibilities.

in this window. After performing the off-beam subtraction an excess of 579 ± 34 events is seen in the data (Fig. 7.8). The error on the beam-related excess combines the errors on the number of on-beam and off-beam events in Tab. 7.6.

The measured excess in the prompt region contains a mixture of both the BRN background and CEvNS signal. Due to the large uncertainty assigned to the BRN prediction from the scaling procedure, this analysis does not have the power to separate the CEvNS signal from the BRN backgrounds. The measured excess is within the uncertainty assigned to the BRN prediction.

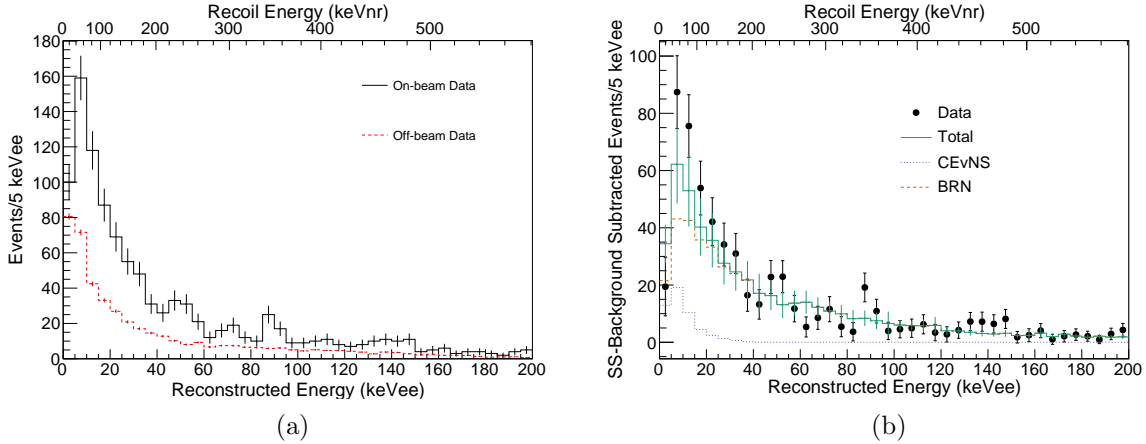


Figure 7.8: Results of an analysis of the full-shielded data in the prompt on-beam window. (a) Distribution of on-beam and off-beam triggers. Note the off-beam distribution is generated from a larger window to reduce statistical fluctuations. (b) Distribution of events after subtraction of off-beam data. The shape of the excess is consistent with the initial BRN predictions.

Counting Experiment Results, Prompt Window < 200 keVee	
On-beam Events	1033 ± 32
Off-beam Events	454 ± 10
Residual	579 ± 34
Predicted Residual	504 ± 152

Table 7.6: Results of the single-bin counting experiment in the prompt window. The measured excess agrees with the MC prediction, but is dominated by the presence of the BRN background and the CEvNS component cannot be directly extracted.

However, this region further compares the MC prediction to the data before moving to the 3D likelihood analysis. The resulting χ^2/ndf value is 34.1/39 performing the same 2D χ^2 analysis described in Sec. 6.6.2. The results of the counting experiment in the prompt window are given in Tab. 7.6.

7.3.5 DELAYED REGION

In the delayed window ($1.4 < t_{\text{trig}} < 4.9 \mu\text{s}$), a reduced energy range of $0 < E_{\text{reco}} < 40$ keVee provides for a more optimal CEvNS search. Once again, the same PSD cut from Fig. 6.2 is applied to this data. An excess of 45 ± 36 events is seen above the steady-state background after performing the off-beam subtraction. The 1.3σ excess above steady-state background is consistent with the

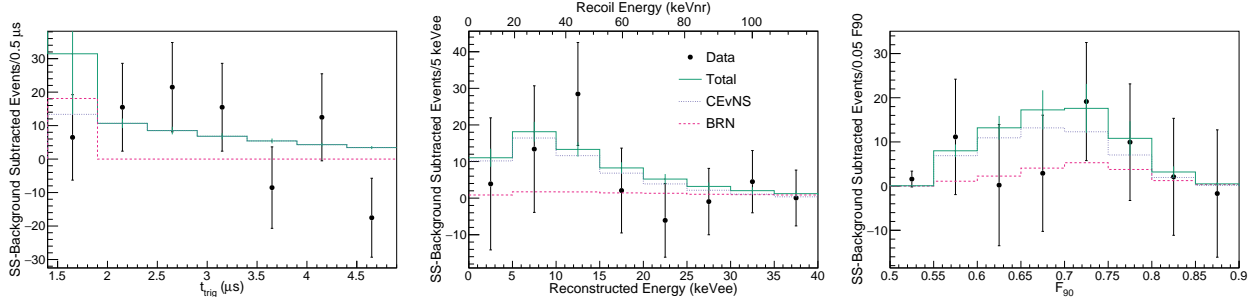


Figure 7.9: Projection of the counting experiment results in the delayed window on t_{trig} (left), reconstructed energy (center), and F_{90} (right). The steady-state background has been subtracted to better show the CEvNS component. The measured excess agrees well with the MC prediction, which largely consists of CEvNS.

Counting Experiment Results, Delayed Window $E_{\text{reco}} < 40$ keVee	
On-beam Events	1120 ± 34
Off-beam Events	1075 ± 14
Residual	45 ± 36
Predicted Residual	71

Table 7.7: Results of the single-bin counting experiment in the delayed region. The measured excess is consistent with the MC prediction, mainly CEvNS. A 1.3σ excess is seen in this dataset. The subsequent 3D likelihood analysis contains more statistical power as it can resolve the shape differences in the different components.

MC prediction, largely CEvNS. The subsequent likelihood analysis, with its ability to include both prompt and delayed regions and better resolve CEvNS from the backgrounds, provides a more statistically powerful result.

The residual shown in energy, F_{90} , and time in Fig. 7.9 represents the main results of the single-bin counting analysis. The results of the counting experiment in the delayed window are given in Tab. 7.7. Using this analysis, it is not possible to resolve whether any part of the delayed signal is consistent with beam-related neutrons. The results of this analysis provide confidence in the likelihood analysis as even with this simple analysis, an excess is seen which is consistent with the CEvNS prediction.

7.4 3D BINNED LIKELIHOOD ANALYSIS

A binned 3D maximum likelihood fit in energy, F_{90} and time is also performed on the full-shielded dataset. The likelihood fit is more powerful than the counting experiment as it applies the 3D shape information of the signal/background prediction probability density functions (pdfs) and the data to better resolve the CEvNS signal from the backgrounds. The likelihood analysis uses the RooFit framework [145] to perform the final fit with the predicted rates and pdfs as described in Sec. 7.4.1. Pseudo-data sets are generated from the central-value pdfs and a range of systematic excursion pdfs to validate the likelihood fit machinery and evaluate systematics. The final fit is performed on the full-shielded on-beam data to extract the CEvNS rate from the data and the overall significance of the result.

An extended binned maximum likelihood analysis is performed and the best fit result is obtained by minimizing the log-likelihood test statistic. For an expected number of events in a given set of parameters $\nu(\boldsymbol{\theta})$ in the extended maximum likelihood formalism, the log-likelihood is [146]

$$\ln L(\boldsymbol{\theta}) = -\nu(\boldsymbol{\theta}) + \sum_{i=1}^n \ln(\nu(\boldsymbol{\theta})f(x_i; \boldsymbol{\theta})) \quad (7.1)$$

where f is the pdf of the parameter set $\boldsymbol{\theta}$ in the i th variable x_i .

7.4.1 PDF GENERATION

The pdfs for the likelihood analysis are formed in roughly the same manner as in Sec. 7.3.1. The chosen range in the three dimensions is largely meant to maximize the ability of the fit to distinguish the CEvNS signal from the BRN and steady state backgrounds. The main difference is the use of expanded cuts in F_{90} space. This section describes the ranges used in the three fit dimensions energy, F_{90} , and time and the generated pdfs for the CEvNS signal and backgrounds.

A range of $-0.1 < t_{\text{trig}} < 4.9 \mu\text{s}$ with a $0.5 \mu\text{s}$ bin width defines the time space for the likelihood analysis. For this analysis, $-0.1 < t_{\text{trig}} < 1.4 \mu\text{s}$ defines the prompt window and the

delayed window is $1.4 < t_{\text{trig}} < 4.9 \mu\text{s}$. These are mainly descriptive definitions when describing the BRN background pdfs as the entire time range without separation into these windows is used in the final likelihood fit. Due to the uncertainty in the neutrino timing, the additional $0.5 \mu\text{s}$ bin before the definition of the prompt window used in Sec. 6.1 is included in the likelihood analysis. The end of the delayed window, which optimized \mathcal{F} , remains the same from the counting experiment. This time window allows for characterization of CEvNS and BRN in the prompt window, while providing a largely BRN-free delayed window for the CEvNS signal.

A range of $0 < E_{\text{reco}} < 120 \text{ keVee}$ with a 10 keVee bin width defines the energy space for the likelihood fit. The CEvNS signal is expected $\leq 40 \text{ keVee}$, but a larger window better constrains the BRN background. The maximum energy is chosen to restrict the fit range to where the detector response is linear (Fig. 4.8). Restricting to this energy range provides an ample region to characterize the BRN background while allowing the CEvNS signal to be present in multiple bins in the fit.

A range of $0.5 < F_{90} < 0.9$ with a bin size of $0.05 F_{90}$ defines the PSD space for the likelihood fit. Although the likelihood fit can theoretically include the entire F_{90} space, the application of a lower bound eliminates the concern of correctly modeling the beam-related electron recoil distribution. The issue in expanding the F_{90} space is the uncertainty of neutron inelastic cross sections on argon in GEANT4, which produce electron recoil events. The upper bound is retained to remove the events with high F_{90} values at low energy in the AmBe data (Fig. 4.20) which are beam-unrelated and theorized to be Cherenkov in origin. Extensive modeling of these events is not considered as part of this analysis and is the main reason for a hard cut to remove them. The CEvNS signal is not expected to be present in this region so this cut does not have a negative effect and removes a possible source of background.

With these ranges, the full 3D likelihood fit is performed over a total of 960 bins. The 3D pdfs used in the likelihood analysis are generated using the defined ranges in energy, F_{90} , and time. The CEvNS and BRN pdfs are generated from the MC while the beam-unrelated background pdf is

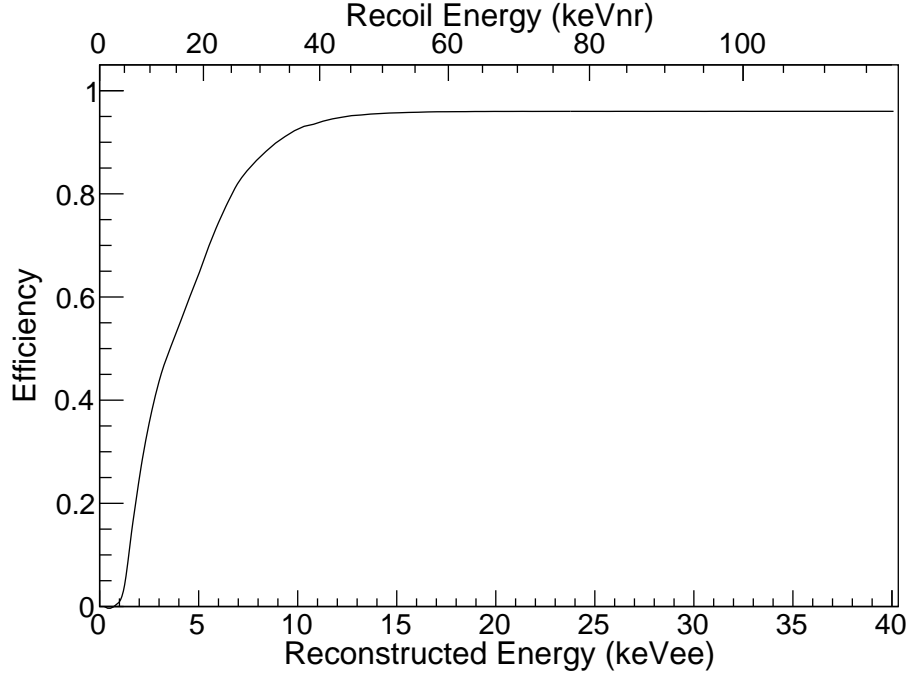


Figure 7.10: Predicted efficiency curve used for the likelihood analysis of the full-shielded data. The CEvNS region of interest is shown and the efficiency curve is flat at energy values greater than those shown in the figure.

generated from the off-beam triggered data. For the MC-generated pdfs, the same efficiencies are applied from Sec. 5.5. The efficiency curve applying the full likelihood cuts is shown in Fig. 7.10.

CEvNS PDF

The CEvNS pdf is generated in the same manner as the predictions in Sec. 7.3.1. The time, energy, and F_{90} likelihood analysis cuts are applied to the MC. For the likelihood fit, the fit is not directly separated into a prompt and delayed component, so these regions are not distinguished by separate distributions. The components of the CEvNS pdf are shown in Fig. 7.11 and the 3D pdf is formed by convolving the time distribution with the energy: F_{90} distribution.

PROMPT BEAM RELATED NEUTRON PDF

The prompt BRN pdf is also generated in the same manner as in Sec. 7.3.1, with the likelihood cuts in energy, F_{90} , and time being applied to the MC predictions. The prompt BRN pdf includes

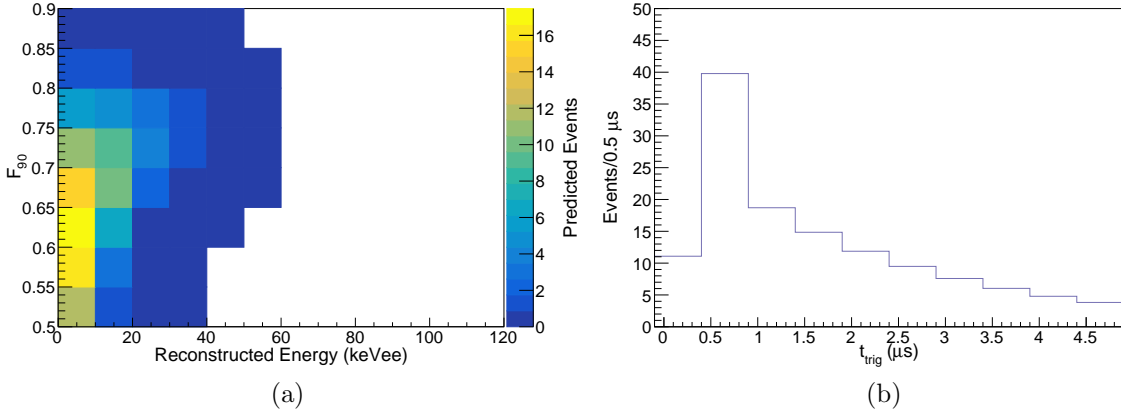


Figure 7.11: Components of the SM predicted CEvNS pdf from the MC used in the binned likelihood analysis. (a) Energy vs F_{90} distribution, (b) Time distribution

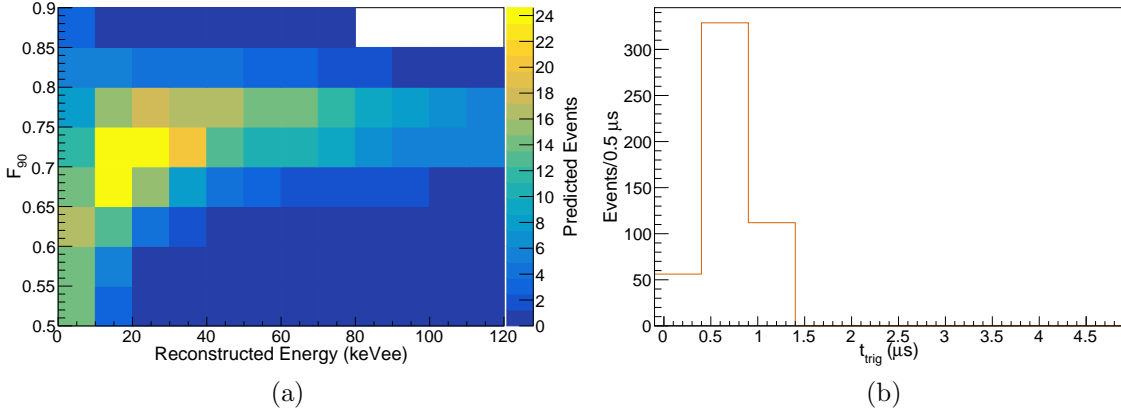


Figure 7.12: Components of the predicted BRN pdf from the MC used in the binned likelihood analysis. (a) Energy vs F_{90} distribution, (b) Time distribution.

the time range of $-0.1 < t_{\text{trig}} < 1.4 \mu\text{s}$ and a separate pdf is considered for the delayed BRN pdf as in the single-bin counting experiment.

STEADY-STATE BACKGROUND PDF

For the steady-state background pdf, the larger $25 \mu\text{s}$ DAQ window is again considered and scaled to the length of the time window considered in the likelihood fit for higher statistics. The measured off-beam data forms the 2D energy: F_{90} distribution in the pdf. To form the 3D pdf, the energy: F_{90} distribution is convolved with a uniform time distribution. From the measured rates in the off-

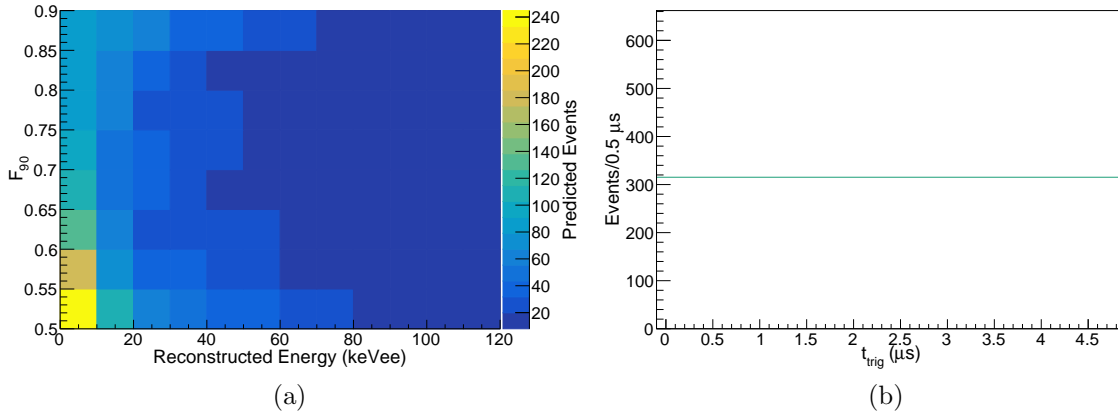


Figure 7.13: Components of the beam-unrelated background pdf from the measured off-beam data in the binned likelihood analysis. (a) Energy vs F_{90} distribution taken directly from the measured off-beam data. (b) Time distribution. The time distribution is uniform based on the evidence that the t_{trig} distribution is relatively uniform in the DAQ window.

beam data with the binning considered in this analysis, there is no concern over large relative statistical errors in a single bin.

BEAM RELATED NEUTRON PDF IN DELAYED WINDOW

The no-water result in the time bin from $1.4 < t_{\text{trig}} < 1.9 \mu\text{s}$ places an upper limit on the predicted number of BRN in that bin. The same methodology from Sec. 7.3.1 is applied to compute the delayed BRN contribution in the single-bin counting analysis. The energy: F_{90} pdf is identical to the prompt BRN pdf with the entire predicted value placed in the first time bin outside the prompt window. The components of the delayed BRN pdf are shown in Fig. 7.14.

PDF NORMALIZATION CONSTRAINTS

In addition to the 3D pdfs that make up the data, normalization constraints on some distributions based on the known uncertainties are added to the likelihood function in the form of Gaussian penalty functions. The addition of the Gaussian constraints modifies the likelihood function in

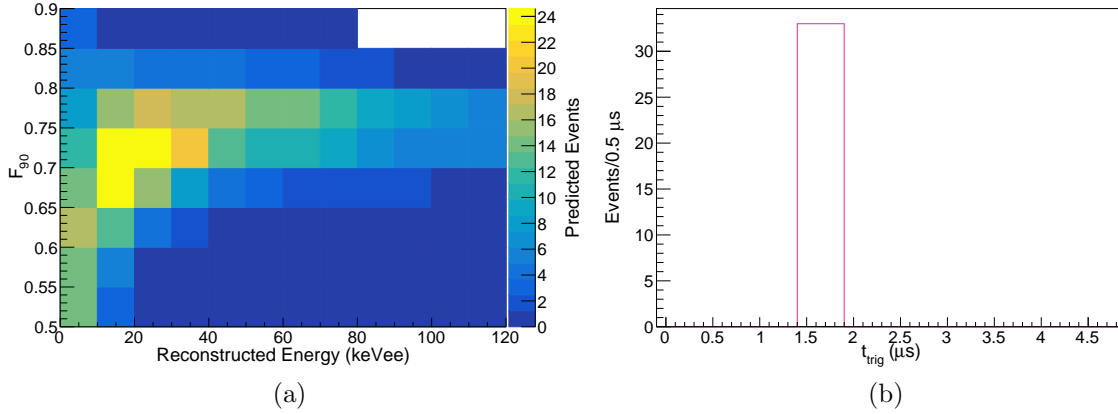


Figure 7.14: Components of the predicted delayed BRN pdf from the MC used in the binned likelihood analysis. (a) Energy vs F_{90} distribution, which is identical to the prompt BRN pdf. (b) Time distribution, which is restricted to the first delayed time bin $1.4 < t_{\text{trig}} < 1.9 \mu\text{s}$.

Eqn. 7.1 to the following:

$$\ln L(\boldsymbol{\theta}) = -\nu(\boldsymbol{\theta}) + \sum_{i=1}^n \ln(\nu(\boldsymbol{\theta}) f(x_i; \boldsymbol{\theta})) - \frac{1}{2} \sum_j \frac{(\nu(\theta_j) - \bar{\nu}(\theta_j))^2}{\sigma_j^2} \quad (7.2)$$

where $\nu(\theta_j)$ represents the number of events in the j th parameter and σ_j is the Gaussian width associated with that constraint.

The systematic uncertainty on the BRN rate dominated by the uncertainty in the SciBath flux normalization scaling procedure sets the prompt BRN pdf constraint width. Agreement of the predicted rate with zero sets the 1σ constraint on the delayed BRN pdf as there are no prior measurements that confirm a non-zero delayed BRN signal in Neutrino Alley. The likelihood fit provides a separate measurement of that component. The statistical error from the oversampling of the off-beam data relative to the time window in the fit sets the beam-unrelated background pdf constraint width. The oversampling reduces the associated statistical error in that measurement. The CEvNS signal is unconstrained and allowed to freely float during the fit.

Likelihood Fit Predicted Rates	
Predicted SM CEvNS (N_{CEvNS})	128
Predicted Prompt BRN (N_{brn})	497 ± 160
Predicted Beam-unrelated Background (N_{ss})	3154 ± 25
Predicted Delayed BRN (N_{delbrn})	33 ± 33

Table 7.8: Predicted rates for the component pdfs used in the likelihood analysis. Note that the errors given in this table represent the width of a gaussian constraint given on the normalization in the fit.

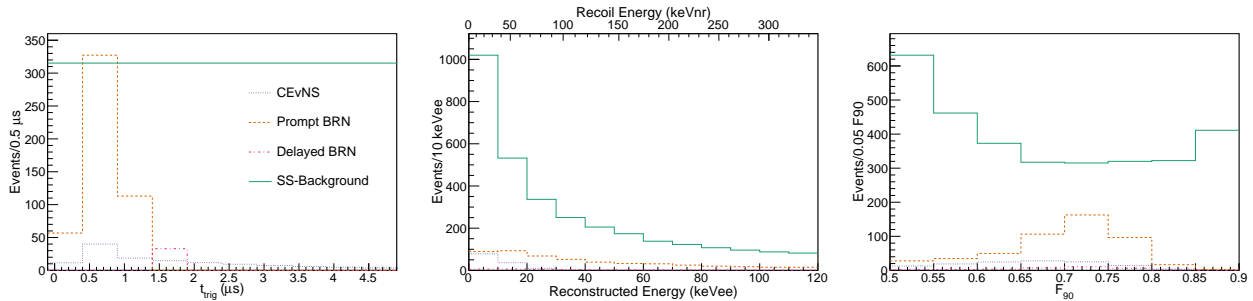


Figure 7.15: Projection of the likelihood fit pdfs on t_{trig} (left), reconstructed energy (center), and F_{90} (right) including all cuts for all pdfs included in the likelihood fit. Note when performing the fit, the full 3D information is considered, the projections here are for clarity.

SUMMARY OF RATES

The summary of expected rates after all cuts for the central-value pdfs is shown in Tab. 7.8. Note where quoted, the error on the expected rate of a parameter represents the width of the Gaussian constraint in the likelihood fit.

Fig. 7.15 shows the 1D projections in time, energy, and F_{90} space of the 3D fit. Fig. 7.16 are the same projections removing the beam-unrelated background so the CEvNS and BRN are more easily seen.

7.4.2 PSEUDO-DATA STUDIES

Pseudo-data sets generated from the central-value (CV) pdfs shown in Fig. 7.15 are used to validate the likelihood fit code and perform CEvNS sensitivity studies. To test for any bias in the likelihood fit, the pseudo-data sets are fit with the central-value pdfs using the binned maximum likelihood

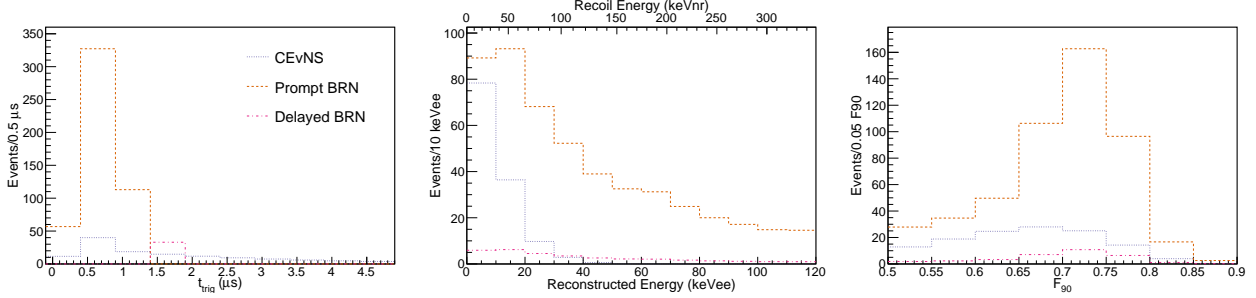


Figure 7.16: Projection of the likelihood fit pdfs on t_{trig} (left), reconstructed energy (center), and F_{90} (right) including all cuts for the CEvNS and BRN components. The beam-unrelated background is not plotted here to better show the CEvNS component.

Parameter	CV Prediction	Mean Best-fit Value	Best-fit RMS
CEvNS	128	128	43
Prompt BRN	497	498	38
Beam-unrelated Background	3154	3154	9

Table 7.9: Results of pseudo-data studies used to test likelihood code for reconstruction bias. The results show the mean best-fit values agree with the central-value predictions.

framework. Performing the likelihood fit with both an unbinned and a binned pseudo-data set checks that using a binned pdf in the fit reduces to a binned likelihood irrespective of the pseudo-data set. The results show no difference in the mean best-fit values with either binned or unbinned pseudo-data sets.

A sample of 10000 pseudo-data sets are generated and fit with the likelihood framework to provide a robust sample size for the central value fit test. As seen in Tab. 7.9, the mean value of the likelihood fit does reconstruct the central-value prediction within the statistical error of the number of pseudo-data sets generated. The RMS value of the distributions gives a good sense of the level of statistical error resulting from the fit to the on-beam data. Fig. 7.17 shows the resulting distributions of the best-fit values for each parameter and the corresponding spread in the results. This study shows that the expectation for this measurement is a $\sim 30\%$ statistical error on the ultimate fit result, based upon the CEvNS signal rate, background rates and the resulting RMS of the best-fit CEvNS distribution.

The null rejection significance of the CEvNS result is computed by comparing the best fit

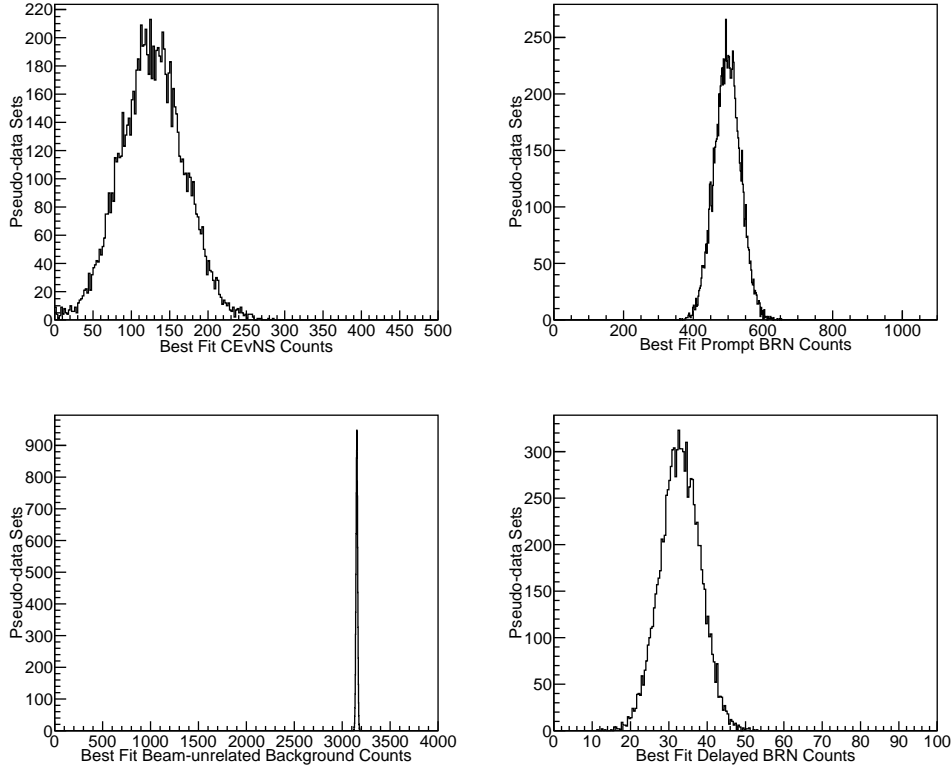


Figure 7.17: Distributions of best-fit results for the normalizations of the pdfs. A large number of pseudo-data sets are generated to reduce the statistical error on the mean value. The mean values of these distributions reconstruct to the central-value predictions, showing no bias is present in the fit machinery. The RMS values seen give a good indication of the magnitude of the statistical error on the parameters from the fit.

likelihood result assuming CEvNS to the null hypothesis ($N_{\text{CEvNS}} = 0$). The important calculation is the difference in the log-likelihood values between the best-fit result and a fit to the same pseudo-data set assuming the null hypothesis.

$$-2 \Delta(\ln L)_{\text{Null}} = -2 \ln L_{\text{Null}} - (-2 \ln L_{\text{Best}}) \quad (7.3)$$

where $\ln L_{\text{Null}}(\ln L_{\text{Best}})$ is the value of the log-likelihood for the null hypothesis (best-fit result). Following Wilks' Theorem [147], the value of $-2 \Delta(\ln L)$ is distributed as a χ^2 distribution with n degrees of freedom where n is the number of parameters profiled over in the fit. In this case, as only the CEvNS signal is profiled over, $n = 1$, and the significance can be computed from the p-value.

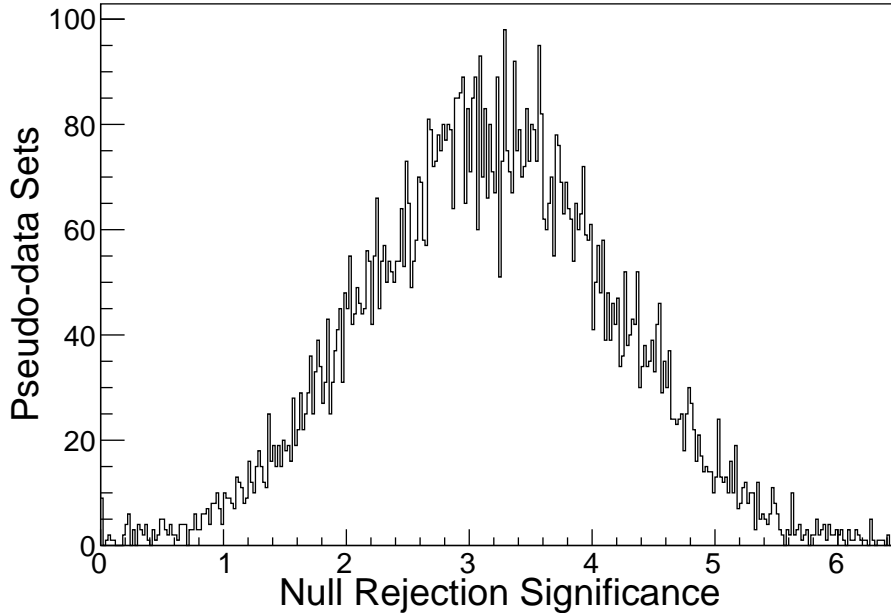


Figure 7.18: Distribution of significance values from the pseudo-data studies. The mean value of this distribution provides the central-value significance expectation for the on-beam data. The mean of this distribution is $> 3\sigma$.

The distribution of the significance values from the pseudo-data studies is seen in Fig. 7.18 and the mean significance for the presence of CEvNS in this dataset is $> 3\sigma$.

7.4.3 LIKELIHOOD FIT SYSTEMATIC ERRORS

Additionally, systematic errors on the best-fit CEvNS rate result from shape changes to the 3D central-value pdfs in energy, F_{90} , and time. The likelihood fit systematic errors are computed by first generating alternative $\pm 1\sigma$ excursion pdfs for each systematic. Then, pseudo-data sets are generated using the excursion pdf and fit with the central-value pdfs. As in the study using the central-value pdfs, a set of 10000 pseudo-data sets are fit for each systematic excursion study. The average difference between the mean best-fit value from the excursion pdf and the central value for a $\pm 1\sigma$ pair of excursion pdfs computes the systematic error from that source. The systematics that change the pdf shape substantially and are found to be non-negligible effects on the best-fit CEvNS rate are described here. The excursion method computes uncorrelated systematic errors

to the best-fit CEvNS rate.

CEvNS PSD SHAPE

The CEvNS energy: F_{90} pdf shape is adjusted in the same manner described in Sec. 6.6.1 and used to generate alternative pdfs. The $\pm 1\sigma$ excursions on the CEvNS F_{90} shape result in a systematic error of 4.5% on the best-fit CEvNS rate.

CEvNS TIMING DISTRIBUTION

A conservative uncertainty of ± 200 ns is assigned to the mean of the timing distribution in CEvNS pdf. The uncertainty is derived from a estimation of the neutrino timing based on the CsI[Na] CEvNS measurement. The applied uncertainty shifts the entire CEvNS distribution relative to t_{trig} . The choice of 500 ns bin widths in time mitigates the concerns about the lack of an absolute neutrino timing measurement. Alternative pdfs are generated using the arrival time mean shift. The $\pm 1\sigma$ excursions on the CEvNS timing result in a systematic error of 2.7% on the best-fit CEvNS rate.

BRN ENERGY SHAPE

A direct sum of the uncertainty from the quenching factor and detector energy calibration described in Sec. 6.6.1 is applied to account for uncertainties in the energy shape of the prompt BRN pdf. The value of Y_γ in the simulation is adjusted by $\pm 4.5\%$ for the $\pm 1\sigma$ alternative pdfs for the BRN energy shape systematic excursion. The $\pm 1\sigma$ excursions on the prompt BRN energy shape result in a systematic error of 5.8% on the best-fit CEvNS rate.

BRN ARRIVAL TIME

There are two systematics considered separately here, both the mean and the width of the prompt BRN arrival time are adjusted.

Likelihood Fit Shape-Related Errors	
Error Source	Fit Event Uncertainty
CEvNS F_{90}	4.5%
CEvNS Arrival Time Mean	2.7%
Beam-Related Neutron Energy Shape	5.8%
Beam-Related Neutron Arrival Time Mean	1.3%
Beam-Related Neutron Arrival Time Width	3.1%
Total Fit Systematic Error	8.5%

Table 7.10: Systematic errors applied to the best-fit CEvNS rate when the likelihood fit is performed on the on-beam data.

For the arrival time mean, an uncertainty on the prompt BRN timing mean of ± 100 ns is applied. This uncertainty covers the spread in measurements of the prompt BRN mean shown in Tab 7.5 from the no-water data and the high energy sideband of the full-shielded data. As with the CEvNS mean time systematic, this has the effect of shifting the distribution in time. Alternative pdfs are generated with the shift in the arrival time mean. The $\pm 1\sigma$ excursions on the prompt BRN arrival time mean result in a systematic error of 1.3% on the best-fit CEvNS rate.

For the width, only one excursion is performed and was included after the data was unblinded. The BRN pdf is regenerated with the Gaussian width of the distribution set to equal the width of the SNS POT pulse of ~ 150 ns. The excursion is driven by the measurements using SciBath and the CENNS-10 Engineering Run where the measured BRN width roughly agreed with the POT pulse with a higher energy threshold than this dataset. An alternative pdf is fit to the data with the adjusted timing width. The excursion on the prompt BRN arrival time width results in a systematic error of 3.1% on the best fit CEvNS rate.

SUMMARY OF SYSTEMATIC ERRORS

The systematic error applied to the best-fit CEvNS for each separate excursion is an average of the $\pm 1\sigma$ excursion results and are summarized in Tab 7.10.

With the systematic errors computed, a fit to the on-beam data can be performed.

7.4.4 FIT TO DATA

A sample of on-beam data is prepared applying the same energy, F_{90} , and time cuts as for the pdfs. Then the likelihood fit is run on the data supplying the central-value pdfs. As mentioned earlier, the CEvNS rate is unconstrained in the fit and allowed to float. The rates of the other pdfs (BRN, beam-unrelated background) are constrained during the fit with the constraints described in Sec. 7.4.1. To extract the best-fit CEvNS rate, a profile-likelihood fit is performed over the BRN and beam-unrelated background normalizations to form the distribution of the log-likelihood ratio $-2\Delta(\ln L)$, defined as:

$$-2\Delta(\ln L) = -2\ln L - (-2\ln L_{\text{Best}}) \quad (7.4)$$

The maximum likelihood analysis computes the difference in $-2\ln L$ values between the best fit and another point on the curve. Therefore the best fit value of $-2\Delta(\ln L)$ will be defined as zero. The statistics-only null rejection significance is extracted from the value of the $-2\Delta(\ln L)$ curve at $N_{\text{CEvNS}} = 0$, which replicates Eqn. 7.3 and computes the value of $-2\Delta(\ln L)_{\text{Null}}$. The $\pm 1\sigma$ statistical error on the fit CEvNS rate is extracted from the profile-likelihood curve from the bounds where the $-2\Delta(\ln L)$ value is equal to one, which from a χ^2 distribution with one degree of freedom provides the 1σ error.

Performing the likelihood fit on the data, the best fit CEvNS rate of $159 \pm 43(\text{stat.}) \pm 14(\text{syst.})$ events agrees with the central-value prediction from the SM of 128 events within 1σ . The measured rates of the CEvNS signal and background components from the likelihood fit are summarized in Tab. 7.11. From the value of $-2\Delta(\ln L)_{\text{Null}} = 15.0$, the data rejects the null CEvNS hypothesis at a significance of 3.9σ (stat. only). The profile-likelihood curve (Fig. 7.19) extracts the statistical error and the statistics-only null rejection significance. To include the systematic error from the likelihood fit into the null rejection significance, the statistical and systematic errors from Sec. 7.4.3 are added in quadrature and the combined error computes how many sigma the best-fit CEvNS rate is from zero. The combined statistical and systematic error produces a final null rejection

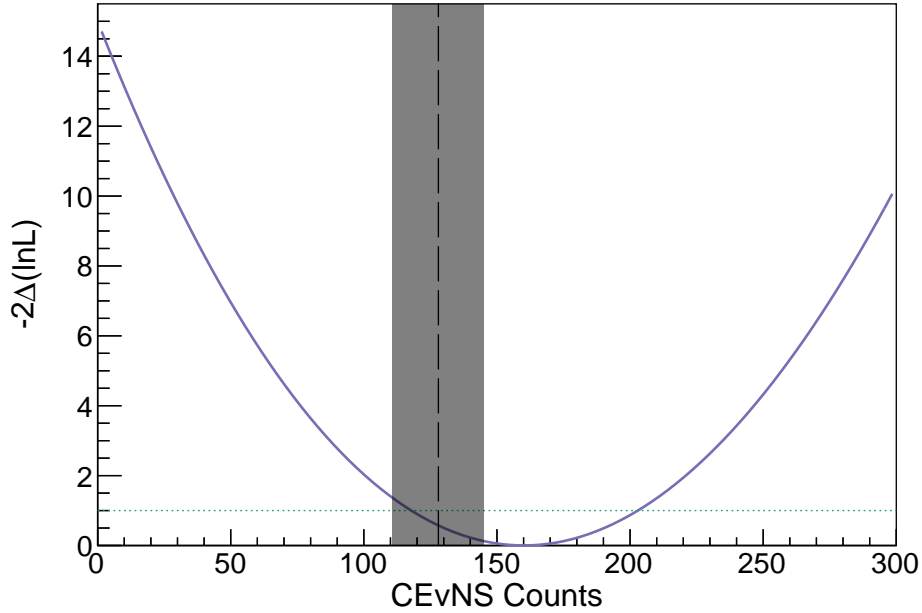


Figure 7.19: Profile-likelihood curve of the CEvNS signal. The best-fit CEvNS rate is extracted from the value of $-2\Delta(\ln L) = 0$ and the 1σ statistical errors from the value of $-2\Delta(\ln L) = 1$. The dashed line represents the SM prediction and the band around that is the total rate systematic error from Tab. 7.3. The measured CEvNS cross section includes this error. The measured CEvNS rate agrees with the SM prediction.

On-beam Data Event Sample	3752
Fit CEvNS	159 ± 43 (stat.) ± 14 (syst.)
Fit Beam Related Neutrons	553 ± 34
Fit Beam Unrelated Background	3131 ± 23
Fit Late Beam Related Neutrons	10 ± 11
$-2\Delta(\ln L)$	15.0
Null Rejection Significance	3.5σ (stat. + syst.)

Table 7.11: Results of the likelihood fit showing the best-fit rates for each component. A considerable excess of CEvNS is seen over background at $> 3\sigma$ significance. Also notable here is that the best-fit delayed BRN rate agrees within 1σ with zero, providing another measurement that is consistent with BRN only appearing in a prompt window around the SNS beam spill.

significance (stat. + syst.) of 3.5σ . The measured rates of the signal and background components of the likelihood fit are summarized in Tab. 7.11.

Projections of the likelihood fit result in time, energy, and F_{90} with the beam-unrelated background subtracted are shown in Fig. 7.20. In these projections, the prompt and delayed BRN

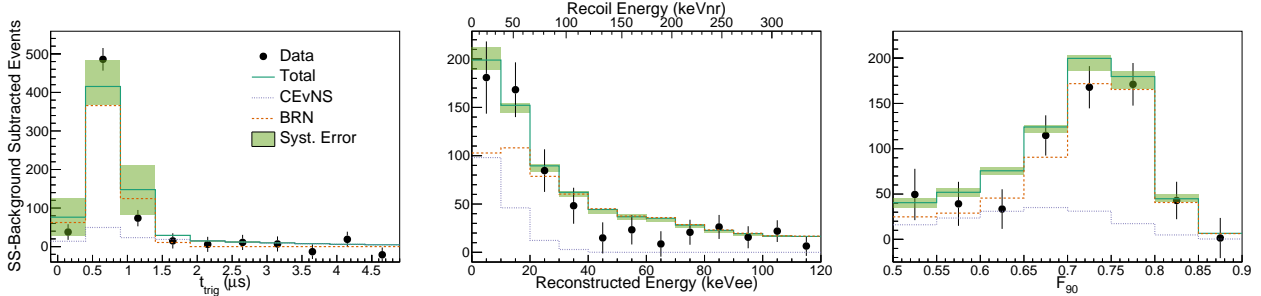


Figure 7.20: Projection of the maximum likelihood pdf function on t_{trig} (left), reconstructed energy (center), and F_{90} (right) along with data and statistical errors. The fit beam-unrelated background is subtracted to better show the CEvNS component. The green band shows the envelope of fit results resulting from the $\pm 1\sigma$ systematic errors on the pdf.

components, treated separately in the fit, are combined into one BRN distribution for clarity. The fit beam-unrelated background component is subtracted out to clearly show the CEvNS component. The envelope covered by the $\pm 1\sigma$ systematic errors in 3D is computed by fitting the alternative pdfs to the data and included in the projections of the data. The data is in good agreement with the fit result including the systematic errors. Note that although these are 1D projections, the likelihood fit takes into account the full 3D information.

The same projections as in Fig. 7.20 can be made using the results of the null hypothesis fit to check the difference between the best-fit and null hypothesis projections. In particular from the resulting projections of the null hypothesis fit, Fig. 7.21, the recoil energy distribution results in a poor fit without the presence of CEvNS. The presence of CEvNS fits the data well. From MC studies, the BRN energy shape is robust and not sensitive to errors in the quenching factor or flux shape. The BRN energy shape is also further constrained by the presence of the higher energy region where no CEvNS is present.

7.4.5 MEASUREMENT OF CEvNS CROSS SECTION

The flux-averaged CEvNS cross section for an argon nucleus is measured for the first time using the results of the likelihood fit. The flux-averaged SM cross section, computed from an average over the neutrino flux, the number of POT, the detector active mass, and the detector efficiency,

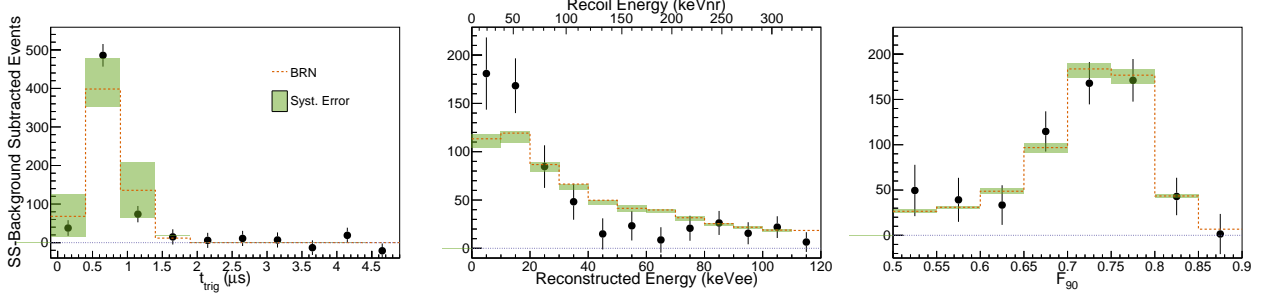


Figure 7.21: Projection of the null hypothesis fit on t_{trig} (left), reconstructed energy (center), and F_{90} (right) along with data and statistical errors. The fit beam-unrelated background is subtracted to better show the CEvNS component. The green band shows the envelope of fit results resulting from the $\pm 1\sigma$ systematic errors on the pdf. The fit is poor without the presence of CEvNS, especially in the recoil energy distribution.

is $\sigma_{\text{SM}} = 1.8 \times 10^{-39} \text{ cm}^2$. With the measured CEvNS rate from the likelihood fit, N_{meas} , and the predicted SM rate, N_{SM} , the measured CEvNS cross section can be computed as:

$$\sigma_{\text{meas}} = \frac{N_{\text{meas}}}{N_{\text{SM}}} \sigma_{\text{SM}} \quad (7.5)$$

The CEvNS rate systematic errors in Tab. 7.3 are applied as an error on N_{SM} . The measured CEvNS cross section is $\sigma_{\text{meas}} = (2.3 \pm 0.7) \times 10^{-39} \text{ cm}^2$, within 1σ of the SM prediction. The error on the cross section is dominated by the statistical error on N_{meas} . The additional systematic errors are from the fit systematic errors and systematic errors on flux, active mass, and detector efficiency. This measurement verifies the N^2 dependence of the CEvNS cross section (Fig. 7.22) after the CsI[Na] measurement.

PARALLEL ANALYSIS RESULTS

A second, parallel analysis is performed on this dataset within the COHERENT collaboration as a crosscheck on the result presented in this work. Major results were not shared between the two groups before analysis cuts were finalized and the likelihood analyses were complete. The parallel analysis used a similar analysis strategy to this work and the main result is also a best-fit CEvNS rate from a likelihood fit using a similar framework to the one presented here. The parallel

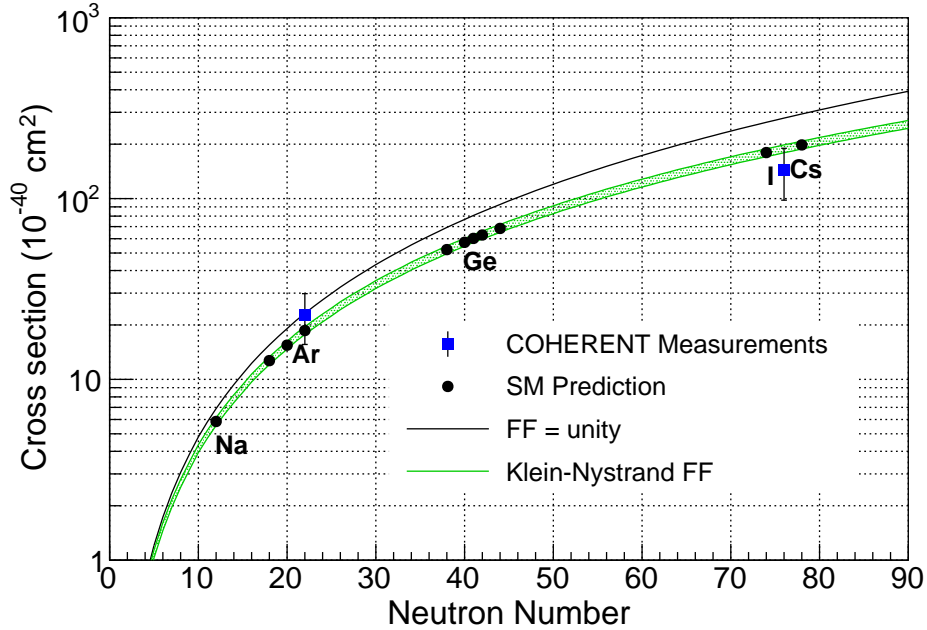


Figure 7.22: CEvNS cross section vs neutron number including the CENNS-10 measurement presented in this work. The COHERENT data points from this work and the earlier CsI[Na] measurement are shown as the blue points with associated error bars. The measurement is consistent with the SM-predicted N^2 dependence of the CEvNS cross section after the previous CsI[Na] measurement. These results provide a measurement of CEvNS on the lightest nuclei to date. The black lines shows the cross section assuming a nuclear form factor equal to unity. The green band represents the Klein-Nystrand [7] model used in this analysis with a $\pm 3\%$ adjustment to the neutron radius R_n .

analysis used different fit ranges and efficiency due to distinctive signal/background optimization philosophies.

The parallel analysis includes a more stringent energy cut in the likelihood analysis and an additional cut on f_{top} to remove events close to the the PMTs. A very similar set of systematics on N_{CEvNS} are evaluated, with differences in the size of these errors due to the more stringent cuts. For example, the more stringent energy cut causes a smaller F_{90} systematic but a larger systematic from the energy calibration due to the removal of any event with $E_{reco} \lesssim 4$ keVee.

The parallel analysis also measures a considerable excess consistent with CEvNS and the SM prediction with a $> 3\sigma$ significance. The resulting flux-averaged cross section, $\sigma_{\text{meas,par}} = (2.2 \pm 0.8) \times 10^{-39} \text{ cm}^2$, agrees extremely well with the measurement presented here and represents an

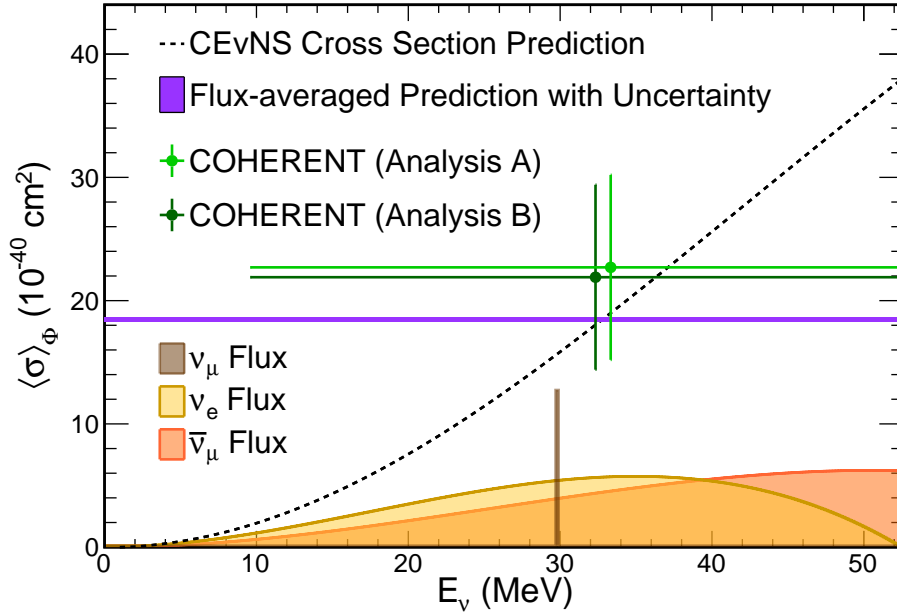


Figure 7.23: Measured CEvNS flux-averaged cross section along with the SM prediction for the two parallel analyses. The result presented in this work is labeled as Analysis A and the parallel analysis is labeled as Analysis B. The flux-averaged cross section measured by the two analyses are in excellent agreement with each other and consistent with the SM prediction.

important check for the first measurement of the CEvNS cross section on argon. The resulting flux-averaged cross section measurements from the two parallel analyses are shown in Fig. 7.23.

7.4.6 CONSTRAINTS ON NON-STANDARD NEUTRINO INTERACTIONS

The measured flux-averaged cross section can be used to place constraints on the allowed non-standard neutrino interaction (NSI) couplings described in Sec. 1.2. Of the ten independent couplings given by Eqn. 1.5, the least well constrained by data (CHARM [13] and oscillation data) [16] before COHERENT are $\epsilon_{ee}^{u,V}$ and $\epsilon_{ee}^{d,V}$. As an example, constraints using the CEvNS cross section result are made on these couplings assuming all other couplings are zero.

NSI appear as a scaling in the CEvNS cross section (Fig. 7.24), so the constraints on these couplings are determined by a comparison of the flux-averaged cross section for each set of NSI couplings to the measured cross section from this dataset. The resulting constraint from the CEvNS cross section measurement is shown in Fig. 7.25 and is consistent with the SM prediction. As the

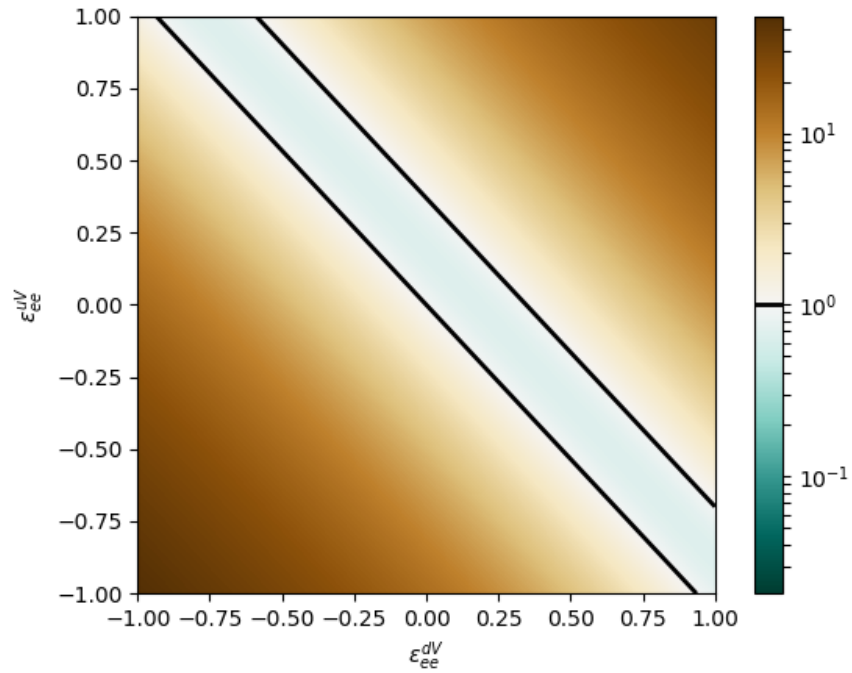


Figure 7.24: Comparison of measured CEvNS cross section to SM CEvNS cross section for constraining NSI parameter space. The black lines show where the cross section is equal to the SM prediction, even in the case of non-zero NSI.

measured flux-averaged cross section is an excess over the SM prediction, the allowed region of NSI couplings separates into two degenerate bands.

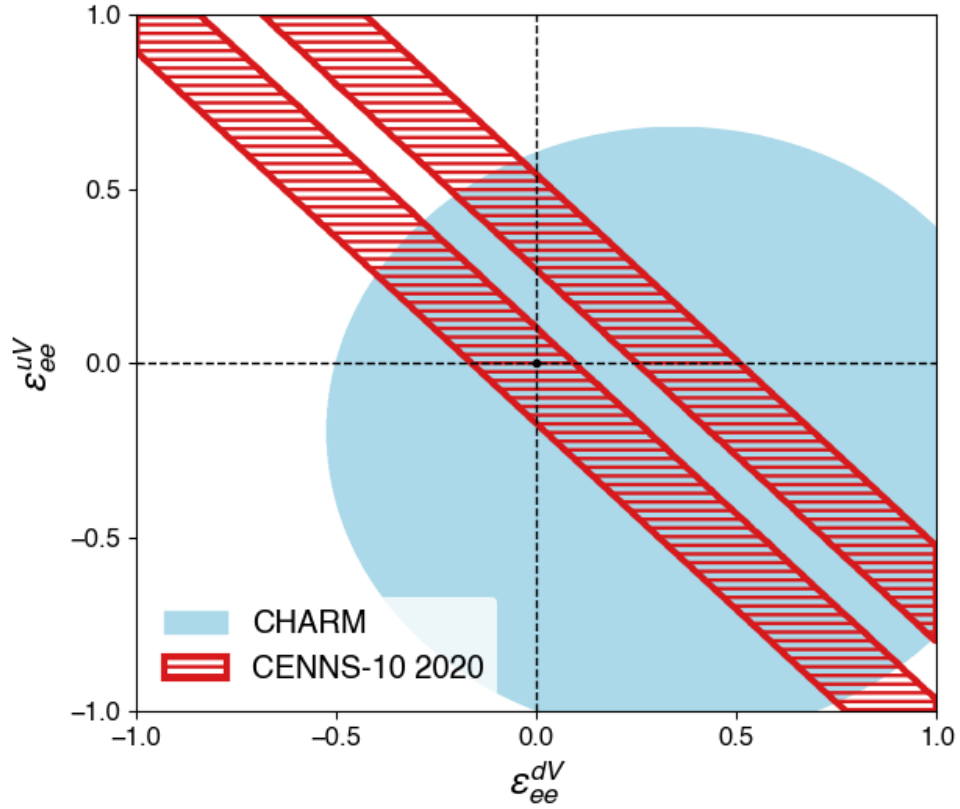


Figure 7.25: Allowed parameter space from this analysis in the two choices of ϵ_{ee} couplings which are least constrained by global data. The allowed region splits into two degenerate bands as a result of the measured cross section being an excess of the SM prediction and the quadratic dependence of the ϵ parameters in the CEvNS cross-section (Eqn. 1.1 and Eqn. 1.6) allowing for degenerate solutions. The measurement is consistent with the SM prediction, shown as the black dashed lines.

CHAPTER 8

CONCLUSIONS

A goal of the COHERENT experiment is to measure the N^2 dependence of the CEvNS cross section through measurements on multiple target nuclei. This goal is met by installing multiple detector targets in Neutrino Alley using neutrinos produced by the SNS. The CsI[Na] detector made the first observation of CEvNS in 2017 [4]. The CENNS-10 liquid argon detector was installed in Neutrino Alley in late 2016 and ran for a short Engineering Run. This run was not sensitive to CEvNS due to the high detector threshold, but was still able to place a limit on the CEvNS cross section and help constrain the beam-related neutron backgrounds [83]. An upgrade to the CENNS-10 detector in the summer of 2017 improved the light collection efficiency of the detector and lowered the energy threshold to be sensitive to CEvNS. The upgrade produced an eight-fold improvement from the light collection efficiency measured in the Engineering Run, lowering the threshold from ~ 80 keVnr to ~ 20 keVnr. Multiple calibration sources, including an *in situ* $^{83\text{m}}\text{Kr}$ calibration, confirm the improvement in the light collection efficiency and measure a linear detector response in the CEvNS region of interest.

A 13.8×10^{22} POT sample of data taken with CENNS-10 over the period of July 2017-December 2018 provides the first detection of CEvNS on argon. A binned likelihood analysis favors the presence of CEvNS over the background-only null hypothesis at $> 3\sigma$. The measured flux-averaged cross section of $(2.3 \pm 0.7) \times 10^{-39} \text{ cm}^2$ is consistent with the SM prediction of $1.8 \times 10^{-39} \text{ cm}^2$. This measurement confirms the CsI[Na] observation of CEvNS while providing a measurement on

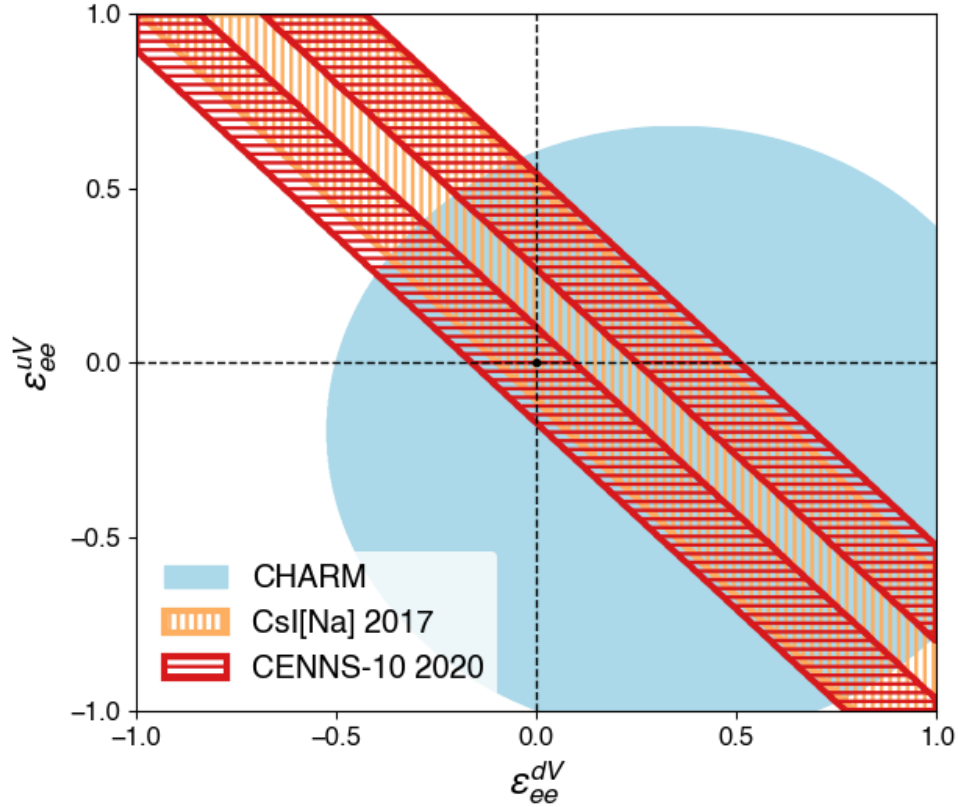


Figure 8.1: Constraints on vector-coupled quark-electron neutrino NSI. Both the CENNS-10 result and the previous CsI[Na] result from [4] are shown. The CENNS-10 result further constrains the parameter space by disfavoring regions allowed by the CsI[Na] measurement. As the measured argon CEvNS cross section is an excess over the SM prediction, the allowed region splits into two degenerate bands. For the CsI[Na] result, being a suppression with respect to the SM, the allowed region is one continuous band. The dashed black lines show the SM prediction at (0,0).

the lightest nuclei to date. The major results presented in this work are published in [148].

Additionally, these results further constrain the allowed parameter space of NSI couplings after the CsI[Na] measurement. The measured argon CEvNS cross section disfavors some of the parameter space allowed by the CsI[Na] measurement. Fig. 8.1 shows the current landscape of measurements of the NSI couplings considered for this result. A joint analysis on the CsI[Na] and CENNS-10 data has not yet been performed and there is natural overlap between the two allowed regions.

The CENNS-10 detector continues operation and has collected an additional > 5 GWhr ($> 11.1 \times 10^{22}$ POT) of data. Along with more refined background measurements, the additional data

will provide a more precise measurement of the CEvNS cross section. After completing its physics run, the CENNS-10 detector is an important test vessel for the future COHERENT liquid argon program.

COHERENT plans measurements of CEvNS with a tonne-scale NaI[Tl] detector array and ~ 10 kg of HPGe detectors, further testing the predicted N^2 dependence of the CEvNS cross section. COHERENT will have three operational CEvNS detectors when the NaI[Tl] and HPGe detector arrays are installed in Neutrino Alley in the near future. Also, a planned tonne-scale D₂O detector will leverage the theoretically well known ν_e -d charged current cross section to measure the SNS neutrino flux to the level of 2-3%. A measurement of the neutrino flux to high precision will reduce a important systematic error for future running of all COHERENT detectors and can be applied to previous COHERENT analyses to lower the flux error.

In the near future, COHERENT plans to replace the CENNS-10 detector with a tonne-scale liquid argon detector, CENNS-750. This detector will leverage the successful operation of CENNS-10 presented here with at least the same energy threshold expected in 25x the active liquid argon volume. CENNS-750 is well equipped to make a precise measurement of the CEvNS cross section on argon with several thousand CEvNS events expected per year of SNS operation. It will also be sensitive to a variety of other physics, including argon inelastic charged/neutral-current cross section measurements important for the DUNE low-energy physics program, accelerator produced dark-matter models [40], further BSM models, and nuclear structure.

BIBLIOGRAPHY

- [1] D. Z. Freedman. “Coherent effects of a weak neutral current.” *Phys. Rev. D* **9**, 1389 (1974).
- [2] V. B. Kopeliovich and L. L. Frankfurt. “Isotopic and chiral structure of neutral current.” *JETP Lett.* **19**, 145–147 (1974).
- [3] F. J. Hasert *et al.* “Observation of neutrino-like interactions without muon or electron in the Gargamelle neutrino experiment.” *Physics Letters B* **46**, 138 – 140 (1973).
- [4] D. Akimov *et al.* (COHERENT). “Observation of Coherent Elastic Neutrino-Nucleus Scattering.” *Science* **357**, 1123–1126 (2017). 1708.01294.
- [5] J. Barranco *et al.* “Probing new physics with coherent neutrino scattering off nuclei.” *Journal of High Energy Physics* **2005**, 021 (2005).
- [6] R. H. Helm. “Inelastic and Elastic Scattering of 187-MeV Electrons from Selected Even-Even Nuclei.” *Phys. Rev.* **104**, 1466–1475 (1956).
- [7] S. R. Klein and J. Nystrand. “Exclusive vector meson production in relativistic heavy ion collisions.” *Phys. Rev. C* **60**, 014903 (1999). 9902259.
- [8] M. Tanabashi *et al.* (Particle Data Group). “Review of Particle Physics.” *Phys. Rev. D* **98**, 030001 (2018).
- [9] P. S. Amanik and G. C. McLaughlin. “Nuclear neutron form factor from neutrino–nucleus coherent elastic scattering.” *Journal of Physics G: Nuclear and Particle Physics* **36**, 015105 (2008).
- [10] B. C. Cañas *et al.* “Future perspectives for a weak mixing angle measurement in coherent elastic neutrino nucleus scattering experiments.” *Physics Letters B* **784**, 159–162 (2018).

- [11] M. Cadeddu and F. Dordei. “Reinterpreting the weak mixing angle from atomic parity violation in view of the Cs neutron rms radius measurement from COHERENT.” *Phys. Rev. D* **99**, 033010 (2019).
- [12] J. Barranco *et al.* “Sensitivity of low energy neutrino experiments to physics beyond the standard model.” *Phys. Rev. D* **76**, 073008 (2007).
- [13] J. Dorenbosch *et al.* “Experimental verification of the universality of electron-neutrino and muon-neutrino coupling to the neutral weak current.” *Phys. Lett.* **180**, 303–307 (1986).
- [14] P. Coloma and T. Schwetz. “Generalized mass ordering degeneracy in neutrino oscillation experiments.” *Phys. Rev. D* **94**, 055005 (2016).
- [15] J. Liao, D. Marfatia, and K. Whisnant. “Degeneracies in long-baseline neutrino experiments from nonstandard interactions.” *Phys. Rev. D* **93**, 093016 (2016).
- [16] P. Coloma *et al.* “Curtailling the dark side in non-standard neutrino interactions.” *Journal of High Energy Physics* **2017**, 116 (2017). ISSN 1029-8479.
- [17] H. Davoudiasl, H.-S. Lee, and W. J. Marciano. “Muon $g - 2$, rare kaon decays, and parity violation from dark bosons.” *Phys. Rev. D* **89**, 095006 (2014).
- [18] M. Abdullah *et al.* “Coherent elastic neutrino nucleus scattering as a probe of a Z prime through kinetic and mass mixing effects.” *Phys. Rev. D* **98**, 015005 (2018). 1803.01224.
- [19] B. Dutta *et al.* “Sensitivity to Z -prime and nonstandard neutrino interactions from ultralow threshold neutrino-nucleus coherent scattering.” *Phys. Rev. D* **93**, 013015 (2016).
- [20] O. G. Miranda *et al.* “Probing neutrino transition magnetic moments with coherent elastic neutrino-nucleus scattering.” *J. High Energ. Phys.* **103** (2019).
- [21] J. Billard, J. Johnston, and B. J. Kavanagh. “Prospects for exploring New Physics in Coherent Elastic Neutrino-Nucleus Scattering.” *JCAP* **11** (2018).

- [22] M. Agostini *et al.* (Borexino). “Limiting neutrino magnetic moments with Borexino Phase-II solar neutrino data.” *Phys. Rev. D* **96**, 091103 (2017).
- [23] F. Zwicky. “Die Rotverschiebung von extragalaktischen Nebeln.” *Helv. Phys. Acta* **6**, 110–128 (1933).
- [24] S. M. Faber and J. S. Gallagher. “Masses and Mass-To-Light Ratios of Galaxies.” *Annual Review of Astronomy and Astrophysics* **17**, 135–187 (1979).
- [25] P. Agnes *et al.* (DarkSide-50). “First results from the DarkSide-50 dark matter experiment at Laboratori Nazionali del Gran Sasso.” *Physics Letters B* **743**, 112009 (2015). 1410.0653.
- [26] E. Aprile *et al.* (XENON). “Dark Matter Search Results from a One Tonne×Year Exposure of XENON1T.” *Phys. Rev. Lett.* **121**, 111302 (2018). 1805.12562.
- [27] D. S. Akerib *et al.* (LUX). “Results from a Search for Dark Matter in the Complete LUX Exposure.” *Phys. Rev. Lett.* **118**, 021303 (2017).
- [28] D. S. Akerib *et al.* (LUX-ZEPLIN). “Projected WIMP sensitivity of the LUX-ZEPLIN (LZ) dark matter experiment.” (2018). 1802.06039.
- [29] C. E. Aalseth *et al.* “DarkSide-20k: A 20 tonne two-phase LAr TPC for direct dark matter detection at LNGS.” *The European Physical Journal Plus* **133**, 131 (2018).
- [30] M. C. Gonzalez-Garcia *et al.* “Neutrino discovery limit of Dark Matter direct detection experiments in the presence of non-standard interactions.” *Journal of High Energy Physics* **2018**, 19 (2018).
- [31] <https://supercdms.slac.stanford.edu/dark-matter-limit-plotter>. Accessed: 2019-12-02.
- [32] P. deNiverville, M. Pospelov, and A. Ritz. “Light new physics in coherent neutrino-nucleus scattering experiments.” *Phys. Rev. D* **92**, 095005 (2015). 1505.07805.

- [33] S.-F. Ge and I. M. Shoemaker. “Constraining Photon Portal Dark Matter with Texono and Coherent Data.” *JHEP* **11**, 066 (2018). 1710.10889.
- [34] B. Dutta, S. Ghosh, and J. Kumar. “Sub-GeV dark matter model.” *Phys. Rev. D* **100**, 075028 (2019).
- [35] B. Dutta *et al.* “Dark matter signals from timing spectra at neutrino experiments.” (2019). 1906.10745.
- [36] B. Lee and S. Weinberg. “Cosmological Lower Bound on Heavy-Neutrino Masses.” *Phys. Rev. Lett.* **39**, 165–168 (1977). URL <https://link.aps.org/doi/10.1103/PhysRevLett.39.165>.
- [37] A. A. Aguilar-Arevalo *et al.* (MiniBooNE). “Dark Matter Search in a Proton Beam Dump with MiniBooNE.” *Phys. Rev. Lett.* **118**, 221803 (2017). 1702.02688.
- [38] Remington Tyler Thornton. *Search for Light Dark Matter Produced in a Proton Beam Dump*. Ph.D. thesis, Indiana U. (2017).
- [39] A. A. Aguilar-Arevalo *et al.* (MiniBooNE-DM). “Dark matter search in nucleon, pion, and electron channels from a proton beam dump with MiniBooNE.” *Phys. Rev. D* **98**, 112004 (2018).
- [40] D. Akimov *et al.* (COHERENT). “Sensitivity of the COHERENT Experiment to Accelerator-Produced Dark Matter.” (2019). 1911.06422.
- [41] W. Xiong *et al.* “A small proton charge radius from an electron-proton scattering experiment.” *Nature* **575**, 147–150 (2019).
- [42] N. Bezginov *et al.* “A measurement of the atomic hydrogen Lamb shift and the proton charge radius.” *Science* **365**, 1007–1012 (2019).

- [43] M. Cadeddu *et al.* “Average CsI Neutron Density Distribution from COHERENT Data.” *Phys. Rev. Lett.* **120**, 072501 (2018).
- [44] X.-R. Huang and L.-W. Chen. “Neutron skin in CsI and low-energy effective weak mixing angle from COHERENT data.” *Phys. Rev. D* **100**, 071301 (2019).
- [45] W. R. Johnson and G. Soff. “The lamb shift in hydrogen-like atoms, $1 \leq Z \leq 110$.” *Atomic Data and Nuclear Data Tables* **33**, 405–446 (1985).
- [46] S. Abrahamyan *et al.* (PREX). “Measurement of the Neutron Radius of ^{208}Pb through Parity Violation in Electron Scattering.” *Phys. Rev. Lett.* **108**, 112502 (2012).
- [47] C. J. Horowitz *et al.* “Weak charge form factor and radius of ^{208}Pb through parity violation in electron scattering.” *Phys. Rev. C* **85**, 032501 (2012).
- [48] C. J. Horowitz, K. S. Kumar, and R. Michaels. “Electroweak measurements of neutron densities in CREX and PREX at JLab, USA.” *Eur. Phys. J. A* **50** (2014).
- [49] K. M. Patton *et al.* “Neutrino-nucleus coherent scattering as a probe of neutron density distributions.” *Phys. Rev. C* **86**, 024612 (2012). ISSN 0556-2813.
- [50] K. Hirata *et al.* “Observation of a neutrino burst from the supernova SN1987A.” *Phys. Rev. Lett.* **58**, 1490–1493 (1987).
- [51] R. M. Bionta *et al.* “Observation of a neutrino burst in coincidence with supernova 1987A in the Large Magellanic Cloud.” *Phys. Rev. Lett.* **58**, 1494–1496 (1987).
- [52] E. N. Alexeyev *et al.* “Detection of the neutrino signal from SN 1987A in the LMC using the INR Baksan underground scintillation telescope.” *Phys. Lett. B* **105**, 209–214 (1988).
- [53] H.-T. Janka. *Neutrino Emission from Supernovae*, pp. 1575–1604 (Springer International Publishing, Cham, 2017). ISBN 978-3-319-21846-5.

- [54] C. J. Horowitz *et al.* “Nonuniform neutron-rich matter and coherent neutrino scattering.” *Phys. Rev. C* **70**, 065806 (2004).
- [55] J. R. Wilson. “Coherent Neutrino Scattering and Stellar Collapse.” *Phys. Rev. Lett.* **32**, 849–852 (1974).
- [56] D. Z. Freedman, D. N. Schramm, and D. L. Tubbs. “The Weak Neutral Current and its Effects in Stellar Collapse.” *Ann. Rev. Nucl. Sci.* **27**, 167–207 (1977).
- [57] C. J. Horowitz, K. J. Coakley, and D. N. McKinsey. “Supernova observation via neutrino-nucleus elastic scattering in the CLEAN detector.” *Phys. Rev. D* **68**, 023005 (2003).
- [58] T. E. Mason *et al.* “The Spallation Neutron Source in Oak Ridge: A powerful tool for materials research.” *Physica B: Condensed Matter* **385-386**, 955–960 (2006).
- [59] O. Moreno and T. W. Donnelly. “Unified approach to electron and neutrino elastic scattering off nuclei with an application to the study of the axial structure.” *Phys. Rev. C* **92**, 055504 (2015).
- [60] S. Agostinelli *et al.* “Geant4—a simulation toolkit.” *Nucl. Instrum. Meth. A* **506**, 250–303.
- [61] J. Allison *et al.* “Geant4 developments and applications.” *IEEE Transactions on Nuclear Science* **53**, 270–278 (2006).
- [62] R. Rapp (COHERENT). “COHERENT Plans for D₂O at the Spallation Neutron Source.” (2019). 1910.00630.
- [63] S. Ajimura *et al.* “Technical Design Report (TDR): Searching for a Sterile Neutrino at J-PARC MLF (E56, JSNS2).” (2017). 1705.08629.
- [64] D. Akimov *et al.* (COHERENT). “COHERENT 2018 at the Spallation Neutron Source.” (2018). 1803.09183.

- [65] J. Engel, S. Pittel, and P. Vogel. “Capture of solar and higher-energy neutrinos by ^{127}I .” *Phys. Rev. C* **50**, 1702–1708 (1994).
- [66] J. R. Distel *et al.* “Measurement of the cross section for the reaction $^{127}\text{I}(\nu_e, e^-)^{127}\text{Xe}_{\text{boundstates}}$ with neutrinos from the decay of stopped muons.” *Phys. Rev. C* **68**, 054613 (2003).
- [67] S. Nakamura *et al.* “Neutrino–deuteron reactions at solar neutrino energies.” *Nucl. Phys. A* **707**, 561–576 (2002).
- [68] J. I. Collar *et al.* “Coherent neutrino-nucleus scattering detection with a CsI[Na] scintillator at the SNS spallation source.” *Nucl. Instrum. Meth. A* **773**, 56–65 (2015).
- [69] J. T. M. de Haas and P. Dorenbos. “Advances in Yield Calibration of Scintillators.” *Nuclear Science, IEEE Transactions on* **55**, 1086 – 1092 (2008).
- [70] “Spallation neutron source final safety assessment document for neutron facilities. Oak Ridge National Laboratory Report 102030102-ES0016-R03.” (2011).
- [71] H. H. Loosli and H. Oeschger. “Detection of ^{39}Ar in atmospheric argon.” *Earth and Planetary Science Letters* **5**, 191–198 (1968).
- [72] P. Benetti *et al.* “Measurement of the specific activity of ^{39}Ar in natural argon.” *Nucl. Instrum. Meth. A* **574**, 83–88 (2007).
- [73] D. Acosta-Kane *et al.* “Discovery of underground argon with low level of radioactive ^{39}Ar and possible applications to WIMP dark matter detectors.” *Nucl. Instrum. Meth. A* **587**, 46–51 (2012).
- [74] J. Xu *et al.* “A study of the trace ^{39}Ar content in argon from deep underground sources.” *Astroparticle Physics* **66**, 53–60 (2015).

- [75] H. O. Back *et al.* “First Large Scale Production of Low Radioactivity Argon from Underground Sources.” (2012). 1204.6024v2.
- [76] H. O. Back *et al.* “First Commissioning of a Cryogenic Distillation Column for Low Radioactivity Underground Argon.” (2012). 1204.6061v2.
- [77] P. Agnes *et al.* (DarkSide). “Results From the First Use of Low Radioactivity Argon in a Dark Matter Search.” *Phys. Rev. D* **93**, 081101 (2016). [Addendum: *Phys. Rev. D* 95,no.6,069901(2017)].
- [78] C. J. Werner *et al.* (MCNP). “MCNP Users Manual - Code Version 6.2.” (2017).
- [79] N. Mascarenhas *et al.* “Results With the Neutron Scatter Camera.” *IEEE Transactions on Nuclear Science* **56**, 1269–1273 (2009).
- [80] R. Tayloe *et al.* “A large-volume detector capable of charged-particle tracking.” *Nucl. Instrum. Meth. A* **562**, 198–206 (2006).
- [81] R. L. Cooper *et al.* “SciBath: A Novel Tracking Detector for Measuring Neutral Particles Underground.” *Proceedings, Meeting of the Division of the American Physical Society, DPF 2011, Providence, USA, August 9-13, 2011* (2011). 1110.4432.
- [82] M. R. Heath. *A First Search for Coherent Elastic Neutrino-Nucleus Scattering with Liquid Argon*. Ph.D. thesis, Indiana U., Bloomington (main) (2019). 10.5967/jmrj-9078.
- [83] D. Akimov *et al.* (COHERENT). “First Constraint on Coherent Elastic Neutrino-Nucleus Scattering in Argon.” *Phys. Rev. D* **100**, 115020 (2019). 1909.05913.
- [84] G. M. Fuller, W. C. Haxton, and G. C. McLaughlin. “Prospects for detecting supernova neutrino flavor oscillations.” *Phys. Rev. D* **59**, 085005 (1999).
- [85] E. Kolbe and K. Langanke. “Role of ν – induced reactions on lead and iron in neutrino detectors.” *Phys. Rev. C* **63**, 025802 (2001). 0003060.

- [86] J. Engel, G. C. McLaughlin, and C. Volpe. “What can be learned with a lead-based supernova-neutrino detector?” *Phys. Rev. D* **67**, 013005 (2003).
- [87] K. Zuber (HALO). “HALO, a supernova neutrino observatory.” *Nuclear and Particle Physics Proceedings* **265-266**, 233–235 (2015).
- [88] S. R. Elliott. “Measuring supernova neutrino temperatures using lead perchlorate.” *Phys. Rev. C* **62**, 065802 (2000).
- [89] <https://p25ext.lanl.gov/~lee/CaptainMills/>. Coherent Captain-Mills (CCM) Experiment.
- [90] J. Hakenmüller *et al.* (CONUS). “Neutron-induced background in the CONUS experiment.” *The European Physical Journal C* **79**, 699 (2019).
- [91] V. Belov *et al.* (ν GeN). “The ν GeN experiment at the Kalinin Nuclear Power Plant.” *Journal of Instrumentation* **10**, P12011–P12011 (2015).
- [92] H. T. Wong. “Taiwan EXperiment On Neutrino - History and Prospects.” *International Journal of Modern Physics A* **33** (2018).
- [93] G. Agnolet *et al.* (MINER). “Background Studies for the MINER Coherent Neutrino Scattering Reactor Experiment.” (2016). 1609.02066.
- [94] R. Strauss *et al.* (ν -cleus). “The ν -cleus experiment: a gram-scale fiducial-volume cryogenic detector for the first detection of coherent neutrino–nucleus scattering.” *The European Physical Journal C* **77**, 506 (2017).
- [95] J. Billard *et al.* (Ricochet). “Coherent neutrino scattering with low temperature bolometers at Chooz reactor complex.” *Journal of Physics G: Nuclear and Particle Physics* **44**, 105101 (2017).

- [96] A. A. Aguilar-Arevalo *et al.* (CONNIE). “Exploring low-energy neutrino physics with the Coherent Neutrino Nucleus Interaction Experiment.” *Phys. Rev. D* **100**, 092005 (2019).
- [97] D. Aristizabal Sierra *et al.* “Proceedings of The Magnificent CE ν NS Workshop 2018.” (2019). 1910.07450.
- [98] Magnificent CE ν NS 2019. <https://indico.cern.ch/event/844613/overview>.
- [99] T. Doke, K. Masuda, and E. Shibamura. “Estimation of absolute photon yields in liquid argon and xenon for relativistic (1 MeV) electrons.” *Nucl. Instrum. Meth. A* **291**, 617–620 (1990).
- [100] `darkmatter.ethz.ch`. Accessed: 2019-11-25.
- [101] C. Regenfus *et al.* “Study of nuclear recoils in liquid argon with monoenergetic neutrons.” *J. Phys.: Conf. Ser.* **375**, 012019 (2012).
- [102] R. Acciarri *et al.* “Effects of Nitrogen Contamination in Liquid Argon.” *JINST* **5**, P06003 (2010).
- [103] E. Morikawa *et al.* “Argon, krypton, and xenon excimer luminescence: From the dilute gas to the condensed phase.” *The Journal of Chemical Physics* **91**, 1469–1477 (1989).
- [104] T. Heindl *et al.* “The scintillation of liquid argon.” *EPL (Europhysics Letters)* **91**, 62002 (2010).
- [105] V. M. Gehman *et al.* “Fluorescence Efficiency and Visible Re-emission Spectrum of Tetraphenyl Butadiene Films at Extreme Ultraviolet Wavelengths.” *Nucl. Instrum. Meth. A* **654**, 116–121 (2011).
- [106] C. Benson *et al.* “Measurements of the intrinsic quantum efficiency and absorption length of tetraphenyl butadiene thin films in the vacuum ultraviolet regime.” *The European Physical Journal C* **78**, 329 (2018). ISSN 1434-6052.

- [107] D. Gastler *et al.* “Measurement of scintillation efficiency for nuclear recoils in liquid argon.” *Phys. Rev. C* **85**, 065811 (2012). 1004.0373.
- [108] W. Creus *et al.* “Scintillation efficiency of liquid argon in low energy neutron-argon scattering.” *JINST* **10**, P08002 (2015). 1504.07878.
- [109] H. Cao *et al.* (SCENE). “Measurement of scintillation and ionization yield and scintillation pulse shape from nuclear recoils in liquid argon.” *Phys. Rev. D* **91**, 092007 (2015). 1406.4825.
- [110] P. Agnes *et al.* (ARIS). “Measurement of the liquid argon energy response to nuclear and electronic recoils.” *Phys. Rev. D* **97**, 112005 (2018). 1801.06653.
- [111] B. Suh and R. Tayloe (COHERENT). “COHERENT Technical Note 019: Extraction of Argon Quenching Factor from a Combined Data Set.” (2019).
- [112] S. J. Brice *et al.* “A method for measuring coherent elastic neutrino-nucleus scattering at a far off-axis high-energy neutrino beam target.” *Phys. Rev. D* **89**, 072004 (2014). 1311.5958.
- [113] <https://www.thinksrs.com/products/uga.html>. Accessed: 2020-01-14.
- [114] <https://www.cryomech.com/products/pt90/>. Accessed: 2020-01-15.
- [115] https://www.metalbellows.com/assets/OTS_Pumps-Compressors.pdf. Accessed: 2020-01-15.
- [116] <http://www.saespuregas.com/Products/Gas-Purifier/Part-Number-Example-monotorr.html>. Accessed: 2020-01-15.
- [117] <https://www.entegris.com/shop/en/USD/products/gas-filtration-and-purification/gas-purifiers/GateKeeper-HGU-Heated-Getter-Gas-Purifiers/p/GateKeeperHGUHeatedGetterGasPurifiers>. Accessed: 2020-01-15.

- [118] <https://epics-controls.org>. Accessed: 2019-12-19.
- [119] https://controlsoftware.sns.ornl.gov/css_phoebus/. Accessed: 2019-12-19.
- [120] T. T. Böhlen *et al.* (FLUKA). “The FLUKA Code: Developments and Challenges for High Energy and Medical Applications.” *Nuclear Data Sheets* **120**, 211–214 (2014).
- [121] A. Ferrari *et al.* (FLUKA). “FLUKA: a multi-particle transport code.” CERN-2005-10 (2005), INFN\TC_05\11, SLAC-R-773.
- [122] <https://assmann-usa.com/products/vertical-storage-tanks>. Accessed: 2020-01-14.
- [123] S. Amerio *et al.* “Design, construction and tests of the ICARUS T600 detector.” *Nucl. Instrum. Meth. A* **527**, 329–410 (2004).
- [124] D. N. McKinsey *et al.* “Fluorescence efficiencies of thin scintillating films in the extreme ultraviolet spectral region.” *Nucl. Instrum. Meth. B* **132**, 351 – 358 (1997).
- [125] C. H. Lally *et al.* “UV quantum efficiencies of organic fluors.” *Nucl. Instrum. Meth. B* **117**, 421–427 (1996).
- [126] <https://intlvac.com>. Accessed: 2020-01-15.
- [127] <https://www.rigolna.com/products/waveform-generators/dg4162/>. Accessed: 2020-02-10.
- [128] B. M. Loer. “bloer/daqman: Citation Release.” (2019).
- [129] B. M. Loer. *Towards a Depleted Argon Time Projection Chamber WIMP Search : DarkSide Prototype Analysis and Predicted Sensitivity*. Ph.D. thesis, Princeton U. (2011).
- [130] P.-A. Amaudruz *et al.* “In-situ characterization of the Hamamatsu R5912-HQE photomultiplier tubes used in the DEAP-3600 experiment.” *Nucl. Instrum. Meth. A* **922**, 373–384 (2019).

- [131] E. A. McCutchan. “Nuclear Data Sheets for $A = 83$.” *Nuclear Data Sheets* **125**, 201 (2015).
- [132] M. Zbořil *et al.* “Ultra-stable implanted $^{83}\text{Rb}/^{83\text{m}}\text{Kr}$ electron sources for the energy scale monitoring in the KATRIN experiment.” *JINST* **8** (2013).
- [133] R. B. Firestone and V. S. Shirley. *Table of isotopes* (John Wiley and Sons, Inc., 1996), 8th edition.
- [134] P. Agnes *et al.* (DarkSide). “CALIS—A CALibration Insertion System for the DarkSide-50 dark matter search experiment.” *JINST* **12**, T12004 (2017).
- [135] R. Saldanha. Private communication.
- [136] W. H. Lippincott *et al.* “Calibration of liquid argon and neon detectors with $^{83}\text{Kr}^m$.” *Phys. Rev. C* **81**, 045803 (2010). 0911.5453.
- [137] L. W. Kastens *et al.* “Calibration of a liquid xenon detector with $^{83\text{m}}\text{Kr}$.” *Phys. Rev. C* **80**, 045809 (2009).
- [138] L. W. Kastens *et al.* “A $^{83}\text{Kr}^m$ source for use in low-background liquid Xenon time projection chambers.” *JINST* **5**, P05006 (2010).
- [139] J. W. Marsh, D. J. Thomas, and M. Burke. “High resolution measurements of neutron energy spectra from Am-Be and Am-B neutron sources.” *Nucl. Instrum. Meth. A* **366**, 340–348 (1995).
- [140] M. R. Heath and J. Zettlemoyer. “CENNS-10 simulation readme. Technical Report - Indiana University.” (2018).
- [141] J. B. Birks. *The Theory and Practice of Scintillation Counting*, volume 27 of *International Series of Monographs in Electronics and Instrumentation* (Pergamon, London, 1964).

- [142] J. B. Birks. “Scintillations from organic crystals: specific fluorescence and relative response to different radiations.” *Proceedings of the Physical Society. Section A* **64**, 874 (1951).
- [143] S. Amoruso *et al.* (ICARUS). “Study of electron recombination in liquid argon with the ICARUS TPC.” .
- [144] R. Tayloe. “Figure of Merit for Cut Optimization in CENNS-10/COHERENT Analysis.” (2018).
- [145] W. Verkerke and D. P. Kirkby. “The RooFit toolkit for data modeling.” *eConf* **C0303241**, MOLT007 (2003). [186(2003)], physics/0306116.
- [146] G. Cowan. “Statistical Methods for Particle Physics Lecture 3: parameter estimation.” www.pp.rhul.ac.uk/~cowan/stat_aachen.html.
- [147] S. S. Wilks. “The Large-Sample Distribution of the Likelihood Ratio for Testing Composite Hypotheses.” *Ann. Math. Statist.* **9**, 60–62 (1938).
- [148] D. Akimov *et al.* “First Detection of Coherent Elastic Neutrino-Nucleus Scattering on Argon.” (2020). *Submitted to Phys. Rev. Lett.*, 2003.10630.
- [149] E. Grace *et al.* “Index of refraction, Rayleigh scattering length, and Sellmeier coefficients in solid and liquid argon and xenon.” (2015). 1502.04213.
- [150] T. Doke *et al.* “Scintillation yields by relativistic heavy ions and the relation between ionization and scintillation in liquid argon.” *Nucl. Instrum. Meth. A* **235**, 136–141 (1985).

APPENDIX A

TUNED SIMULATION PARAMETERS

Tuned MC parameters	
Ar scintillation Yield	40 $\frac{\gamma}{keV}$
PMT QE	18%
TPB Efficiency	1.64
TPB Transmission Probability (Visible Light)	100%
Teflon Reflection Probability (Visible)	99.0%
TPB Thickness	2 μm
TPB Attenuation Length (Visible)	Top Cylinder: 0.5 mm Center Cylinder: 0.5 mm Bottom Cylinder: 0.5 mm
PMT TPB Attenuation Length (Visible)	Top PMT: 0.5 mm Bottom PMT: 0.5 mm
PMT TPB Reflection Probability (Visible)	Top PMT: 11% Bottom PMT: 16%
Cylinder TPB Reflection Probability (Visible)	0.0%
LAr Scintillation spectrum	128 nm
LAr Rayleigh Scattering	from [149]
LAr Index of Refraction	from [149]
Fano factor	0.1 [150]
Singlet time constant	6 ns
Triplet time constant	1.3 μs
LAr absorption length	20 m (all λ)

Table A.1: Description of parameters used within the CENNS-10 GEANT4 simulation.

Jacob C. Zetlemoyer

Curriculum Vitae

Education

Ph.D. Physics, May 2020	Indiana University, Bloomington, IN
M.S. Physics, 2015	Indiana University, Bloomington, IN
B.S. Physics, 2014	Drexel University, Philadelphia, PA

Research Experience

Research Assistant, Indiana University, COHERENT Experiment, June 2016-present

CENNS-10 Liquid Argon Detector for COHERENT

- Designed and implemented light collection upgrade of the CENNS-10 liquid argon detector based on literature. Improved light collection efficiency by a factor of ~ 10 by replacing TPB coated acrylic cylinder with evaporatively coated teflon cylinder and TPB coated PMTs.
- After the upgrade, installed the upgraded CENNS-10 detector with additional shielding at the Spallation Neutron Source at Oak Ridge National Laboratory. Fully calibrated detector response using LED pulser, gamma and neutron sources. Co-lead day to day operations of the CENNS-10 detector at the SNS after the upgrade.
- Led effort to fully simulate the upgraded CENNS-10 liquid argon detector using the Geant4 package. Implemented CENNS-10 geometry and full optical photon simulation to recreate detector response and characterization of backgrounds and calibration sources.
- Developed algorithms with a C++/ROOT framework to process data from the upgraded CENNS-10 detector and push detector thresholds as low as possible and take advantage of pulse shape discrimination capabilities of liquid argon detectors.
- Performed analysis of the first physics data from the CENNS-10 liquid argon detector which successfully made the first measurement of coherent elastic neutrino-nucleus scattering (CEvNS) on a liquid argon target with the CENNS-10 detector.
- Built liquid argon test chamber at Oak Ridge National Laboratory meant for R&D studies for a ton-scale detector for COHERENT which could be used for gas-dopant, wavelength shifter, and readout tests for future liquid argon detectors.

Research Assistant, Indiana University, EXO-200 and nEXO Liquid Xenon Experiments, August 2014-June 2016

- Modelled the preliminary design of the nEXO detector and simulated cosmogenic backgrounds using the Geant4 and FLUKA simulation packages. Results used in preliminary estimation of detector sensitivity.
- Designed and built small chamber to test cold electronics at liquid xenon temperature. Chamber used to test prototype silicon photomultiplier (SiPM) readout electronics designed for the nEXO experiment.

Awards

2020 William Koss Memorial Award, Indiana University Department of Physics

U.S. Department of Energy Office of Science Graduate Research (SCGSR) Fellow June 2017-June 2018

Leadership Positions

COHERENT CENNS-10 Liquid Argon Detector Shift Coordinator June 2018-April 2020

Professional Affiliations

Member, American Physical Society; Division of Particles and Fields, Division of Nuclear Physics, Forum for Early Career Scientists, Forum for Graduate Student Affairs.

Teaching Experience

Teaching Assistant, Physics P222 for science majors, recitation instructor, Spring 2016

Teaching Assistant, Physics P201 for non-science majors, laboratory instructor, Fall 2014, Spring 2015

Publications

Papers

1. D. Akimov *et al.* [COHERENT Collaboration] "First Detection of Coherent Elastic Neutrino-Nucleus Scattering on Argon," arXiv:2003.10630 [hep-ex].
2. D. Akimov *et al.* [COHERENT Collaboration] "Sensitivity of the COHERENT Experiment to Accelerator-Produced Dark Matter," arXiv:1911.06422 [hep-ex].
3. D. Akimov *et al.* [COHERENT Collaboration] "First Constraint on Coherent Elastic Neutrino-Nucleus Scattering in Argon," Phys. Rev. D. **100** (2019) no.11, 115020.
4. D. Akimov *et al.* [COHERENT Collaboration] "Observation of Coherent Elastic Neutrino-Nucleus Scattering," Science **357** (2017) no.6356, 1123-1126.
5. D. Akimov *et al.* [COHERENT Collaboration] "COHERENT 2018 At the Spallation Neutron Source," arXiv:1803.09183 [physics.ins-det].
6. J. B. Albert *et al.* [nEXO Collaboration] "Sensitivity and Discovery Potential of nEXO to Neutrinoless Double Beta Decay," Phys.Rev. C. **97** (2018) no.6, 065503.
7. J. B. Albert *et al.* [EXO-200 Collaboration] "Search for Neutrinoless Double Beta Decay with the Upgraded EXO-200 Detector," Phys.Rev.Lett. **120** (2018) no.7, 072701.
8. J. B. Albert *et al.* [EXO-200 Collaboration] "Searches for Double Beta Decay of ^{134}Xe with EXO-200," Phys.Rev. D **96** (2017) no.9, 092001.

9. J. B. Albert *et al.* [EXO-200 Collaboration] "Search for nucleon decays with EXO-200," *Phys.Rev. D* **97** (2018) no.7, 072007.
10. D. S. Leonard *et al.* [EXO-200 Collaboration] "Trace radioactive impurities in final construction materials for EXO-200," *Nucl.Instrum.Meth. A* **871** (2017) 169-179.
11. J. B. Albert *et al.* [EXO-200 Collaboration] "Measurement of the Drift Velocity and Transverse Diffusion of Electrons in Liquid Xenon with the EXO-200 Detector," *Phys.Rev. C* **95** (2017) no.2, 025502.

Talks and Posters

1. "First Detection of CEvNS on an Argon Target with the CENNS-10 Liquid Argon Detector", Invited Talk. Fermilab Special Seminar, Batavia, IL, January 2020.
2. "First Detection of CEvNS on an Argon Target with the CENNS-10 Liquid Argon Detector", Invited Talk. Lawrence Livermore National Laboratory Special Seminar, Livermore, CA, January 2020.
3. "New Results from a CEvNS Search with the CENNS-10 Liquid Argon Detector", Invited Talk. Fermilab Joint Experimental-Theoretical Physics Seminar, Batavia, IL, January 2020.
4. "Results of a CEvNS Search with the CENNS-10 Liquid Argon Detector", Invited Talk. Magnificent CEvNS 2019, Chapel Hill, NC, November 2019.
5. "Prospects for a CEvNS Measurement on a Liquid Argon Target", Invited Talk. Lawrence Berkeley National Laboratory, March 2019.
6. "COHERENT: First Results and Prospects for a CEvNS Measurement on a Liquid Argon Target", Invited Talk. Particle and Astrophysics Seminar, University of Tennessee, Knoxville, February 2019.
7. "The World's Smallest Neutrino Detector: First Measurement of Coherent Elastic Neutrino Nucleus Scattering (CEvNS)", Invited Talk. Undergraduate Research Seminar, Tennessee Technological University, March 2018.
8. "Results of a CEvNS Search with the CENNS-10 Liquid Argon Detector", Contributed Talk. 2019 Fall Meeting of the APS Division of Nuclear Physics, Crystal City, VA, October 2019.
9. "A Search for CEvNS with the CENNS-10 Liquid Argon Detector for COHERENT," Contributed Talk, Workshop: The Magnificent CEvNS, Chicago, IL, November 2018.
10. "Measuring Coherent Elastic Neutrino Nucleus Scattering with the CENNS-10 Liquid Argon Detector", Poster Presentation. Neutrino 2018 - XXVIII International Conference on Neutrino Physics and Astrophysics, Heidelberg, Germany, June 2018.
11. "Status of the CENNS-10 Liquid Argon Detector for the COHERENT Experiment", Contributed Talk. 2017 Fall Meeting of the APS Division of Nuclear Physics, Pittsburgh, PA, October 2017.
12. "Detector Technologies for the COHERENT Experiment", Contributed Talk. APS April Meeting 2017, Washington, DC. January 2017.

13. "Studying Coherent Elastic Neutrino-Nucleus Scattering in Liquid Argon at the SNS", Indiana University Nuclear Physics Seminar, November 2016.